Leon Mishnaevsky Jr

COMPUTATIONAL MESOMECHANICS OF COMPOSITES

Numerical analysis of the effect of microstructures of composites on their strength and damage resistance

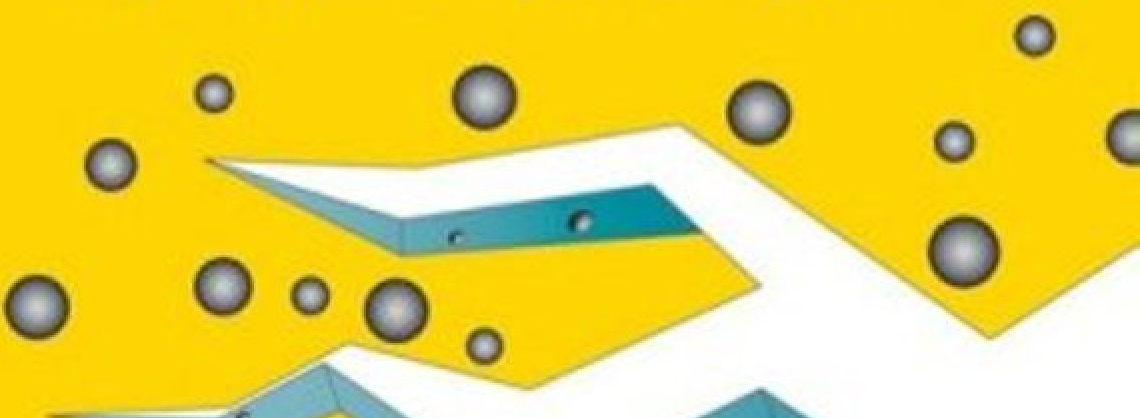

WILEY

Computational Mesomechanics of Composites

Numerical analysis of the effect of microstructures of composites on their strength and damage resistance

LEON MISHNAEVSKY JR

Risø National Laboratory, Technical University of Denmark, Roskilde, Denmark

John Wiley & Sons, Ltd

Computational Mesomechanics of Composites

Numerical analysis of the effect of microstructures of composites on their strength and damage resistance

LEON MISHNAEVSKY JR

Risø National Laboratory, Technical University of Denmark, Roskilde, Denmark

John Wiley & Sons, Ltd

Other Wiley Editorial Offices

John Wiley & Sons Inc., 111 River Street, Hoboken, NJ 07030, USA

Jossey-Bass, 989 Market Street, San Francisco, CA 94103-1741, USA

Wiley-VCH Verlag GmbH, Boschstr. 12, D-69469 Weinheim, Germany

John Wiley & Sons Australia Ltd, 42 McDougall Street, Milton, Queensland 4064, Australia

John Wiley & Sons (Asia) Pte Ltd, 2 Clementi Loop #02-01, Jin Xing Distripark, Singapore 129809

John Wiley & Sons Canada Ltd, 6045 Freemont Blvd, Mississauga, Ontario, L5R 4J3, Canada

Wiley also publishes its books in a variety of electronic formats. Some content that appears in print may not be available in electronic books.

Anniversary Logo Design: Richard J. Pacifico

Library of Congress Cataloging in Publication Data

Mishnaevsky, L. (Leon)
Computational mesomechanics of composites : numerical analysis of the effect of microstructures of composites on their strength and damage resistance / Leon Mishnaevsky, Jr.
p. cm.
ISBN 978-0-470-02764-6 (cloth)
1. Composite materials—Mechanical properties—Mathematical models. 2. Micromechanics—Mathematical models. 3. Numerical analysis. I. Title.
TA418.9.C6M588 2007
620.1′183—dc22 2007013494

British Library Cataloguing in Publication Data

A catalogue record for this book is available from the British Library

ISBN 978-0-470-02764-6

Typeset in 10/12pt Times by Integra Software Services Pvt. Ltd, Pondicherry, India
Printed and bound in Great Britain by Antony Rowe Ltd, Chippenham, Wiltshire
This book is printed on acid-free paper responsibly manufactured from sustainable forestry in which at least two trees are planted for each one used for paper production.

Contents

About the Author

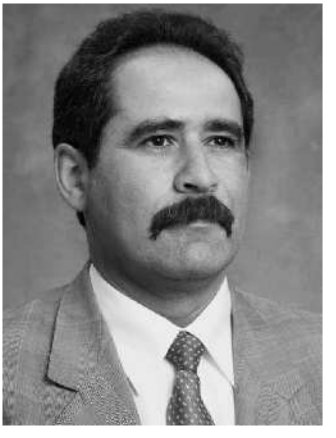

Leon Mishnaevsky Jr, born in 1964 in Kiev (Ukraine), graduated from the Kiev Civil Engineering University in 1987, received his doctorate from the USSR Academy of Sciences in 1991 and his Dr.-Habil. degree in Mechanics from the Darmstadt University of Technology (Germany) in 2005. From 1981 till 1994 he worked at the Institute for Superhard Materials, Ukrainian Academy of Sciences, Kiev. After a one year research stay at the Vienna University of Technology (Austria) in 1994–1995, he joined the State Materials Testing Institute (MPA), University of Stuttgart as a Humboldt fellow and later as a Research Associate. After being awarded the Heisenberg Fellowship of the German Research Council (DFG) in 2003, he started his work at the Darmstadt University of Technology, sharing his time between Darmstadt and Stuttgart. The author has held appointments as a Visiting Research Professor at the Rutgers University (USA), Visiting Scholar at The University of Tokyo, and Science University of Tokyo (Japan) and Massachusetts Institute of Technology (USA), Invited Professor at the China University of Mining and Technology (China) and Ecole Nationale Supérieure d'Arts et Métiers (France). His honors include Fellowships of the Japan Society for the Promotion of Science (JSPS) and Japan Science and Technology Agency (STA), Engineering Foundation Fellowship, Humboldt Fellowship, as well as the Heisenberg Fellowship of the DFG, mentioned above. After his Habilitation, he joined the Risø National Laboratory in Denmark as a Senior Scientist. He has published a book *Damage and Fracture in Heterogeneous Materials* and over 100 research papers in the areas of computational mechanics of materials, micromechanics, fracture and damage mechanics, tribology and mechanical engineering.

Preface

The strength and damage resistance of parts and components, made from composite materials, determine the quality and reliability of machines and devices, used in many areas of industry and in everyday life. The mechanical properties and strength of composites depend on their microstructures, i.e. on the content, geometries, distribution and properties of phases and constituents in the composites. This dependence can be used to improve the reliability, strength and damage resistance of the materials. For example, drilling tools, produced from hard alloys with graded microstructures, exhibit four to five times higher service life than the tools made from the alloys with homogeneous microstructures (Lisovsky, 2001). The fracture toughness and lifetime of tool steels are increased by 30 % if large primary carbides in the steels are replaced by dense dispersion of small carbides ('double dispersion' structure) (Berns *et al.*, 1998). The fracture toughness of metal matrix composites can be doubled, if the reinforcing elements are localized in layers, which alternate with layers of unreinforced metal matrix (McLelland *et al.*, 1999). The fracture toughness of Al_2O_3 ceramics can be increased 2.3 times by introducing SiC nanoparticles in the ceramics (Tan and Yang, 1998). There are a lot of examples of unusual properties of biomaterials, which are related to their peculiar microstructures. For instance, nacre, mother of pearl, which consists of 95 % $CaCO_3$, has a work of fracture that is 3000 times more than that of the monolithic $CaCO_3$ (Ramachamndra Rao, 2003). The high fracture toughness of nacre is determined, among other factors, by the brick-mortar, layered microstructure of nacre, and the interlocking of the mineral platelets (Sarikaya *et al.*, 2002; Katti *et al.*, 2005).

Thus, service properties, strength and damage resistance of composites can be improved by changing their microstructures. With the development of material technologies (e.g. powder metallurgy, heat treatment technology, nanotechnology, etc.), the production of materials with required, pre-defined microstructures became technologically possible. Therefore, the problem of the determination of the optimal microstructures of composites has acquired practical importance.

In order to investigate interrelationships between the microstructures and strength of composites, a lot of experimental, theoretical and numerical investigations have been carried out. In many cases, links between some averaged parameters of microstructures (e.g. grain size, volume content of phases and distance between inclusions) and the overall properties or strength of composites were established experimentally or theoretically. However, not only the volume content, and other averaged properties or properties of single microstructural elements influence the mechanical behavior and strength of composites. The synergistic effects and interaction between many microstructural elements, the gradation and localization of microstructural elements have a strong influence on the mechanical behavior and strength of composite materials as well.

The area of the mechanics of materials, which deals with the theoretical and numerical analysis of the effect of microstructures on the material properties, taking into account the interaction between many microstructural elements, their arrangement and heterogeneity, is referred to as the *mesomechanics of materials*. Computational mesomechanics seeks to develop and to employ numerical tools for the analysis of interrelationships between microstructures and mechanical behavior of materials, and, ultimately, for the material design.

The concepts and methods of the analysis of relationships between microstructures and mechanical properties, strength and damage resistance of composites are the subject matter of this book.

In Chapter 1, the classification of composites, and the mechanisms of their deformation, damage and fracture are described. In Chapter 2, the concept of the mesoscale analysis in the mechanics of materials is formulated. The microstructure-related mechanisms of high strength and stiffness of biomaterials, as well as different concepts of the material improvement by varying microstructures and the statistical methods of the microstructure description are briefly reviewed.

Chapter 3 contains short overviews of the concepts of fracture mechanics of materials, statistical models of failure and damage mechanics, and methods of numerical analysis of damage and fracture in materials. The methods of the analysis of the microstructure–strength relationships of composite materials (e.g. the shear lag model, homogenization, variational bounds, etc.) are discussed in Chapter 4.

In Chapter 5, the concept of computational experiments as a basis for the numerical optimization of materials is formulated. Several program codes, developed to automatize the generation of three-dimensional (3D) mesomechanical models of composites, are described. One of the programs, Meso3D, generates automatically 3D microstructural FE models of material (multiparticle unit cells) with pre-defined (graded, clustered, random, real, etc.) arrangements of inclusions on the basis of the geometrical description of microstructures, and carries out the statistical analysis of generated microstructures. Another program, 'Voxel2FEM', generates 3D microstructural models of materials on the basis of the microstructure description, given in the form of voxel array data. The program 'Voxel2FEM' allows generation of 3D microstructural models of materials with not only round or ellipsoidal inclusions, but with inclusions of arbitrary form and distributions. Furthermore, a subroutine for the numerical modeling of void growth in the ductile phase of composites and brittle damage in hard particles (with random scattering of properties) was developed.

Both 2D and 3D numerical mesomechanical experiments, carried out with the use of these numerical tools, are described in Chapters 6–10. The effects of the arrangements of inclusions, their sizes, gradients, etc., on the deformation and damage evolution in composites are analyzed numerically, using the numerical tools described in Chapter 5. In Chapter 11, the methods of mesomechanical analysis are applied to the analysis of the contact damage and wear of composite tool materials. Chapter 12 discusses possible applications of the methods of mesomechanics of composites to nanostructured materials. The main conclusions are summarized in Chapter 13.

References

Berns, H., Melander, A., Weichert, D., Asnafi, N., Broeckmann, C. and Gross-Weege, A. (1998). A new material for cold forging tool, *Composites Materials Science*, **11** (142), 166–180.

Katti, K. S., Katti, D. R., Pradhan, S. M. and Bhosle, A. (2005). Platelet interlocks are the key to toughness and strength in nacre, *Journal of Materials Research*, **20** (5), 1097–1100.

Lisovsky, A. F. (2001). Properties of cemented carbides alloyed by metal melt treatment. in: *Proc. 15th International Plansee Seminar*, Eds G. Kneringer, P. Rodhammer and H. Wildner. Plansee Holding AG, Reutte P/M Hard Materials, Vol. 2, 168–179.

Mclelland, A. R. A., Atkinson, H. V. and Anderson, P. R. G. (1999). Thixoforming of a novel layered metal matrix composite, *Materials Science and Technology*, **15** (8), 939–945.

Ramachamndra Rao, P. (2003) Biomimetics, *Sadhan, a,* **28** (3–4), 657–676.

Sarikaya, M., Fong, H., Sopp, J. M., Katti, K.S. and Mayer, G. (2002). Biomimetics: nanomechanical design of materials through biology, 15th ASCE Engineering Mechanics Conference June 2–5, 2002, Columbia University, New York, NY.

Tan, H. L. and Yang, W. (1998) Toughening mechanisms of nano-composite ceramics, *Mechanics of Materials*, 30, 111–123.

Leon Mishnaevsky Jr
Technical University of Denmark
Denmark

Acknowledgements

Some parts of the investigations, described in this book, have been carried out during the author's work at the Institute for Materials Testing, Materials Science and Strength of Materials (IMWF)/Staatliche Materialprüfungsanstalt (MPA), University of Stuttgart and at the Institute of Mechanics, Darmstadt University of Technology (Germany) as well as during his research stay at the Massachusetts Institute of Technology (USA). The support of the Deutsche Forschungsgemeinschaft (DFG) via the Heisenberg Fellowship, which enabled most of the described work to be carried out, is gratefully acknowledged by the author. The final version of the book was written during the author's work at the Risø National Laboratory in Denmark.

The author wants to express his deepest gratitude to Professor Dr Dietmar Gross (Darmstadt University of Technology, Germany) and to Professor Dr Siegfried Schmauder (University of Stuttgart, IMWF, Germany) for their permanent support, valuable advices and many stimulating discussions. Further, the author is very grateful to Professors W. Craig Carter (Department of Materials Science and Engineering, MIT), Mitch Denda (Rutgers University, NJ), Mark Kachanov (Tufts University, MA), Valery Levitas (Texas Tech University, TX), and Tadashi Shioya (The University of Tokyo) for their support, inspiring discussions and important advices.

Stimulating discussions with Professors Martin Levesque (Polytechnique Montréal), Thomas Michelitsch (University of Sheffield), Xie Heping and Zhou Hongwei (China University of Mining and Technology, Beijing) are gratefully acknowledged.

The author is deeply grateful to Dr Povl Brøndsted (Risø National Laboratory, Denmark) for his support and motivation, and valuable advice and discussions. Further, the author is very grateful to Drs Bent F. Sørensen, Jakob Ilsted Bech, Lars P. Mikkelsen, Helmuth L. Toftegaard, Rasmus C. Østergaard and other colleagues at the Risø National Laboratory for the interesting discussions, helpfulness and collaboration.

Some materials from previous publications of the author and other publications are reproduced here with kind permissions from Elsevier, Balkema, Hanser and Sage publishers.

The author is grateful to Professor M. Levesque and Professor M. Sarikaya for permission to use the micrographs from their investigations.

The valuable comments and suggestions toward the improvement of this book, made by Lennart Mischnaewski, are gratefully acknowledged.

Finally, I would like to thank my parents, Simone Mischnaewski and Dr Leonid Mischnaewski, for motivation, encouragement, support and valuable advices.

Leon Mishnaevsky

1
Composites

1.1 Classification and types of composites

Composites are materials, which:

- consist of two or more chemically dissimilar constituents with different properties, separated by interfaces;
- are artificially produced by physical combination of ingredient materials, and differ therefore from alloys (where one or more phases result from phase transformation), structures and natural materials.

The composites can be considered as homogeneous at the macroscale, but are heterogeneous at the microscale, i.e. at the scale comparable with the geometrical sizes of the constituents. The properties of composites depend on the properties of the constituent phases, their geometry and relative amounts.

There are two commonly used classifications of composites:

- classification according to the matrix materials: metal matrix composites, organic matrix composites, ceramic matrix composites;
- classification according to the geometry of reinforcing phase and mechanisms of reinforcements: particle, fiber, short fiber reinforced composites.

The materials can be further classified as continuously and discontinuously reinforced composites. The first group includes the long fiber reinforced composites. Miracle and Donaldson (Miracle and Donaldson, 2001) defined these materials, as composites with reinforcement, the properties of which do not vary with fiber length, and are not improved if the fiber or filament length is further increased.

Discontinuously reinforced composites include particulate and short fiber reinforced composites.

Computational Mesomechanics of Composites L. Mishnaevsky Jr

An important group of composites, which has attracted growing interest from researchers, is composites with interpercolating structures, where both phases form continuous networks in the material (Clarke, 1992).

Fiber reinforced composites are often characterized by their high specific strength and specific modulus parameters (i.e. strength to weight ratios), and are widely used for applications in low-weight components. Three groups of fiber reinforcement are used: whiskers, fibers and wires. Materials for wires include typically steel, molybdenum and tungsten. Fine wires have relatively large diameters, as compared with fibers and whiskers. Fibers are made usually from either polymers or ceramics, and tend to have much higher strengths than bulk materials, thanks to their smaller diameters. Whiskers are thin single crystals (such as graphite, silicon carbide, silicon nitride and aluminum oxide), with almost no defects, and therefore, very high strength. They are often made from ceramics (aluminum oxide, silicon carbide, silicon oxide, boron carbide and beryllium oxide), graphite, etc.

In *particle reinforced composites*, small particles of one phase are randomly distributed in the matrix of another phase. In many cases, the reinforcing phase (particles) is harder and stiffer than the matrix. As the matrix materials, metals, alloys, polymers, ceramics, etc. can be used. Particle reinforcement can be by ceramics, metallic or other particles of different sizes and shapes.

Metal matrix composites (MMCs) combine the advantages of metals and composites, in particular, high strength and high fracture toughness. They may be used at high temperatures, have high abrasion and creep resistances, as well as high thermal conductivity. Often, composites with aluminium, magnesium, iron, copper or titanium matrices are used. The reinforcement of MMCs can include silicon carbide, boron, alumina, refractory metals, carbon (continuous), or silicon carbide whiskers, chopped fibers of alumina and carbon, and silicon carbide and alumina particles (discontinuous reinforcements).

A special case of particle reinforced composites is *dispersion strengthened* composites (which are often considered either as a separate group, or even classified as alloys rather than as composite materials). Dispersion strengthened composites are metals or alloys, reinforced by small volume content (several volume percent) of fine hard particles. The dispersed phases can be metallic or nonmetallic (often, metal oxides), with sizes of the order 10–100 nm. High strength and high melting point dispersed particles, such as carbides, nitrides, oxides and borides, present efficient obstacles for the dislocation movement, which increase the strength of the particle reinforced material. An example of this group of materials is aluminum reinforced by aluminum oxide particles.

Cermets, consisting of metal matrix and ceramic particles, can be considered as both ceramic and metal matrix composites. The most commonly used cermets are the cemented carbides, which are composed of hard particles of refractory carbide ceramic (tungsten carbide, WC, or titanium carbide, TiC) and the metal matrix (cobalt or nickel). The metal content in cermets is typically relatively low (below 20 %). These composites are used extensively in machining and drilling tools. The carbide particles ensure the shape stability and sharpness of the tools, while the matrix ensures higher toughness of the materials.

Ceramic matrix composites (CMCs) were developed with the purpose to retain the advantages of ceramic materials (high strength, stiffness, resilience to oxidation and to high temperatures), while compensating for their low fracture toughness by reinforcement with another ceramic or other material in the ceramic matrix. The increased fracture toughness is achieved as a result of the interaction between cracks and reinforcement phase, which impedes or hinders the crack growth. The fracture toughness of CMCs is normally several times higher than the fracture toughness of ceramics. Typical examples of matrix materials are silicon carbides and silicon nitrides (Si_3N_4) (nonoxide matrix), reinforced by SiC particles, whiskers or fibers, and alumina (Al_2O_3), reinforced by carbon, Al_2O_3 or SiC.

The toughness of ceramic composites can be further increased by using *transformation toughening* (i.e. introducing constituents, which exhibit phase transitions under mechanical loading). The particles of partially stabilized zirconium, dispersed in the ceramic matrix material undergo transformation to the stable monoclinic phase, when they are subject to the stress field in front of a propagating crack. This transformation results in some increase of the particle volume, and in the higher compressive stresses, which can lead to the crack growth arrest.

Polymer matrix composites (PMCs) consist of polymer as the matrix, reinforced with fibers, short fibers or particles. They have high tensile strength and stiffness, low density, low temperature and electroconductivity. The main materials for the polymer matrix are:

- polyesters and vinylesters, which are widely used and inexpensive; these materials are often reinforced by glass fibers;
- epoxies, which are more expensive and have better mechanical properties than the polyesters and vinyl resins; they are also utilized extensively in PMCs for aerospace applications;
- polyimide and thermoplastic resins, which are used for high temperature applications.

Examples of microstructures (SEM micrographs) of polymer (polypropylene) matrix composites reinforced with short glass fibers and particles are given in Figure 1.1.

High strength glasses, carbon, boron and polymers, as well as some oxides, carbides, nitrides and other chemical compounds are used as fiber materials in the polymer matrix composites. *Glass fiber reinforced polymer* (GFRP) composites are widely used in

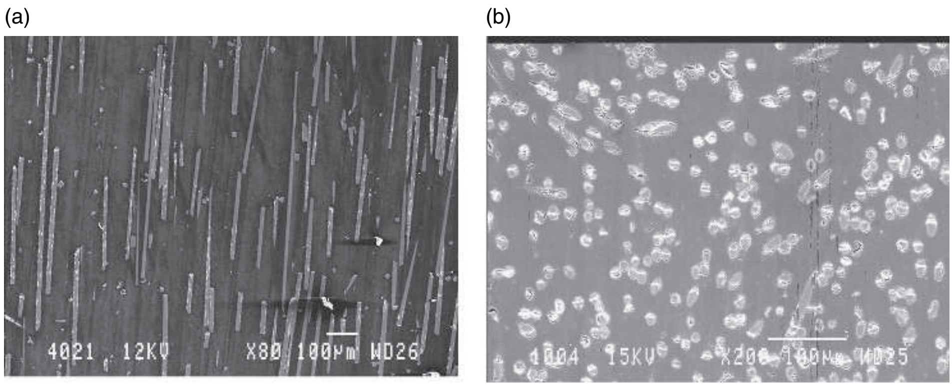

Figure 1.1 SEM micrographs of polymer matrix composites reinforced with (a) short glass fibers and (b) glass particles. Courtesy of Professor M. Levesque, École Polytechnique de Montréal.

low-weight constructions, due to the high strength of glass fibers, as well as due to the availability of efficient and low cost production technologies of the materials. Carbon is another fiber material which is often used in advanced PMCs. *Carbon fibers* have very high specific modulus and specific strength, even at elevated temperatures and under the high moisture conditions.

Aramid fibers have very high longitudinal tensile strengths and tensile moduli, even at high temperatures, yet, relatively low compression strength. They are used often in protective materials, pressure vessels, tires, ropes and sport goods. Among the most common aramid materials, one can name Kevlar and Nomex. Aramid fibers are often used in composites with epoxy or polyester matrices.

Some very promising properties have been achieved in *carbon–carbon composites*, which are produced using the carbonization of the polymer matrix. Carbon–carbon composites have high strength and stiffness, even at high temperatures, large fracture toughness, low coefficients of thermal expansion and relatively high thermal conductivity and thermal shock resistance, however, they are relatively expensive. The materials are used as friction materials, turbine engine components, etc.

Hybrid composites are obtained by introducing two or more different kinds of reinforcement in the matrix, and have often better properties than composites containing only one reinforcement type. The most widely used system is the polymeric resin reinforced by carbon and glass fibers. In this case, the strong but expensive carbon fibers are combined with not so stiff but inexpensive glass fibers. These composites are stronger and tougher than glass reinforced plastics, but are not as expensive as carbon reinforced composites.

The continuously reinforced composites are used most often in the form of *laminates*. Composite laminates represent several unidirectional composite layers (plies, reinforced by long fibers) stacked and bound together to ensure the high strength and stiffness in several directions. A scheme of a cross-ply laminate is shown in Figure 1.2. The composite laminates are widely utilized in areas where low weight as well as high stiffness and strength of construction are required, notably, aircraft and space engineering, automotive applications, energy-related applications, as elements of ships, aerospace and other lightweight constructions.

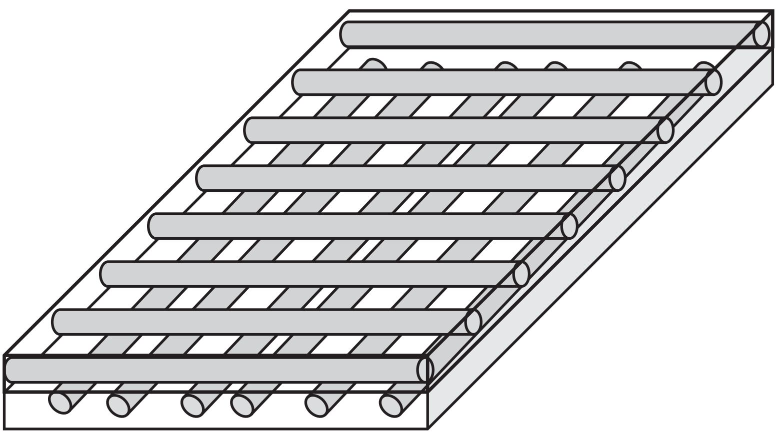

Figure 1.2 *Schematic diagram of a cross-ply laminate: two layers.*

1.2 Deformation, damage and fracture of composites: micromechanisms and roles of phases

Depending on the microgeometry and type of the reinforcement of composites, the deformation and failure mechanisms may vary strongly. Let us consider the mechanisms and the role of microstructures in the deformation and destruction of different groups of composites.

1.2.1 Particle and short fiber reinforced composites

When a particle reinforced composite is subject to a mechanical load, the entire load is born initially by the matrix. The matrix is deformed, and its elastic deformation and plastic flow lead to the load transfer to the particles. The hard particles restrain movement of dislocations in the matrix phase, and therefore influence (increase) the strength and stiffness of the composites. Thus, the main mechanisms of the influence of the particles on the deformation of particle reinforced composites are the load transfer (i.e. the matrix transfers some of the applied stress to the particles, which bear a part of the load), and constraining the matrix deformation by the particles.

At some degree of deformation, the microcracks or voids form in particles, matrix or on the interface. Depending on the properties of the phases, different damage mechanisms become active:

- *Particle cleavage*. If brittle particles (e.g. ceramics) are placed in a ductile but strong and tough matrix, particle cleavage is the main damage mode in the initial stages of deformation.
- *Debonding on the particle–matrix interface*. If the bond strength of the interface is low compared with the failure strengths of both the particles and the matrix, the initial damage may occur at the interfaces. Often, the stress concentration on broken particles causes the initiation of the void growth in the matrix and/or interface debonding. Figure 1.3 shows the debonding and failure of glass particles and the formation of a crack between the failed particles.
- *Void growth*. In metallic and polymer matrices, ductile fracture occurs, which involves the nucleation, growth and coalescence of cavities. The cavity nucleation in the matrix is associated with the inhomogeneity of plastic deformation in the vicinity of inclusions (Rice and Tracey, 1969; Derrien, 1997), and takes place often near broken particles, near microcracks formed at the particle–matrix interfaces or at the dislocation pile-ups near inclusions. Once voids are formed in the ductile metallic or polymer matrix, they grow and expand as a result of high local plastic strains and high stress triaxiality in the matrix.
- *Matrix cracking*. In a brittle matrix, the formation of matrix cracks can be observed. Similarly, the voids can coalesce and form large propagating cracks in a ductile matrix.

In the polymer matrix, the crazing damage mechanism is observed, especially at high strain rates. The crazes represent filaments, consisting of molecular chains and forming bridges between two crack faces (Schirrer, 2001).

Figure 1.4 shows schematically three main mechanisms of damage in particle reinforced composites: particle cracking, interface debonding and void growth in the matrix.

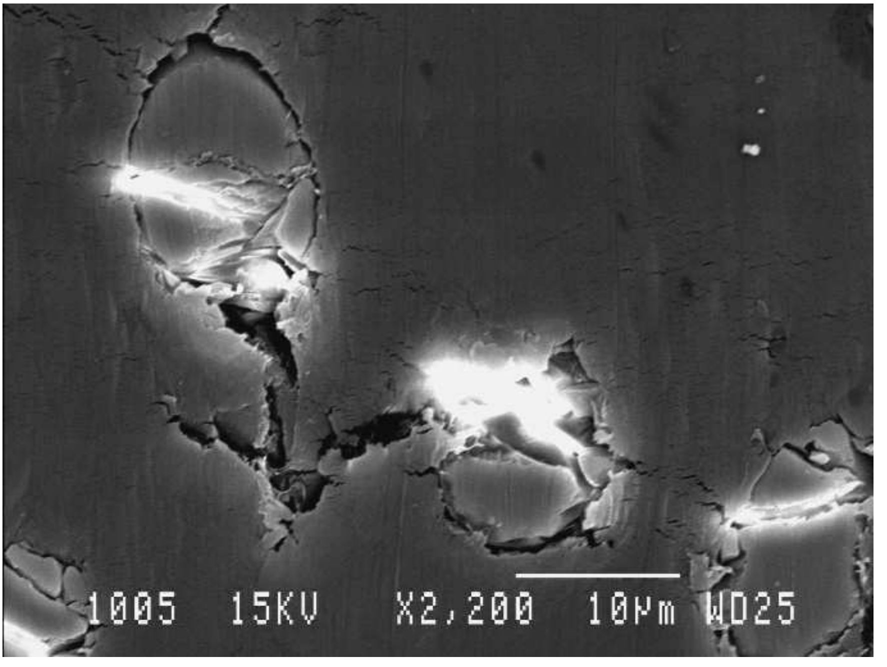

Figure 1.3 *SEM micrograph. Debonding and failure of glass particles and the formation of a crack between the failed particles. Courtesy of Professor M. Levesque, École Polytechnique de Montréal.*

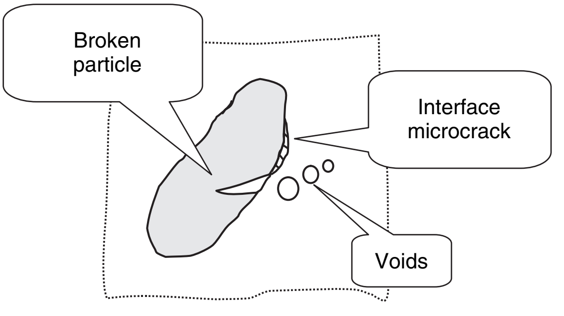

Figure 1.4 *Schematic diagram of different damage mechanisms in particle reinforced composites: particle breakage, interface debonding and void growth in the matrix.*

After the initial stage of diluted microcracking at local heterogeneities in the material, the defects begin to interact, join together and form large cracks. In the ductile matrix, the voids begin to coalesce, which leads to the failure of the matrix ligaments between them, and finally to the formation of a macrocrack in the volume. Pineau (Pineau, 2004) identified two possible mechanisms of the cavity coalescence in metals: cavity growth until the voids join together; and formation of shear bands between growing cavities (in the shear bands, smaller voids form often on smaller precipitates).

After the cracks form, the largest cracks begin to grow, and this growth is controlled by a number of mechanisms: interaction and joining with microcracks in front of the crack tip (e.g. microcracks on failed inclusions), by crack–void and crack–dislocation interaction, by sequential rupture of atomistic bonds (Lawn, 1975a) and other atomistic, dislocational and micromechanical mechanisms. The microstructure of composites influences the mechanisms of crack propagation as well as damage and fracture resistance. So, microcracks formed by particle cleavage or by particle–matrix interface debonding may cause the crack path deviation (see, for instance, Broeckmann, 1994). A microcrack array, formed in brittle inclusions or weak interfaces, may amplify or shield the stress concentration on the crack tip, and therefore delay or speed up the fracture (Kachanov *et al*., 1990). The netlike or layered arrangements of brittle inclusions in the matrix can cause the crack to follow the direction of highly reinforced regions, and to deviate from the initial mode I direction. Such a crack deviation leads to an increase in the fracture toughness of the composite (Mishnaevsky Jr *et al*., 2003a).

Figure 1.5 shows some examples of the toughening mechanisms in particle reinforced composites: the crack path deviation (e.g. due to the crack–microcrack interaction or crack shielding by a microcrack array) and crack branching. Further, the crack bridging mechanisms can be operative, and lead to the toughening of the composites.

The deformation and damage mechanisms in *short fiber reinforced composites* are in many ways similar to those in the particle reinforced composites (e.g. the load transfer from the matrix to fibers, etc.). In metal matrix short fiber reinforced composites, the matrix yielding starts in the vicinity of fiber ends. Following the local plastic deformation in the matrix, the interface debonding begins in the vicinity of the fiber ends, and that leads to the matrix crack initiation from the debonded fiber ends (Goh *et al*., 2004).

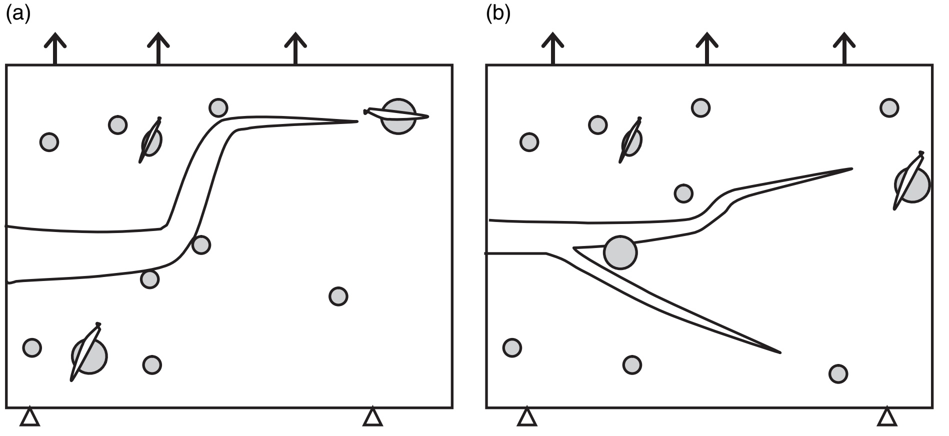

Figure 1.5 *Mechanisms of toughening of particle reinforced composites: (a) crack deviation and (b) crack branching.*

1.2.2 Long fiber reinforced composites

If a long fiber reinforced composite is subject to mechanical loading, the role of fibers is to bear the applied load, whereas the matrix binds the fibers together and ensures the load transfer and redistribution to and between the fibers.

Under *longitudinal tensile loading*, the main part of the load is born by the fibers, and they tend to fail first in metal and polymer matrix composites. After the weakest fibers fail, the load on the remaining intact fibers increases. This may cause the failure of other, initially the neighboring, fibers. According to Cooper (Cooper, 1971), the mechanisms of failure of the composites at this stage can be classified into 'single fracture' (after one phase fails, another phase can not bear any load and fails instantly) and 'multiple fracture' mechanisms (after one component fails, other components can bear the applied load, but become progressively damaged and ultimately fail). In the case of multiple failures, the stress–strain curve looks similar to the ductile stress–strain curve, with a zigzag part corresponding to the stage of accumulation of the cracks before failure.

The cracks in the fibers cause higher stress concentration in the matrix, which can lead to the matrix cracking. However, if the fiber–matrix interface is weak, the crack will extend and grow along the interface. The crack deviation into the interfaces may be beneficial for the fracture toughness of composites (Evans, 1997).

The failure of glass fibers in polymer matrix composites (SEM image) is shown in Figure 1.6.

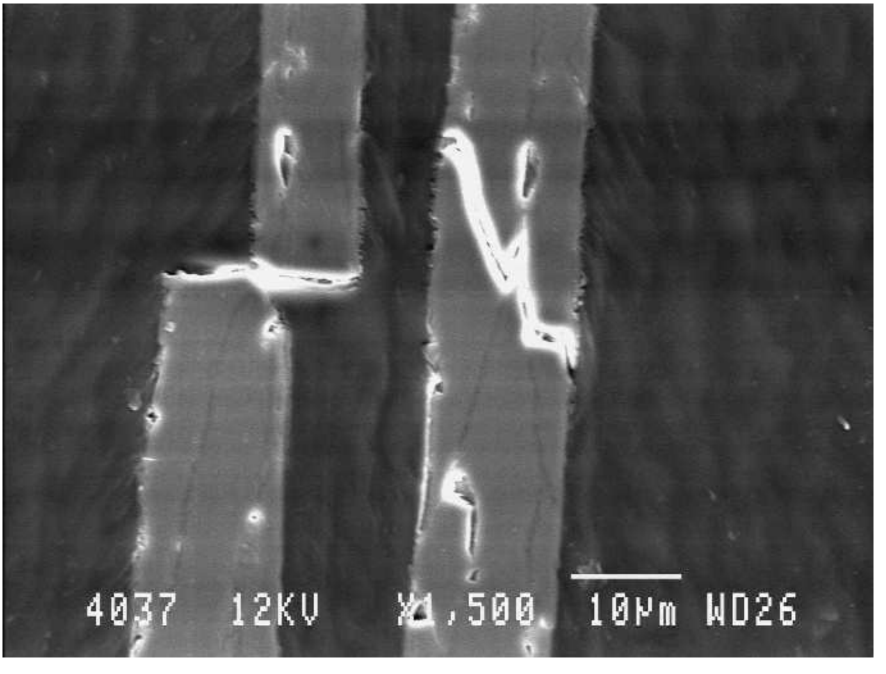

Figure 1.6 SEM micrograph. Failure and following deformation of glass fibers in the polymer matrix composites, subject to tensile loading. Courtesy of Professor M. Levesque, École Polytechnique de Montréal.

In the case of ceramic and other brittle matrix composites, the crack is formed initially in the matrix. If intact fibers are available behind the crack front and they are connecting the crack faces, the crack bridging mechanism is operative. In this case, the load is shared by the bridging fibers and crack tip, and the stress intensity factor on the crack tip is reduced. A higher amount of bridging fibers leads to lower stress intensity factor on the crack tip, and the resistance to crack growth increases with increasing crack length (R-curve behavior) (Sørensen and Jacobsen, 1998, 2000). The extension of a crack, bridged by intact fibers, leads to debonding and pull out of fibers that increase the fracture toughness of the material.

Mechanisms, similar to the toughening mechanisms in particle reinforced composites (crack branching, deflection), operate in fiber reinforced composites as well. While the crack deflection, crack branching and bridging are the most important toughening mechanisms for short fiber composites, the fiber debonding, fiber fracture and pull out are observed most often in long fiber composites.

The main damage mechanisms in long fiber reinforced composites under tensile loading are shown schematically in Figure 1.7.

Under *tensile loading at an angle to the fiber direction*, several failure mechanisms are operative: tensile fiber failure (operative at low angles between the interface and applied force), shear along the interface, tensile interface debonding and matrix cracking (the latter two mechanisms are observed at high angles between the interface and applied force) (Stölken and Evans, 1998).

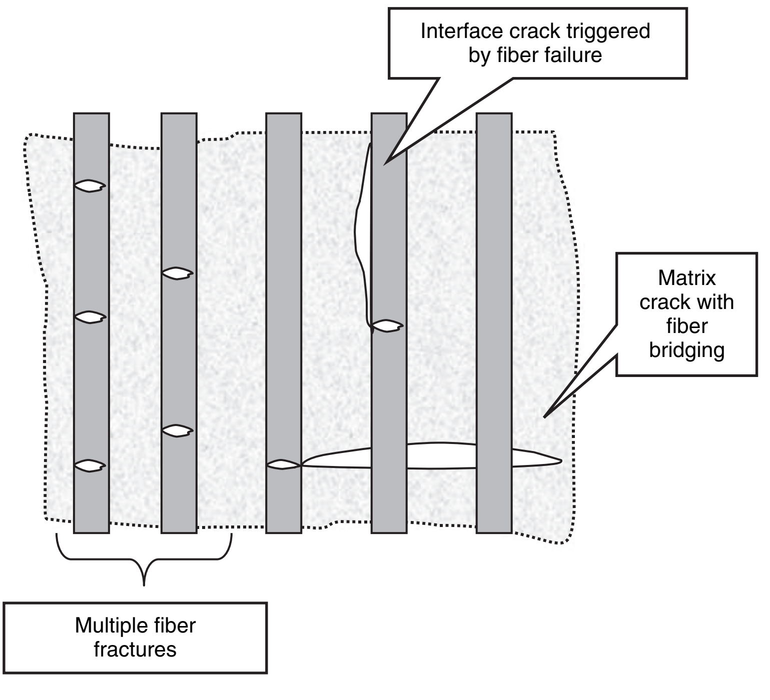

Figure 1.7 *Schematic diagram of different damage mechanisms in fiber reinforced composites: fiber cracking, interface debonding and matrix cracking.*

The *compressive strength* of composites is often sufficiently lower than their tensile strength (Budiansky and Fleck, 1993). Failure of the polymer matrix composites is caused usually by localized buckling or kinking of fibers. Further, fiber crushing and shear banding can be observed in the composites under compressive loading (Hahn and Williams, 1984).

1.2.3 Laminates

The main mechanism of damage of laminates at the initial stages of failure is the *matrix cracking* (called also transverse cracking in the case of 90° plies, or intralaminar cracking), which is observed first of all in the plies with maximum angle between the fibers and load direction (Nairn, 2000; Kashtalyan and Soutis, 2005). After a transverse crack in the matrix initiates, it propagates quickly from one side of the ply to another (tunneling mechanism). Other matrix cracks are formed in the ply (normally, at a constant distance from one another). The *delamination cracks* are initiated at the tips of the transverse microcracks (Varna and Berglund, 1991; Lundmark, 2005). Delaminations may lead in turn to the fiber breakage in the main load-bearing layers, with fiber oriented along the loading direction (Kashtalyan and Soutis, 2005). The crack system, which is formed in the cross-ply laminates, is shown schematically in Figure 1.8.

The following mechanisms of damage initiation in composite laminates were further described by Ladeveze *et al*. (Ladeveze *et al*., 2006): *diffuse damage*, associated with fiber–matrix debonding, and *diffuse delamination* (formation of microvoids and microcracks at the interface between plies). The diffuse damage, which is observed often under

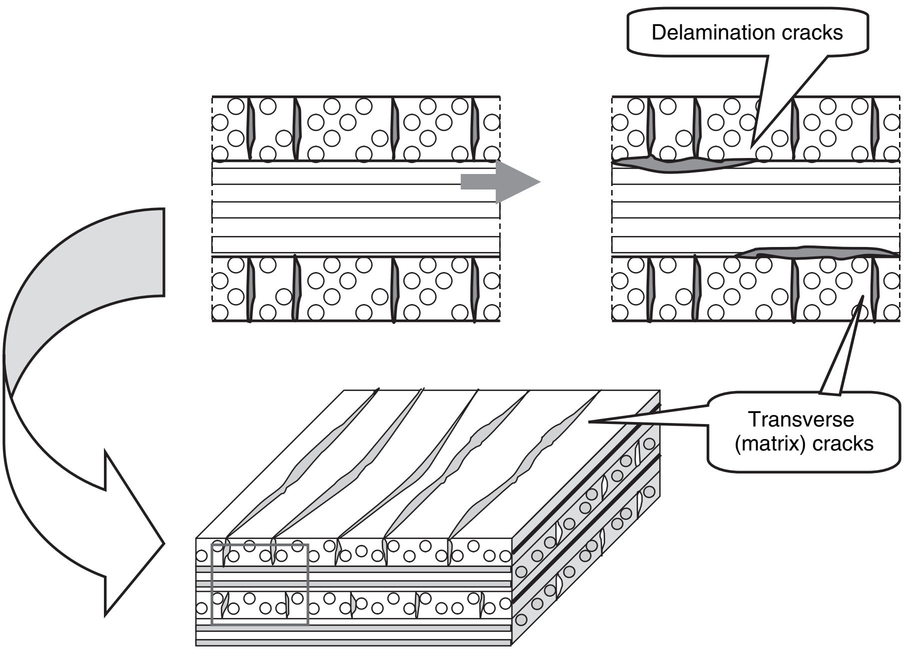

Figure 1.8 *Schematic diagram of crack systems in a cross-ply laminate.*

shear loading, leads to the reduction in the stiffness of plies, and therefore influences the conditions of the formation of transverse cracks.

References

Broeckmann, C. (1994). Bruch karbidreicher Stähle – Experiment und FEM-Simulation unter Berücksichtigung des Gefüges, Dissertation, Ruhr-Universitaet Bochum.

Budiansky, B. and Fleck, N. A. (1993). Compressive failure of fibre composites, *Journal of the Mechanics and Physics of Solids*, **41** (1), 183–211.

Clarke, D. R. (1992). Interpenetrating phase composites, *Journal of American Ceramic Society*, **75**, 739–759.

Cooper, G. A. (1971). The structure and mechanical properties of composite materials, *Review of Physics in Technology*, **2**, 49–91.

Derrien, K. (1997) Modélisation par des méthodes d'homogénéisation de l'endommagement et de la rupture de composites Al/SiCp, PhD Thesis, ENSAM, Paris.

Evans, A. G. (1997). Design and life prediction issues for high-temperature engineering ceramics and their composites, *Acta Materialia*, **45** (1), 23–40.

Goh, K. L., Aspden, R. M. and Hukins, D. W. L. (2004). Review: finite element analysis of stress transfer in short-fibre composite materials, *Composites Science and Technology*, **64** (9), 1091–1100.

Hahn, H. T. and Williams, J. G. (1984). Compressive failure mechanisms in unidirectional composites, NASA TM 85834.

Kachanov, M., Montagut, E. L. E. and Laures, J. P. (1990). Mechanics of crack– microcrack interaction, *Mechanics of Materials*, **10**, 59–71.

Kashtalyan, M. and Soutis, C. (2005). Analysis of composite laminates with intra- and interlaminar damage, *Progress in Aerospace Sciences*, **41**(2), 152–173.

Ladeveze, P., Lubineau, G. and Marsal, D. (2006). Towards a bridge between the micro- and mesomechanics of delamination for laminated composites, *Composites Science and Technology*, **66**, 698–712.

Lawn, B. R. (1975a). An atomistic model of kinetic crack growth in brittle solids, *Journal of Materials Science*, **10** (3), 469–480.

Lundmark, P. (2005). Damage mechanics analysis of inelastic behaviour of fiber composites, Dr Thesis, Lulea, LTU.

Miracle, D. B. and Donaldson, S. (2001). Introduction to composites, in: *ASM Handbook: Vol. 21, Composites*, Eds D. B. Miracle and S. Donaldson, ASM International, Material Park, OH, pp. 3–17.

Mishnaevsky Jr, L., Lippmann, N. and Schmauder, S. (2003a). Computational modeling of crack propagation in real microstructures of steels and virtual testing of artificially designed materials, *International Journal of Fracture*, **120** (4), 581–600.

Nairn, J. (2000) Matrix microcracking in composites, in: *Comprehensive Composite Materials*, Eds A. Kelly and C. Zweben, Elsevier, Amsterdam, Vol. 2 pp. 403–432.

Pineau, A. (2004) Physical mechanisms of damage, in: *Local Approach to Fracture*, Eds J. Besson *et al*., ENSMP, Paris, pp. 33–77.

Rice, J. R. and Tracey, D. M. (1969). On the ductile enlargement of voids in triaxial stress fields, *Journal of the Mechanics and Physics of Solids*, **17**, 201–217.

Schirrer, R. (2001). Damage mechanisms in amorphous glassy polymers: crazing, in: *Handbook of Materials Behavior Models*, Elsevier, New York.

Stölken, J. S. and Evans, A.G. (1998). A microbend test method for measuring the plasticity length scale. *Acta Materialia*, **46** (14), 5109–5115.

Sørensen, B. F. and Jacobsen, T. K. (1998). Large scale bridging in composites: R-curve and bridging laws. *Composites A*, **29**, 1443–1451.

Sørensen, B. F. and Jacobsen, T. K. (2000). Crack growth in composites – Applicability of R-curves and bridging laws, *Plastics, Rubber and Composites*, **29**, 119–133.

Varna J. and Berglund L. A. (1991). Multiple transverse cracking and stiffness reduction in cross-ply laminates, *Journal of Composites Technology Research*, **13** (2), 97–106.

2

Mesoscale level in the mechanics of materials

2.1 On the definitions of scale levels: micro- and mesomechanics

The following scale levels are usually recognized in the analysis of the material behavior:

- Macroscale (or a specimen scale), of the order of more than 1 mm. Material behavior at this scale level is analyzed using continuum mechanics methods.
- Micro- and mesoscale (or a microstructure scale), between 1 μm and 1 mm. Material behavior at this scale level falls into the area of materials science, and is analyzed using methods of both physics and mechanics of materials, including micromechanics and fracture mechanics.
- Nano- and atomistic scales, less than 1 μm. Material behavior at this scale level falls into the area of the physics of materials.

The question arises as to what is the difference between 'mesolevel' and 'microlevel' in the mechanics of materials.

The term 'mesomechanics' has gained relatively wide acceptance after it was introduced by Panin and co-workers (Panin, 1998) as the name for a new area of research ('physical mesomechanics'), the main purpose of which has been defined as the development of the theoretical basis of material improvement, using experimental and theoretical studies of physical processes in loaded materials at the mesolevel.

Needleman (Needleman, 2000) defined 'mesoscale continuum mechanics' as 'intermediate between direct atomistic and an unstructured continuum description of deformation processes'. As a characteristic feature of this scale level, it was noted that 'size matters' at the mesoscale level.

Panin (Panin, 1998) suggested a more detailed classification, with meso I and meso II levels (defined as related to the rotation modes inside structural elements of deformation,

Computational Mesomechanics of Composites L. Mishnaevsky Jr

and to the self-correlated rotations of many structural elements, respectively). The meso I level corresponds to the level 'inside microstructural elements' (grains), while the meso II level is related to the 'conglomerates' of microstructural elements. Actually, Needleman's 'mesoscale continuum mechanics' corresponds to both Panin's meso I and II levels, and to both micromechanics and mesomechanics in the above classification.

Kocks (cited by Estrin, 1999) stated that ' "mesoscopic" should refer to cases where the structural scale is, say, of the order of 100 μm' (scale between 'microscopic', associated with the microscope and micrometer, and 'macroscopic').

Mishnaevsky Jr and Schmauder (Mishnaevsky Jr and Schmauder, 2001) defined the mesolevel in the material structure as a range of scale levels which are two to three orders of magnitude greater than defects of structure (which varied in the 10^{-9}–10^{-5} m scale range) and one to three orders of magnitude smaller than a specimen or workpiece in the following. The levels of the description can be related to the methods of the control of material properties: whereas the improvement at macrolevel can be done by modifying the specimen construction, the improvement of the strength and reliability of materials at micro- and mesolevel is carried out by heat treatment, metal working, impregnation, powder metallurgy methods, etc.

Following Mishnaevsky Jr (Mishnaevsky Jr, 2005b), one may state that the mesomechanics of materials studies quantitatively the interaction and *synergistic effects of many elements of microstructures* (as inclusions, voids, shear bands, microcracks, etc., or generally the heterogeneity of materials) on the strength and mechanical properties of materials, whereas micromechanics deals with the effects of single elements and averaged parameters of microstructures on the mechanical behavior of materials. Computational mesomechanics seeks to create the necessary numerical tools for the analysis of the mechanical behavior and degradation of materials, which allows the computational analysis of the interaction between many elements of microstructures and microstructure evolution, and can serve as a basis for the material design.

2.2 Size effects

Needleman (Needleman, 2000) defined 'mesoscale' as a scale level at which 'size matters'. The influence of geometrical size of components on the mechanical behavior and strength of materials was observed in numerous experiments, carried out on metals (Fleck *et al.*, 1994), ceramics (Xu and Rowcliffe, 2002), concretes (Bazant and Yavari, 2005) and polymers (Tjernlund, 2005). The common observation is that 'smaller is stronger': the smaller a specimen or an element of the microstructure, the higher its strength.

2.2.1 Brittle and quasi-brittle materials

The interest of the research community in the size effect in materials was first aroused in connection with the testing of materials for civil engineering use. The necessity to predict the strength of concretes for large-scale structures on the basis of testing much smaller specimens led to intensive scientific efforts in this area.

Several explanations for the size effect in concretes, ceramics and other quasi-brittle materials have been suggested. The oldest model of the size effect is based on Weibull's statistical theory of strength (Weibull, 1939). It can be easily demonstrated in the framework of the weakest link theory, that increasing the specimen volume leads to the increased probability to find a crack in the volume, which may cause fracture at a given stress. For the uniform uniaxial applied stress, this theory leads to the following formula for the tensile strength of the material:

$$\overline{\sigma} \propto V^{-1/m} \tag{2.1}$$

where V is volume and m is the Weibull modulus.

Another, *deterministic size effect* in quasi-brittle materials is related to the stress redistribution and localization of damage during the crack growth. In these materials, when a crack grows, a finite size fracture process zone forms and extends. Bazant and Yavari (Bazant and Yavari, 2005) demonstrated that while 'the rate of energy dissipated at the front of a propagating fracture . . . is nearly independent of the structure size, the rate of energy released from the structure into the front would increase with the structure size if the nominal strength of the structure were assumed to be constant' (Bundesen, 2004). They concluded that the nominal strength decreases with increasing structure size under these conditions (Bazant, 2004).

Dyskin *et al*. (Dyskin *et al*., 2001) investigated the size effect in heterogeneous materials by considering microscopic random stress fields in materials with random microstructures under uniform and nonuniform macroscopic loading. Dyskin and colleagues demonstrated that Gaussian *stress fluctuations* lead to a size effect in which the tensile strength reduces as the square root of the logarithm of the sample size. For the case of nonuniform loading, they suggested another model which accounts for the linear part of the macroscopic stress distribution. Dyskin and colleagues concluded that 'macroscopic stress nonuniformity plays a crucial role in the mechanism of size effect'.

2.2.2 Metals

The size effect in metals is controlled by the micromechanisms of *plastic deformation*, and the damage initiation and growth in the materials. Yielding stress of metallic materials increases with decreasing the grain size in the materials according to the Hall–Petch relation:

$$\tau = \tau_c + Cd^{-1/2} \tag{2.2}$$

where τ is the yielding stress, τ_c and C are parameters of the material, and d is grain size. This effect is controlled by the *inhibition of the dislocation glide* due to the formation of pile-ups of dislocations at the grain boundaries.

During the plastic deformation of ductile metallic matrix reinforced by hard inclusions, the dislocations have to bow around the inclusions. The shear stress necessary for a *dislocation to bow around the inclusions*, is inversely proportional to the distance between inclusions. Due to this effect, the flow stress of composites increases with decreasing particle size, when the volume content of reinforcement is kept constant (Lloyd, 1994; Nan and Clarke, 1996).

Strong size effects are observed at the nano and submicrometer scale levels. The indentation hardness in the micro-indentation hardness experiments may increase by a factor of two or even three as the indentation depth decreases to micrometers and submicrometers (Xue *et al.*, 2002). The special case of thin metallic films on a substrate, in which the plastic flow in the films is constrained by the film surfaces, is discussed below.

A number of authors argued that the size effect in materials is caused by the *gradients of plastic shear* in small zones, which result in the storage of geometrically necessary dislocations (Fleck *et al.*, 1994; Abu Al-Rub, 2004). Due to the complex geometry of loading or material inhomogeneity, the plastic strain gradients are generated in the material, and lead to the storage of the dislocations, necessary for the compatible deformation in parts of the material. An increase of the dislocation density due to the strain gradients lead to the increase of the yield stress of the material. According to Fleck and colleagues, the size effect becomes pronounced when the grain size or particle spacing lie below approximately 10 μm.

The size effect, associated with the *damage growth* (e.g. void initiation at the local inhomogeneities), influences the strength and damage of metals. In this case, the higher density of brittle inclusions and other inhomogeneities, which are considered sites of the potential defect initiation in the material, leads to the higher density of defects, and to the higher likelihood of failure (similarly to the size effects in quasi-brittle materials).

Therefore, the characteristic lengths in metals can be associated with the grain sizes, sizes of the dislocation cells, magnitude of the strain gradient, distances between inclusions or inhomogeneities, etc.

In polymers, the structural length scale can be associated with molecular length (for amorphous thermoplastics) or with the distance between adjacent cross-links (for thermosets) (Tjernlund, 2005).

2.2.3 Thin films

An example of the realization of the concept 'small is stronger' is thin films, metallic or polymer layers with thickness of 10–1000 nm, used often in microelectronics, photonics, etc. According to Nix (Nix, 1989), thin films are commonly much stronger than corresponding bulk materials. Shan and Sitaraman (Shan and Sitaraman, 2003) demonstrated that the yield stress of Ti thin film is about three times the 'bulk' value, while the elastic modulus did not change. The higher yield stress of thin films, as compared with bulk materials, is caused by large strain gradients, as well as by constraints of the dislocation movement by interfaces (Mishnaevsky Jr and Gross, 2004b; Trondl *et al.*, 2006).

On the basis of investigations of the deformation of thin films, the concept of a 'critical film thickness' has been formulated. In the framework of this concept, a film thickness is determined, below which the strength of film is much higher than above. This critical thickness is defined as the thickness at which the film on a 'thick, lattice-mismatched substrate can begin to accomodate misfit dislocations' (Freund and Nix, 1996), or a thickness 'below which a dislocation-free coherently strained interface would be stable and above which a misfit dislocation structure, semi-coherent interface, would be stable' (Hirth and Feng, 1990). To determine the critical thickness of thin metallic films, several theories of film deformation have been developed. Table 2.1 shows some models and methods for the determination of critical film thicknesses.

More detailed reviews of the small scale effects in thin metallic films are given elsewhere (Mishnaevsky Jr and Gross, 2004a,b, 2005).

Table 2.1 *Overview: yield strength of thin metallic films as a function of the film thickness.*

Reference	Main ideas	Main results
Arzt, 1988	Shear stress necessary for yielding by 'the motion of dislocations which are constrained to "channel" through the film' (*dislocations channeling mechanism* of the plastic deformation of films) can be determined from the condition that a dislocation loop (or one half of a loop, for the case of the 'free' film surface) fits inside the film (i.e. the condition that the film surface is inpenetrable to the dislocations)	Yield stress was shown to be proportional to $1/h$, where h is the film thickness
Freund, 1987, 1994; Nix, 1989; Thompson, 1993; Freud and Nix, 1996	Yielding stress of thin metallic films is determined by the analysis of the energy changes related to the extension of a misfit dislocation (the equilibrium condition of the dislocation growth in a film)	Yield stress is proportional to $(1/h)$ ln h (Freund), $(1/h)$ $(\ln h+f)$ (Nix) or $A/h+B/d$ (Thompson), where f is a function of the elastic shear moduli of components and the oxide thickness, d – grain size and A and B are parameters
von Blanckenhagen *et al.*, 2001a,b	Plastic deformation in thin films is simulated using the *discrete dislocation simulation method*. The formation of a dislocation pile-up in a single grain and local stresses on the grain boundary, which determine the start of global plastic deformation, were examined. The authors demonstrated that the smaller dimension (either grain size or film thickness) controls the flow stress of the film.	Yield stress is proportional to $\sqrt{K_{HP}^2/d+\tau_{source}^2}$, where K_{HP} is a constant, d is the grain diameter and τ_{source} is the source activation stress

2.3 Biocomposites

Natural biological materials often demonstrate extraordinary strength, damage resistance and hardness. For instance, nacre, which consists of 95 % $CaCO_3$, has a work of fracture that is 3000 times higher than that of monolithic $CaCO_3$ (Ramachamndra Rao, 2003). In order to explore sources of the high strength and toughness of biomaterials, a number of investigations of the microstructures, damage and deformation mechanisms and the strength of different materials (bones, nacre, teeth, etc.) have been carried out. Let us look at the results of some of these investigations.

2.3.1 Nacre

A relatively well investigated case of biocomposite is nacre, mother of pearl. As noted above, nacre has a strength two times higher and a toughness thousands of times higher than its main constituent material, namely calcium carbonate. Many authors sought to investigate the mechanisms, which determine the high toughness of nacre (Jackson *et al*., 1988; Sarikaya *et al*., 2002).

Sarikaya *et al*. (Sarikaya *et al*., 2002) investigated nacreous mollusk shells, which are built as a brick (aragonite)-and-mortar (polymer) structure at the microlevel. They described the *brick–mortar microstructure* of nacre as follows: mineral platelets are surrounded by a thin film organic matrix and successively stacked to form a layered nanocomposite. The platelets are closely packed at each layer, and staggered through the thickness. That leads to the following behavior under loading: 'when the resolved stresses are normal to the platelet plane, the organic matrix bridges between the platelets, keeping them together and preventing uncontrolled crack growth; if the resolved stresses are shear, then the platelets slide successively over the organic matrix.' Sarikaya and colleagues concluded that layered industrial composites could be further toughened and strengthened for use in practical applications by using the segmented design encountered in nacre.

According to Smith *et al*. (Smith *et al*., 1999), the high fracture resistance of nacre is determined by its polymer adhesive. The adhesive fibers elongate in a stepwise manner, when nacre is loaded, as folded domains or loops are pulled open. The sawtooth pattern of the force–extension curve in the protein is a result of the successive domain unfolding. During the crack propagation in the nacre, the energy is absorbed by the interface debonding and by the shearing of the protein layer (Smith *et al*., 1999). If the crack propagates normally to the layers of bricks, it deflects around the aragonite bricks (Okumura and de Gennes, 2001).

Qi *et al*. (Qi *et al*., 2005) investigated the mechanical behavior of nacre numerically, using a micromechanical model. The mechanical behavior of the organic matrix was modeled taking into account the unfolding of protein molecules. The nonlinear stress–strain behavior was observed, with an apparent 'yield' stress (related to the unfolding events in the organic layers and to the mitigation of load transfer to the aragonite tablets) and hardening (related to the shear in the organic layers).

Katti *et al*. (Katti *et al*., 2005) demonstrated that the features observed in the microstructure of nacre, namely the relative rotation between platelet layers, platelet penetration and the geometric peculiarities (e.g. elongated sides) determine the high toughness and strength of nacre. Katti and colleagues observed interlocked platelets of nacre, and demonstrated that *interlocking* is the key mechanism for the high toughness and strength of nacre. The rotation between platelet layers is a necessary condition for the formation of interlocks.

In the conch shell with a crossed-lamellar structure, the toughness is determined by the complex structure of stacked laths, which cause the crack deflection and multiple cracking, according to Currey (Currey, 1984), Currey *et al*. (Currey *et al*., 1995) and Kamat *et al*. (Kamat *et al*., 2000).

2.3.2 Sponge spicules

Sarikaya *et al*. (Sarikaya *et al*., 2001) investigated the microstructures and mechanical properties of the Antarctic sponge *Rosella racovitzea*. They observed that the spicules are highly flexible and tough. While both the elastic modulus and nanohardness of the spicules are about half that of fused silica, the fracture strength and fracture energy

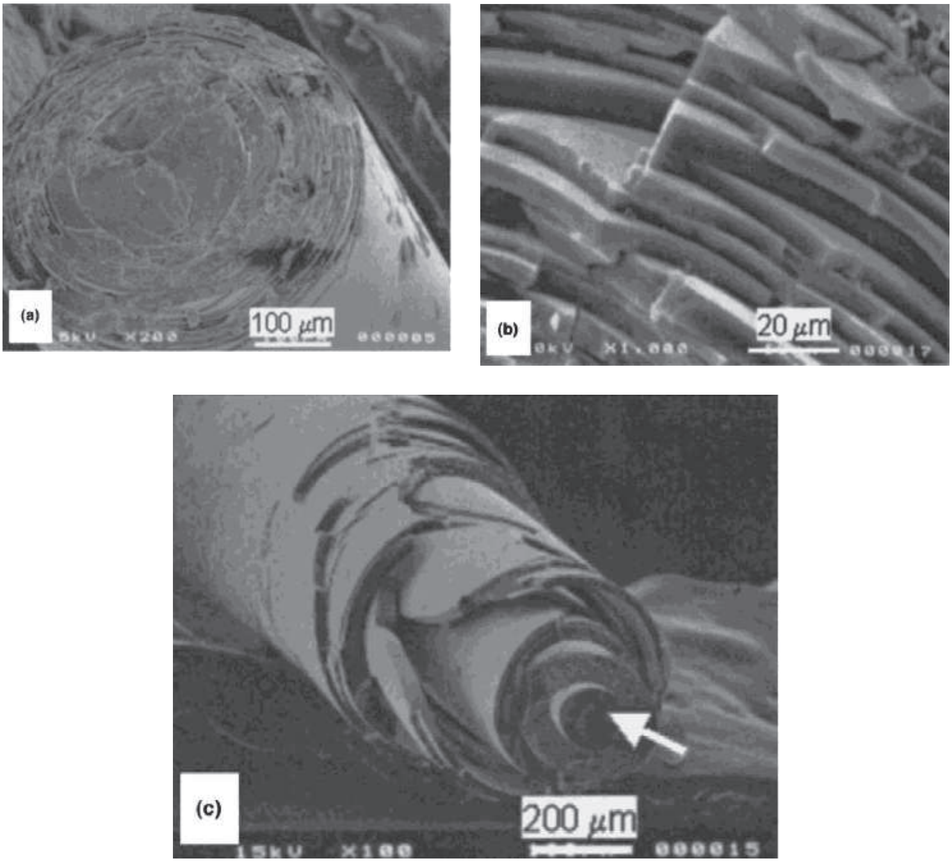

Figure 2.1 *SEM images of the fractured surface of a* Rosella racovitzea *spicule showing layering at (a) low and (b) high magnifications. (c) SEM image of a fractured spicule from a 3-point bend test. Reprinted from* J. Mater. Res., **16***(5), Sarikaya, M.* et al.*, pp. 1420–1435, Copyright (2001), with permission from Materials Research Society.*

of the spicules are several times those of silica rods of similar diameter. The layered structure of the spicules, with layers parallel to the axis of the spicule and randomly distributed layer thicknesses, was observed. Further, it was observed that the stress–strain curves from bulk testing of the spicules have a ‘sawtooth’ behavior. Figure 2.1 gives the SEM images of the fractured surface of a *R. racovitzea* spicule at different magnifications. The authors assumed that the layered structure (seen in Figure 2.1) is responsible for the high toughness of the spicules.

2.3.3 Bamboo

Amada (Amada, 1995) and Amada *et al*. (Amada *et al*., 1997) studied the microstructures of the bamboo, which allow it to withstand high velocity winds. Amada and colleagues demonstrated that bamboo can be considered as a *functionally graded material* and as a hierarchically designed composite. The microstructure of bamboo changes from the outer to the inner of the material: it was shown that the density of distribution of the vascular bundles, which act as the reinforcing component, is the highest in the outer green layer. The nodes, which are placed periodically along the length of the bamboo, ensure high tensile strength, stiffness and rigidity on the macroscale. An analysis of the stresses experienced by the bamboo during bending indicates that the maximum stresses are generated at the outer part of the culm as well.

2.3.4 Teeth

Teeth consist generally of an outer hard layer (enamel) and an inner tougher material (dentine). The microstructures and properties of mammalian teeth have been investigated by Fong *et al*. (Fong *et al*., 2000) and Sarikaya *et al*. (Sarikaya *et al*., 2002). According to Sarikaya *et al*., a mammalian tooth is an intricately structured and functionally gradient composite material, in which both enamel (on the outside) and dentine (on the inside) are coupled through an interface region (called the dentine–enamel junction) (Figure 2.2). Enamel is composed of long crystallites packed as bundles in enamel rods. The enamel

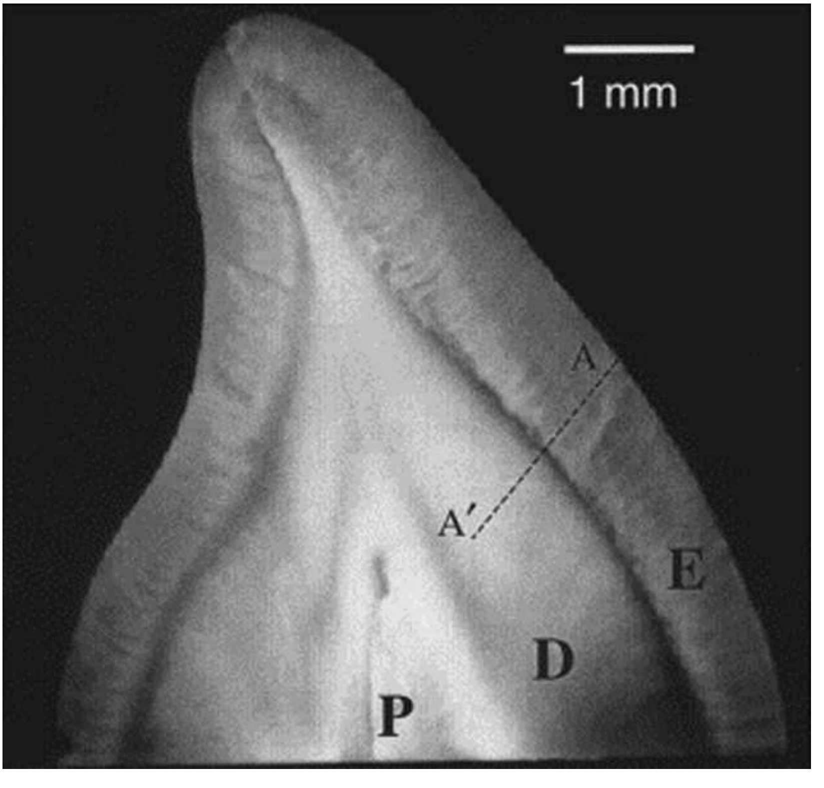

Figure 2.2 *Image of a cross-section of a human incisor sample displaying pulp (P), dentine (D) and enamel (E) regions. Reprinted from* Mater. Sci. Eng., C, **7***(2), Fong, H.* et al. *'Nanomechanical . . . ', pp. 119–128, Copyright (2000), with permission from Elsevier.*

rods are organized unidirectionally normal to the surface of the tooth. This leads to the high hardness and wear resistance of teeth. Dentine is primarily composed of mineralized collagen fibrils that form a randomly intertwined, continuous network; such a structure makes dentine a soft but extremely tough material. A tooth, consisting of a combination of enamel and dentine, represents a functionally gradient composite material, which is similar to cutting and grinding tools.

2.3.5 Bones

Bone consists of an organic matrix (mainly collagen I), mineral phase (crystalline hydroxyapatite) and living cells. While the organic matrix ensures high tensile strength of the bone, the mineral phase is responsible for the stiffness and compressive strength (Pompe and Gelinsky, 2001).

At the nanoscale level, bone matrix consists of mineralized collagen fibrils, in which mineral nanocrystals are embedded (Jäger and Franzl, 2000). At this scale level, bones demonstrate rather high strength and even insensitivity to damage (Gao *et al*., 2003).

At the microlevel, mineralized collagen fibers merge in lamellae (sheets), which can form so-called osteons or a Haversian system. Osteons represent cylinders, formed from several laminae wrapped in concentric layers around a central canal, and oriented roughly parallell to the bone axis. The cracking in a bone under loading may occur at weak interfaces between the lamellae. When the bones fail, an extensive microcracking is observed.

At the macrolevel, long bones represent gradient materials, consisting of a dense cortical (compact) layer at the outer surface, and a porous cancellous bone inside (Rho *et al*., 1998). The deformation at which bones break can be up to 10 % (Currey and Kohn, 1976; Currey, 1984; Currey *et al*., 1995; Weiner and Wagner, 1998; Zioupos, 1998; Reilly and Currey, 2000).

Buskirk *et al*. (Buskirk *et al*., 2002) considered natural holes (foramina) in leg bones of horses, which allow the blood vessels to pass through the hard outer surfaces. These holes never appear as fracture sites of bones. Buskirk and colleagues found that the holes are embedded in a stiffer region, and that the *stiffness gradation* around the holes ensures the high strength of the bones with the natural holes. They demonstrated that the composition in the vicinity of the natural hole reduces the stress concentration. Taking into account the dependence of the Young modulus and strength on density and porosity, the authors suggested a way to improve the strength of plates with a hole by using graded properties distribution.

Peterlik *et al*. (Peterlik *et al*., 2006) investigated the influence of bone microstructure on the toughness, and demonstrated that various toughening mechanisms are active in bones (e.g. crack ligament bridging, crack deflection and multiple microcracking). Further, they observed the transition from a brittle to a quasi-ductile fracture mode, at some angles between the collagen and the crack. According to Peterlik and colleagues, the *variation of fibril angles* across the bone tissue has several advantages over perfect alignment with respect to the fracture resistance of bones. In particular, the variation of fibril angles ensures higher fracture energy, and leads to a more ductile fracture behavior of bones.

Giraud-Guille (Giraud-Guille, 1998) analyzed the collagen networks in compact bone, and concluded that superimposed, discrete layers of lamellae of fibrils 'prove their resistance to mechanical constraints'. She compared the cylindrical concentric lamellae consisting of collagen fibrils in bones with the chitin–protein networks in crustaceans, and observed the strong similarity in the microgeometries of the tissues. In both cases, as well as in many other biological tissues, the '*plywood structure*' (i.e. the multilayered microstructure, with laminae formed from fibrils) is observed.

The peculiarities of bone tissues at the nanoscale level were investigated by Jäger and Franzl (Jäger and Franzl, 2000) and Gao and colleagues (Gao *et al*., 2003). Jäger and Franzl (Jäger and Franzl, 2000) considered the structure of collagen fibrils as assemblies of parallel collagen molecules arranged with a longitudinal stagger, and demonstrated that the staggered arrangement of mineral platelets (which is observed in nature) ensures much higher strength than the strictly parallel arrangement.

Gao *et al*. (Gao *et al*., 2003) and Ji and Gao (Ji and Gao, 2004) showed numerically that the stress field becomes more and more uniform as the thickness of platelets, which constitute the reinforcement of biomaterials at the nanolevel, decreases. They developed the virtual internal bond (VIB) model–based finite element analysis (which incorporates an atomic cohesive force law into the constitutive model of the material), and applied it to analyze failure mechanisms in nanomaterials. The optimal aspect ratio of the mineral platelets was determined from the condition that the protein and mineral fail at the same time. It was shown that 'the smaller the platelets, the larger the optimal aspect ratio; the larger the aspect ratio, the larger the stiffening effect'. According to Gao *et al*. (Gao *et al*., 2003), the strength of nanoscaled mineral platelets in biocomposites is maintained despite defects. The nanometer size of the mineral crystals is therefore a result of fracture strength optimization, which ensures the maximum tolerance of flaws.

On the basis of the short overview of these and other literature sources on the microstructures and strength of biomaterials, some peculiarities of biomaterials, which are responsible for their high strength and damage resistance, can be listed (Mishnaevsky Jr, 2004c, 2005b):

- structural hierarchy (two to three orders of lamellar microstructures with different microarchitectures);
- graded distributions of reinforcement, pores, etc.; distribution of reinforcement follows the expected stress distribution;
- bundles of fibers as reinforcement;
- smallest nanometer-sized building blocks of biocomposites: the fracture strength for the brittle material platelets is equal to the theoretical strength of a perfect material;
- low content of matrix/glue, and high volume content of reinforcement;
- large aspect ratio and staggered arrangement of reinforcing inclusions;
- fractal, smooth, multilevel interface from one material to another.

In this list, only microstructural and not chemical peculiarities of the materials are included. Therefore, they can be transferred to the industrial composites.

2.4 On some concepts of the improvement of material properties

In the last decades, several new technologies and methods for the improvement of composite materials have been developed: new coatings, gradation of properties, double dispersion structures, interpenetrating phase composites, and so on. In the following, we present a brief overview of some directions of the improvement of composites, which lead to the higher strength and damage resistance compared with the conventional homogeneous composites.

2.4.1 Gradient composite materials

These are composites with a smooth variation of phase properties, content or microstructural parameters in one or several directions (see, for instance, Miyamoto *et al*., 1999). One of the oldest examples of a gradient material, mentioned above, is the blades of ancient Japanese swords. The steel swords contained a tough core and hardened edge, with a graded transition between them (Suresh and Mortensen, 1998; Suresh, 2001).

Initially, the materials with graded properties were produced with the use of special casting and heat treatment regimes, or as multilayers using welding and facing technologies. With the development of powder metallurgy and other technologies (e.g. self-spreading high-temperature synthesis), it became possible to produce new types of graded materials, with smooth and controlled phase and properties distribution. The gradient materials are employed in high temperature aerospace components, cutting tools, biomedical devices, etc. The graded composition of materials makes it possible to influence the thermal stress distribution and the local crack resistance, and to reduce the local stress concentration. Compared with layered materials (coated composites, multilayers), gradient materials allow to reduce high interfacial stresses and to exclude the debonding on interfaces, and to increase the lifetime of materials under cyclic loading. Drilling tools made from WC/Co hard alloys with gradient microstructures have four to five times service life of similar tools with homogeneous microstructures (Lisovsky, 2001).

2.4.2 The application of coatings

This is one of the oldest technologies to improve the reliability and lifetime of materials and components. In the aircraft industry, hard coatings are used to increase the corrosion and thermal resistance of turbine blades. Various coatings are used to improve the quality and lifetime of cutting tools, gas turbine blades, optical devices, and other devices and components. The application of coatings can lead to the improvement of several orders of magnitude in the performances of components: for instance, Berríos-Ortíza *et al*. (Berríos-Ortíza *et al*., 2004) demonstrated that the fatigue life of stainless steels, coated with ZrN_x films, increases by 400–1100 %, as compared with uncoated steels.

2.4.3 Layered metal matrix composites

These consist of alternate lamellae of reinforced and unreinforced metal matrix, and exhibit much higher fracture toughness, as compared with homogeneously reinforced composites (Ellis and Lewandowski, 1994; McLelland *et al*., 1999). Ellis and Lewandowski (Ellis and Lewandowski, 1994) demonstrated that layered discontinuously reinforced composites have nearly two times higher fracture toughness, as compared with conventional composites. McLelland and colleagues developed the technology of production of layered aluminum matrix composites, based on thixoforming, and demonstrated that these composites have only slighly improved fracture toughness under impact loading, but strongly improved toughness under slow crack growth conditions.

2.4.4 Surface composites

As developed by Singh and Fitz-Gerald (Singh and Fitz-Gerald, 1997), this is another group of composite materials rather close both to the gradient and coated composites. In these materials, the second phase is distributed in near surface regions, where the 'phase composition is linearly graded as a function of distance from the surface'. Differing from functionally gradient materials (FGMs), the graded properties of surface composites are achieved by transforming the surface of the bulk material into truncated cone-like structures using a multiple pulse irradiation technique, followed by the deposition of the surface phase. This leads to the uniform distribution of the surface phase as clusters on the surface. The cluster size decreases as a function of depth from the surface. Surface composites demonstrate higher adhesion of the surface phase with the bulk material, than normal coated composites.

A schematic diagram of the phase arrangement and distribution in layered, graded and surface composites is shown in Figure 2.3.

2.4.5 Agglomerates of small scale inclusions and the 'double dispersion' microstructures of steels

Berns *et al*. (Berns *et al*., 1998) developed a new tool material with a 'double dispersion' microstructure, in which the coarse hard phase (primary carbides) is replaced by a dense dispersion of small carbides. This material ensures sufficiently (30 %) higher fracture toughness and lifetime than the standard materials for the cold forging tools. Figure 2.4 shows the primary carbide distribution in steel with fine carbides (randomly arranged), coarse carbides and the double dispersion microstructure.

Peng *et al*. (Peng *et al*., 2001a) developed a composite with an Al matrix, reinforced by agglomerates of saffil short fibers. The agglomerates (diameter 0.4–1 mm) were manufactured by tumbling fibers of length $< 200\,\mu m$. Peng and colleagues carried out the 3-point loading tests of the conventional homogeneous composites and the newly developed composites. From their results, it follows that the energy absorbed by the composite during the bending test is 28–70 % higher for the composites reinforced with the fiber agglomerates, than for the conventional homogeneous fiber reinforced composites.

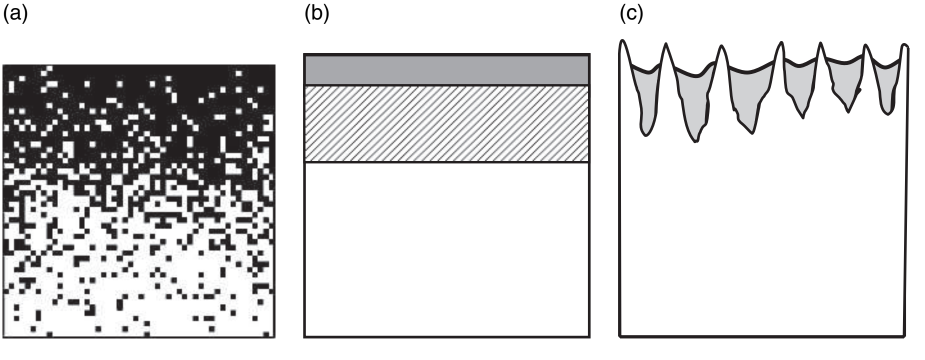

Figure 2.3 *Schematic diagram of (a) gradient, (b) layered and (c) 'surface' composites.*

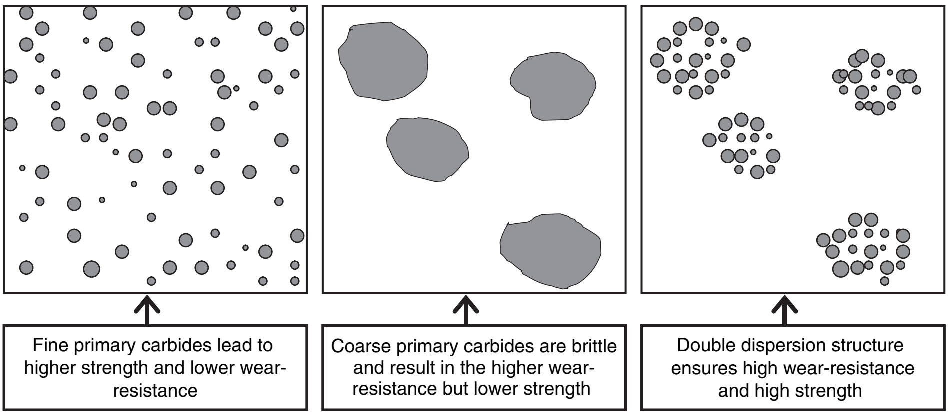

Figure 2.4 *Schematic diagram of the 'double dispersion microstructures' of tool steels (developed by Berns et al., 1998).*

2.4.6 Inclusion networks

Raj and Thompson (Raj and Thompson, 1994) demonstrated that fracture toughness of metal matrix composites can be increased if precipitates are not distributed randomly, but form continuous networks in the composites. Tan and Yang (Tan and Yang, 1998) have shown that dispersed Si nanoparticles distributed along the grain boundaries in nanocomposite alumina ceramics ensure higher toughness of the ceramics by the mechanism of switching from intergranular to transgranular cracking. Broeckmann (Broeckmann, 1994) and Gross-Weege *et al.* (Gross-Weege *et al.*, 1996) studied numerically and experimentally the damage and fracture in ledeburitic chromium steels. They demonstrated that the fracture toughness of the steels can be increased by using netlike arrangements of primary carbides instead of band-like microstructures of steels (which leads to the increasing width of the crack path). Increasing the cell size in the netlike structure of steels leads to larger crack path deviation and increased fracture toughness. In their computational experiments, Mishnaevsky Jr *et al.* (Mishnaevsky Jr *et al.*, 2003a, 2004a) demonstrated numerically that the netlike arrangement of brittle primary carbides ensures the highest fracture toughness of tool steels among all the considered microstructures (including clustered, random and gradient). Figure 2.5 shows the simulated crack path in an artificial netlike microstructure of tool steel. It can be seen that the crack path follows the layers of high density of brittle carbides, and therefore deviates from the mode I crack path.

2.4.7 Interpenetrating phase composites (IPCs)

IPCs, in which each phase forms a completely interconnected contiguous network, received widespread attention after the publication of the review by Clarke (Clarke, 1992). Examples of IPCs are DIMOX materials (Lanxide Corp.), and C^4 materials (interpenetrating Al/Al_2O_3 composite) (Clarke, 1992). Wegner and Gibson (Wegner and Gibson, 2000) demonstrated that the elastic modulus, yield strength and effective thermal expansion coefficient of IPCs are higher that those of non-IPCs (especially if the phase properties are very different). Peng *et al.* (Peng *et al.*, 2001b) observed an increase of

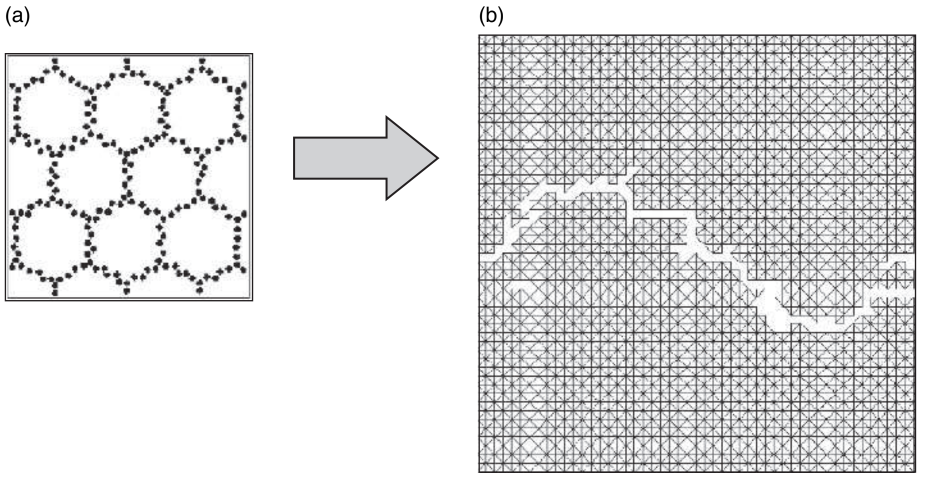

Figure 2.5 *A designed netlike microstructure of (a) a tool steel and (b) the simulated crack path in the microstructure. Black areas correspond to the primary carbides and the white areas correspond to the 'matrix' phase. Reprinted from* Int. J. Mater. Res.*,* **94***(6), Mishnaevsky Jr, L. 'Micromechanisms . . . ', pp. 676–681, Copyright (2003), with permission from Carl Hanser Verlag GmbH & Co. KG.*

the order of 7–8 % in the elastic moduli of interpenetrating Al/Al_2O_3 composites, as compared with conventional homogeneous composites. Among the main advantages of IPCs, one can list isotropic properties (no weak direction), possibility to increase the composite stiffness by making the stiff phase continuous, as well as possibility of synergistic improvement of different material properties by using different interconnected phase networks.

2.4.8 Hyperorganized structure control

In 1994, a consortium of several Japanese Universities and industrial firms started a 'Synergy Ceramics Projects' (Kanzaki *et al.*, 1999), supported by the Ministry of Trade and Industry of Japan. In the framework of this project, the idea to create a new family of ceramic materials, by tailoring material properties using the 'simultaneous control of different structural elements, such as shape and size, at plural scale levels' is realized. The tailoring of materials properties is carried out in the framework of the concept of '*Hyperorganized Structure Control*'. The structural elements of ceramic materials are classified by size at the four size levels: atomic, nanoscale (dislocations, grain boundaries), microscale (dispersoids, pores, grains) and macroscale (layers, films). The idea is to control microstructures both at the atomic and nanoscale levels, and on the microlevel to optimize conflicting material properties.

Kanzaki *et al*. (Kanzaki *et al*., 1999) presented an example of the required combination of material properties which can be difficult to achieve by one-level change of microstructure: strength and toughness. While the strength can be increased by homogenizing microstructures, the homogeneous microstructures have low fracture toughness. However, by varying microstructures of ceramics at several scale levels, the improvement

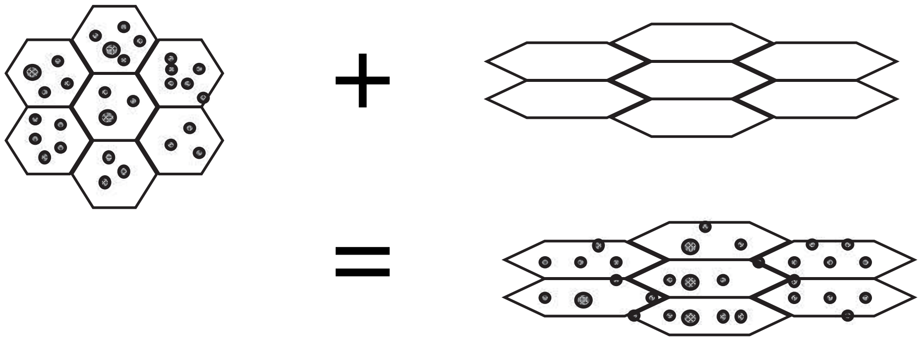

Figure 2.6 *An example of the 'hyperorganized structure control': combination of the oriented anisotropic grains with the intragranular dispersion of nanoparticles, leading to both high strength and high toughness of the composite (after Kanzaki* et al.*, 1999).*

of the conflicting properties can be achieved. For instance, the toughness of a composite can be improved at microlevel by using elongated grains aligned in the same direction. The strength can be improved by placing dispersed nanoparticles inside grains. Thus, the simultaneous improvement of both strength and fracture toughness can be achieved by combination of aligned anisotropic grains with the intragranular dispersion of nanoparticles. For instance, a material with elongated Al_2O_3 grains and $LaAl_{11}O_{18}$ platelets in alumina matrix was developed, which demonstrated both high fracture toughness (6 MPa $m^{1/2}$) and strength of over 600 MPa. The idea of combining the aligned elongated grains with the intragranular dispersion of nanoparticles in the grains, which ensure both high strength and high toughness of the composite, is illustrated in Figure 2.6.

2.4.9 Summary

One can conclude that properties of composites may be improved by varying the arrangements and distributions of their microstructural elements. The following microstructures are shown to have a beneficial effect on the strength and/or fracture resistance of composites:

- gradation of phase distribution or properties;
- coatings, or clusters of another phase on the surface;
- IPCs, netlike arrangement of inclusions;
- double dispersion microstructures;
- multiscale control of properties, e.g. combination of aligned anisotropic grains and nano reinforcement in the grains.

2.5 Physical mesomechanics of materials

Strongly nonlinear effects, pattern formation and stability losses at different scale levels have been observed during the deformation of materials in many experimental studies. In order to analyze these effects, a series of experimental and theoretical studies of the material behavior at the mesolevel has been carried out at the Institute of Strength Physics and Materials Science of the Russian Academy of Sciences (Tomsk, Russia). Panin (Panin, 1998) modeled the destruction of materials, as a cooperative hierarchical self-organization process, which is followed by competitive processes of the accumulation and dissipation of energy. The main points of the concept of the physical mesomechanics of materials, formulated by Panin and colleagues, are summarized in Table 2.2.

Several other research groups analyzed the deformation and fracture processes as synergical, hierarchical processes. Ivanova (Ivanova, 1982) developed a synergetical model of fatigue fracture of metals. She assumed that fatigue fracture is determined by the cooperative behavior of two competitive mechanisms of microfracture, i.e. microshear and microbreakage, each of them depending on critical density of dislocations or disclinations, respectively. A parameter of the stability of the material microstructure was introduced, and defined as:

$$\Delta = \frac{\mu a}{\Delta HE} \tag{2.3}$$

where μ is shear modulus, a is critical elastic energy, E the Young modulus of the material and ΔH the change in the enthalpy of the material. Depending on

Table 2.2 *Main points of the physical mesomechanics of solids.*

Concept	Main points
Structural levels of deformation	During the deformation of solids, the interaction between deformation processes at many structural levels takes place. The following scale levels can be recognized: microlevel (scale level of dislocations and their ensembles), macrolevels, and several mesolevels: mesolevel I (related to rotations inside microstructural elements of the material, grains or dislocational cells), and mesolevel II (related to self-consistent rotations of blocks of microstructural elements)
Elementary process	The elementary process of plastic deformation is a translational–rotational vortex
Role of rotational mode	The translational and rotational modes of deformation are interrelated: a local shear in an element of a microstructure is followed by the rotation (at higher and/or lower scale level). The shears generate elastic and elastoplastic self-oscillations
Mechanisms of plastic flow	Plastic deformation and fracture in materials are caused by loss of shear stability in regions of high stress concentration at different scales. These processes are of a relaxational nature. Relaxation shear with constrained rotation leads to the formation of local torsion-bending zones, which represent secondary stress concentrators in materials, and cause further relaxation shears with self-excited oscillations. The shears, formed as a result of the local shear stability loss, can be observed at several scale levels: as the formation of macrobands at macroscale, localized deformation bands within conglomerates of microstructural elements at mesolevel or as nucleation of the dislocation core at the microlevel
Self-organization	The interaction between relaxation shears at many scale levels lead to self-organization effects, and to the formation of dissipative structures and patterns of plastic deformation

the value of this parameter, local instabilities of the material were investigated. It was shown that the condition of the rotational local instabilities, corresponding to the local fracture is:

$$\Delta \leq \left(\frac{\tau}{\sigma}\right)^2$$

where τ and σ are critical shear and tensile stresses, respectively. The condition of the translational local instabilities can be written as:

$$\mu/E \geq \frac{\tau}{\sigma}$$

Bershadsky (Bershadsky, 1978) formulated the 'principle of inertia of structure', which means that a structure of material is changed under loading in such a way that these changes (e.g. damage degree) are minimal. He developed further a mathematical model of the material failure as a two-level hierarchical system, which ensures the minimum of changes of the material structure.

Summarizing, one may state that the physical mechanisms of deformation and strength of materials are controlled by nonlinear, self-organizing processes, which are influenced by the interaction of different scale levels and many microstructural elements in the materials.

2.6 Topological and statistical description of microstructures of composites

The influence of microstructures of materials on their strength and deformation behavior goes far beyond the 'rule-of-mixture' and load redistribution effects. The spatial heterogeneity and localization of the elements of microstructures play important roles in the deformation and damage of materials (Mishnaevsky Jr and Shioya, 2001). The spatial arrangement of phases in composites can be characterized with the use of different topological and statistical parameters and functions.

In the case of *percolating (interpenetrating) microstructures* of materials (for instance, hard alloys with a carbide skeleton), the connectivity and contiguity parameters of microstructure influence the strength of the composite. The *connectivity* of skeleton from particles is defined as an average number of particles which are joined with some given particle.

To characterize the microstructures of cemented carbides, Gurland (Gurland, 1958) introduced the contiguity parameter, which is defined as an averaged ratio of the grain–grain boundary surface to the total surface of a particle:

$$C_\alpha = \frac{2S_{\alpha\alpha}}{2S_{\alpha\alpha} + S_{\alpha\beta}} \tag{2.4}$$

where C_α is the contiguity of phase α, $S_{\alpha\alpha}$ is the surface area between the grains of the α phase per unit volume, and $S_{\alpha\beta}$ is the surface area between the α and β phases. Lee and Gurland (Lee and Gurland, 1978) characterized the microstructure of interconnected composites by the volume fraction of the continugous phase.

Fan *et al*. (Fan *et al*., 1992) extended this approach and introduced several other parameters, characterizing the microstructures of interconnected composites. In particular, they introduced the degree of separation of phases F_s, defined as:

$$F_s = 1 - f_{\alpha c} - f_{\beta c} \tag{2.5}$$

where $f_{\alpha c}$ and $f_{\beta c}$ are the continuous volume fractions of the α and β phases ($f_{\alpha c} = C_\alpha f_\alpha,\ f_{\beta c} = C_\beta f_\beta$) and f_α and f_β are the volume contents of the phases. To characterize the interpenetrating microstructures, Lessle *et al*. (Lessle *et al*., 1998) introduced the 'matricity' parameter, defined as 'the fraction of the skeleton lines of one phase S, and the length of the skeleton lines of the participating phases'.

Ghosh and co-workers (Ghosh *et al*., 1995; Moorthy and Ghosh, 1998; Lee *et al*., 1999; Li *et al*., 1999) used Dirichlet tessellation of real microstructures of materials to develop microstructural finite element models of the materials. Boselli *et al*. (Boselli *et al*., 1999) proposed the finite-body tessellation method, which represents a generalization of the concept of a Dirichlet–Voronoi tessellation for the case of high volume fractions of particles of various sizes and shapes. The finite-body tessellation method includes the representation of a material as a network of cells, such that every point within a cell is closer to the interface of the corresponding particle than to any other. Using this method, Boselli and colleagues investigated numerically the influences of the particle morphology, homogeneity and inhomogeneity on the fatigue behavior of composites. They found that 'the coefficient of variation of the mean near-neighbor distance, derived from particle interfaces using finite-body tessellation, was essentially independent of particle shape, size distribution, orientation and area fraction in homogeneous (random) distributions, but showed great sensitivity to inhomogeneity.' The coefficient of variation was also seen to be sensitive to anisotropic clustering, the presence of which was identified via nearest-neighbor angles and cell orientations.

A number of statistical functions and parameters have been proposed to characterize composite microstructures. In many works, the radial distribution function (RDF) is used to characterize microstructures of materials. This function $g(r)$ is defined as:

$$g(r) = \frac{n(r)}{4\rho\pi r^2 \Delta r} \tag{2.6}$$

where $n(r)$ is the mean number of particles in a shell of width Δr at distance r from the center of a given particle and ρ is the mean particle density. Figure 2.7 shows an example of determination of this function. In the case depicted, $n(r) = 7$.

Segurado *et al*. (Segurado *et al*., 2003) used the analysis of radial distribution functions of sphere (particles) centers to characterize different clustered microstructures of composites, and to generate particle dispersions with different levels of clustering. Gácsi *et al*. (Gácsi *et al*., 2002) quantified the degree of particle clustering in real microstructures of aluminum-based SiC particle reinforced composites, using RDFs as well. Gácsi and colleagues characterized the microstructures also using average cluster radii, the mean distance from places with lowest particle probability to the cluster centers and the mean intercluster distance regarding the clustered arrangement.

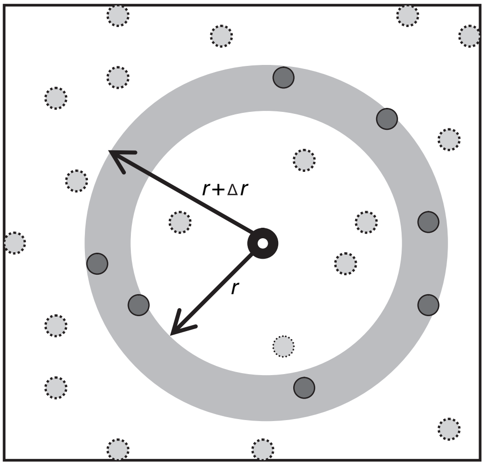

Figure 2.7 Determination of the RDF.

Further, the nearest-neighbor distribution (NND) function is widely used to characterize microstructures of materials. This function is determined as the probability of finding the nearest neighbor (particle) at some given distance from a given particle. A schematic determination of the NND is shown in Figure 2.8, where three inclusions form a 'cluster' (with equal distances between inclusions), one inclusion is close to the 'cluster' and the last one is far away from the 'cluster'. The NND function is defined only for nonpercolating, nontouching inclusion systems. Apewokin (Apewokin, 2004) applied the NND and the RDFs to characterize quantitatively the relationship between clustering and material properties. It was shown that the RDF takes into account the long range microstructural heterogeneities in the composites.

Several comprehensive reviews of the statistical methods of characterization of inhomogeneous microstructures of composites have been published by Torquato (Torquato, 2000, 2002a,b). Some of the methods, discussed in the review by Torquato (Torquato, 2002b) are summarized in Table 2.3. Torquato formulated the Unified Theoretical Approach, based on the canonical n-point correlation function, which allows to generalize and to relate different statistical correlation functions.

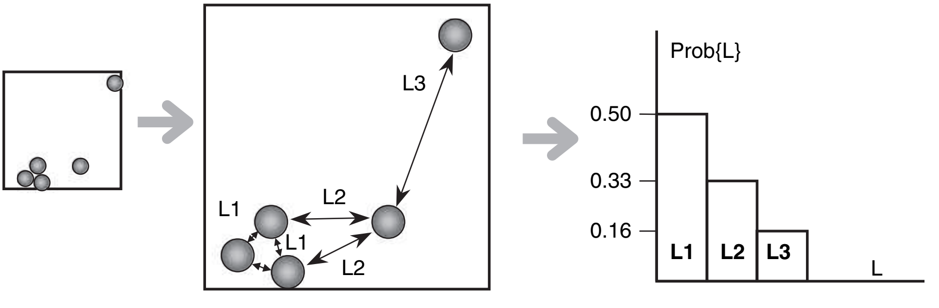

Figure 2.8 Schematic diagram of the determination of the NND function.

Table 2.3 *Statistical characterization of inhomogeneous microstructures of composites (Torquato, 2002b).*

Concept	Main points
n-point phase probability functions	The function is defined as the probability that *n* points at given positions $x1,\ x2,\ \ldots,\ xn$ can be found in the same phase *i*
Surface correlation function	Surface correlation function is defined in the simplest case as the specific surface $s(x)$ (interface area per unit volume) at point *x*
Lineal path function $L(z)$	For statistically isotropic media, this function gives the probability that a line segment of length *z* lies wholly in phase *j*, when randomly thrown into the sample. According to Torquato, this function 'contains a coarse level of connectedness information about phase'
Pore size probability density function $P(\delta)$	Pore size probability density function is defined as the probability that 'a randomly chosen point is located at a distance between δ and $\delta + \Delta\delta$ from the nearest point on the pore–solid interface'
Two-point cluster function	Two-point cluster function $C(x1, x2)$ is the probability of finding two points *x*1 and *x*2 in the same cluster of phase *i*. A cluster of phase *i* is defined as the part of phase *i* that can be reached from a point in phase *i* without passing through phase *j*. In contrast to the two-point probability function, this function contains topological 'connectedness' information

References

Abu Al-Rub, R. K. (2004). Material length scales in gradient-dependent plasticity/damage and size effects: theory and computation, PhD Thesis, Louisiana State University.

Amada, S. (1995). Hierarchical functionally gradient structures of bamboo, barley and corn, *MRS Bulletin, Functionally Gradient Materials*, **20** (1), 35–37.

Amada, S., Ichikawa, Y., Munekata, T., Nagase, Y. and Shimizu, H. (1997). Fiber texture and mechanical graded structure of bamboo, *Composites: Part B (Engineering)*, **28** (1–2), 13–20.

Apewokin, S. (2004). Quantitative characterization of discontinuously reinforced metal matrix composite microstructure using digital image analysis, Georgia Tech.

Arzt, E. (1988). Size effects in materials due to microstructural and dimensional constraints: a comparative review, *Acta Materialia*, **46** (16), 5611–5626.

Bazant, Z. P. (2004). Scaling theory for quasi-brittle structural failure, *Proceedings of the Natural Academy of Sciences USA*, **101** (37), 13400–13407.

Bazant, Z. P. and Yavari, A. (2005). Is the cause of size effect on structural strength fractal or energetic–statistical?, *Engineering Fracture Mechanics*, **72**, 1–31.

Berns, H., Melander, A., Weichert, D., Asnafi, N., Broeckmann, C. and Gross-Weege, A. (1998). A new material for cold forging tool, *Composites Materials Science*, **11** (142), 166–180.

Berríos-Ortíza, J. A., La Barbera-Sosaa, J. G., Teerb, D. G. and Puchi-Cabrera, E. S. (2004). Fatigue properties of a 316L stainless steel coated with different ZrN deposits, *Surface and Coatings Technology*, **179** (2–3), 145–157.

Bershadsky, L. I. (1978). Informational model of irreversible processes, *Proceedings of the Academy of Science of Ukraine*, **5**, 416–422.

Blanckenhagen, B. von, Gumbsch P. and Arzt, E. (2001a). Discrete dislocation simulation of thin film plasticity, *Materials Research Society Symposium Proceedings*, **673**, P2.3.1–P2.3.6.

Blanckenhagen, B. von, Gumbsch P. and Arzt, E. (2001b). Dislocation sources in discrete dislocation simulations of thin film plasticity and the Hall–Petch relation, *Modeling and Simulation in Materials Science and Engineering*, **9**, 157–169.

Boselli, J., Pitcher P. D., Gregson, P. J. and Sinclair, I. I. (1999). Secondary phase distribution analysis via finite body tessellation, *Journal of Microscopy*, **195**, 104–112.

Broeckmann, C. (1994). Bruch karbidreicher Stähle – Experiment und FEM-Simulation unter Berücksichtigung des Gefüges, Dissertation, Ruhr-Universitaet Bochum.

Bundesen, L. Q. (2004). Biography of Zdeněk P. Bažant, *Proceedings of the National Academy of Sciences of the USA*, **101** (37), 13397–13399.

Buskirk, S. R., Venkataraman, S., Ifju, P. G. and Rapoff, A. J. (2002). Functionally graded biomimetic plate with hole, in: *Proceedings of the 43rd AIAA/ASME/ASCE/AHS/ASC Structures, Structural Dynamics, and Materials Conference*, Denver, CO, AIAA Paper 2002–1330.

Clarke, D. R. (1992). Interpenetrating phase composites, *Journal of American Ceramic Society*, **75**, 739–759.

Currey, J. D. (1984). *The Mechanical Adaptions of Bones*, Princeton University Press, Princeton, NJ.

Currey, J. D. and Kohn, A. J. (1976). Fracture in crossed-lamellar structure of Conus shells, *Journal of Materials Science*, **11**, 1615–1623.

Currey, J. D., Zioupos, P. and Sedman, A. (1995). Microstructure–property relationships in vertebrate bony hard tissues, in: *Biomimetics*, Eds M. Sarikaya and I. A. Aksay, AIP Press, Woodbury, NY, pp. 117–144.

Dyskin, A. V., Vliet, M. R. A. V. and Mier, J. G. M. V. (2001). Size effect in tensile strength caused by stress fluctuations, *International Journal Fracture*, **108** (1), 43–61.

Ellis, L. Y. and Lewandowski, J. J. (1994). Effects of layer thickness on impact toughness of Al/Al-SiCp laminates, *Materials Science Engineering*, **A183**, 59–67.

Estrin, Y. (1999). Syntheses: playing scales – a brief summary, *Modelling and Simulation in Materials Science and Engineering*, **7**, 747–751.

Fan, Z. G., Tsakiropoulos, P. and Miodownik, A. P. (1992). Prediction of the Young's modulus of particulate composites, *Materials Science and Technology*, **8**, 922–929.

Fleck, N. A., Muller, G. M., Ashby, M. F. and Hutchinson, J. W. (1994). Strain gradient plasticity: theory and experiment. *Acta Metallurgica et Materialia*, **42** (2), 475–487.

Fong, H., Sarikaya, M., White, S. N. and Snead, M. L. (2000). Nanomechanical properties profiles across DEJ of human incisor teeth, *Materials Science and Engineering*, **7** (2,) 119–128.

Freund, L. B. (1987). The stability of a dislocation threading a strained layer on a substrate, *Journal of Applied Mechanics*, **54**, 553–557.

Freund, L. B. (1994). The mechanics of dislocations in strained-layer semiconductor materials, *Advanced Applied Mechanics*, **30**, 1–66.

Freund, L. B. and Nix, W. D. (1996). A critical thickness condition for a strained compliant substrate/epitaxial film system, *Applied Physics Letters*, **69** (2), 173–175.

Gao, H., Ji, B., Jäger, I. L., Arzt, E., and Fratzl, P. (2003). Materials become insensitive to flaws at nanoscale: lessons from nature, *Proceedings of the National Academy of Sciences of USA*, **100** (10), 5597–5600.

Gácsi, Z., Kovács, J. and Pieczonka, T. (2002). Characterisation of particle arrangement using the radial distribution function, in: *Proceedings of the 3rd International Powder Metallurgy Conference*, Eds S. Saritas, I. Uslan and Y. Usta, TTMD Turkish Powder Metallurgy Association, Gazi University, Ankara, Turkey, pp. 542–551.

Ghosh, S., Lee K. and Moorthy, S. (1995). Multiple analysis of heterogeneous elastic structures using homogenization theory and Voronoi cell finite element method, *International Journal of Solids and Structures*, **32** (1), 27–62.

Giraud-Guille, M. -M. (1998). Plywood structures in nature, *Current Opinion in Solid State and Materials Science*, **3** (3), 221–227.

Gross-Weege, A., Weichert, D. and Broeckmann, C. (1996). Finite element simulation of crack initiation in hard two- phase materials, *Computational Materials Science*, **5**, 126–142.

Gurland, J. (1958). The measurement of grain contiguity in two-phase alloys, *Transactions of the American Institute of Mining, Metallurgical and Petroleum Engineers*, **212**, 452–455.

Ivanova, V. S. (1982). Synergetics of fracture and mechanical properties, in: *Synergetics and fatigue fracture of metals*, Nauka, Moscow, pp. 6–29.

Jackson, A. P., Vincent, J. F. V. and Turner, R. M. (1988). The mechanical design of nacre, *Proceedings of the Royal Society of London*, **234**, 415–440.

Jäger, I. and Fratzl, P. (2000). Mineralized collagen fibrils – a mechanical model with a staggered arrangement of mineral particles, *Biophysical Journal*, **79**, 1737–1746.

Ji, B. and Gao, H. (2004). A study of fracture mechanisms in biological nano-composites via the virtual internal bond model, *Materials Science and Engineering, A*, **366**, 96–103.

Kamat, S., Su, X., Ballarini, R. and Heuer, A. H. (2000). Structural basis for the fracture toughness of the shell of the conch *Strombus gigas, Nature*, **405**, 1036–1040.

Kanzaki, S., Shimada, M., Komeya, K. and Tsuge, A. (1999). Recent progress in the synergy ceramics project, *Key Engineering Materials*, **161–163**, 437–442.

Katti, K. S., Katti, D. R., Pradhan, S. M., and Bhosle, A. (2005). Platelet interlocks are the key to toughness and strength in nacre, *Journal of Materials Research*, **20** (5), 1097–1100.

Lee, H. C. and Gurland, J. (1978). Hardness and deformation of cemented tungsten carbide, *Materials Science and Engineering*, **33**, 125–133.

Lee, K., Moorthy, S. and Ghosh, S. (1999). Multiple scale computational model for damage in composite materials, *Computer Methods in Applied Mechanics and Engineering*, **172**, 175–201.

Li, M., Ghosh, S. and Richmond, O. (1999). An experimental-computational approach to the investigation of damage evolution in discontinuously reinforced aluminium matrix composite, *Acta Materialia*, **47** (12), 3515–3532.

Lisovsky, A. F. (2001). Properties of cemented carbides alloyed by metal melt treatment, in: *Proceedings of the 15th International Plansee Seminar*, Eds G. Kneringer, P. Rodhammer and H. Wildner, Plansee Holding AG, Reutte, Vol. 2, 168–179.

Lloyd, D. J. (1994). Particle reinforced aluminum and magnesium matrix composites, *International Materials Reviews*, **39**, 1–23.

McLelland, A. R. A., Atkinson, H. V. and Anderson, P. R. G. (1999). Thixoforming of a novel layered metal matrix composite, *Materials Science and Technology*, **15** (8), 939–945.

Mishnaevsky Jr, L. (2004c). Computational design of bioinspired composite materials: an approach based on numerical experiments, in: *Proceedings of the 3rd Materials Processing for Properties and Performance Conference*, Vol. 3, Eds K. A. Khor, R. V. Ramanujan, C. P. Ooi and J. H. Zhao, Institute of Materials East Asia, Singapore, pp. 226–232.

Mishnaevsky Jr, L. (2005b). Numerical experiments in the mesomechanics of materials, Habilitation Thesis, TU Darmstadt, Darmstadt.

Mishnaevsky Jr, L. and Gross, D. (2004a). Micromechanisms and mechanics of damage and fracture in thin film/substrate systems, *International Applied Mechanics*, **40** (2), 33–51.

Mishnaevsky Jr, L. and Gross, D. (2004b). A dislocation-density based model of deformation and damage initiation in thin polycrystalline films, in: *Proceedings of the 15th European Conference on Fracture*, Stockholm, CD ROM.

Mishnaevsky Jr, L. and Gross, D. (2005). Deformation and failure in thin films/substrate systems: methods of theoretical analysis, *Applied Mechanics Reviews*, **58** (5), 338–353.

Mishnaevsky Jr, L. and Schmauder, S. (2001). Continuum mesomechanical finite element modeling in materials development: a state-of-the-art review, *Applied Mechanics Reviews*, **54** (1), 49–69.

Mishnaevsky Jr, L. and Shioya, T. (2001). Optimization of materials microstructures: information theory approach, *Journal of the School of Engineering, The University of Tokyo*, **48**, 1–13.

Mishnaevsky Jr, L., Lippmann, N. and Schmauder, S. (2003a). Computational modeling of crack propagation in real microstructures of steels and virtual testing of artificially designed materials, *International Journal of Fracture*, **120** (4), 581–600.

Mishnaevsky Jr, L., Weber, U. and Schmauder, S. (2004a). Numerical analysis of the effect of microstructures of particle-reinforced metallic materials on the crack growth and fracture resistance, *International Journal of Fracture*, **125**, 33–50.

Miyamoto, Y., Kaysser, W. A., Rabin, B. H., Kawasaki, A. and Ford, R. G. (1999). *Functionally Graded Materials, Design, Processing and Applications*, Kluwer, Dordrecht.

Moorthy, S. and Ghosh, S. (1998). A Voronoi cell finite element model for particle cracking in elastic-plastic composite materials, *Computer Methods in Applied Mechanics and Engineering*, **151**, 377–400.

Nan, C. -W. and Clarke, D. R. (1996). The influence of particle size and particle fracture on the elastic/plastic deformation of metal matrix composites, *Acta Materialia*, **44**, 3801–3811.

Needleman, A. (2000). Computational mechanics at the mesoscale, *Acta Materialia*, **48** (1), 105–124.

Nix, W. D. (1989). Mechanical properties of thin films, *Metallurgical Transactions A*, **20**, 2217–2245.

Okumura, K. and de Gennes, P. (2001). Why is nacre strong? Elastic theory and fracture mechanics for biocomposites with stratified structures, *European Physical Journal*, **E4**, 121–127.

Panin, V. (Ed.) (1998), *Physical Mesomechanics of Heterogeneous Media and Computer-Aided Design of Materials*, Cambrige International Science Publishing, Cambridge.

Peng, H. X., Fan Z. and Evans J. R. G. (2001a). Novel MMC microstructure with tailored distribution of the reinforcing phase, *Journal of Microscopy*, **201** (2), 333–338.

Peng, H. X., Fan Z. and Evans J. R. G. (2001b). Bi-continuous metal matrix composites, *Materials Science and Engineering, A*, **303**, 37–45.

Peterlik, H., Roschger, P., Klaushofer, K. and Fratzl, P. (2006). From brittle to ductile fracture of bone, *Nature Materials*, **5**, 52–55.

Pompe, W. and Gelinsky M. (2001). Biological materials: failure of bone and teeth, in: *Encyclopedia of Materials: Science and Technology*, Eds K. H. J. Buschow, R. W. Cahn, M. C. Flemings, B. Ilschner, E. J. Kramer and S. Mahajan, Elsevier (Pergamon), Oxford, Vol. 1, pp. 580–584.

Qi, H. J., Bruet, B. J. F, Palmer, J. S., Ortiz, C. and Boyce, M. C. (2005). Micromechanics and macromechanics of the tensile deformation of nacre, in: *Mechanics of Biological Tissues*, Eds G. A. Holzapfel and R. W. Ogden, Springer-Verlag, Graz, pp. 175–189.

Raj, R. and Thompson, L. R. (1994). Design of the microstructural scale for optimun toughness in metallic composites, *Acta Metallurgica et Materialia*, **42** (12), 4135–4142.

Ramachamndra Rao, P. (2003). Biomimetics, *Sadhan, a*, **28** (3–4), 657–676.

Reilly, G. and Currey, J. (2000). The effects of damage and microcracking on the impact strength of bone, *Journal of Biomechanics*, **33**, 337–343.

Rho, J. -Y., Kuhn-Spearing, L. and Zioupos, P. (1998). Mechanical properties and the hierarchical structure of bone, *Medical Engineering and Physics*, **20** (2), 92–102.

Sarikaya, M., Fong, H., Sopp, J. M., Katti, K. S. and Mayer, G. (2002). Biomimetics: nanomechanical design of materials through biology, in: *15th ASCE Engineering Mechanics Conference* June 2–5, 2002, Columbia University, New York, NY.

Sarikaya, M., Fong, H., Sunderland, N., Flinn, B. D., Mayer, G., Mescher, A. and Gaino, E. (2001). Biomimetic model of a sponge-spicular optical fiber—-mechanical properties and structure, *Journal of Materials Research*, **16** (5), 1420–1435.

Segurado, J., González, C. and LLorca, J. (2003). A numerical investigation of the effect of particle clustering on the mechanical properties of composites. *Acta Materialia*, **51**, 2355–2369.

Shan, Z. and Sitaraman, S. K. (2003). Elastic-plastic characterization of thin films using nanoindentation technique, *Thin Solid Films*, **437**, 176–181.

Singh, R. K. and Fitz-Gerald, J. (1997). Surface composites: a new class of engineered material, *Journal of Materials Research*, **12**, 769–774.

Smith, B., Schaffer, T., Viani, M., Thompson, J., Frederick, N., Kindt, J., Belcher, A., Stucky, G. Morse, D. and Hansma, P. (1999). Molecular mechanistic origin of the toughness of natural adhesives, fibres and composites, *Nature*, **399**, 761–763.

Suresh, S. (2001). Graded materials for resistance to contact deformation and damage, *Science*, **292** (5526), 2447–2451.

Suresh, S. and Mortensen, A. (1998). *Fundamentals of Functionally Graded Materials*, Institute of Materials, London.

Tan, H. L. and Yang, W. (1998), Toughening mechanisms of nano-composite ceramics, *Mechanics of Materials*, **30**, 111–123.

Thompson, C. V. (1993). The yield stress of polycrystalline thin films, *Journal of Materials Research*, **8**, 237.

Tjernlund, J. A. (2005). Length-scale effects in yielding and damage development in polymer materials, Solid Mechanics Licentiate thesis, Stockholm.

Torquato, S. (2000). Modeling of physical properties of composite materials, *International Journal of Solids and Structures*, **37**, 411–422.

Torquato, S. (2002a). *Random Heterogeneous Materials: Microstructure and Macroscopic Properties*, Springer-Verlag, New York.

Torquato, S. (2002b). Statistical description of microstructures, *Annual Review of Materials Research*, **32**, 77–111.

Trondl, A., Gross, D., Mishnaevsky Jr, L. and Huber, N. (2006). 3D FEA of size effects in deformation of then metallic films, *Proceedings of Applied Mathematics and Mechanics*, **6**, 517–518.

Wegner, L. D. and Gibson, L. J. (2000). The mechanical behaviour of interpenetrating phase composites. I: Modeling. II: A case study of a three-dimensionally printed material, *International Journal of Mechanical Sciences*, **42** (5), 925–942, 943–964.

Weibull, W. (1939). A statistical theory of the strength of material, *The Royal Swedish Institute for Engineering Research, Proceedings*, No. 151, 1–45.

Weiner, S. and Wagner H. D. (1998). The material bone: structure–mechanical function relations, *Annual Review of Materials Science*, **28**, 271–298.

Xu, Z. -H. and Rowcliffe, D. (2002). Nanoindentation on diamond-like carbon and alumina coatings, *Surface and Coatings Technology*, **161** (1), 44–51.

Xue, Z., Huang Y., Hwang K. C. and Li, M. (2002). The influence of indenter tip radius on the micro-indentation hardness, *Journal of Engineering Materials and Technology*, **124** (3), 371–379.

Zioupos, P. (1998). Recent developments in the study of failure of solid biomaterials and bone: 'fracture' and 'pre-fracture' toughness, *Materials Science and Engineering, C*, **6**, 33–40.

3

Damage and failure of materials: concepts and methods of modeling

In this chapter, a brief overview of the main concepts of fracture and damage mechanics, as well as the statistical theory of strength is given.

Consider some volume of an elastic material subject to a mechanical load. For a two-dimensional problem, the stress and strain fields are described by the following set of equations (plus the corresponding kinematic and static boundary conditions):

- kinematic equations $\varepsilon_{ij} = \frac{1}{2}\left(\frac{\partial u_i}{\partial x_j} + \frac{\partial u_j}{\partial x_i}\right)$
- constitutive equations $\sigma_{ij} = \sum_{k,l} D_{ijkl}\varepsilon_{kl}$
- equilibrium equations $\sum_j \frac{\partial \sigma_{ij}}{\partial x_j} = F_i$

where u is displacement, ε is strain, σ are the stress tensor components, F are body forces, D are elastic material constants and $x_i,\ x_j,\ x_k$ are coordinates. In more complex cases of plastic, viscoplastic and other nonlinear material behavior and/or dynamic loadings, nonlinear, time-dependent versions of these equations are used to describe the material deformation.

3.1 Fracture mechanics: basic concepts

Fracture mechanics is the basic approach used to describe failure behavior of materials under loading. The subject of fracture mechanics is the analysis of conditions of the formation, growth and stability of cracks in solids. Fracture mechanics includes a number of concepts and approaches which were developed to analyze different aspects and features of the material destruction, such as the Griffith energy theory of failure, analysis

Computational Mesomechanics of Composites L. Mishnaevsky Jr

of stress distribution near cracks and crack interaction, and the Dugdale model of the plasticity effects in materials failure. If only cracks in a linearly elastic isotropic material are considered, the term 'linear elastic fracture mechanics' (LEFM) is used.

3.1.1 Griffith theory of brittle fracture

The energy criterion of crack propagation has been derived by Alan Arnold Griffith (Griffith, 1920) for the case of an ideal brittle material. If a crack of length $2l$ is introduced into an infinite plate under tensile loading (Figure 3.1), the elastic stresses relax around the crack and reduce the elastic potential energy Π. To increase the crack length l by a value $\mathrm{d}l$, some work should be applied which is proportional to $\mathrm{d}l$. According to Griffith, this work is caused by the surface formation energy. The crack grows if the potential energy Π, which is released when the crack front moves by $\mathrm{d}l$, is equal or greater than the fracture work:

$$-\Pi < \gamma \mathrm{d}l \tag{3.1}$$

where γ is the specific work of fracture (per unit new surface).

From the energy analysis, one can derive:

$$\frac{\mathrm{d}\Pi}{\mathrm{d}l} = -\frac{2B\pi\sigma^2 l}{E} \tag{3.2}$$

where B is the thickness, E is the Young modulus of the material and σ is stress.

Substituting this formula into the condition for crack growth, one derives the Griffith formula for the critical stress:

$$\sigma_c = \left(\frac{2\gamma E}{\pi l}\right)^{1/2} \tag{3.3}$$

Later, it was shown (Irwin, 1958) that the main part of the work of fracture is spent on plastic deformation and other irreversible effects, and not on the formation of new

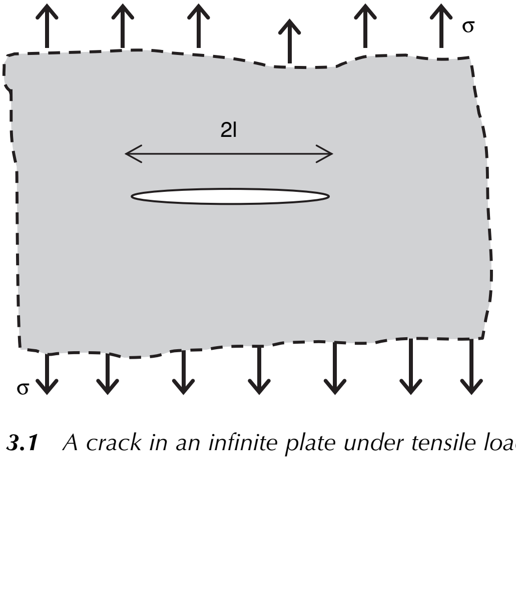

Figure 3.1 A crack in an infinite plate under tensile loading.

surfaces (different from the initial assumptions made by Griffith). For a ductile material, the plastic work of deformation γ_p is introduced into Equation (3.3):

$$\sigma_c = \left[\frac{(2\gamma + \gamma_p)E}{\pi l}\right]^{1/2} \tag{3.4}$$

3.1.2 Stress field in the vicinity of a crack (Figure 3.2)

Since the destruction of a material is a local process, it is influenced first of all by the stress distribution in the vicinity of the crack tips. Westergaard (Westergaard, 1939) derived formulae for the stress distribution in the vicinity of a sharp crack in an elastic plate:

$$\sigma_{ij}(x, y) = \frac{K}{(2\pi r)^{1/2}} f_{ij}(x, y) \tag{3.5}$$

where *x, y* are coordinates, *i, j* can be *x,y, z, f(x,y)* is a function of the coordinates, which can be found elsewhere and *K* is the stress intensity factor, which for the Griffith problem is determined as $K_I = \sigma(\pi l)^{1/2}$. (The subscript *I* here means that the tensile normal crack is considered.)

3.1.3 Stress intensity factor and energy release rate

According to Irwin (Irwin, 1957), a crack starts to grow if the *stress intensity factor* reaches or exceeds some critical level K_{Ic}:

$$K_I = K_{Ic} \tag{3.6}$$

Equations (3.3) and (3.6) are equivalent, if:

$$K_{Ic} = \left(\frac{\gamma E}{1 - \nu^2}\right)^{1/2} \tag{3.7}$$

Equation (3.7) establishes the link between the energy approach by Griffith and the stress analysis by Irwin.

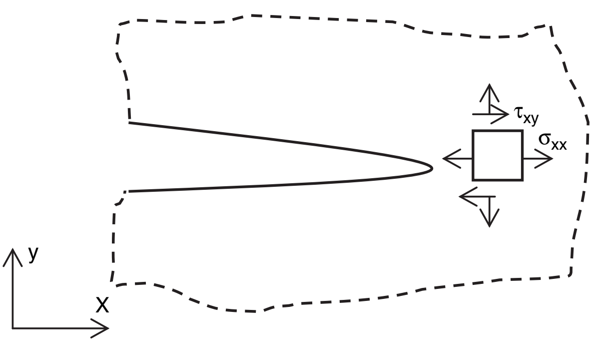

Figure 3.2 *Stress distribution near a crack.*

Taking into account the three main crack opening modes, the energy release rate (for the plain strain case) can be calculated by:

$$G = \frac{1-\nu^2}{E}(K_{\mathrm{I}}^2 + K_{\mathrm{II}}^2) + \frac{1+\nu}{E}K_{\mathrm{III}}^2 \tag{3.8}$$

where $K_{\mathrm{I,II,III}}$ are the stress intensity factors for the three crack opening modes, respectively, G is the energy of the system, which is released when a crack grows by a unit surface (Yokobori, 1978).

In the general case, the stress intensity factor is determined by:

$$K = Y\sigma(\pi l)^{1/2} \tag{3.9}$$

where Y is a dimensionless function, depending on the loading conditions, shape of the specimen and material properties.

3.1.4 *J*-integral and other models of plastic effects

The linear elastic fracture mechanics can be generalized to the case of nonlinear elastic, elastoplastic and plastic materials with the use of the method of invariant integrals. The *J-integral*, which represents a generalization of G for an elastoplastic case, is calculated as the energy absorbed per unit area as the crack grows:

$$J = \int_C \left(W\mathrm{d}y - \sigma_{jk}\boldsymbol{n}_k \frac{\mathrm{d}u_j}{\mathrm{d}x}\mathrm{d}s\right) \tag{3.10}$$

where C is some contour around the crack tip, $\boldsymbol{n}_k$ is the normal vector to the contour, u_j are displacements and W is the strain energy density within the contour. The most important property of the J-integral is that it is invariant with respect to the shape of the contour C (as long as it contains the same singularity).

An approach to the analysis of the plastic effects of fracture was suggested by Irwin (Irwin, 1958, 1960) and Dugdale (Dugdale, 1960). A small plastic zone is introduced near the crack tip, where all the plastic effects are localized. Outside this zone, the material is supposed to be linear-elastic. The stress $\sigma_y(x, 0)$ inside some zone of size λ near the crack tip is constant and equal to the yield stress (σ_0). The size of the plastic zone, according to the Irwin model, is given by:

$$r = \frac{1}{2\pi}\left(\frac{K_{\mathrm{I}}}{\sigma_t}\right)^2 \tag{3.11}$$

where σ_t is the yield stress of the material.

Still another parameter of the fracture resistance of elastoplastic materials is the crack tip opening displacement (CTOD). A crack begins to grow when the CTOD δ reaches some critical value δ_c: $\delta = \delta_c$. For the case of a round crack, the crack opening displacement can be determined on the basis of the Dugdale model by the formula:

$$\delta = \frac{8\sigma l}{\pi E}\ln\sec\left(\frac{\pi\sigma}{2\sigma_0}\right) \tag{3.12}$$

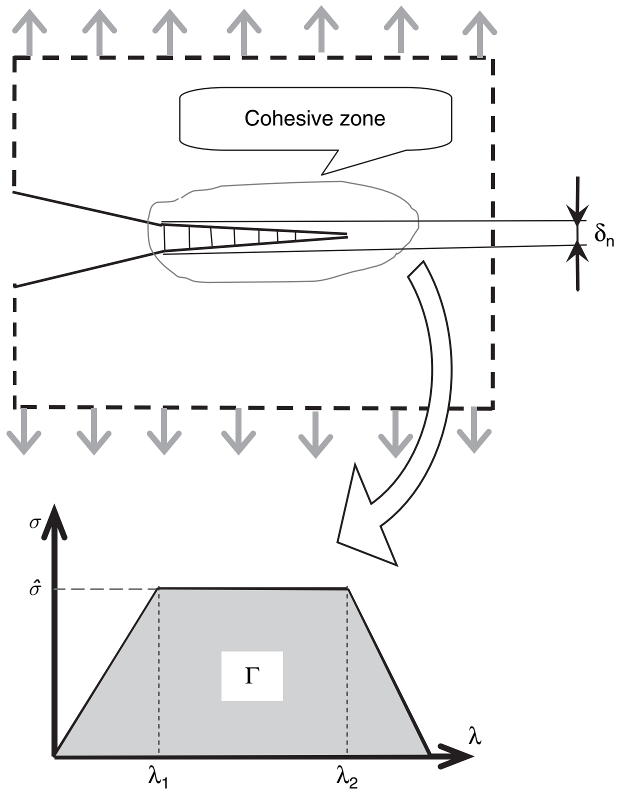

Figure 3.3 *Cohesive zone model. Traction–separation law is embedded into the model as the boundary condition along the interface. Here δ_n is the normal component of the relative displacement of the crack face across the interface, σ is stress and Γ is energy.*

If $\sigma << \sigma_0$, this formula can be reduced to the Griffith equation by assuming $\gamma = \sigma_0\delta_c$.

The idea of Dugdale to consider the area ahead of crack tips as a *cohesive zone* with nonzero tractions was further used by Needleman (Needleman, 1987), Tvergaard (Tvergaard, 1990) and Tvergaard and Hutchinson (Tvergaard and Hutchinson, 1992, 1994, 1996) in their cohesive zone models (CZMs). In the framework of a CZM, the constitutive behavior of the cohesive zone is described by a so-called traction–separation law. A traction–separation law is embedded into the model as the boundary condition along the expected fracture path. Figure 3.3 shows schematically the CZM and the simple, widely used traction–separation law. The relation is such that with increasing crack opening, the traction reaches a maximum, then decreases and eventually vanishes so that complete decohesion occurs. In the model, developed by Tvergaard and Hutchinson, this law is described by:

$$\Phi(\delta_n, \delta_t) = \delta_n^c \int_0^{\lambda} \sigma(\lambda')d\lambda'$$

$$\lambda = \sqrt{(\delta_n/\delta_n^c)^2 + (\delta_t/\delta_t^c)^2}$$

$$T_n = \partial\Phi/\partial\delta_n = \frac{\sigma(\lambda)}{\lambda}\frac{\delta_n}{\delta_n^c};\ T_t = \partial\Phi/\partial\delta_t = \frac{\sigma(\lambda)}{\lambda}\frac{\delta_t}{\delta_t^c} \tag{3.13}$$

where Φ is the potential from which the tractions (T_n, T_t) are derived, λ is the nondimensional separation measure, δ_n, δ_t are normal and tangential components of relative displacements of crack faces across the interface and δ_n^c, δ_t^c are critical values of the components. The CZMs are widely used in the numerical analysis of fracture.

The concepts and methods of fracture mechanics represent the basis of any analysis of the strength of materials, including the analysis of the microstructure–strength relationships of materials.

3.2 Statistical theories of strength

Mechanical properties of materials, their fracture resistance and strength feature a high degree of variability. The variability of material properties at the microlevel influences the macroscopic properties of materials to a large degree. A number of statistical and probabilistic models of material destruction, which relate the statistical variation of material properties at the microlevel with the material characteristics at macrolevel (e.g. likelihood of failure, stiffness or strength), have been developed.

3.2.1 Worst flaw and weakest link theories

The most famous paper on the statistical theory of strength was published by Waloddi Weibull in 1939 (Weibull, 1939). Weibull sought to explain the statistical variability of failure strengths of materials. He considered a material as consisting of many volume elements, with given independent (and randomly varied) 'risks of rupture'. The failure condition is that one of the cracks in a specimen reaches the critical (Griffith's) size *(worst flaw theory)*. The strength of a specimen is calculated as the stress at which the biggest crack in the material propagates. Assuming a probability distribution law of the volume element strengths (using the probability law, which is now called the Weibull distribution), Weibull calculated the strength as a function of the volume of the specimen.

The 'probability of rupture' for a given volume V is calculated by:

$$P_F = 1 - \exp\left[-V\left(\frac{\sigma}{\sigma_o}\right)^m\right] \tag{3.14}$$

where σ is stress and σ_0 and m are constants of the material. It was shown that 'ultimate stress and the standard deviation increase as the volume V increases'. Figure 3.4 shows schematically the 'worst flaw concept', which also illustrates the limitations of this concept: the effect of other, 'nonworst' flaws is neglected in this model.

The *weakest link concept* has been further analyzed by Freudenthal (Freudenthal, 1968). The weakest link concept means that the fracture of a specimen is determined by the local strength of its weakest element. If the strength of elements is determined by the single flaws available in the elements, the weakest link concept is reduced to the worst

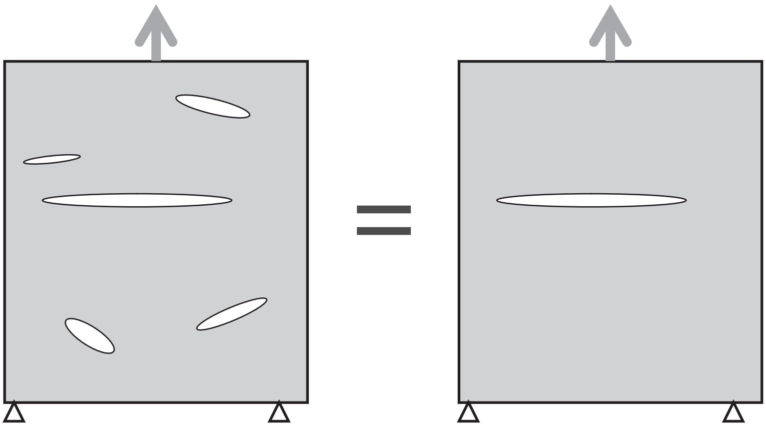

Figure 3.4 *Worst flaw theory. A specimen fails if the biggest crack reaches a critical size.*

flaw concept. Using the simple probabilistic reasoning, Freudenthal derived the following formula for the probability of fracture of a given volume V of material:

$$P_{\mathrm{F}}(V) = 1 - \exp(-cV) \tag{3.15}$$

where c is the mean density of defects. The formula was derived for the case when the volume fails if only one (critical) defect is available there.

If the volume fails when n (and not just 1) defects are there, Equation (3.15) takes the form:

$$P_{\mathrm{F}}(V) = 1 - \frac{\Gamma(n+1) - \Gamma(cV, n+1)}{\Gamma(n+1)} \tag{3.16}$$

where $n = n_0\sigma_s/\sigma$ is the amount of inhomogeneities (defects) in a unit volume, σ is stress, n_0, σ_s are material parameters, $\Gamma()$ is the gamma function, $c = 1/v_0$, v_0 is the average volume per heterogeneity in the material and V is volume. Introducing the Cauchy probability distribution for the defect sizes, Freudenthal derived the following formula for the failure probability:

$$P_{\mathrm{F}} = 1 - \exp\left[-\left(\frac{\sigma}{\sigma_{\mathrm{c}}}\right)^{2\alpha}\right] \tag{3.17}$$

where α is a parameter of the Cauchy probability distribution for the defect sizes and σ_c is critical stress. Further, Freudenthal considered the weakest link concept on the basis of the asymptotic theory of extreme values, and derived the Weibull-type probability strength distributions using the statistics of extremes.

In order to generalize the statistical theories of strength to the case of multiaxial loading, the normal stress averaging method (based on the integration of the stresses normal to the tangential areas of a spherical unit surface), and principle of independent actions as well as some fracture mechanics based approaches have been used. In the framework of the principle of independent actions, the total failure probability is determined as a function of all tensile principal stresses (σ_1, σ_2, σ_3):

$$P_F = 1 - \exp\left\{-\int_V \left[\left(\frac{\sigma_1}{\sigma_{01}}\right)^{m1} + \left(\frac{\sigma_2}{\sigma_{02}}\right)^{m2} + \left(\frac{\sigma_3}{\sigma_{03}}\right)^{m3}\right] \mathrm{d}V\right\} \tag{3.18}$$

where σ_{01}, σ_{02}, σ_{03}, m_1, m_2 and m_3 are Weibull parameters (Tripp *et al.*, 1989). The principle of independent action is the statistical formulation of the maximum stress failure criterion.

Both the normal stress averaging method and the principle of independent action neglect the shear stresses in the material.

Batdorf and Crose (Batdorf and Crose, 1974) developed a statistical theory of failure on the basis of the weakest link statistics and the linear elastic fracture mechanics. Assuming that the failure occurs if a crack is subject to some critical stress (depending on its orientation), they calculated the probability of failure P_i due to the ith crack in the critical stress range (between σ_c and $\sigma_c + \Delta\sigma_c$) as the product of the probabilities P_1 and P_2:

$$P_i = P_1 P_2 \tag{3.19}$$

where P_1 is the probability that a crack having a critical stress in a given range exists in the volume element and P_2 is the probability that the normal to the crack plane lies in some range.

The failure probability of a volume with many cracks was calculated as:

$$P_{\mathrm{F}} = \exp\left(-\sum_i P_i\right) = \exp\left(-\int \mathrm{d}V \int \frac{\mathrm{d}N}{\mathrm{d}\sigma_{\mathrm{c}}} \frac{\Omega}{4\pi} \mathrm{d}\sigma_{\mathrm{c}}\right) \tag{3.20}$$

where N is the number of cracks, σ_c is the critical stress for a given crack, Ω is the angle at which the fracture occurs at σ_c. The theory was generalized by Batdorf and Heinisch (Batdorf and Heinisch, 1978) to take into account the shear on the crack planes.

A number of other probabilistic and statistical theories of strength and failure have been developed on the basis of the weakest link model. Often, this model includes the critical defect density condition. Chudnovsky (Chudnovsky, 1973) proposed a model of a body as an ensemble of elements, grouped into layers, which can fail if a critical amount of elements in the layer fails. In the framework of the statistical theory of macroscopic failure, he determined the probability of material failure using the formula of conditional probabilities. Mishnaevsky Jr (Mishnaevsky Jr, 1996b, 1998a) modeled the formation of cracks as an aggregation of randomly formed microdefects, and used the percolation threshold as a parameter of the critical defect density, necessary for the crack formation.

3.2.2 Random processes and stochastic equations

Takeo Yokobori (Yokobori, 1978) applied the theory of *random processes* to the analysis of strength and fracture of solids. Considering local failure as a n-step random process with n possible states, he derived a system of differential equations for the probabilities of transition of ith into jth state (e.g. from the material state without a crack, to the material state with a crack or to the material state after failure). For the model of failure as a three-state process, the formulae are as follows:

$$\frac{dP_1}{dt} = -m_{12}P_1(t) \qquad \frac{dP_2}{dt} = m_{12}P_1(t) - m_{23}P_2(t) \qquad \frac{dP_3}{dt} = m_{23}P_2(t) \qquad \sum_i P_i = 1 \tag{3.21}$$

where P_1, P_2, P_3 are probabilities that the material is in one of the three states (1 = no defects, 2 = the volume contains a crack, 3 = the failed volume after crack propagation), respectively, m_{ij} is the probability of a transition from ith into jth state. In order to illustrate the transition of the system from one state to another, Yokobori used the Shannon diagrams. Figure 3.5 shows failure as a three-state random process.

For cyclic loading, the differentiation on t is substituted by the differentiation by the number of cycles. That leads to the following (simplified) formula for the lifetime N of a material under cyclic loading:

$$N = 1/m_{12} + 1/m_{23}. \tag{3.22}$$

Determining the values m_{ij} on the basis of the physical analysis of failure mechanisms, Yokobori derived formulae for the crack growth rate under cyclic loading, failure probability, and analyzed the effects of creep and statistical variations of the crack sizes on the material fracture.

Xing (Xing, 1996) developed nonequilibrium statistical fracture mechanics, based on the methods of the stochastic theory. The microcrack evolution is described with the use of the generalized Langevin equation. Taking into account the micromechanisms of microfracture, Xing determined the probability function of microcrack distribution and the probability of fracture. Mishnaevsky Jr and Schmauder (Mishnaevsky Jr and Schmauder, 1997b) employed the stochastic differential equations and Fokker–Planck equation to analyze the damage localization in materials under mechanical loading. They observed the increasing damage localization as the microcrack density in the material increased.

Bogdanoff and Kozin (Bogdanoff and Kozin, 1985) analyzed the cumulative damage in materials under cyclic loading, using the Markov chain model, and obtained the cumulative distribution functions of the time to failure and crack sizes. A Markov process model of R-curve behavior was suggested by Xi and Bazant (Xi and Bazant, 1997).

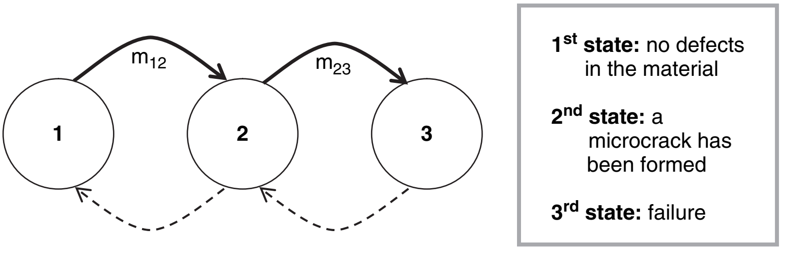

Figure 3.5 Failure as a three-state random process.

Dolinski (Dolinski, 1998) modeled the fatigue crack growth in metals as a Markov stochastic process. Taking into account the crack growth retardation (reduction of crack growth rate after an overload), he determined the probability distribution of fatigue lifetimes. Mishnaevsky Jr and Schmauder (Mishnaevsky Jr and Schmauder, 1997a) suggested to consider the local failure event as a fuzzy, smooth transition from the nondamaged, intact material to the failed state of a material, and employed the fuzzy set theory to analyze the effect of the material heterogeneity on the degree of failure (fuzzy damage parameter) of the heterogeneous material. In their simulations, they observed that the material becomes more heterogeneous due to the localized damage growth, as the damage evolution goes on.

3.2.3 Fiber bundle models and chains of fiber bundles

Many feature of the interrelationships between microfailure and macrostrengths of disordered materials and the load redistribution after the local failure in composites, in particular, fiber reinforced composites, can be investigated with the use of *fiber bundle models*. This model was developed initially by Daniels (Daniels, 1945), and then expanded, modified and generalized by other authors.

Daniels considered a bundle of N fibers with identical elastic properties under uniform tensile stress (Figure 3.6). When a fiber breaks, the load from the broken fiber is distributed equally over all the remaining fibers (*global load sharing*). The tensile response of the fiber bundle is given by:

$$\sigma = (1 - P_{\mathrm{F}})\varepsilon E \tag{3.23}$$

where E is Young modulus of the fibers, ε is applied strain and P_{F} is probability of fiber failure. The strength of fibers is a random value, which is described most often by the Weibull probability distribution:

$$P_{\mathrm{F}} = 1 - \exp\left[-\frac{L}{L_0}\left(\frac{\sigma_{\mathrm{f}}}{\sigma_0}\right)^m\right] \tag{3.24}$$

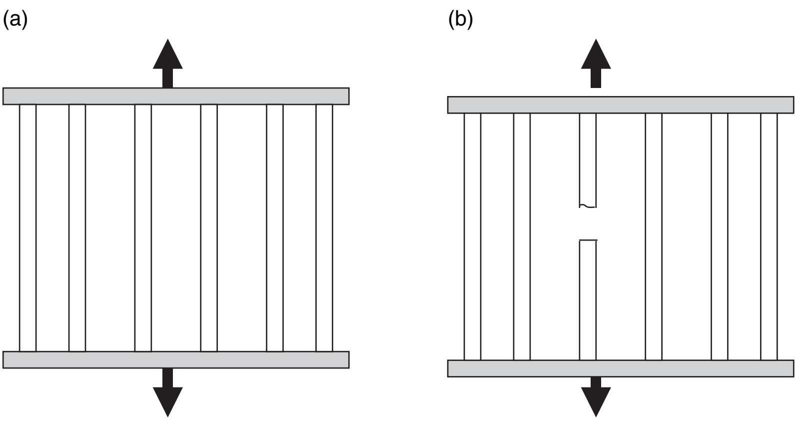

Figure 3.6 *Fiber bundle model (a) without and (b) with a failed fiber.*

where L is fiber length, m is the Weibull modulus, L_0 and σ_0 are parameters and σ_f is stress on a fiber. Differentiating the formula ($d\sigma/d\varepsilon = 0$), one may determine the maximum stress on the bundle (at which the decreasing branch of the force–displacement curve begins) (Calard, 1998; Zok, 2000):

$$\sigma_{\max} = \sigma_0 (meL/L_0)^{-1/m} \tag{3.25}$$

Gücer and Gurland (Gücer and Gurland, 1962) developed a model for 'dispersed fracture' as a chain of elements, each of them considered as a fiber bundle. The strength of the bundles was analyzed using Daniels' theory, while the failure of the chain was studied using the weakest link theory. The probability of failure of a chain of n bundles in the stress interval from σ to $\sigma + \Delta\sigma$ is calculated as the probability of failure of a bundle multiplied by the probability of nonfailure of the remaining $(n-1)$ bundles:

$$P_F = nf(\sigma)[1 - F(\sigma)]^{n-1} \tag{3.26}$$

where $f(\sigma)$ is the probability distribution of the bundle breaking strength and $F(\sigma) = \int_0^\sigma f(\sigma)d\sigma$ is the associated cumulative function. The theoretical predictions of strength of composites, made with this theory, are generally higher than the corresponding experimental values. The model of Gücer and Gurland (Gücer and Gurland, 1962) was developed further by Rosen (Rosen, 1964, 1965), who studied the damage in composites as a failure of chains of bundles with fibers of limited (critical) length. Zweben (Zweben, 1968) studied the influence of the stress concentration from a broken fiber on its closest neighbors, and demonstrated that failure of even a few fibers can lead to the failure of the whole specimen. Several recently developed versions of the fiber bundle models, which take into account the nonlinear behavior of fibers and the matrix, interface effects and real micromechanisms of composite failure, are discussed in more detail in Chapter 10.

The statistical models of strength allow the scattering and random variations of material properties at the microlevel and the inhomogeneities of the material microstructure to be taken into account. Generally, the basic ideas of the statistical theories of strength and failure (as the two-scale approach, the concepts of defect accumulation at the microscale and material weakening at the macroscale, etc.) are rather close to the ideas of the continuum damage theory.

The interrelation between the continuum damage theory and the statistical theories of strength was analyzed by Krajcinovic and Silva (Krajcinovic and Silva, 1982). Krajcinovic and Silva derived a damage evolution law for brittle and brittle–ductile materials on the basis of the probabilistic analysis of the damage growth as a failure of bars in a system of parallel bars under loading. Krajcinovic and Rinaldi (Krajcinovic and Rinaldi, 2005) studied the damage process in quasi-brittle materials using the methods of statistical mechanics and lattice models. On the basis of the scaling procedures, they derived a set of analytical relations which relate micro- and macro-scale damage processes. Continuum damage mechanics can be applied to relate micro- and macroproperties of materials, as well as locally, to describe local damage growth. Various concepts and methods of the damage mechanics are discussed in the next section.

3.3 Damage mechanics

The most traditional approach to the modeling of failure processes – linear and nonlinear fracture mechanics – was developed initially for the macroscopic analysis of failure of parts and specimens. In order to take into account the complex microgeometries of the materials, the analysis of local failure (damage) processes is necessary. This is done in the framework of damage mechanics.

According to Becker and Gross (Becker and Gross, 1987), there are two main directions in continuum damage mechanics: 'phenomenological damage models, usually embedded in a rational thermodynamical framework, containing free parameters' (which have to be determined); and a 'micromechanically oriented way'. The first direction is presented in works by Lemaitre (Lemaitre, 1992), Lemaitre and Chaboche (Lemaitre and Chaboche, 1985) and Krajcinovic (Krajcinovic, 1996); the second is done by Kachanov (Kachanov, 1980, 1987a,b).

Krajcinovic and Silva (Krajcinovic and Silva, 1982) proposed the following classification for damage models:

(1) "purely phenomenological models featuring a-priori legislated damage law" (Davison and Stevens, 1973; Lemaitre, 1992);
(2) "theories based on the generalization of the materials science models" (Leckie and Hayhurst, 1974);
(3) "models based on the statistical approach".

The damage models can be further classified according to the damage mechanisms and materials, which they are applicable to. Failure processes in composite materials are controlled by two main mechanisms: brittle fracture (low energy consuming) and ductile fracture (high energy consuming). While the brittle mechanism of fracture can be well described in the framework of fracture mechanics and/or probabilistic approaches, ductile fracture is apparently a more complex nonlinear process, which includes several stages (e.g. void nucleation, void growth and coalescence) and is influenced by plastic flow, interaction between dislocations and obstacles, hardening behavior of the material and other material-dependent factors.

Let us look at some models of damage initiation and evolution in materials.

3.3.1 Models of elastic solids with many cracks

While the formation of a single macro- or microcrack in an elastic brittle material is adequately described by the methods of fracture mechanics, an analysis of the effect of the distribution of microcracks and their interaction on effective elastic properties and fracture resistance of microcracked solids requires much more sophisticated approaches. The methods which enable this problem to be simplified and to solve it for some cases have been developed by M. Kachanov (Kachanov, 1980, 1987a,b), Horii and Nemat-Nasser (Horii and Nemat-Nasser, 1986), Kemeny and Tang (Kemeny and Tang, 1990) and Hornby *et al*. (Hornby *et al*, 1996).

Mark Kachanov (Kachanov, 1987a,b; Kachanov *et al*., 1990) developed a method of stress analysis in elastic solids with many cracks, based on the superposition technique and the application of the self-consistency method applied to the average tractions on the individual cracks. Using this method, it is possible to derive approximate analytical solutions for stress intensity factors, and to construct full stress field in solids with many cracks.

Dong and Denda (Dong and Denda, 1996; Denda and Dong, 1997) developed a model and a boundary element code for the growth analysis of multiple cracks in isotropic elastic solids, and analyzed the critical failure conditions of microcracked solids. In their model, the crack opening displacement of each crack is represented by the distribution of dislocation dipoles along the crack line.

A detailed review of damage models, which considers the relations between damage and microcrack arrays and the effective properties of elastic-brittle materials, is given by Kachanov (Kachanov, 1987a).

3.3.2 Phenomenological analysis of damage evolution (continuum damage mechanics)

The phenomenological approach to the modeling damage originates from the works by L. Kachanov (Kachanov, 1968) and Rabotnov (Rabotnov, 1966). Lazar Kachanov (Kachanov, 1968) introduced the concept of the damage parameter, which is defined as the ratio of the effective area of the intersections of all microcracks/cavities in a section of a representative volume element (RVE) with a given plane to the area of the section of the RVE:

$$R = \frac{S_{\mathrm{D}}}{S}, \tag{3.27}$$

where S_{D} is the effective area of the intersections of all microcracks/cavities in a section of a RVE with a given plane and S is the area of the section of a RVE (Figure 3.7). The initiation and accumulation of microcracks (damage) is described in the framework of this concept by the damage evolution law, which presents (in a general case) a relation between the damage parameter growth rate and loading conditions, accumulated damage

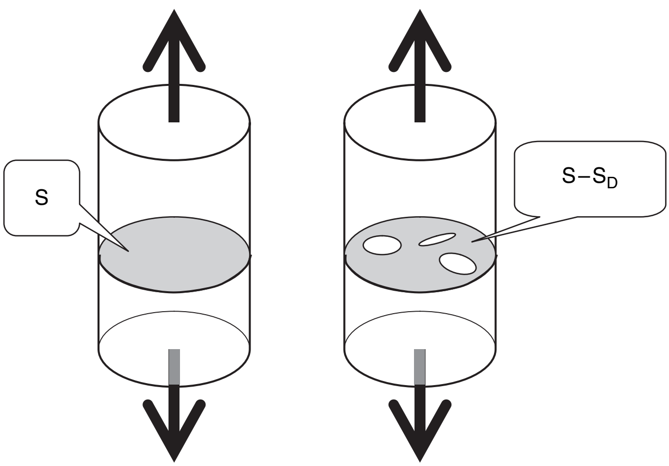

Figure 3.7 *Damage parameter and effective stress concept: reduction of the effective area of a section due to microcrack formation.*

and properties of the material. The phenomenological damage evolution law, suggested by L. Kachanov, is as follows:

$$\dot{\psi}_R = -\mathrm{A_K}\left(\frac{\sigma}{\psi_R}\right)^{\mathrm{b_k}} \tag{3.28}$$

where $\mathrm{A_K}$ and $\mathrm{b_K}$ are constants of the material and $\psi_R = 1 - R$, where R is the damage parameter as defined above.

The interaction between microcracks or voids can be taken into account by using the 'effective stress concept' (Rabotnov, 1966) and the 'strain equivalence principle' (Lemaitre, 1992). The 'effective stress' was defined by Rabotnov, as the 'stress related to the surface which effectively resists the load' (i.e. S-S_D in the above) (Lemaitre, 1992). Using the above definition of the damage variable, the effective stress is determined (for uniaxial tensile loading) as follows:

$$\sigma_{\mathrm{eff}} = \frac{\sigma}{1-R} \tag{3.29}$$

The 'strain equivalence principle' means that 'any strain constitutive equation for a damaged material may be derived in the same way as for a virgin material except that the usual stress is replaced by the effective stress' (Lemaitre, 1992). The works by Lemaitre, Chaboche and Krajcinovic, as well as many others, are based on the phenomenological approach as well as on some kind of the effective stress concept.

3.3.3 Micromechanical models of void growth in ductile materials

Several micromechanical models of damage evolution in ductile materials are based on the continuum mechanical analysis of the expansion of voids in ductile materials under mechanical loading.

McClintock (McClintock, 1968) considered a plastic material, containing a regular array of 3D cylindrical voids with elliptical sections. Assuming that fracture takes place, if the neighboring voids touch, McClintock derived a criterion for the ductile fracture of the voided material, and demonstrated that 'the relative void expansion per unit applied strain increment increases exponentially with the transverse stress' (Rice and Tracey, 1969). The damage rate as a function of stresses was given in the form:

$$\frac{\mathrm{d}R}{\mathrm{d}\varepsilon_{\mathrm{eq}}} \sim \frac{\sqrt{3}}{2(1-n)}\sinh\left[\frac{\sqrt{3}(1-n)}{2}\frac{\sigma_a+\sigma_b}{\sigma_{\mathrm{eq}}}\right] + \frac{3}{4}\frac{\sigma_a-\sigma_b}{\sigma_{\mathrm{eq}}} \tag{3.30}$$

where dR is the damage increment, a, b are two semiaxes of the cylindrical voids, $\varepsilon_{\mathrm{eq}}$ is the equivalent strain, n is the hardening exponent and σ_a, σ_b are two of the principal stresses.

Rice and Tracey (Rice and Tracey, 1969) studied the effect of the triaxiality of the stress state on the growth of a spherical void in a plastic material in a general remote stress field. On the basis of the analysis of the spherically symmetric void expansion field, Rice and Tracey derived an exponential relationship between the stress triaxiality parameter and the average radial velocity of the surface of the growing void:

$$\dot{r} \sim \exp\left(\frac{3}{2}\frac{\sigma_m}{\sigma_{eq}}\right) \tag{3.31}$$

where σ_m is the the mean stress and σ_{eq} is von Mises equivalent stress, the ratio σ_m/σ_{eq} is referred to as the stress triaxiality parameter, r is the void radius. The spherical void in a remote simple tension strain rate field, considered by Rice and Tracey, is presented in Figure 3.8. Assuming that the failure strain is inversely proportional to the void growth rate, Hancock and Mackenzie (Hancock and Mackenzie, 1976) determined the failure strain of a material as follows:

$$\varepsilon = \alpha \exp\left(-\frac{3}{2}\frac{\sigma_m}{\sigma_{eq}}\right) \tag{3.32}$$

where α is a material constant. The following damage criterion (or damage indicator) (Fischer *et al.*, 1995) has been derived on the basis of this model:

$$R = \int_0^{\varepsilon_{pl,c}} \exp^{(3/2\eta)} d\varepsilon_{pl} \tag{3.33}$$

where ε_{pl} is the effective plastic strain, $\varepsilon_{pl,c}$ is the critical plastic strain and η is stress triaxiality ($\eta = \sigma_m/\sigma_{eq}$).

This criterion was tested and verified experimentally for the Al matrix of Al/SiC composites by Wulf (Wulf, 1985) and Wulf *et al.* (Wulf *et al.*, 1993), and will be used in the simulations presented in the following chapters.

3.3.4 Thermodynamic damage models

In many works, the constitutive behavior of damaged (voided) materials is analyzed with the use of thermodynamic potentials of the materials.

Gurson (Gurson, 1977) determined the yield surface for a material with voids using the maximum plastic work principle. Materials with long cylindrical or spherical voids were considered. The yield function for the material with spherical voids was determined as a function of stresses and the volume of voids in the form:

$$\Phi = \left(\frac{\sigma_{eq}}{\sigma_y}\right)^2 + 2f\cosh\left(\frac{3\sigma_m}{2\sigma_y}\right) - 1 - f^2 = 0 \tag{3.34}$$

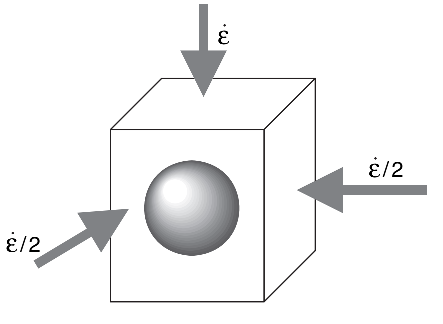

Figure 3.8 *Spherical void in a remote simple tension strain rate field (considered by Rice and Tracey, 1969).*

where σ_y is yield stress, f is the void volume fraction, σ_{eq} is equivalent stress and σ_m is mean stress. The growth of the void volume fraction is given by:

$$\dot{f} = \dot{f}_g + \dot{f}_n, \tag{3.35}$$

where $\dot{f}_g$ is the rate of growth of available voids and $\dot{f}_n$ is the void nucleation rate.

An improved version of the Gurson model for materials with strengthening was suggested by Tvergaard (Tvergaard, 1981). In this model, two adjustable coefficients $(q_1,\ q_2)$ were introduced into the yield function:

$$\Phi = \left(\frac{\sigma_{eq}}{\sigma_y}\right)^2 + 2q_1 f \cosh\left(\frac{3q_2\sigma_m}{2\sigma_y}\right) - (1 + (q_1 f)^2) = 0 \tag{3.36}$$

Introducing these coefficients makes it possible to bring predictions closer to the results of the numerical analyses at small void volume fractions.

In order to describe the void coalescence, Needleman and Tvergaard (Needleman and Tvergaard, 1984) introduced in this model a function, which takes into account the loss of material stiffness due to the void coalescence:

$$f^*(f) = \begin{cases} f & \text{if} \quad f \le f_c \\ f_c - \frac{1/q_1 - f_c}{f_f - f_c}(f - f_c), & \text{if} \quad f > f_c \end{cases} \tag{3.37}$$

where f_c is the critical value of f, f_f is the value of f at the final fracture stage. The Gurson–Tvergaard–Needleman (GTN) model is the most widely used model of ductile failure.

Rousselier (Rousselier, 1987) described the mechanical behavior of voided materials, using thermodynamic and plastic potentials, and derived a yield function as follows:

$$\Phi = \frac{\sigma_{eq}}{1 - f} + c_1 f \exp\left[c_2\sigma_m/(1 - f)\right] - \sigma_y = 0 \tag{3.38}$$

where c_1, c_2 are constants. Kussmaul and colleagues (Kussmaul *et al.*, 1993) applied the Rousselier damage model to the analysis of the destruction of reactor pressure vessel steels, and demonstrated that this model leads to the correct predictions of both the failure loads and crack growth in fracture specimens.

Lemaitre (Lemaitre, 1992) developed the 'state kinetic coupling theory', which describes the mechanical behavior of damaged materials, using two potentials: state potential (a function of state variables) and the potential of dissipation (which accounts for the 'kinetic laws of evolution of the flux dissipative variables'). On the basis of this approach, he derived an energy damage criterion and a constitutive equation for the damage. The damage evolution law, derived by Lemaitre, is as follows:

$$\dot{R} = -(\mathrm{d}F_d/\mathrm{d}\overline{Y})(1 - R)\sqrt{(2/3)\dot{\varepsilon}_{p,i,j}\dot{\varepsilon}_{p,i,j}} \tag{3.39}$$

where R is the damage parameter, F_d is the potential of dissipation, which includes a damage term and $\overline{Y}$ is the associated variable for a damage parameter, $\dot{p} = \sqrt{(2/3)\dot{\varepsilon}_{p,i,j}\ \dot{\varepsilon}_{p,ij}}$ – accumulated plastic strain rate.

For the case of plastic damage, this law takes the form:

$$\dot{R} = \frac{\sigma_{eq}^2 H R_v}{2Ec(1-R)^2}\sqrt{(2/3)\dot{\varepsilon}_{p,i,j}\dot{\varepsilon}_{p,i,j}} \tag{3.40}$$

where E is the young modulus of the material, c is the 'energy strength of damage' (material constant), $H = 1$ if the accumulated plastic strain reaches the damage threshold and H = 0 otherwise, ν is Poisson's ratio, R_v is the triaxiality function $[R_v = 2(1+\nu)/3 + 3(1-2\nu)(\sigma_m/\sigma_{eq})^2]$.

Fonseka and Krajcinovic (Fonseka and Krajcinovic, 1981) developed a damage model for brittle materials, in which the damage surface is supposed to be a hyperbola in the strain space. They derived incremental stress–strain law for a damaged material by differentiating the Helmholtz free energy for small deformation. The coefficients of linear relationships between components of the damage tensor and strain tensor were obtained for different conditions of loading.

Many of the thermodynamical damage models have been implemented in finite element (FE) and other codes, and are widely used in micromechanical simulations.

More detailed reviews of investigations in the area of continuum damage mechanics are given in the books by Lemaitre (Lemaitre, 1992), Lemaitre and Chaboche (Lemaitre and Chaboche, 1985) and Krajcinovic (Krajcinovic, 1996).

3.3.5 Nonlocal and gradient enhanced damage models

Often, damage models are based on local constitutive equations, which do not include any material length scale. However, neglecting the effect of the material length scale in the analysis of the material behavior, especially, in the case of strongly heterogeneous strain fields, may lead to mesh sensitivity in the numerical analysis of the material failure. In order to overcome this problem, nonlocal damage models were developed by several authors (Bazant and Pijaudier-Cabot, 1989; Bazant, 1994; Bazant and Jirasek, 1995; Tvergaard and Needleman, 1995).

In the framework of nonlocal damage models, the damage growth is described not as a function of the local strain tensor in a point, but rather as a function of the strain averaged over some representative volume around the point, and the delocalization is related to the damage mechanisms. Tvergaard and Needleman (Tvergaard and Needleman, 1995) suggested a nonlocal constitutive formulation of an elasto-viscoplastic version of the Gurson damage model. The delocalization was incorporated 'into the constitutive relation in terms of an integral condition on the rate of increase of the void volume fraction'. The rate of increase of void volume fraction was determined by:

$$\dot{f}(\mathrm{x}) = \frac{1}{W(x)}\int_V \dot{f}_{\mathrm{local}}(\hat{x})w(x-\hat{x})\mathrm{d}\hat{\mathbf{V}} \tag{3.41}$$

where $\dot{f}_{\mathrm{local}}$ is the local void growth density in the point $\mathbf{x}$, given by Equation (3.35),

$$w(\mathbf{z}) = \left[1 + \left(\frac{z}{L}\right)^p\right]^{-q}$$

where L is the material characteristic length,

$$z = \sqrt{\mathbf{z} \cdot \mathbf{z}}, \ p = 8 \text{ and } q = 2 \text{ and}$$

$$W(\mathbf{x}) = \int_V w(x - \hat{x}) \mathrm{d}\hat{\mathbf{V}}.$$

The material length parameter L can be interpreted in this case as the average void spacing. Using this approach, Tvergaard and Needleman investigated the localization of plastic flow in shear bands, and plastic deformation of fiber reinforced metal matrix composites, and demonstrated that the mesh sensitivity in the analysis of the problems can be removed by using nonlocal damage models.

Bazant (Bazant, 1994) and Bazant and Jirasek (Bazant and Jirasek, 1995) developed a nonlocal model of solids with interacting growing microcracks, which takes into account the amplification and shielding of microcracks, and analyzed the damage localization in loading of microcracked solids. In this model, the authors replaced M. Kachanov's matrix relations for crack interaction by an integral equation.

Fish and Yu (Fish and Yu, 2001) developed a nonlocal damage theory by introducing the concept of nonlocal phase fields (stress, strain, etc.), defined as weighted averages over the phases in the characteristic volume.

Another way to take into account the effect of strain gradient and the size effect in the damage analysis is to include the second and higher gradients of strains and stresses into the material models. Starting from the nonlocal theory, Peerlings *et al.* (Peerlings *et al.*, 1996) developed a gradient enhanced model of damage in quasi-brittle materials. Using the strain-based continuum damage model proposed by Simo and Ju (Simo and Ju, 1987) and the stress–strain relation for a damaged material in the form:

$$\boldsymbol{\sigma} = (1 - R)^4 \boldsymbol{H} : \boldsymbol{\varepsilon} \tag{3.42}$$

Peerlings and colleagues introduced the nonlocal equivalent strain in a certain point $\boldsymbol{x}$ as a weighted average of local equivalent strains over surrounding volume V:

$$\overline{\varepsilon}_{\mathrm{eq}}(x) = \frac{1}{V} \int_V g(\xi) \varepsilon_{\mathrm{eq}}(x + \xi) dV \tag{3.43}$$

where ${}^4\boldsymbol{H}$ is the fourth order Hookean stress tensor, $\overline{\varepsilon}_{\mathrm{eq}}$ is nonlocal equivalent strain, $\boldsymbol{\varepsilon}$ and $\boldsymbol{\sigma}$ are linear strain and Cauchy stress tensors, $g(\xi)$ is the weight function and ξ is the relative position vector pointing to the volume $\mathrm{d}V$. Expanding the local equivalent strain into a Taylor series, and neglecting higher order terms, they transformed Equation (3.43) into:

$$\overline{\varepsilon}_{\mathrm{eq}}(x) = \varepsilon_{\mathrm{eq}} + c\nabla^2 \varepsilon_{\mathrm{eq}} \tag{3.44}$$

where c is the dimension length squared. Thus, the averaging was replaced by a partial differential equation for the nonlocal scalar measure of strain, which is considered as an additional independent variable. By including the second order gradient terms of strain in the material model, they introduced an internal length, which determines the width of the localization zone in softening.

The detailed overview of nonlocal and gradient-enhanced models is given in Peerlings *et al.* (Peerlings *et al.*, 2001).

3.4 Numerical modeling of damage and fracture

The numerical simulation of damage and fracture of materials with the use of different discretization methods, in particular, finite elements, requires some specific solutions in order to overcome the discrepancies between the quasi-continuum statement of a problem, its discrete representation and the random, discontinuous nature of crack growth.

In many problems, the *failure condition* of a specimen, defined by the critical levels of the stress intensity factors, J-integral or the energy release rate, should be determined. The stress intensity factor (SIF) can be determined numerically with the use of the following approaches (Petit *et al.*, 1996; Mirzaei, 2006):

- Point matching: SIF is determined from the stress or displacement fields.
- Energy methods: SIF is calculated from the energy release rate, which is determined in the framework of FE analyses.

The idea of the point matching approach is to correlate *finite element method* (FEM) solutions with the analytical formulae for SIF. SIF is calculated from the nodal point displacement field in the points close to the crack tip, by plotting SIF against the distance r from the crack tip, and extrapolating the plot to $r = 0$ ('displacement extrapolation'):

$$K_{\mathrm{I}} \propto \lim_{r \to 0} \frac{u}{\sqrt{r}} \tag{3.45}$$

Instead of extrapolating the numerical results for the SIF–displacement field relationship, the results for SIF–stress field can be extrapolated as well ('stress matching'):

$$K_{\mathrm{I}} \propto \lim_{r \to 0} (\sigma \sqrt{2\pi r}) \tag{3.46}$$

The *energy release rate* can be determined from the rate of change of the total potential energy with crack growth. Carrying out two FE analyses for the cases of crack lengths a and $a + \Delta a$, one calculates the strain energies W for both cases. The energy release rate is determined as $(W1 - W2)/\Delta a$. This method (*finite or global crack extension method*) is rather efficient, since an estimation of the global energy does not require a very fine mesh (Mirzaei, 2006) The disadvantage of this method is that it requires carrying out at least two numerical analyses.

The *virtual crack extension method* (VCEM) requires only one analysis. By distorting some elements (shifting nodal coordinates) between two contours around the crack tip, one changes the stiffness of the elements. That makes it possible to calculate the energy release rate as the derivative of the stiffness matrix with respect to the strength length ('stiffness derivative technique', Parks, 1974). Further, the energy release rate in the linear elastic case can be determined as the J-integral, calculated along a contour or a surface surrounding the crack tip. Shih *et al.* (Shih *et al.*, 1986) proposed the *energy domain integral method* to determine the energy release rate, which was applied initially, to the thermally stressed materials. The method is based on the determination of the J-integral for two connected contours around the crack, consisting of a large external contour and a very small contour around the crack tip. The implementation of the method is based on VCEM techniques.

One of the challenges of the numerical analysis of stress fields in cracked elastic solids is the analysis of *crack tip singularities*. In order to simulate a crack tip singularity numerically, the FE mesh is often refined near the crack tip. Alongside the mesh refinement, special FEs have been developed to deal with the crack tip singularities. FEs, in which stress or displacement variations around the crack tip are incorporated into the shape functions of elements (Tracey, 1971), quarter point singular elements (8-node isoparameteric quadrilateral elements, with mid-side nodes placed on a quarter of the side) (Barsoum, 1976) or other special elements are placed at the crack front in the FE mesh. This makes it possible to analyze the stress fields in cracked elastic solids.

In order to simulate the crack propagation in materials, various methods are applied. Ingraffea (Ingraffea, 2006) and Ingraffea and Wawrzynek (Ingraffea and Wawrzynek, 2004) classified the methods of FE implementation of fracture models as follows:

(1) nongeometrical representation, which includes methods based on the local reduction of element stiffness used to represent the crack path [‘constitutive methods’, as computational cells, smeared crack, element elimination] and kinematic methods (extended finite element method (XFEM), enriched elements);
(2) geometrical representation, which includes constrained shape (i.e. if the crack path is prescribed by the faces of existing elements or by some theory-based assumptions) and arbitrary shape methods (meshfree, adaptive FEM/boundary element method (BEM), lattice methods, etc.).

Taking this classification into account, we present here a short overview of the methods of the numerical implementation of fracture models.

Cracking of a specimen changes its geometry; thus, the corresponding continuum mechanical problem must be modified. The FE mesh modification, which follows the crack advancement, is considered to be the most straightforward way to represent the crack growth.

The oldest methods of fracture modeling are those, in which the crack path has to follow the faces of FEs (Ingraffea, 2006). In the framework of the *node decoupling/splitting* approach, nodes are duplicated, decoupled along the crack path and assigned to two faces of the crack (Figure 3.9). Its disadvantage is that the crack path is constrained to boundaries of FEs, and the results are therefore mesh-dependent.

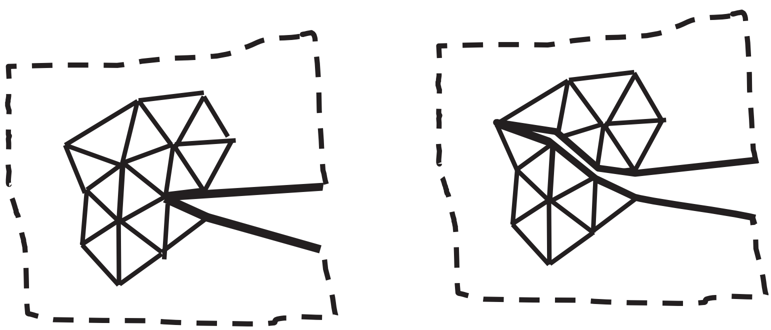

Figure 3.9 *Schematic diagram of nodal decoupling. The crack follows the faces of FEs.*

The problem of the mesh-dependency in the nodal decoupling can be overcome by using the *remeshing approach*. After each iteration of the crack extension, the FE mesh is constructed anew or corrected, according to the new geometry of the body. Most often, only small regions of the body, where the crack extends, are remeshed. This approach was implemented in the Frac2D and Frac3D finite element software, developed in the Cornell Fracture Group.

Another approach to the modelling of the crack growth, which involves the modification of the FE mesh, is the *element elimination technique* (EET). This technique is based on the removal of FEs, which satisfy some local failure condition. Figure 3.10 shows FE elimination. In the framework of the commercial software ABAQUS, the removal of elements from the mesh can be implemented using the subroutine VUMAT of ABAQUS Explicit (Mishnaevsky Jr, 2004b), or with the MODEL CHANGE and RESTART options of ABAQUS standard. The second approach was realized by Mishnaevsky Jr *et al.* (Mishnaevsky Jr *et al.*, 2004a) as well, and enabled the simulations of the crack growth in tool steels. The apparent weakness of this method is that not only the geometry, but also the mass and volume of the domain under consideration are changed (reduced) during the fracture simulations. Further, the iteration steps in the analysis must be kept very low, to take into account the interaction between evolving microcracks in a correct way.

The element elimination method is sometimes confused with the *element weakening method* (EWM). In the framework of this method, elements in which the damage parameter or any other failure criterion exceeds the critical level, are not removed from the mesh, but weakened. This is done by setting their stiffness to a very low value. In order to avoid numerical problems related to strong local loss of equilibrium, the stresses may be set to be equal to zero in several steps (called 'relaxation steps'). Wulf (Wulf, 1985) used this method to simulate the crack growth in composites, and demonstrated that the simulated crack path corresponds well to the experimental path.

Mishnaevsky Jr *et al.* (Mishnaevsky Jr *et al.*, 2004a) compared the element elimination and element weakening methods, and demonstrated that they yield very close results when employed to simulate the crack propagation in microstructures of steels.

One should note that element weakening differs in principle from element removal: while the element elimination is in fact a kind of mesh modification, the element weak-

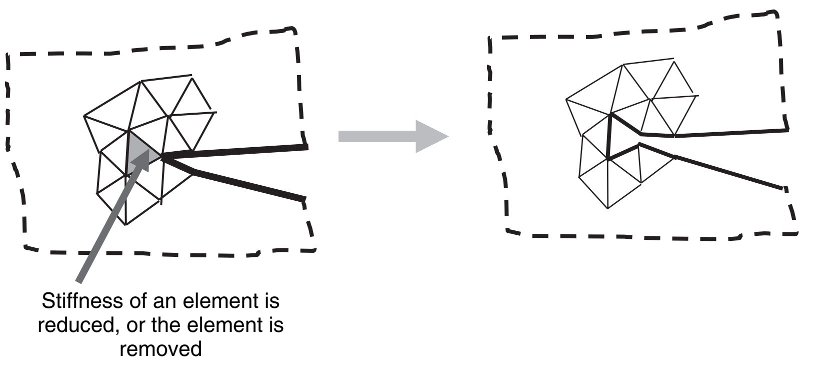

Figure 3.10 *Element elimination approach to the damage modeling (Mishnaevsky Jr et al., 2004a).*

ening approach belongs to the group of properties modification approaches ('constitutive methods', according to Ingraffea and Wawrzynek, 2004).

Another way to model the crack path by changing element properties and not the mesh itself, is realized in the framework of *smeared crack models* (Weihe *et al.*, 1998; Weihe and Kroeplin, 1995). In these models, a crack is considered as a continuous degradation (reduction of strength/stiffness) along the process zone. The displacement jump is smeared out over some characteristic distance across the crack, which is correlated with the element size. The degradation of individual failure planes is described by the constitutive law. In the fixed crack model (Rashid, 1968), which presents the classical version of the smeared crack model, the degradation is controlled by the maximum tensile stresses only; other versions of the smeared crack model (rotating crack model, multiple fixed model) allow to take into account the variations of crack growth direction during crack propagation, and the formation of secondary cracks. The disadvantage of the smeared crack model (as well as other properties modification approaches, like element weakening) is that the model does not exclude the stress transfer across a widely open crack in some cases (Jirasek, 1998b). A detailed review and analysis of different smeared crack models, which are often used in simulations of the fracture of concrete, is given by Weihe *et al.* (Weihe *et al.*, 1998).

Fracture of materials is a multiscale process, which includes the interaction between the large growing cracks, voids or microstructure heterogeneities (available or evolving along the crack path) and the fracture zone. This can be simulated by placing some *unit cells*, or special elements along the expected crack path.

Andersson (Andersson, 1977) simulated crack propagation by analyzing the void growth and coalescence ahead of a crack tip. He used axisymmetric cylindrical unit cells from a rigid perfectly plastic material, with a spherical void, and varied the ratio between the size of void and the radius of the cell. Andersson has shown that the dissipation of energy per unit of fracture surface during the void growth is proportional to the distance between voids.

In the framework of the *computational cell method* (CCM), developed by Xia and Shih (Xia and Shih, 1995, 1996) and Xia *et al.* (Xia *et al.*, 1995), crack propagation is assumed to be a result of the void growth in front of the crack tip (Figure 3.11). Void growth is confined to a layer, the thickness of which is equal to the mean distance between inclusions which cause void initiation. The layer consists of cubic cells, each of them contains a cavity of given size. The void growth in each cell may be described, e.g. with the Gurson–Tvergaard model. When the void volume fraction in a cell reaches some critical level, the cell is removed and therefore the crack grows.

A generalized formulation of cell models is given by Broberg (Broberg, 1997) in his cell model of materials. In this model, a material is represented as a number of cells, defined as the 'smallest material unit that contains reasonably sufficient information about crack growth in the material'. A cell is characterized by its size and cohesion–decohesion relation. The cell model of materials bears some fundamental similarity with the Voronoi cell approach by Moorthy and Ghosh (Moorthy and Ghosh, 1998). In both cases the material is divided into the smallest representative material units, different by their sizes and properties, which serve as elements in FE mesh.

The simulation of crack growth can be further realized using finite elements with the special constitutive behavior, notably, *cohesive elements*, which can be placed in the

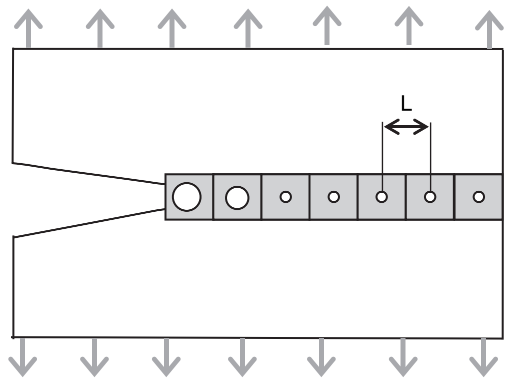

Figure 3.11 *Schematic diagram of the computational cell model of fracture (after Xia and Shih, 1995, 1996). The crack path is modeled as failure of cells with voids placed in front of the crack tip. The cells become damaged when the voids grow.*

FE mesh in sites of potential damage initiation (e.g. on the interfaces). The constitutive behavior of the cohesive elements is described by the traction–separation law (cf. Section 3.1).

Recently, several methods were developed, in which the FE formulations with *embedded discontinuity* or *enriched shape functions* are used. Their advantage is that the path of a displacement discontinuity (crack) is in this case fully independent of the FE mesh.

FEs with *embedded discontinuities*, proposed and described by Belytschko *et al.* (Belytschko *et al.*, 1988), Jirasek (Jirasek, 1998) and Jirasek and Zimmermann (Jirasek and Zimmermann, 2001), make it possible to analyze the cracks or other discontinuities running with an arbitrary trajectory across FEs. This approach seeks to combine strong points of both discrete and smeared approaches to the crack simulation using the corresponding choice of the kinematic representation of localized fracture. The discontinuity, which crosses the element and divides it into two parts, is represented by additional degrees of freedom, corresponding to the normal and tangential components of the displacement jump. The displacement field is decomposed into two parts, a continuous and a 'discontinuous part due to the opening and sliding of crack' (Jirasek and Belytschko, 2002), and only the part of the nodal displacement related to the continuous deformation is used to calculate the strains in the bulk material.

The *generalized finite element method* (GFEM), based on the partition of unity, was presented by Babuska and Mellenk (Babuska and Mellenk, 1996; Babuska *et al.*, 2004). This method combines the advantages of the meshless methods and the standard FEM. Taking into account that the nodal shape functions sum up to unity in the modeled area, Babuska and colleagues suggested to enrich the element shape functions by assumed local functions. The same concept is used in the XFEM. In the framework of this method, 'part of the displacement field is approximated by a discontinuous displacement enrichment based on a local partition of unity' (Xi and Belytschko, 2003). The displacement field is presented as the sum of the regular displacement field (for the case without any discontinuities) and the enriched displacement field. Discontinuous enrichment functions are added to take into account cracks, and singular enrichment functions are added to account for the crack tips. The XFEM allows to simulate 3D cracks as well as crack branching and intersection (Sukumar *et al*., 2000). Jirasek and Belytschko (Jirasek and Belytschko, 2002) compared the XFEM and the embedded discontinuity model, and came to the conclusion that the XFEM ensures some advantages over the embedded discontinuity model, e.g. better numerical robustness and superior kinematic properties.

Further, meshfree and other connectivity-free as well as adaptive methods are used for the analysis of crack propagation. Askes *et al*. (Askes *et al*., 2000) applied the *element free Galerkin method* (EFGM) for the discretization of structures, which are described by the gradient-dependent damage models. Since the shape functions in the EFGM are formulated on the basis of the moving least squares principle, not on the basis of element connectivity, one can easily obtain higher order continuity shape functions. Askes *et al*. (Askes *et al*., 2000) demonstrated that the EFGM is a rather efficient tool for the analysis of higher order continua, and employed it for the comparison of different gradient damage models (second and fourth order explicit and implicit models).

References

Andersson, H. (1977). Analysis of a model for void growth and coalescence ahead of a moving crack tip, *Journal of Mechanics and Physics of Solids*, **25**, 217–233.

Askes, H., Pamin, J. and de Borst, R. (2000). Dispersion analysis and element-free Galerkin solutions of second- and fourth-order gradient-enhanced damage models, *International Journal of Numerical Methods in Engineering*, **49** (6), 811–832.

Babuska, I. and Melenk, J. M. (1996). The partition of unity finite element method: basic theory and applications, *Computer Methods in Applied Mechanics and Engineering*, **139**, 289–314.

Babuska, I., Banerjee, U. and Osborn, J. E. (2004). Generalized finite element method: main ideas, results, and perspective, *International Journal of Computational Methods*, **1** (1), 67–103.

Barsoum, R. S. (1976). On the use of isoparametric finite elements in linear fracture mechanics, *International Journal of Numerical Methods in Engineering*, **10**, 25–37.

Batdorf, S. B. and Crose, J. G. (1974). A statistical theory for the fracture of brittle structures subjected to nonuniform polyaxial stresses, *Journal of Applied Mechanics*, **41** (2), 459–464.

Batdorf, S. B. and Heinisch Jr, H. L. (1978). Weakest link theory reformulated for arbitrary fracture criterion, *Journal of American Ceramic Society*, **61** (7–8), 355–358.

Bazant, Z. P. (1994). Nonlocal damage concept based on micromechanics of crack interactions, *Journal of the Engineering Mechanics Division*, **120** (3), 593–617.

Bazant, Z. P. and Jirasek, M. (1995). Continuum damage due to interacting microcracks: new nonlocal model and localization analysis, in: *Fracture of Brittle Disordered Materials: Concrete, Rock* and Ceramics, Eds. G. Baker and B.L. Karihaloo, E & F Spon, London, pp. 423–437.

Bazant, Z. P. and Pijaudier-Cabot, G. (1989). Measurement of characteristic length of nonlocal continuum, *Journal of Engineering Mechanics*, **115** (4), 755–767.

Becker, W. and Gross, D. (1987). A one-dimensional micromechanical model of elastic-microplastic damage evolution, *Acta Mechanica*, **70**, 221–233.

Belytschko, T., Fish J. and Engelmann, B. E. (1988). A finite element with embedded localization zones, *Computer Methods in Applied Mechanics and Engineering*, **70**, 59–89.

Bogdanoff, J. L. and Kozin, F. (1985). *Probabilistic Models of Cumulative Damage*, John Wiley & Sons, Ltd, New York.

Broberg, K. B. (1997). The cell model of materials, *Computational Mechanics*, **19** (7), 447–452.

Calard, V. (1998). Approches statistiques-probabilistes du comportement mécanique des composites à matrice céramique, Dr Thesis, LCTS, Laboratoire des Composites Thermostructuraux, Bordeaux.

Chudnovsky, A. I. (1973). On fracture of macrobodies, in: *Studies in Elasticity and Plasticity*, Leningrad University Press, Leningrad, pp. 3–43.

Daniels, H. E. (1945). The statistical theory of the strength of bundles of threads, *Proceedings of the Royal Society of London*, **183** (A995), 405–435.

Davison, L. and Stevens, A. L. (1973). Thermomechanical constitution of spalling elastic bodies, *Journal of Applied Physics*, **44**, 668–674.

Denda, M. and Dong, Y. F. (1997). Complex variable approach to the BEM for multiple crack problems, *Computer Methods in Applied Mechanics and Engineering*, **141** (3–4), 247–264.

Dolinski, K. (1998). Stochastic modeling of fatigue crack growth in metals, in: *Probamat-21st Century: Probabilities and Materials*, Ed. G. Frantziskonis, NATO ASI Series, Kluwer, Rordecit, Vol., Vol. 46, pp. 511–531.

Dong, Y. F. and Denda, M. (1996). Computational modeling of elastic and plastic multiple cracks by the fundamental solution, *Finite Elements in Analysis and Design*, **23** (2–4), 115–132.

Dugdale, D. S. (1960). Yielding of steel sheets containing slits, *Journal of the Mechanics and Physics of Solids*, **8**, 100–112.

Fischer, F. D., Kolednik, O., Shan, G.X. and Rammerstorfer, F. G. (1995). A note on calibration of ductile failure damage indicators, *International Journal of Fracture*, **73**, 345–357.

Fish, J. and Yu, Q. (2001). Two-scale damage modeling of brittle composites, *Composites Science and Technology*, **61**, 2215–2222.

Fonseka, G. U. and Krajcinovic, D. (1981). The continuous damage theory of brittle materials. Parts 1 and 2, *Journal of Applied Mechanics*, **48**, 809–824.

Freudenthal, A. M. (1968). Statistical approach to brittle fracture, in: *Fracture. An Advanced Treatise*, Ed. H.Liebowitz, Academic Press, New York, pp. 592–618.

Griffith, A. A. (1920). The phenomena of rupture and flow in solids, *Philosophical Transactions of the Royal Society of London, Series A*, **211**, 163–198.

Gücer, D. E. and Gurland, J. (1962). Comparison of the statistics of two fracture modes, *Journal of the Mechanics and Physics of Solids*, **10**, 365–373.

Gurson, A. L. (1977). Continuum theory of ductile rupture by void nucleation and growth: Part I. Yield criteria and flow rules for porous ductile media, *Journal of Engineering Materials Technology*, **99**, 2–15.

Hancock, J. W. and Mackenzie, A. C. (1976). On the mechanisms of ductile failure in high-strength steels subjected to multi-axial stress-states, *Journal of the Mechanics and Physics of Solids*, **24** (2–3), 147–160.

Horii, H. and Nemat-Nasser, S. (1986). Brittle failure in compression: splitting, faulting and brittle-ductile transition, *Philosophical Transactions of the Royal Society*, **319**, 337–374.

Hornby, P. G., Mühlhaus, H. B. and Dyskin, A. B. (1996). Bifurcations in a dipole asymptotic model of crack arrays, a closer look, in: *Proceedings of 4th International Conference on Computer-aided Assessment and Control*, Eds H. Nisitani, M. H. Aliabadi, S. I. Nisida and D. J. Cartwright, Computational Mechanics, Ashurst, pp. 693–700.

Ingraffea, A. R. (2006). Computational fracture mechanics, in: *The Encyclopedia of Computational Mechanics*, Eds E. Stein, R. de Borst and T. Hughes, John Wiley & Sons, Ltd, Chichester, Vol. 2, pp. 375–402.

Ingraffea, A. R. and Wawrzynek, P. A. (2004). Computational fracture mechanics: a survey of the field, in: *Proceedings of the European Congress on Computational Methods in Applied Sciences* *and Engineering, ECCOMAS 2004*, Eds P. Neittaanmäki, T. Rossi, S. Korotov, E. Oñate, J. Périaux and D. Knörzer, University of Jyväskylä, Jyväskylä.

Irwin, G. R. (1957). Analysis of stresses and strains near the end of a crack transversing a plate, *Journal of Applied Mechanics Transcations*, **79**, 361–364.

Irwin, G. R. (1958). Fracture, in: *Handbuch der Physik*, Springer Verlag, Berlin, pp. 551–594.

Irwin, G. R. (1960, republished 1997). Plastic zone near a crack and fracture toughness, in: *Selected Papers on Foundations of Linear Elastic Fracture Mechanics*, SPIE Milestone Series, Vol. MS 137, Ed. R.J. Sanford, SPIE Optical Engineering Press, co-published by Society of Experimental Mechanics, Bethel, pp. 280–285.

Jirasek, M. (1998b). Finite elements with embedded cracks, LSC Report, Lausanne.

Jirasek, M. and Belytschko, T. (2002). Computational resolution of strong discontinuities, in: *Proceedings of 5th World Congress on Computational Mechanics*, Eds H. A. Mang, F. G. Rammerstorfer and J. Eberhardsteiner, Vienna University of Technology, Austria, http://wccm.tuwien.ac.at

Jirasek, M. and Zimmermann, Th. (2001). Embedded crack model: I. Basic formulation, *International Journal for Numerical Methods in Engineering*, **50**, 1269–1290.

Kachanov, L. M. (1968). *Introduction to Continuum Damage Mechanics*, Nijhoff, Dordrecht.

Kachanov, M. (1980). Continuum model of medium with cracks, *Journal of the Engineering Mechanics Division*, **106**, 1039–1051.

Kachanov, M. (1987a). On modelling of anisotropic damage in elastic-brittle materials – A brief review, in: *Damage mechanics in composites*, Eds A. S. D. Wang and G. K.Haritos, ASCE, New York, pp. 99–105.

Kachanov, M. (1987b). Elastic solids with many cracks: a simple method of analysis, *International Journal of Solids and Structures*, **23** (1), 23–43.

Kachanov, M., Montagut, E. L. E. and Laures, J. P. (1990). Mechanics of crack–microcrack interaction, *Mechanics of Materials*, **10**, 59–71.

Kemeny, J. M. and Tang, F. F. (1990). A numerical damage model for rock based on microcrack growth, interaction and coalescence, in: *Damage Mechanics in Engineering Materials*, Eds J. W. Ju, D.Krajcinovic and H. L.Shreyer, ASME, New York, pp. 103–111.

Krajcinovic, D. (1996). *Damage Mechanics*, North-Holland, Amsterdam.

Krajcinovic, D. and Rinaldi, A. (2005). Statistical damage mechanics–Part I. Theory, *Journal of Applied Mechanics*, **72** (11), 76–85.

Krajcinovic, D. and Silva, M. A. G. (1982). Statistical aspects of the continuous damage theory, *International Journal of Solids and Structures*, **18** (7), 551–562.

Kussmaul, K., Eisele, U. and Seidenfuss, M. (1993). On the applicability of local approaches for the determination of the failure behaviour of ductile steels, *Journal of Pressure Vessel Technology*, **115**, 214–220.

Leckie, F. A. and Hayhurst, D. R (1974). Creep rupture of structures, *Proceedings of the Royal Society of London, Series* A, **340** (1622), 323–347.

Lemaitre, J. (1992). *A Course on Damage Mechanics*, Springer, Berlin.

Lemaitre, J. and Chaboche, J. L. (1985). *Mecanique des materiaux solides*, Dunod, Paris.

McClintock, F. A. (1968). A criterion for ductile fracture by the growth of holes, *Journal of Applied Mechanics*, **6**, 363–371.

Mirzaei, M. (2006). *Lecture Notes on Fracture Mechanics*, Tarbiat Modares University, Tehran.

Mishnaevsky Jr, L. (1996b). Determination for the time to fracture of solids, *International Journal Fracture*, **79** (4), 341–350.

Mishnaevsky Jr, L. (1998a). *Damage and Fracture in Heterogeneous Materials*, Balkema, Rotterdam.

Mishnaevsky Jr, L. (2004a). Three-dimensional numerical testing of microstructures of particle reinforced composites, *Acta Materialia*, **52** (14), 4177–4188.

Mishnaevsky Jr, L. (2004b). Werkstoffoptimierung auf dem Mesoniveau, Report for the German Research Council (DFG), MPA Stuttgart.

Mishnaevsky Jr, L. and Schmauder, S. (1997a). Damage evolution and heterogeneity of materials: model based on fuzzy set theory, *Engineering Fracture Mechanics*, **57**, 625–636.

Mishnaevsky Jr, L. and Schmauder S. (1997b). Damage evolution and localization in heterogeneous materials under dynamical loading: stochastic modelling, *Computational Mechanics*, **20** (7), 89–94.

Mishnaevsky Jr, L., Weber, U. and Schmauder, S. (2004a). Numerical analysis of the effect of microstructures of particle-reinforced metallic materials on the crack growth and fracture resistance, *International Journal of Fracture*, **125**, 33–50.

Moorthy, S. and Ghosh, S. (1998). A Voronoi cell finite element model for particle cracking in elastic-plastic composite materials, *Computer Methods in Applied Mechanics and Engineering*, **151**, 377–400.

Needleman, A. (1987). A continuum model for void nucleation by inclusion debonding, *Journal of Applied Mechanics*, **54**, 525–531.

Needleman, A. and Tvergaard, V. (1984) An analysis of ductile rupture in notched bars, *Journal of the Mechanics and Physics of Solids*, **32**, 461–490.

Parks, D. M. (1974). A stiffness derivative finite element technique for determination of crack tip stress intensity factors, *International Journal of Fracture*, **10** (4), 487–502.

Peerlings, R. H. J., de Borst, R., Brekelmans, W. A. M. and de Vree, J. H. P. (1996). Gradient enhanced damage for quasi-brittle materials, *International Journal for Numerical Methods in Engineering*, **39** (19), 3391–3403.

Peerlings, R. H. J., Geers, M. G. D., de Borst, R. and Brekelmans, W. A. M. (2001). A critical comparison of nonlocal and gradient-enhanced softening continua, *International Journal of Solids and Structures*, **38**, 7723–7746.

Petit, C., Vergne A. and Zhang, X. (1996). A comparative numerical review of cracked materials, *Engineering Fracture Mechanics*, **54** (3), 423–439.

Rabotnov, Yu. N. (1966). *Creep in Elements of Constructions*, Nauka, Moscow.

Rashid, Y. R. (1968). Ultimate strength analysis of prestressed concrete pressure vessels, *Nuclear Engineering and Design*, **7**, 334–344.

Rice, J. R. and Tracey, D. M. (1969). On the ductile enlargement of voids in triaxial stress fields, *Journal of the Mechanics and Physics of Solids*, **17**, 201–217.

Rosen, B. W. (1964). Tensile failure of fibrous composites, *AIAA Journal*, **2**, 1985–1991.

Rosen, B. W. (1965). *Fibre Composite Materials*, American Society for Metals, *Metals park*, H.

Rousselier, G. (1987). Ductile fracture models and their potential in local approach to fracture, *Nuclear Engineering and Design*, **105**, 97–111.

Shih, C., Moran, B. and Nakamura, T. (1986). Energy release rate along a three-dimensional crack front in a thermally stress body, *International Journal of Fracture* **30**, 79–102.

Simo, J. C. and Ju, J. W. (1987). Strain- and stress - based continuum damage models. 1: Formulation, *International Journal of Solids and Structures*, **23** (7), 821–840.

Sukumar, N., Moes, N., Moran, B. and Belytschko, T. (2000). Extended finite element method for three-dimensional crack modeling, *International Journal of Numerical Methods in Engineering*, **48**, 1549–1570.

Tracey, D. M. (1971). Finite elements for determination of crack tip elastic stress intensity factors, *Engineering Fracture Mechanics*, **3**, 255–265.

Tvergaard, V. (1981). Influence of voids on shear band instabilities under plane strain conditions, *International Journal of Fracture*, **17** (4), 389–407.

Tvergaard, V. (1990). Material failure by void growth to coalescence, *Advanced Applied Mechanics*, **27**, 83–151.

Tvergaard, V. and Hutchinson, J. W. (1992). The relation between crack growth resistance and fracture process parameters in elastic-plastic solids, *Journal of the Mechanics and Physics of Solids*, **40**, 1377–1397.

Tvergaard, V. and Hutchinson, J. W. (1994). Toughness of an interface along a thin ductile layer joining elastic solids, *Philosophical Magazine A*, **70**, 641

Tvergaard, V. and Hutchinson, J. W. (1996). On the toughness of ductile adhesive joints, *Journal of the Mechanics and Physics of Solids*, **44**, 789–800.

Tvergaard, V. and Needleman, A. (1995). Effects of nonlocal damage in porous plastic solids, *International Journal of Solids and Structures*, **32**, 1063–1077.

Weibull, W. (1939). A statistical theory of the strength of material, *The Royal Swedish Institute for Engineering Research, Proceedings*, No. 151, 1–45.

Weihe, S. and Kroeplin, B. (1995). Fictitiuos crack models: a classification approach, in: *Proceedings of the 2nd International Conference on Fracture Mechanics of Concrete and Concrete Structures*, Ed. F. H. Wittmann, Aedificatio, Freiburg, Vol. 2, pp. 825–840

Weihe, S., Kröplin, B. and de Borst, R. (1998). Classification of smeared crack models based on material and structural properties, *International Journal of Solids and Structures*, **35** (12), 1289–1308.

Westergaard, H. M. (1939). Bearing pressures and cracks, *ASME Journal of Applied Mechanics*, **6**, A49–A53.

Wulf, J. (1985) Neue Finite-Elemente-Methode zur Simulation des Duktilbruchs in Al/SiC, Dissertation MPI für Metallforschung, Stuttgart.

Wulf, J., Schmauder, S. and Fischmeister, H. F. (1993). Finite element modelling of crack propagation in ductile fracture, *Computational Materials Science*, **1**, 297–301.

Xi, G. and Belytschko T. (2003). New crack-tip elements for XFEM and applications to cohesive cracks, *International Journal for Numerical Methods in Engineering*, **57**, 2221–2240.

Xi, Y. and Bazant, Z. P. (1997). Random growth of crack with R-curve: Markov process model, *Engineering Fracture Mechanics*, **57** (6), 593–608.

Xia, L. and Shih, C. F. (1995). Ductile crack growth–II. Void nucleation and geometry effects on macroscopic fracture behavior, *Journal of the Mechanics and Physics of Solids*, **43** (11), 1953–1981.

Xia, L. and Shih, C. F. (1996). A fracture model applied to the ductile/brittle regime, *Journal de Physique IV*, **6**, 363–372.

Xia, L., Shih, C. F. and Hutchinson, J. W. (1995). A computational approach to ductile crack growth under large scale yielding conditions, *Journal of the Mechanics and Physics of Solids*, **43** (3), 389–413.

Xing, X .S. (1996). On theoretical framework of nonequilibrium statistical fracture mechanics, *Engineering Fracture Mechanics*, **55** (5), 699–716.

Yokobori, T. (1978). *The Scientific Basis of Strength and Fracture of Materials* Naukova Dumka, Kiev.

Zok, F. W. (2000). Fracture and fatigue of continuous fiber-reinforced metal matrix composites, in: *Comprehensive Composite Materials*, Eds A. Kelly and C. Zweben, Pergamon, Oxford, Vol. 3, pp. 189–220.

Zweben, C. (1968). Tensile failure of fiber composites, *AIAA Journal*, **6**, 2325–2331.

4

Microstructure–strength relationships of composites: concepts and methods of analysis

The methods of the analysis of relationships between microstructures, and overall properties and strength of composites have been developed from the simplest relationships between averaged values (e.g. Voigt/Reuss estimations) to the complex multiscale numerical models, which take into account the nonlinear behavior of components, evolving microstructures and real inhomogeneous phase arrangements.

In this Chapter, we consider several approaches and methods of the analysis of the interrelations between the microstructures and the mechanical behavior and strength of materials, in particular:

- models of the interaction between inclusions and dislocations in the matrix;
- shear lag model and its versions and generalizations;
- homogenization and multiscale models of materials;
- elastic solutions for the overall properties, variational bounds, effective field and effective medium methods;
- unit cell models and the incorporation of material microstructures into discrete numerical models.

4.1 Interaction between elements of microstructures: physical and mechanical models

As discussed in Section 1.2, there are two main mechanisms of interaction between elements of microstructures of composites: load transfer and sharing (e.g. when the matrix transfers some of the applied stress to the particles, which bear part of the load), and constraining the matrix deformation by the particles or fibers (in the cases of particle or short fiber reinforced composites). In this section, we discuss methods of modeling the mechanisms of interaction between microstructural elements in composites.

4.1.1 Theories of constrained plastic flow of ductile materials reinforced by hard inclusions

In order to investigate the effect of hard nondeformable reinforcing inclusions on the plastic flow in the matrix, physical (dislocational) mechanisms of the matrix deformation and the interaction of dislocations with inclusions are analyzed. The physical mechanisms of the size effects in material, in particular, the effect of the grain size on the flow stress (Hall–Petch effect), dispersion strengthening (Orowan effect) and the strain gradient effect have been discussed in Chapter 2. In this section, we list several approaches to the mathematical modeling of the constraining effects.

4.1.1.1 Orowan effect

The Orowan effect (i.e. bowing of moving dislocations between inclusions) can be responsible for the hardening of a composite with ductile matrix and many small particles. In this case, the influence of an array of hard particles on the yield stress of the composite can be described by the Orowan formula (Wilkinson *et al.*, 2001):

$$\tau = G\boldsymbol{b}/L \tag{4.1}$$

where G is the shear modulus, $\boldsymbol{b}$ is the Burgers vector and L is the interparticle spacing. This formula is derived by considering the force balance on a segment of a dislocation, bowing between two inclusions (Shtremel, 1997).

4.1.1.2 Strain gradient theory

In the deformation of the plastic matrix reinforced by hard nondeforming particles, local strain gradients are generated between the particles (Fleck *et al.*, 1994). The plastic strain gradients lead to the storage of the geometrically necessary dislocations, which are required to ensure the compatible deformation of the matrix. The density of the geometrically necessary dislocations is proportional to the magnitude of the strain gradient. The total density of dislocations, which is presented as a sum, or a harmonic sum of the densities of statistically stored and geometrically necessary dislocations, increases with increasing the strain gradient. Thus, the material is hardened due to the storage of the geometrically necessary dislocations, caused by the strain gradient between the inclusions.

A phenomenological model for the hardening effect was developed by Fleck *et al.* (Fleck *et al.*, 1994). According to Fleck and colleagues, 'the magnitude of the plastic strain gradient is of the order of the average shear strain in the crystal divided by the local length scale λ of the deformation field'. In the case of metals containing nondeformable particles, the local length scale can be calculated as follows:

$$\lambda = r/v_{\mathrm{p}} \tag{4.2}$$

where r is the radius and v_p is the volume content of the particles. Plastic strain gradient with magnitude λ requires the storage of *geometrically necessary dislocations* of density ρ_G:

$$\rho_G \approx \frac{4\gamma}{\boldsymbol{b}\lambda} \tag{4.3}$$

where $\boldsymbol{b}$ is the Burgers vector and γ is the plastic shear strain. The macroscopic shear yield stress can be written in the form:

$$\tau = \mathrm{C}G\boldsymbol{b}\sqrt{\rho_G + \rho_S} \tag{4.4}$$

where C is a constant of the order of 0.3, G is the shear modulus and ρ_s is the density of the statistically stored dislocations.

Taking into account Equations (4.2) and (4.3), one derives for the case of metal, containing nondeformable particles:

$$\tau = \mathrm{C}G\boldsymbol{b}\sqrt{\rho_S + 4\gamma v_p/\boldsymbol{b}r} \tag{4.5}$$

This formula relates the volume content of the hard inclusions and their radius to the shear stress in the material. Fleck and colleagues demonstrated that 'the greater is the imposed strain gradient the greater the degree of hardening'.

Following this work by Fleck and colleagues, a number of the strain gradient theories have been developed, which account for the size effect in the materials (Fleck and Hutchinson, 1997; Aifantis, 1999; Gao *et al*., 1999).

4.1.1.3 Constitutive models based on the dislocation density analysis

Several constitutive models of metal deformation are based on the structure evolution equation, expressed in terms of the dislocation density in the material. This approach was proposed by Kocks (Kocks, 1966, 1976), and developed further by other researchers (Estrin and Mecking, 1984; Estrin, 1998; Roters *et al*., 2000).

In the one parameter model of Kocks (Kocks, 1966, 1976), the kinetic equation, which relates the equivalent plastic strain rate and the equivalent stress in the power law, is written as:

$$\dot{\varepsilon}_p = \dot{\varepsilon}_0(\sigma/\hat{\sigma})^m \tag{4.6}$$

where $\dot{\varepsilon}_p$ is the equivalent plastic strain rate, $\dot{\varepsilon}_0$ and m are material parameters, and σ and $\hat{\sigma}$ are equivalent stress and the internal variable, characterizing the microstructural state of the material.

The internal variable $\hat{\sigma}$ is related to the total dislocation density ρ by:

$$\hat{\sigma} = M\alpha G\boldsymbol{b}\sqrt{\rho} \tag{4.7}$$

where $\boldsymbol{b}$ is the Burgers vector, M is the average Taylor factor, G is shear modulus and α is a coefficient. Considering the storage and recovery of dislocations as competing effects influencing the variation of the dislocation density, Kocks derived the equation for the evolution of the dislocation density in the material:

$$\frac{\mathrm{d}\rho}{\mathrm{d}\varepsilon_\mathrm{p}} = M\left(\frac{1}{\boldsymbol{b}L} - k_2\rho\right) \tag{4.8}$$

where L is the spacing between obstacles (nondeforming particles) (in a more general case, the mean free path of dislocations), ε_p is the plastic strain and k_2 is a recovery coefficient.

Equations (4.6)–(4.8) describe the isotropic hardening of the material, related to the immobilization of mobile dislocations on obstacles (particles). These formulae take into account the recovery (annihilation of stored dislocations) as well [second term of the right-hand side of Equation (4.8)]. If a single phase material is modeled and only the dislocation structure is considered as an obstacle to moving dislocations, the term $M/\boldsymbol{b}L$ is transformed into $Mk_1\sqrt{\rho}$, where k_1 is a proportionality coefficient.

According to Estrin (Estrin, 1998), the one internal variable model provides the prototype for the description of the material behavior, but is not sufficient for the adequate description of the material microstructures evolution. The two internal variables model, which considers the density of mobile and forest (relatively immobile) dislocations, was proposed by Estrin (Estrin, 1998), and verified experimentally. An even more sophisticated model, which considers three dislocation populations (mobile dislocations, immobile dislocations inside cells and on the cell walls), was developed by Roters *et al.* (Roters *et al.*, 2000). Considering the evolution of the density of each group of dislocations, they calculated the effective shear stress and the macroscopic flow stress in materials. The equation for the evolution of the dislocation density [in the simplest case, Equation (4.8)] together with Equations (4.6) and (4.7) describes the constrained plastic deformation of metals.

4.1.1.4 Polycrystal plasticity

The deformation of material is considered at the level of grains/crystals. In the simplest version of this approach, the deformation of metal is assumed to be due to the slips (dislocations motion) through the crystal lattices. Different slip systems can be active in different grains: for instance, FCC crystals have 12 potential slip systems of type (1 1 1) <1 1 0>.

The slip process on a slip plane is controlled by the shear stress resolved along the slip direction (this concept is referred to as the Schmid law). For the case of uniaxial tensile loading of a crystal, the potential slip system of which is defined by a slip plane normal and slip direction, the resolved shear stress is calculated as:

$$\tau = \sigma\cos\varphi\cos\lambda \tag{4.9}$$

where $\cos\varphi\cos\lambda$ is called the Schmid factor, σ is applied stress, φ is the angle between the loading direction and the slip plane normal and λ is the angle between the loading direction and the slip direction. When the value reaches some critical level, a slip occurs on the slip system. If slips occur on multiple slip systems, the corresponding plastic velocity gradient tensor is calculated as a sum of contributions from all slip systems. The nonuniqueness of the solution, related to the possible choice of different active systems, was addressed by Taylor (Taylor, 1938), and Bishop and Hill (Bishop and Hill, 1951). According to Taylor, the preferred solution should correspond to the minimum of the internal plastic work.

The crystal plasticity concept was formulated for the case of finite deformations in the works by Asaro and Rice (Asaro and Rice, 1977) and Asaro (Asaro, 1983a,b). The formulation is based on the multiplicative decomposition of the total deformation gradient into inelastic (flow of the material through the lattice without distorting the lattice) and elastic (rigid body rotation and elastic deformation) components. The overall properties of the material are determined by averaging procedures. Assuming some grains to be rigid, one can employ the crystal plasticity approach to analyze the deformation behavior of metal matrix composites.

4.1.1.5 Discrete dislocation analysis

Van der Giessen and Needleman (Van der Giessen and Needleman, 1995) developed a method of modeling the material plasticity as the collective motion of a large number of discrete dislocations, which are represented as displacement discontinuities in a linear elastic medium. The stress and displacement fields are determined in the framework of the analysis of the linear elastic boundary value problem, as superpositions of the fields due to the discrete dislocations and image fields, corresponding to the boundary conditions. The model includes lattice resistance to dislocation motion, dislocation nucleation and annihilation, as well as the effect of obstacles. The long range interactions between dislocations are taken into account via the continuum elasticity fields. Van der Giessen and Needleman applied this method to analyze the deformation behavior of a composite reinforced by a periodic array of square particles.

4.1.2 Shear lag model and its applications

The shear lag model is widely used to analyze the fiber–matrix stress transfer in undamaged and damaged composites. This model was developed initially by Cox (Cox, 1952) and then expanded and modified by many authors. Assuming that the load transfer from matrix to fiber occurs via shear stresses on the interface between them, Cox considered the force balance in a section of the fiber, and derived the formula which relates the rate of change of the stress along the fiber length, and the interfacial shear stress (Figure 4.1):

$$\frac{\mathrm{d}\sigma}{2\mathrm{d}x} = -\frac{\tau}{r} \tag{4.10}$$

where r is the radius of the fiber, τ is the interface shear stress and x is the coordinate along the fiber length. This formula is referred to as the *basic shear lag equation*.

After some manipulations, this model leads to the following second order differential equation:

$$\frac{\mathrm{d}^2\sigma}{\mathrm{d}x^2} - \beta^2\sigma = -\beta^2\sigma_\infty \tag{4.11}$$

where β is the so-called shear lag parameter, σ_∞ is the far-field fiber stress and σ is fiber stress.

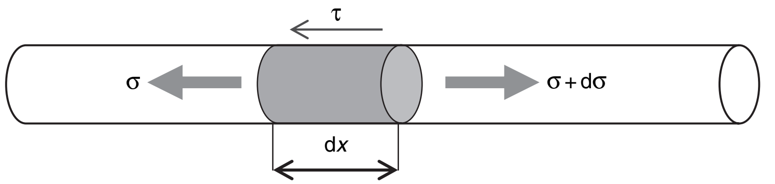

Figure 4.1 *Shear lag model.*

Solving this equation, one determines the stress distribution along the axis x of the fiber:

$$\sigma = E\varepsilon[1 - \cosh(\beta x)\sec h(\beta x r)] \tag{4.12}$$

where E is the Young modulus of the fiber and ε is the strain in the composite. Cox derived a formula for the shear lag parameter β for the case of a cylindrical fiber of radius r, embedded into a cylindrical layer of matrix:

$$\beta = \frac{1}{r}\sqrt{\frac{2G_{\mathrm{m}}}{E\ln(s/r)}} \tag{4.13}$$

where G_{m} is the matrix shear modulus, s is the average distance between the fiber axes, r is the fiber radius and E is the axial modulus of the fiber.

Using Equations (4.10)–(4.12), one can determine the critical fiber length l_{cr}, at which both the matrix and fiber fail at the same strain. Assuming constant shear stress τ in Equation (4.10), Kelly and Tyson (Kelly and Tyson, 1965) derived the following formula for the critical fiber length:

$$l_{\mathrm{c}} = \frac{\sigma_{\mathrm{c}} r}{\tau_{\mathrm{c}}} \tag{4.14}$$

where σ_{c} is the fiber failure stress and τ_{c} is the matrix fiber interfacial shear strength. Figure 4.2 shows the effect of the fiber length of the stress distribution in the fiber under tensile loading. If $l < l_{\mathrm{c}}$ (the case of discontinuous reinforcement), the stress in the fiber is below the critical level, and the fiber is not utilized fully. If $l > l_{\mathrm{c}}$ (longer fibers), a large part of the fiber is overloaded, and multiple cracking can be observed in the fiber.

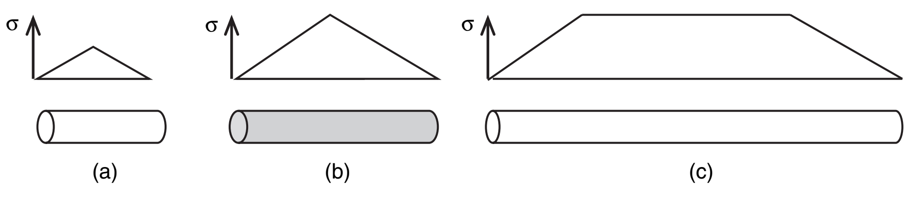

Figure 4.2 *Stress distribution in the fiber (subject to the tensile loading) along the length: (a) short fiber (discontinuous reinforcement,* $l < l_{\mathrm{c}}$*); (b) critical fiber length (*$l = l_{\mathrm{c}}$*); (c) longer fiber (*$l > l_{\mathrm{c}}$*).*

If the fiber length is equal to the critical size ($l = l_c$), both the matrix and fiber fail at the same load, ensuring the most efficient reinforcement of the composite. Kelly and Tyson used this model to explain the experimental observation that the fiber breaking strength is a linear function of the wire content in different composites.

Nairn (Nairn, 1997) carried out a rigorous theoretical analysis of a model, for which the shear assumptions are exact. Using axisymmetric elasticity equations, he demonstrated that the rigorous analysis leads to Equation (4.11) as well. Nairn demonstrated further that the shear lag method gives reasonably good estimations of average axial stress in the fiber and total strain energy in the specimen, yet, the method is not applicable for low fiber volume fractions. For the case of a broken fiber embedded into the ductile matrix, the shear-lag model was generalized by Landis and McMeeking (Landis and McMeeking, 1999). They derived the shear lag equation for this case, and verified the model by comparing it with FE analysis.

The application of the shear lag model to the analysis of the load transfer and damage evolution in fiber reinforced composites is discussed in Chapter 10.

4.2 Multiscale modeling of materials and homogenization

One of the challenges of the theoretical analysis of the microstructure–strength relationships of materials is the necessity to consider several different length scales. While the geometry of a problem and boundary conditions are usually given on the macroscale, the microstructure of material is defined on the micro-mesoscale, and the damage and deformation mechanisms are controlled by atomistic, nanoscale and dislocational processes. Direct numerical analysis of the material behavior, which takes into account both macroscopic boundary conditions and microgeometries, would require very large computational resources. To overcome this problem, several strategies are employed:

- *Multiscale modeling:* the material behavior is modeled at the scale levels of both microstructures and the sample; the lower scale model is subject to the boundary conditions, acting via the macromodel, while the mechanical behavior of the material in the macromodel is determined taking into account finer microscale features incorporated into the micromodel. In the simplest models, upper scale–lower scale relationships are one-sided, while more sophisticated models allow simultaneous global-local analysis at several levels.
- *Homogenization and averaging of properties and microfields:* the material is considered as a homogeneous equivalent medium at the macrolevel, and the effective properties of the medium are determined on the basis of the analysis of the microstructure, microgeometry and properties of the materials.

Another approach can be the direct incorporation of the microgeometries into macroscale models of the deformation and/or failure of the specimen (Silberschmidt and Werner, 2001). This approach may be employed only if the dimensions of the specimen are comparable with the dimensions of microstructural elements (e.g. in thin films or other small scale objects), and requires considerable computational sources.

Figure 4.3 shows schematically two methods of introducing microstructures of materials into macroscopic models of materials: homogenization and multiscale modeling.

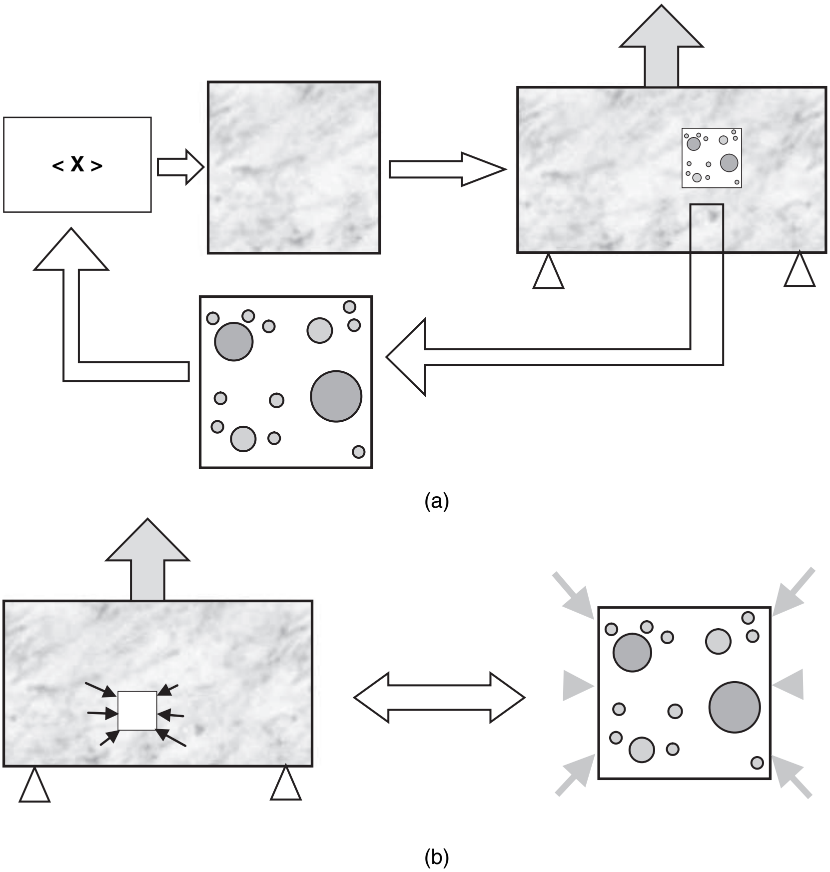

Figure 4.3 Methods of introducing the microstructures of materials into macroscopic models of materials: (a) homogenization of material properties on the basis of the analysis of a RVE of the microstructure; (b) multiscale modeling.

4.2.1 Multiscale modeling

Different techniques are used to establish the links between the micro- and macromodels in the framework of multiscale modeling.

In the simplest case, *submodelling techniques* are used to analyze the material behavior at two or more scale levels. A small region is taken as a submodel of the considered domain, and analyzed taking into account fine features (e.g. microstructure) of the material. The homogeneous boundary conditions for the submodel are determined on the basis of the finite element analysis of the macromodel.

Mishnaevsky Jr *et al*. (Mishnaevsky Jr *et al*., 1999a) simulated the deformation of a compact tension (CT) specimen of AlSi cast alloy, and determined boundary conditions for a microstructural model (displacement distribution at the surfaces of a $100 \times 100\,\mu$m cube at the notch of the specimen). The 3D real microstructure of the cast alloy was reconstructed on the basis of the serial sectioning, and introduced into the micromodel of the small cube. As a result, the local stress and strain distributions were obtained from the microstructural model of the region in the vicinity of the notch of the CT specimen, and compared with experiments. A similar approach was employed by Mishnaevsky Jr *et al.* (Mishnaevsky Jr *et al.*, 2001, 2003a,b) to determine the failure conditions of primary carbides in tool steels and to analyze the crack propagation in short rod specimens.

The submodelling techniques are often used to analyze the mechanical behavior of materials with complex multilevel microstructures. In this case, 'meso-micro' or 'meso-meso' linkage, rather than 'macro-meso' modeling is dealt with. Some hierarchical micro- and mesomechanical unit cell models of materials are discussed in Section 4.4.1.

The upper scale–lower scale relationships in the case of the submodelling techniques are one-sided: the macromodel determines the boundary conditions of the micromodel, while the micromodel does not influence the macromodel. Alternatively, the micromodel delivers the constitutive law for the macromodel, but, again, the models are not coupled. A lot of scientific effort was directed at the development of truly multiscale computational techniques, where upper scale models can include finer microscale features, while the lower scale model is subject to the boundary conditions, acting via the macromodel.

The term *global-local finite element* was introduced in the pioneering work by Mote Jr in 1971 (Mote Jr, 1971). Mote Jr combined the conventional and finite element Ritz methods by coupling global and local dependent variable representation, which led to increased solution accuracy. Following this work, many versions of the global-local method were developed (Noor, 1986; Mao and Sun, 1991).

Different multiscale computational techniques can be grouped as follows (Haidar *et al.*, 2003):

- domain decomposition techniques;
- multiple scale expansion (homogenization) methods;
- superposition based methods.

In the framework of the *domain decomposition techniques*, a macroscale model is decomposed into a series of connected subdomains. This approach was employed by Zohdi *et al.* (Zohdi *et al.*, 2001). They carried out large-scale micromechanical simulations by decomposing the global problem into a set of computationally smaller, decoupled problems, which deal with subdomains of the global domain. According to Zohdi and colleagues, the computational costs of the global microstructural solution, obtained by assembling the solutions of boundary value problems of nonoverlapping subdomains, can be thousands and even millions times less than the global exact solution. Zohdi *et al.* (Zohdi *et al.*, 2001) investigated the partitioning error in the substructuring approach, and methods to lower the error.

Using the *two-scale expansion techniques*, Fish and Yu (Fish and Yu, 2001) developed a model of damage in brittle composites. The idea was to carry out simultaneously both homogenization and the analysis of the evolution of damage (instead of doing first the homogenization, and then the damage analysis, as in macromechanical studies, or vice versa, as in micromechanical analysis). This was done by using a double-scale asymptotic expansion of the damage parameter. Fish and Yu generalized the homogenization method based on double-scale asymptotic expansion to take into account the damage effects. They derived a closed form equation relating local fields to overall strains and damage.

The *superposition based methods* are based on the hierarchical decomposition of the solution space into global and local effects. In 1990, Belytschko *et al.* (Belytschko *et al.*, 1990) proposed to overlay arbitrary local mesh on the global mesh to enhance the accuracy of solutions of problems with high gradients. Fish (Fish, 1992) developed a s-version of the finite element method (FEM), based on the adaptive FEM and error estimation. The idea of the s-version is to increase the resolution by superimposing an additional, refined local mesh on a coarse global mesh. Several other adaptive versions of the FEM have been developed recently: h-version (where convergence is achieved by mesh refinement), p-version (in which the convergence is achieved by increasing polynomial degree), hp-d version (combination of h- and p-extensions in a hierarchical domain decomposition), generalized FEM.

A further superposition technique, called the *composite grid method* was suggested by Fish and colleagues (Fish *et al.*, 1996, 1997a). Using the decomposition of a hybrid system into a hierarchical global-local problem and an indefinite local system, they analyzed the deformation of laminated composite shells. In so doing, some regions of the laminate were modeled as a 3D solid model, and for the rest, the shell model was used.

Takano *et al.* (Takano *et al.*, 1999) developed the finite element mesh superposition technique, which allows to overlay arbitrarily local fine mesh on the global rough mesh. Using this approach together with the asymptotic homogenization method, Takano and colleagues developed a four level hierarchical FE model of textile composite materials, and carried out the stress analysis in these materials.

In the framework of the *multiscale finite element approach* (called FE2), developed by Feyel and Chaboche (Feyel and Chaboche, 2000), the microstructure of a material is introduced into the macroscopic models of the material at the level of the Gauss points. The material behavior in each Gauss point of the macroscopic mesh is determined in finer FE simulations. The method is implemented on the basis of interleaved FE algorithms, which constitute a sequence of Newton–Raphson algorithms, and includes local steps on macroscopic and microscopic scales. The authors applied the method to analyze the deformation of long fiber SiC/Ti composites under four point bending loading. The simulations are carried out using the FETI (domain decomposition) method and parallel computation.

Ghosh and co-workers (1995), Lee *et al.* (Lee *et al.*, 1999) and Moorthy and Ghosh (Moorthy and Ghosh, 1998) developed the *hierarchical multiple scale* model, based on coupling the Voronoi cell FEM (VCFEM) for the mesoscopic analysis and the conventional displacement based FEM for macro-analysis. In the framework of the hierarchical model, the authors used the adaptive schemes and mesh refinement strategies to divide the considered volume into subdomains with periodic and nonperiodic microstructures. In the periodic microstructure areas they used the asymptotic homogenization. In the nonperiodic microstructure subdomains, the VCFEM is used. This approach was used to simulate the damage initiation (by particle cracking or splitting) in discontinuously reinforced MMCs.

4.2.2 Homogenization

Suquet (Suquet, 1987, 1997) formulated the concept of homogenization as follows (Ponte Castañeda and Suquet, 1998; Bornert *et al.*, 2001; Lévesque, 2004). In order to determine the constitutive equations for the averaged effective or macroscopic properties of a heterogeneous material, one should go though the following steps:

- Definition of a *volume element*, which is statistically *representative* for the whole material microstructure under consideration. The size of the representative volume element (RVE) should be large enough compared with the size of microstructural elements to contain a sufficient number of microinhomogeneities. However, RVE should be small enough to allow a micromechanical analysis of the RVE in the framework of available computational resources. The heterogeneous material is considered as an equivalent homogeneous medium, the properties of which are assumed to be the same as those determined in the analysis of the RVE.
- *Localization* (macro–micro transition): microscopic boundary conditions (e.g. strain tensor) are determined on the basis of the macroscopic strain tensor, taking into account the geometry, prescribed macroscopic quantities, constitutive laws, etc.
- *Homogenization* (micro–macro transition): macroscopic output variables are determined on the basis of the analysis of the microscopic behavior of the RVE. As a result, macroscopic properties of the equivalent homogeneous medium are evaluated.

The concept of homogenization is applicable only if at least two length scales in the problem can be defined.

4.3 Analytical estimations and bounds of overall elastic properties of composites

In this section, we list some analytical concepts and approaches used to predict the macroscopic overall properties and the mechanical response of materials.

The *macroscopic response* or *effective/overall properties* of composite materials represents the constitutive properties of materials at the scale level much higher than the size of microstructural elements, and depends on the microstructure of the composites, i.e. on the volume content, local properties and spatial distributions of phases (constituents).

According to Hori and Nemat-Nasser (Hori and Nemat-Nasser, 1999), there exist two basic mathematical strategies to obtain the overall response of a heterogeneous material:

- *Mean field theory* (or average field theory). In the framework of this theory, 'macrofields are defined as the volume [weighted] averages of corresponding microfields', and the effective properties are determined as 'relations between averaged microfields'. This theory uses the concept of the RVE ('simple microstructure models'), which models the statistically homogeneous microstructure of the material.
- *Asymptotic homogenization theory* (or mathematical homogenization theory). This is based on the asymptotic expansions of displacement and strain fields about macroscale values, and was formulated by Bensoussan *et al*. (Bensoussan *et al*., 1978) and Sanchez-Palencia (Sanchez-Palencia, 1980). The material is modeled as an infinite series of unit cells under far field load. The big difference in the characteristic sizes of the microstructure and the considered volume makes it possible to carry out asymptotic series expansion of the variables. The theory allows high order terms in the singular perturbation expansion, and the analysis of micro–macro relationships can be

carried out more rigorously than in the case of the mean field theory. The asymptotic homogenization theory was developed initially for linearly elastic materials, and then generalized to nonlinear elastic, plastic and viscoelastic materials (Suquet, 1987; Fish *et al.*, 1997b; Yu and Fish, 2002; Searcy, 2004). The asymptotic homogenization approach was further used to study the overall properties of fiber reinforced metal matrix composites (Jansson, 1992), and composites with interfacial damage (Lene, 1986). Hori and Nemat-Nasser (Hori and Nemat-Nasser, 1999) developed a hybrid theory, which combines the mean field and homogenization theory.

In the following, we briefly review some techniques, bounds and estimations used to establish relationships between the overall properties of composites and their microscopic properties and microstructures.

4.3.1 Rule-of-mixture and classical Voigt and Reuss approximations

The intuitive answer to the question about the macroscopic response of a material consisting of phase A with Young modulus E_A and volume content v_A, and phase B with Young modulus E_B and volume content v_B is the 'rule of mixture'. A rule-of-mixture-type formula was derived by Woldemar Voigt in 1889 (Voigt, 1889), initially for the estimation of the elastic constants of polycrystals. The idea of the Voigt approach was to determine elastic moduli by averaging stresses (expressed in terms of strains) over all possible lattice orientations (or phases), assuming strain uniformity throughout the material.

Considering Figure 4.4, one can derive the rule-of-mixture-type formula for Young modulus of the composite, assuming that the average strain of each phase is equal to the applied strain:

$$\varepsilon_f = \varepsilon_m = \varepsilon_{comp} \tag{4.15}$$

where ε is strain and subscripts f, m and comp denote fiber, matrix and the composite, respectively. Both the fibers and matrix are considered as linear-elastic materials:

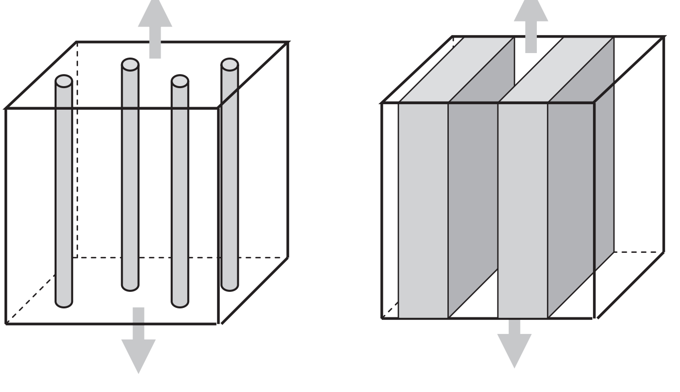

Figure 4.4 A special case for which the Voigt formulae are exact.

$\sigma_f = E_f \varepsilon_{comp}$ and $\sigma_m = E_m \varepsilon_{comp}$. The force balance in the fiber direction can be written as:

$$P_{comp} = \sigma_{comp} A_{comp} = P_f + P_m \tag{4.16}$$

where $P_f = \sigma_f A_f$ and $P_m = \sigma_m A_m$, A_f and A_m are cross-sectional areas of the fiber and matrix, $P_{f,m,comp}$ are forces acting on the fiber, matrix and composite, respectively and σ is stress (in the fiber, matrix or averaged over the composite). Taking Equations (4.15) and (4.16) into account, one can derive the relationship:

$$E_{comp} = E_f v_f + E_m v_m \tag{4.17}$$

where $E_{f,m,comp}$ are the Young moduli of the fiber, matrix and composite, respectively.

Reuss (Reuss, 1929) proposed to determine the elastic moduli by averaging strains, expressed in terms of stresses, assuming stress uniformity. For the case shown in Figure 4.5, the Reuss estimates can be calculated as follows. It is assumed that the average stress of each phase is equal to the applied stress:

$$\sigma_f = \sigma_m = \sigma_{comp} \tag{4.18}$$

If both fibers and matrix are linearly elastic, it follows from the force balance that:

$$E = \frac{E_f E_m}{E_f v_f + E_m v_m} \tag{4.19}$$

In their works, both Voigt and Reuss sought to provide exact estimations of the elastic moduli of materials with random microgeometries. However, as shown by Hill (Hill, 1964), these estimations give only upper and lower bounds for the elastic moduli of a

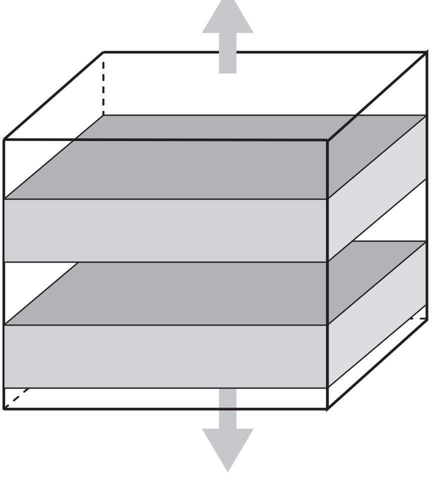

Figure 4.5 *A model material for which the Reuss formula is applicable.*

composite with an arbitrary random geometry. The Reuss estimation gives the lower bound of the elastic moduli for the composite, and the Voigt estimation gives the upper bound:

$$\frac{E_\mathrm{f}E_\mathrm{m}}{E_\mathrm{f}v_\mathrm{f}+E_\mathrm{m}v_\mathrm{m}} \leq E \leq E_\mathrm{f}v_\mathrm{f}+E_\mathrm{m}v_\mathrm{m} \tag{4.20}$$

The Voigt and Reuss estimations correspond to the exact solution only for the special cases shown in Figures 4.4 and 4.5, respectively. For the cases $v_\mathrm{f}=0$ or $v_\mathrm{m}=0$, the Voigt and Reuss estimations are reduced to the same values.

Hill's analysis was based on the results by Bishop and Hill (Bishop and Hill, 1951). Bishop and Hill demonstrated that the volume average of the strain energy density of an inhomogeneous material is equal to the product of the averaged stresses and strains, if the material contains a sufficiently large number of grains and is statistically homogeneous:

$$<\sigma\varepsilon>=<\sigma><\varepsilon> \tag{4.21}$$

One should note that Hill's bounds are rather wide, and are therefore of limited usefulness for the practical determination of material properties.

4.3.2 Hashin–Shtrikman bounds

The most widely used bounds for the overall properties of composites have been proposed by Hashin and Shtrikman (Hashin and Shtrikman, 1962a,b, 1963). Hashin and Shtrikman formulated a *variational principle for nonhomogeneous linear elasticity*. The volume integral:

$$U_\mathrm{p}=U_0-\frac{1}{2}\int\left[p_{ij}H(p_{ij})-p_{ij}\varepsilon'_{ij}-2p_{ij}\varepsilon^0_{ij}\right]\mathrm{d}V \tag{4.22}$$

subject to the subsidiary and boundary conditions $L_\mathrm{o}(\varepsilon'_{ij})_{,j}+p_{ij,j}=0$ and $u'_i(S)=0$, is stationary for $p_{ij}=L(\varepsilon_{ij})-L_\mathrm{o}(\varepsilon_{ij})$. Here $p_{ij}=L_\mathrm{o}(\varepsilon_{ij})-\sigma_{ij}$ is the stress polarization tensor, $L_\mathrm{o}(\varepsilon_{ij})$ is the function relating the stress and strain tensor in Hooke's law, V and S are the volume and surface of the body, $u'_i=u_i-u^\mathrm{o}_i$, $u^\mathrm{o}_i(S)$ is surface displacement, superscript prime means differentiation, H is the operator given by $H=(L-L_\mathrm{o})^{-1}$, σ^o_{ij} and σ_{ij} are the known and unknown stress fields in the deformed elastic body, $\varepsilon'_i=\varepsilon_i-\varepsilon^\mathrm{o}_i$ and $U_0=\frac{1}{2}\int\sigma^\mathrm{o}_{ij}\varepsilon^\mathrm{o}_{ij}\mathrm{d}V$.

Using this variational principle, they derived analytical expressions which provide bounds for the elastic constants of a heterogeneous material with a random isotropic distribution of phases. For the case of spherical particles randomly distributed in the matrix, the formulae are:

$$\begin{aligned} k_- &= k_\mathrm{m}+\frac{v_\mathrm{p}}{\dfrac{1}{k_\mathrm{p}-k_\mathrm{m}}+\dfrac{3v_\mathrm{m}}{3k_\mathrm{m}+4G_\mathrm{m}}} \\ k_+ &= k_\mathrm{p}+\frac{v_\mathrm{m}}{\dfrac{1}{k_\mathrm{m}-k_\mathrm{p}}+\dfrac{3v_\mathrm{p}}{3k_\mathrm{p}+4G_\mathrm{p}}} \end{aligned} \tag{4.23}$$

$$G_{-} = G_{\mathrm{m}} + \frac{v_{\mathrm{p}}}{\dfrac{1}{G_{\mathrm{p}} - G_{\mathrm{m}}} + \dfrac{6(k_{\mathrm{m}} + 2G_{\mathrm{m}})v_{\mathrm{m}}}{5G_{\mathrm{m}}(3k_{\mathrm{m}} + 4G_{\mathrm{m}})}}$$

$$G_{+} = G_{\mathrm{p}} + \frac{v_{\mathrm{m}}}{\dfrac{1}{G_{\mathrm{m}} - G_{\mathrm{p}}} + \dfrac{6(k_{\mathrm{p}} + 2G_{\mathrm{p}})v_{\mathrm{p}}}{5G_{\mathrm{p}}(3k_{\mathrm{p}} + 4G_{\mathrm{p}})}} \tag{4.24}$$

where k_{p}, G_{p} and k_{m}, G_{m} are the bulk and shear moduli for the particles and the matrix, respectively, v_{m}, v_{p} are the volume fractions and subscripts $-$ and $+$ mean the lower and upper bounds, respectively. The lower bound is obtained with the softer phase taken as the matrix, and the upper bound is derived for the case of the harder phase taken as the matrix.

Figure 4.6 gives an example of the variation of the estimations of bulk modulus for a model material (with the bulk moduli 10 GPa for spherical particles and 100 GPa for the matrix), obtained with the use of Voigt, Reuss and Hashin–Shtrikman formulae. Both lower and upper Hashin–Shtrikman bounds ($-$ and $+$) are presented.

Using the classical energy principles, Walpole (Walpole, 1966) suggested variational bounds of the Hashin–Shtrikman type for the overall elastic behavior of composites with aligned ellipsoidal reinforcements, which take into account both the aspect ratios of the fibers and the volume fractions of the fibers. Later, Walpole (Walpole, 1969) obtained results for infinitely long fibers and thin disks, oriented randomly or aligned. Willis (Willis, 1977) developed general bounds for transversally isotropic composites reinforced by aligned ellipsoidal inclusions.

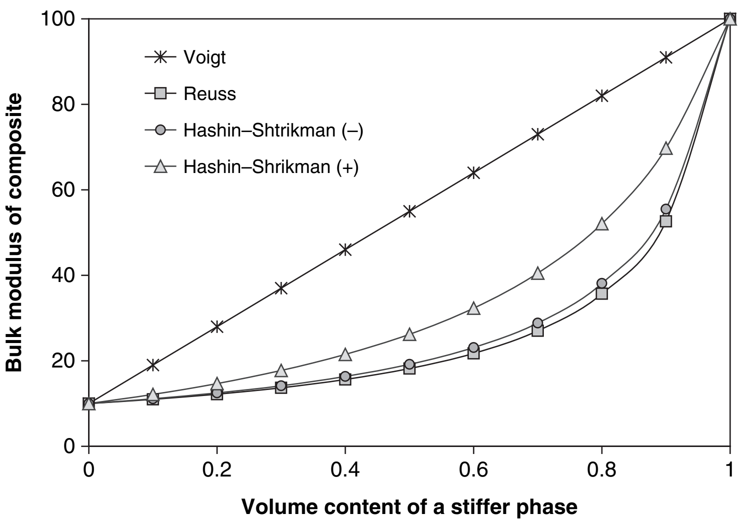

Figure 4.6 *Estimations of bulk modulus of a model material with the use of Voigt, Reuss and Hashin–Shtrikman formulae.*

4.3.3 Dilute distribution model

If the volume fraction of inclusions is very small, the interaction between reinforcing elements can be neglected. In this case, the *dilute distribution model* can be used to analyze the effective elastic properties of composites.

The dilute distribution model, as well as many other micromechanical approaches, is based on the theory developed by Eshelby (Eshelby, 1957). Eshelby considered the stress and strain fields in a medium with an elliptical region which undergoes a transformation and changes its shape or size. He has shown that uniform stress and strain states are induced in the transformed elastic homogeneous inclusion ('elliptical region'), embedded into an infinite matrix subject to uniform strain. Eshelby introduced a so-called Eshelby tensor $\boldsymbol{S}$, which relates the strains in an inclusion in the infinite elastic matrix ($\varepsilon_{\mathrm{constr}}$) with the strain of the same inclusion, placed outside the matrix and free of the stresses imposed by the matrix ($\varepsilon_{\mathrm{unconstr}}$):

$$\varepsilon_{\mathrm{constr}} = S\varepsilon_{\mathrm{unconstr}} \tag{4.25}$$

where $\boldsymbol{S}$ is the Eshelby tensor. The tensor $\boldsymbol{S}$ is a function of the elastic properties of the bodies, and the inclusion shape.

In order to determine the elastic moduli of a material reinforced by very few inclusions, the problem of a single spherical or ellipsoidal inclusion in an infinite matrix medium, subjected to homogeneous boundary conditions at infinity, is solved on the basis of the Eshelby approach. For the case of isotropic spherical particles in an isotropic matrix, subject to homogeneous stress boundary conditions, the analysis yields the following formulae for the effective bulk and shear moduli:

$$\begin{aligned} k &= k_{\mathrm{m}}\left[1 + v_{\mathrm{p}}\frac{k_{\mathrm{p}} - k_{\mathrm{m}}}{k_{\mathrm{m}} + \alpha(k_{\mathrm{p}} - k_{\mathrm{m}})}\right] \\ G &= G_{\mathrm{m}}\left[1 + v_{\mathrm{p}}\frac{G_{\mathrm{p}} - G_{\mathrm{m}}}{G_{\mathrm{m}} + \beta(G_{\mathrm{p}} - G_{\mathrm{m}})}\right] \end{aligned} \tag{4.26}$$

where $\alpha = (1+\nu_{\mathrm{m}})/3(1-\nu_{\mathrm{m}})$, $\beta = 2(4\text{–}5\nu_{\mathrm{m}})/15(1-\nu_{\mathrm{m}})$; $\nu_{\mathrm{m}} = (3k_{\mathrm{m}} - 2G_{\mathrm{m}})/(6k_{\mathrm{m}} + 2G_{\mathrm{m}})$, α, β are coefficients and ν_{m} is Poisson's ratio of the matrix. Apparently, the estimations obtained with the use of the dilute distribution model become less exact when the volume content of the reinforcement increases above a few percent.

4.3.4 Effective field method and Mori–Tanaka model

In the approach, suggested by Mori and Tanaka (Mori and Tanaka, 1973), each inclusion behaves as an isolated inclusion, subject to the averaged stress fields acting on it from all the other inclusions (cf. Figure 4.7). The stresses, acting on an inclusion and caused by the presence of other inclusions, are superimposed on the applied stress. The idea of Mori and Tanaka was to combine the Eshelby approach and the effective field concept. This is done by defining the strain concentration tensor, which relates the strain in the inclusion to the unknown strain in the matrix (instead of the applied strain, as in the case of the dilute distribution model). Benveniste (Benveniste, 1987) expanded the relations suggested by Mori and Tanaka, and provided a general method for determining the

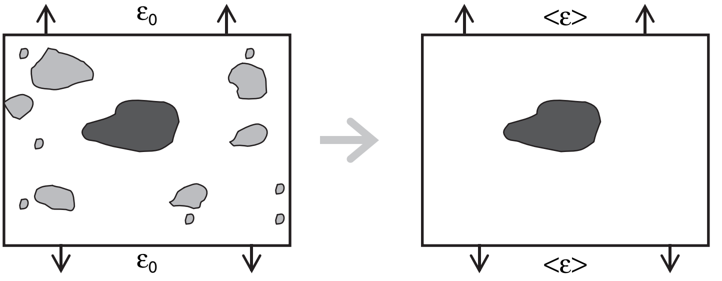

Figure 4.7 Mori–Tanaka model. The interaction between inclusions is taken into account by averaging strain fields acting on a given inclusion from all the other inclusions.

effective properties, based on this theory. The Mori and Tanaka approach belongs to the group of effective field methods (Levin, 1976; Kanaun, 1983).

This model leads to the same formulae as the lower Hashin–Shtrikman bound (i.e. when the matrix is the softer phase) for spheres and many other inclusion shapes. According to Böhm (Böhm, 1998), the estimations of overall Young and shear moduli of composites with spherical particles and aligned reinforcement based on the Mori–Tanaka method are somewhat lower than the experimental results, but are still very close.

4.3.5 Composite sphere and composite cylinder assemblage

A geometrical model of composites, called *composite sphere assemblage* (CSA) was developed by Hashin (Hashin, 1962). A volume is filled with composite spheres, each of them consisting of a spherical particle surrounded by a concentric matrix shell. The spheres can be of any size, but the volume fractions of the spherical particle and matrix layer are the same for all the spheres. Figure 4.8 schematically shows the CSA model. Hashin analyzed this model by variational methods, and derived a closed-form exact solution for the effective bulk modulus and bounds for the effective shear

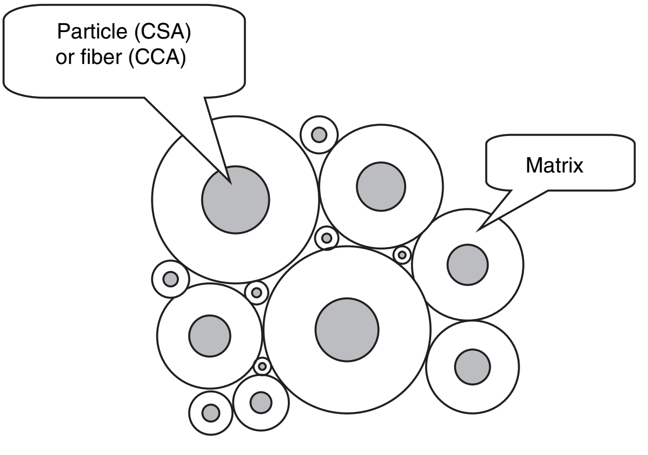

Figure 4.8 Schema of the CSA or CCA model of a composite, introduced by Hashin (Hashin, 1962) and Hashin and Rosen (Hashin and Rosen, 1964).

modulus. The formula for the effective bulk modulus is written as (Hashin, 1962; Christensen, 1979):

$$k = k_{\mathrm{m}} + \frac{v_{\mathrm{p}}(k_{\mathrm{p}} - k_{\mathrm{m}})}{1 + \dfrac{(1 - v_{\mathrm{m}})(k_{\mathrm{p}} - k_{\mathrm{m}})}{k_{\mathrm{m}} + \frac{4}{3}G_{\mathrm{m}}}} \tag{4.27}$$

Following this work, Hashin and Rosen (Hashin and Rosen, 1964) proposed a so-called *composite cylinder assemblage* (CCA) model for the analysis of long fiber reinforced composites with an overall transversely isotropic behavior. The CCA model consists of an assembly of randomly distributed composite cylinders (each consists of a long inner circular fiber surrounded by an outer concentric matrix) with different radii which fill the whole volume of a representative element (similarly to CSA). Hashin and Rosen obtained bounds for the transverse shear modulus on the basis of the variational analysis of this model. One should mention that the Hashin and Shtrikman bounds for fiber reinforced composites are different from the Hashin and Rosen bounds.

An improved version of the CCA, called the *generalized self-consistent method*, was suggested by Christensen and Lo (Christensen and Lo, 1979). Christensen and Lo considered a cylindrical fiber surrounded by a matrix shell, which is placed into a material with effective properties of the composite (Figure 4.9). Using the exact elastic solutions for cylindrical geometries, they analyzed the elastic response of this cell, and derived differential equations for the effective transverse shear modulus of a unidirectional composite. A generalized self-consistent schema gives very good results for the composites with spherical particles and aligned reinforcement.

4.3.6 Self-consistent models and other effective medium methods

The self-consistent model (SCM) (Figure 4.10) was suggested initially by Hershey (Hershey, 1954) and Kröner (Kröner, 1958) for single crystals and polycrystals, and then extended by Budiansky (Budiansky, 1965). In the framework of the self-consistent approach, a microstructure of a polycrystal or a composite is modeled as a single crystal or single inclusion, embedded into some equivalent medium, which represents the influence of all other microstructural elements on this single inclusion. The effects of other microstructural elements on a given inclusion are smeared over the equivalent medium (matrix). The properties of the equivalent medium are determined in a self-consistent way.

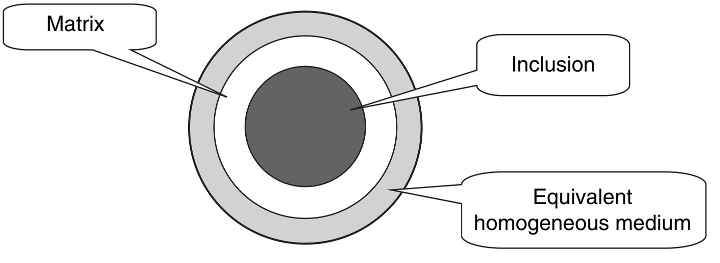

Figure 4.9 *Generalized self-consistent model by Christensen and Lo (Christensen and Lo, 1979).*

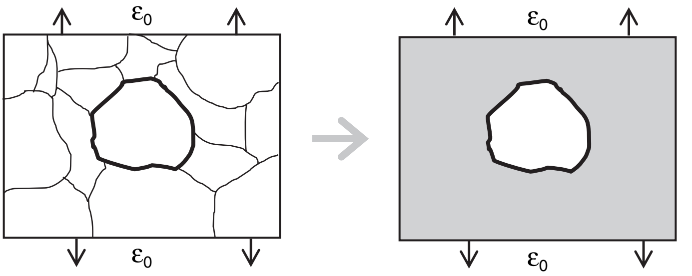

Figure 4.10 *Self-consistent model. The influence of other particles or defects on a given particle is smeared over the equivalent medium.*

The principal difference with the Mori–Tanaka (effective field) method is that the effective properties of the embedding material with inclusions (instead of effective stress and/or strain fields) are considered.

For the case of isotropic spherical particles, isotropically distributed in an isotropic matrix, the effective bulk and shear moduli can be calculated by the formulae:

$$k = k_m + v_p(k_p - k_m)\left[1 + \alpha_1\left(\frac{k_p}{k} - 1\right)\right]^{-1}$$

$$G = G_m + v_p(G_p - G_m)\left[1 + \beta_1\left(\frac{G_p}{G} - 1\right)\right]^{-1} \tag{4.28}$$

where $\alpha_1 = 3k/(3k+4G)$ and $\beta_1 = 6(k+2G)/5(3k+4G)$ (Seelig, 2000). The effective moduli obtained by applying the homogeneous stress or strain boundary conditions are equivalent.

According to Norris (Norris, 1985), the SCMs can be grouped into symmetric models (where the phases are interchangeable) and asymmetric (where one phase is taken as a matrix phase, and all other phases as inclusions). The asymmetric SCM were considered by Wu (Wu, 1966) and Boucher (Boucher, 1974). If spherical inclusions in a matrix are considered, the formulae (4.28) hold for both classes of the self-consistent theories, and are symmetric with respect to changing the ‘m’ to ‘p’.

According to Hill (Hill, 1965) and Berryman (Berryman, 1980), the results of SCMs are always within the Hashin–Shtrikman bounds. The self-consistent approach allows microstructures with some degree of regularity to be described well, but not clustered structures or microstructures with large differences between properties of the phases. The SCMs lead to apparently false estimations of the elasticity moduli for some specific cases. For instance, if $k_p = 0$, $G_p = 0$ and $k_m = \infty$ (i.e. incompressible matrix with holes), the SCM estimation gives zero stiffness ($k = 0$) for the material with 50 % hole content v_p (Budiansky, 1965). In reality, however, a material with 50 % holes still has nonzero stiffness.

The model developed by Christensen and Lo (Christensen and Lo, 1979), mentioned above, represents in fact a generalized CCA model. However, it is called the generalized self-consistent method, because the outer cylindrical layer is assigned the effective properties of the material.

Another approach, which belongs to the group of effective medium methods, is the *differential effective medium approximation*. The idea of the differential effective medium approximation (Roscoe, 1973; Boucher, 1974; McLaughlin, 1977) is to add a given inclusion volume iteratively, in 'small portions', to the effective material (initially homogeneous matrix). Then, the new effective properties of the effective matrix are re-calculated after each addition of small inclusions volumes, using the dilute approximation. For spherical inclusions, this approach leads to the following differential equations for the elastic moduli of the composite:

$$\begin{aligned} \frac{\mathrm{d}k}{\mathrm{d}v_{\mathrm{p}}} &= \frac{(k+4G/3)(k-k_{\mathrm{p}})}{v_{\mathrm{p}}(k_{\mathrm{p}}+4G/3)} \\ \frac{\mathrm{d}G}{\mathrm{d}v_{\mathrm{p}}} &= \frac{5G(k+4G/3)(G-G_{\mathrm{p}})}{v_{\mathrm{p}}[3G(k+8G/9)+2G_{\mathrm{p}}(k+2G)]} \end{aligned} \tag{4.29}$$

Norris (Norris, 1985) demonstrated that the effective properties of a composite, calculated with this method, may depend not only on the volume fractions of phases, but also on the 'construction path' of the composite.

4.3.7 Method of cells and transformation field analysis

Physical fields in multiphase materials can be described using piecewise approximations, where the fields or some components of the fields are assumed to be uniform in the phases, subcells or small volumes of materials. This idea was realized in the framework of the *transformation field analysis* (TFA), developed by Dvorak (Dvorak, 1992). In this approach, a microstructure is divided into subvolumes, in which local fields are presumed to be uniform. The stress and strain fields and overall thermomechanical properties of multiphase materials are presented in the form of piecewise uniform approximations in subvolumes of discretized unit cells. The total strains and stresses in the phases are decomposed into the elastic strains/stresses due to the certain surface tractions, and an eigenstrain/eigenstress in phases. The eingenstrain and eigenstrain are referred to as *transformation fields* (Dvorak *et al.*, 1994), and are further decomposed into terms related to the inelastic and thermal effects. The local stress fields in the subvolumes can be evaluated as follows:

$$\sigma_p(t) = \mathbf{B}_p\sigma(t) + \sum_{k=1}^{N} \mathbf{F}_{pk}\lambda_p \tag{4.30}$$

where $\mathbf{B}_p$ is the concentration factor tensor for phase p, $\sigma_p(t)$ is the local stress at time t, $\sigma(t)$ is the overall stress at time t, N is the amount of subvolumes, λ_p is the eigenstress in the pth subvolume and $\mathbf{F}_{pk}$ is the transformation concentration factor tensor, defining the stress in a pth subvolume due to the unit eigenstress in the kth subvolume. The transformation factor tensor can be determined in terms of compliances of phases, the vector of linear thermal expansion coefficients and the mechanical strain concentration factor matrix. The overall response can be expressed in terms of overall elastic compliance $\mathbf{M}$ or stiffness $\mathbf{L}$:

$$\varepsilon(t) = \mathbf{M}\sigma(t) + \mu(t) \tag{4.31}$$

where $\mathbf{M} = \mathbf{L}^{-1}$ and $\mu(t)$ is the uniform overall strain, when the volume is free of surface tractions. Dvorak and colleagues noted that the unit cell models, Mori–Tanaka, self-consistent or Eshelby approaches can be considered as special cases of TFA. The transformation field approach was generalized by Chaboche *et al.* (Chaboche *et al.*, 2001), who introduced the damage effects into the model.

In the framework of the *method of cells* (MOC), suggested by Aboudi (Aboudi, 1989, 1999), a periodic square array of fibers is represented as a unit cell, consisting of four rectangular subcells. Three subcells are assigned the matrix behavior and the fourth subcell represents the fiber. Approximating the displacement fields in the subcells in terms of a linear expansion in local coordinates, and taking into account the equilibrium conditions, Aboudi obtained the expansion coefficients and estimated the macro- and microscopic stresses and strains. Figure 4.11 shows the model of a unidirectional fiber reinforced composite as a double periodic array of fibers, and its representation as a unit cell in the framework of the MOC.

The *generalized method of cells* (GMC) (Paley and Aboudi, 1992) uses the first order representation of the displacement field in each subcell. Therefore, the piecewise uniform strain and stress fields in the cell are determined. In the generalized version, the repeating unit cells are subdivided into several subcells, to which phase properties are assigned. This method can be applied to the analysis of more complex microgeometries, than can be analyzed with the use of MOC (Aboudi, 1999).

Later, Aboudi *et al.* (Aboudi *et al.*, 2001) proposed a new method, called the *high fidelity generalized method of cells* (HFGMC). In this method, the displacement fields in subvolumes are approximated by quadratic functions of local coordinates. This led to the linear (and not piecewise uniform) strain and stress fields at the subvolume level (Aboudi *et al.*, 2003). The approach, used by Aboudi and colleagues, is based on asymptotic homogenization techniques and on the higher order theory for functionally gradient materials, developed by Aboudi *et al.* (Aboudi *et al.*, 1999). The HFGMC produces excellent results not only in the analysis of the overall properties of composites (already achieved in the framework of GMC), but also in the analysis of local strain and stress fields.

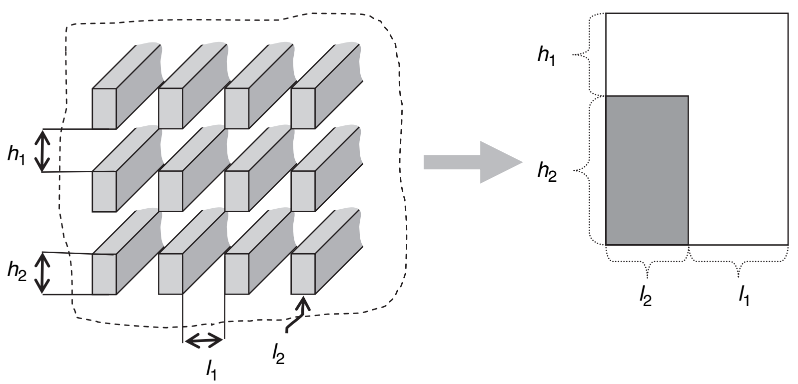

Figure 4.11 *Method of cells. Model of a unidirectional fiber reinforced composite as double periodic array of fibers, and its representation as a unit cell (after Aboudi and Pindera, 1992).*

4.3.8 Incorporation of detailed microstructural information: three-point approximation

The incorporation of more detailed microstructural information into the bounds or estimations of overall properties could improve the estimations. Several research groups carried out analytical investigations in order to include more detailed and realistic microstructural description into analytical and numerical–analytical models of the material behavior.

Using the truncated perturbation series as trial fields in the variational analysis, Beran (Beran, 1965) obtained three-point bounds on the effective conductivity. On the basis of Beran's approach, Beran and Molyneux (Beran and Molyneux, 1966) and McCoy (McCoy, 1970) developed bounds for the effective shear and bulk moduli of elastic composites. The microstructure of a material is taken into account via the three-point correlation function, which is defined as:

$$\hat{S}_3(r_1, r_2, r_3) = \langle f(x+r_1) f(x+r_2) f(x+r_3) \rangle \tag{4.32}$$

where $f(x) = 1$ in material 0, and $f(x) = 1$ in material 1, x is the point location, r_1, r_2, r_3 are coordinates and $<\ldots>$ gives the volume average over the spatial coordinate x.

The results by Beran and Molyneux and McCoy were simplified by Milton (Milton, 1981), who derived simple relations between three-point functions, which enabled the Beran–Molyneux three-point bounds to be obtained in concise form. Milton introduced the following averages of any physical property $\sqcap$ of a composite:

$$\begin{aligned}
\langle \prod \rangle &= \prod\nolimits_1 v_1 + \prod\nolimits_2 v_2 \\
\langle \prod \rangle_\zeta &= \prod\nolimits_1 + (\prod\nolimits_2 - \prod\nolimits_1)\zeta \\
\langle \prod \rangle_\eta &= \prod\nolimits_1 + (\prod\nolimits_2 - \prod\nolimits_1)\eta \\
\tilde{\prod} &= \prod\nolimits_1 v_2 + \prod\nolimits_2 v_1
\end{aligned} \tag{4.33}$$

where v_1 and v_2 are the volume contents of the first and second phases and ζ and η are geometric parameters of the microstructures which are defined via the three-point function:

$$\zeta = \lim\nolimits_{\Delta \to 0} \frac{9}{2 v_1 v_2} \int_\Delta^\infty \mathrm{d}r \int_{-1}^{+1} \mathrm{d}u \frac{S_3(r,s,u)}{2rs} (3u^2 - 1)$$

$$\eta = \frac{5\zeta}{21} + \lim\nolimits_{\Delta \to 0} \frac{150}{7 v_1 v_2} \int_\Delta^\infty \mathrm{d}r \int_{-1}^{+1} \mathrm{d}u \frac{S_3(r,s,u)}{8rs} (35u^4 - 30u^2 + 3)$$

Using the formulae in (4.33), Milton presented the Beran–Molyneux–McCoy bounds in the following form:

$$k_- = \left[\langle 1/k \rangle - \frac{4 v_1 v_2 (1/k_1 - 1/k_2)^2}{4\langle 1/\tilde{k} \rangle + 3 \langle 1/G \rangle_\zeta} \right]^{-1} \qquad k_+ = \langle k \rangle - \frac{3 v_1 v_2 (k_1 - k_2)^2}{3\langle \tilde{k} \rangle + 4 \langle G \rangle_\zeta}$$

$$G_- = \left[\langle 1/G \rangle - \frac{v_1 v_2 (1/G_1 - 1/G_2)^2}{\langle 1/\tilde{G} \rangle + 6\Xi} \right]^{-1} \qquad G_+ = \left[\langle G \rangle - \frac{6 v_1 v_2 (G_1 - G_2)^2}{6\langle \tilde{G} \rangle + \theta} \right] \tag{4.34}$$

where k_1, G_1 and k_2, G_2 are the bulk and shear moduli for the phases, and:

$$\Theta = \left[10\langle k\rangle^2\langle 1/k\rangle_\zeta + 5\langle G\rangle\langle 3G+2k\rangle\langle 1/G\rangle_\zeta + \langle 3k+G\rangle^2\langle 1/G\rangle_\eta\right]/\langle 9k+8G\rangle^2$$
$$\theta = \left[10\langle G\rangle^2\langle k\rangle_\zeta + 5\langle G\rangle\langle 3G+2k\rangle\langle G\rangle_\zeta + \langle 3k+G\rangle^2\langle G\rangle_\eta\right]/\langle k+2G\rangle^2$$

The determination of the microstructural parameters ζ and η still presents a major challenge. A number of studies on the estimation of these parameters have been carried out (Milton and Phan-Thien, 1982; Berryman and Milton, 1988).

Torquato (Torquato, 1998) developed a new *exact perturbation expansion approach* to the estimation of the effective stiffness tensor of macroscopically anisotropic composites. The approach is based on the exact series expansion for the effective stiffness tensor of two-phase composites, truncated after third order terms. Using this method, Torquato derived accurate approximate relations for the effective elastic moduli of different 2D and 3D composite media. For the 3D case, the formulae, derived by Torquato, take the form:

$$\frac{k}{k_m} = \frac{1 + \dfrac{4G_m}{3k_m}k_{mp}v_p - \dfrac{10G_m}{3(k_m+2G_m)}k_{mp}\mu v_m\zeta}{1 - k_{mp}v_p - \dfrac{10G_m}{3(k_m+2G_m)}k_{mp}\mu v_m\zeta} \tag{4.35}$$

$$\begin{aligned}\frac{G}{G_m} = &\left\{1 + \frac{9k_m+8G_m}{6(k_m-2G_m)}\mu v_p - \frac{2k_{mp}\mu G_m}{6(K_m-2G_m)}v_m\zeta\right.\\ &\left.-\frac{\mu^2}{6}\left(\frac{3k_m+G_m}{k_m+2G_m}\right)^2 v_m\eta + 5G_m\left[\frac{2k_m+3G_m}{(k_m+2G_m)^2}\right]v_m\zeta\right\} / \left\{1-\mu v_p\right.\\ &-\frac{2k_{mp}\mu G_m}{3(k_m-2G_m)}v_m\zeta - \frac{\mu^2}{6}\left(\frac{3k_m+G_m}{k_m+2G_m}\right)^2 v_m\eta\\ &\left.+5G_m\left[\frac{2k_m+3G_m}{(k_m+2G_m)^2}\right]v_m\zeta\right\}\end{aligned} \tag{4.36}$$

where ζ and η are parameters of the three-point approximation, $k_{mp} = (k_p - k_m)/(k_p + 4G_m/3)$ and $\mu = (G_p - G_m)/\left[G_p + G_m(9k_m+8G_m)/(6k_m+12G_m)\right]$.

According to Böhm (Böhm, 1998), the estimates developed by Torquato (Torquato, 1998), 'give the best analytical predictions currently available for the overall thermoelastic response of inhomogeneous materials'.

4.3.9 Generalized continua: nonlocal and gradient-enhanced models

Classical continuum models do not reflect properly the effects of strain localization in materials, neither the scale effects. That leads often to the mesh dependence of numerical solutions, in particular, in the analysis of material degradation. In order to describe the material behavior, influenced by small scale microstructures, a number of enriched (generalized) continuum models have been developed, in which 'nonstandard deformation and/or stress quantities account for the influence of the microstructure on deformation process' (Peerlings *et al*., 2001). The generalization of the continuum models is carried out by adding nonlocal or gradient terms to the constitutive equations.

A *nonlocal constitutive model of composites* was developed by Drugan and Willis (Drugan and Willis, 1996). According to them, 'the leading-order correction to a macroscopically homogeneous constitutive equation consists of an additional term proportional to the second gradient of the ensemble average of strain' for two-phase composites with isotropic and statistically uniform phase distribution. On the basis of the Hashin–Shtrikman variational approach, Drugan and Willis derived an explicit closed-form expression of the nonlocal constitutive equation, which includes an integral of the two-point distribution function of the phases. Drugan and Willis demonstrated, that the minimum RVE size (which the 'effective modulus' constitutive models of composites may be applied to) is rather small (of the order of two reinforcement diameters).

In the following works by Willis (Willis, 2001) and Luciano and Willis (Luciano and Willis, 2000, 2001a,b) the nonlocal constitutive responses of random composites subject to deterministic and random body forces were analyzed, and bounds for the nonlocal effective relations were derived.

In the *gradient-enhanced models*, which originate from the classical works by Toupin (Toupin, 1962), and Mindlin (Mindlin, 1964, 1965), second and higher gradients of the stress and strains are included in the constitutive models of materials. Aifantis (Aifantis, 1999) proposed gradient-enhanced elasticity and plasticity theories, and applied them to the analysis of size effects in materials. Kouznetsova (Kouznetsova, 2002) developed a second-order computational homogenization procedure, in which the deformation tensor, and the first and second gradient of the displacement field are used to define the boundary conditions on a RVE. At the microstructural scale, standard first-order equilibrium and constitutive equations were used. Kouznetsova applied this method to simulate the size effects in the deformation behavior of elasto-viscoplastic porous aluminum.

The nonlocal and gradient-enhanced damage models, in particular, the nonlocal Gurson model developed by Tvergaard and Needleman (Tvergaard and Needleman, 1995) are briefly discussed in Chapter 3.

4.3.10 Nonlinear material behavior

Several approaches have been developed for the determination of the overall properties of nonlinear composites.

For the case of nonlinear polycrystals, Sachs (Sachs, 1928) and Taylor (Taylor, 1938) derived estimations, which are similar to the Voigt and Reuss estimations for the linear elastic materials, respectively. Bishop and Hill (Bishop and Hill, 1951) demonstrated that the Taylor and Sachs estimates provide bounds of the material behavior, similar to the Hill bounds for the linear case.

Later, several approaches were proposed, which are based on the estimations of properties of nonlinear composites in terms of properties for linear or nonlinear comparison media with the same microgeometry.

Talbot and Willis (Talbot and Willis, 1985, 1996) suggested a generalization of the Hashin–Shtrikman approach to the nonlinear composites. Considering a linear and homogeneous comparison material, they constructed trial fields using the corresponding Green functions. The trial fields were substituted into the energy and complementary energy functionals, allowing the bounds for the energy to be determined. In some cases, the nonlinear comparison medium should be considered to solve the problem.

Ponte Castañeda (Ponte Castañeda, 1991, 1992) developed a new variational approach, which leads to the effective energy potentials of nonlinear composites defined in terms of the corresponding energy potential for fictitious 'linear comparison composites' with the same microgeometries. The resulting bounds are given as functions of the bounds for the linear comparison composite. This procedure can be used to obtain nonlinear bounds and estimates from any bounds and estimates for linear composites.

Further, Ponte Castañeda (Ponte Castañeda, 1998) developed three-point bounds for the effective response of nonlinear composites. These three-point bounds were obtained on the basis of the Milton bounds, and the variational procedure for the derivation of nonlinear bounds presented by Ponte Castañeda in 1991 (Ponte Castañeda, 1991).

Detailed reviews of analytical models of micromechanics can be found in the literature (Christensen, 1979; Hashin, 1983; Mura, 1987; Nemat-Nasser and Hori, 1993; Böhm, 1998; Markov, 1999; Buryachenko, 2001; Torquato, 2002a; Milton, 2002).

4.4 Computational models of microstructures and strength of composites

Real microstructures of materials are very complex, inhomogeneous and often localized. The analytical estimation of the overall properties of composites is a nontrivial problem even in the case of linear-elastic components and relatively simple microstructures. Therefore, the generalization of the analytical estimations and bounds on the complex microstructures (e.g. via three-point correlation function) and nonlinear phase behavior presents an even bigger challenge for specialists. In such complex cases, the interrelationships between microstructures and the strength and overall properties of composites can be analyzed with the use of discretized numerical models, which incorporate discrete, real or generic microstructures of materials.

Böhm (Böhm, 1998) classified the theoretical approaches toward the analysis of discrete microstructures as follows:

- Periodic microfield approaches or unit cell methods: assuming the periodic phase arrangement, one analyses a repeating unit cell in the microstructure (e.g. Li, 1999).
- Embedded cell approach: the material is represented as a cut-out (unit cell) with a real microstructure, embedded into a region of the material with effective properties (e.g. Dong and Schmauder, 1996).
- 'Windowing approach': microstructure samples, chosen using 'mesoscale test windows', randomly placed in a heterogeneous material, are subject to homogeneous boundary conditions. By averaging the results for several 'windows', one can obtain bounds for the overall behavior of the material (Nemat-Nasser and Hori, 1993).
- Modeling the full microstructure of a sample (Silberschmidt and Werner, 2001).

The unit cell approach is most widely used in the mechanics of materials. In the next section, the techniques and areas of the application of the unit cell approach are reviewed.

4.4.1 Unit cell models of composites

Fiber reinforced composites subject to transverse loading present the simplest object of the numerical unit cell analysis of the mechanical behavior of materials, taking into account their microstructures. The statistical periodicity of the fiber arrangement is apparent, and the problem is simply reduced to the 2D version (Figure 4.12).

The most widely used 2D unit cells for unidirectional fiber reinforced composites are designed on the basis of the assumption of a squared or hexagonal arrangement of fibers. When designing unit cells, the symmetries of the model geometry should be taken into account to determine the minimized, but representative unit cells. Li (Li, 1999) proposed the following procedure for the selection of a unit cell model for a composite. First, a periodic element (whose translations in the x- and y-directions cover and reproduce all the microstructure) is chosen. The examples of different periodic elements for unidirectional fiber reinforced composite are shown in Figure 4.13. Then the representative part of the periodic element is reduced by taking into account the symmetry about the $x = 0$ and $y = 0$ axes. Finally, the remaining quarter of the periodic element is further reduced using the 180° rotational symmetry transformation (Figure 4.14). Applications of the unit cell approach to unidirectional fiber reinforced composites are discussed in more detail in Chapter 10.

For the analysis of unidirectional fiber reinforced composites under nontransverse loading, as well as short fiber and particle reinforced composites, *axisymmetric unit cells* are often applied (Figure 4.15). Shen *et al.* (Shen *et al.*, 1994) developed unit cells with cylinder, truncated cylinder, double-cone and spherical reinforcements (plane strain and axisymmetric models) to study the effect of shapes, concentration and distribution

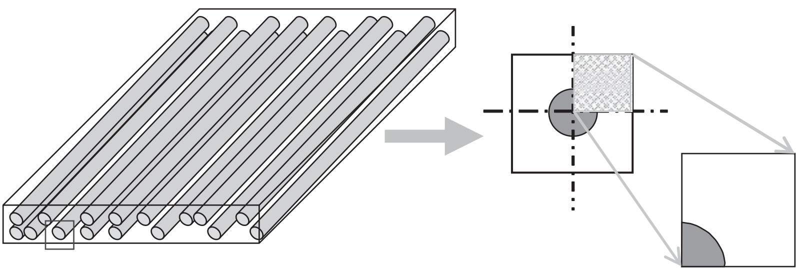

Figure 4.12 *Plane strain unit cell model of a fiber reinforced composite.*

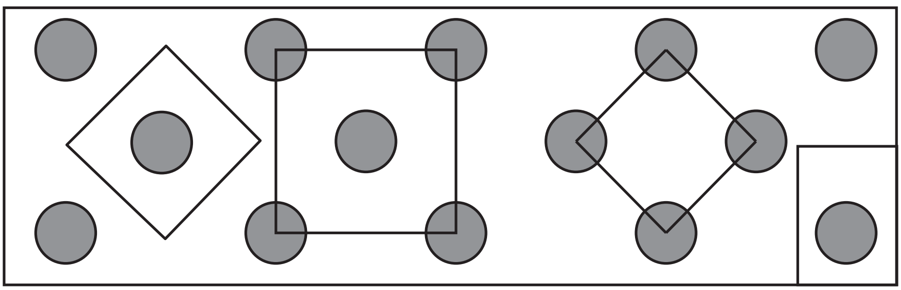

Figure 4.13 *Different periodic elements in a composites with hexagonal and cubic arrangement of fibers (after Li, 1999).*

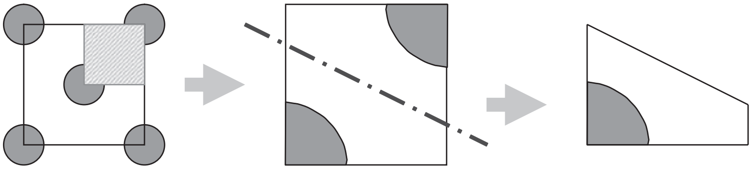

Figure 4.14 Selection of the minimal unit cell of a composite, using symmetry analysis (after Li, 1999).

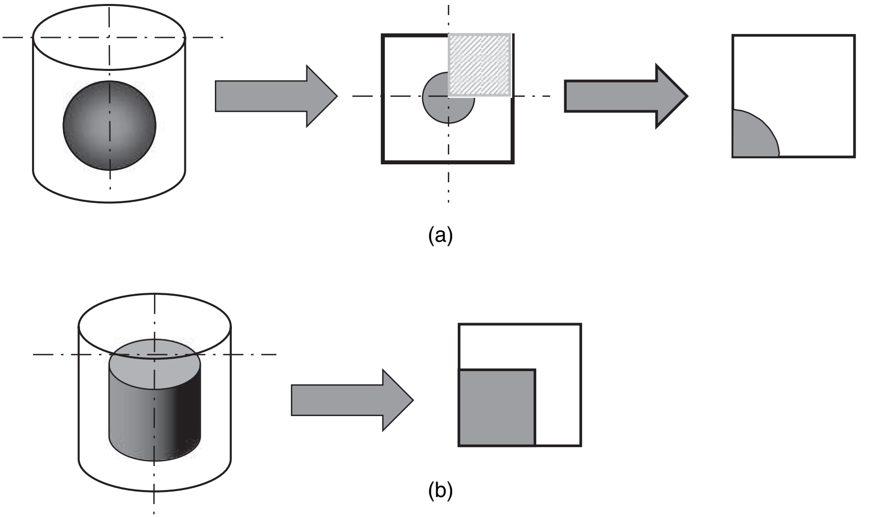

Figure 4.15 Axisymmetric unit cell models of (a) particle and (b) short fiber reinforced composites.

of inclusions on the mechanical response of the composites. Søvik (Søvik, 1996) employed an axisymmetric model of a unit cell with a round particle to analyze the relations between stresses in particles and averaged macrostresses in AlMgSi alloys. Figure 4.15 shows two examples of axisymmetric unit cell models of short fiber and particle reinforced composites.

A more detailed analysis of 3D effects of the inclusion shapes on the material behavior can be carried out using *3D unit cells*. Figure 4.16 gives two examples of the most often used cells: cubic and hexagonal/cylindrical. The cylindrical unit cells are used as approximations of the hexagonal cells (Kuna and Sun, 1996).

Fang *et al*. (Fang *et al*., 1996) studied the effect of particle shapes, orientation and volume fraction on the elastic moduli and stress–strain curves of Al alloy reinforced with Al_2O_3 particles, using many various 3D hexagonal and cubic unit cells with spherical, cylindrical, cubic and rectangular particles with different orientations. It was shown that the higher the aspect ratio of particles in a given direction, the more effective is the reinforcement in that direction.

Both types of widely used unit cell models, cubic and hexagonal/cylindrical cells, have some disadvantages even when applied to the ideal periodic microstructures of

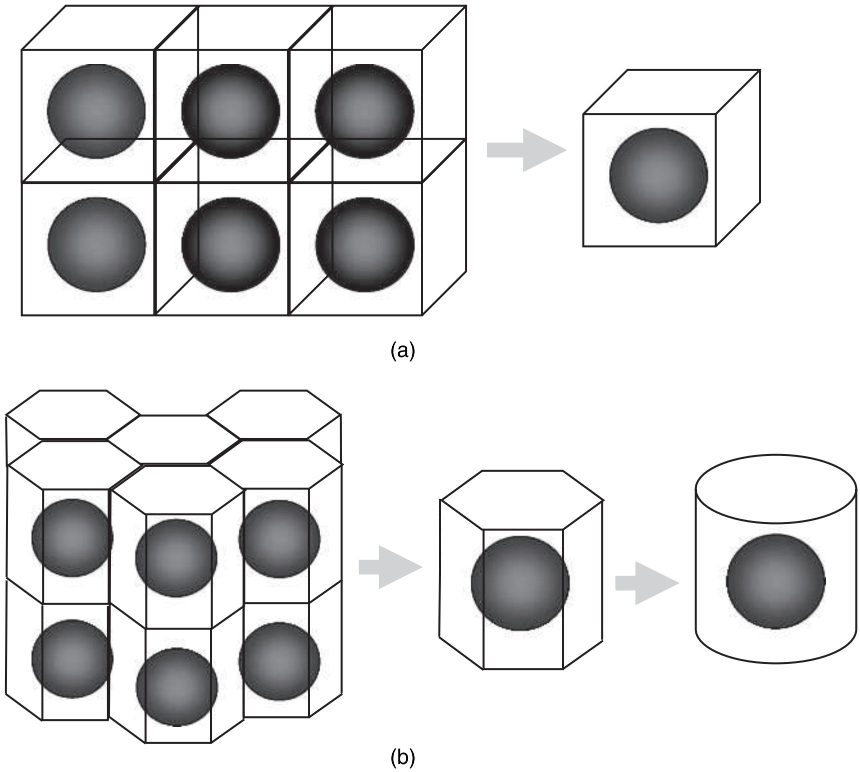

Figure 4.16 Typical unit cells: (a) cubic and (b) hexagonal/cylindrical (Bao et al., 1991).

composites. Cylindrical unit cells can not fill the space fully, and, therefore, the assumption about the 10 % porosity of the materials is implicitly made in the analysis. This is the case for the squared axisymmetric cells as well, which represent cylindrical cells, and, therefore, can not fill the volume. Cubic cells can fill space, and, therefore, no porosity of the material is implicitly assumed. However, maximum volume content of the spherical reinforcement in the cells can be only up to 54 %, while the volume content of reinforcement in the case of random dense packing of spheres can reach 60–64 % (Mozhev and Garishin, 2005). Thus, cubic unit cells are not applicable for the analysis of the mechanical behavior of composites with high volume content of reinforcing particles.

The unit cell models of materials can be used also to analyze the *damage initiation and evolution* in materials. Unit cells with damaged elements [for instance, broken or debonded inclusion (Michel, 1993; Mozhev and Kozhevnikova, 1996, 1997) or damaged matrix (Mishnaevsky Jr *et al*., 1999a)] have been used to analyze the effect of the microcracks on the mechanical behavior of composites, and the inclusion–microcrack interaction. Figure 4.17 shows several examples of unit cell models of a damaged material: a material with voids, and cracked and partially debonded particles.

Bao (Bao, 1992) studied the effect of cracks in particles and interfacial debonding on the strength and creep resistance of composites (Al, Ti and Ni alloys reinforced with Al_2O_3). A three phase damage cell model (hexagonal unit cell with a fractured

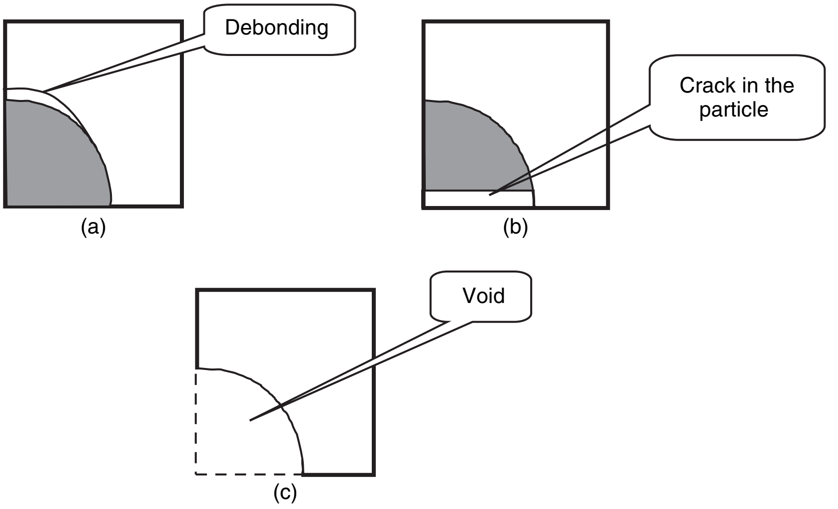

Figure 4.17 *Unit cells with damage: (a) axisymmetric unit cell, with partial interface debonding (Mozhev and Kozhevnikova, 1997); (b) cell with cracked particle; (c) void in the matrix (Steglich and Brocks, 1997).*

particle with the crack plane perpendicular to the direction of load; the cell is transformed into an axisymmetric one), embedded into the composite with undamaged particles was used. Further, a unit cell model with debonding at the end of cylindrical particles was considered. The effects of the total particle volume fraction, fraction of failed particles and the hardening exponent of the matrix on the stress–strain behavior were studied.

Llorca *et al*. (Llorca *et al*., 1991) studied the effect of the void nucleation in the matrix on the deformation of Al/SiC composites (particles and whiskers reinforced), using axisymmetric cylindrical unit cells with reinforcements of different shapes (cylinders, whiskers and spheres). Llorca and colleagues obtained the overall stress–strain response, and distributions of void volume fraction, stress and strain distribution in matrix for MMCs with different reinforcements. It was shown that the factors which increase the constraints on plastic flow (e.g. hydrostatic stress) tend to decrease the overall strain to matrix failure. Michel (Michel, 1993) studied the effect of particle cracking and debonding on the void growth in the matrix of Al/SiC composites, using axisymmetric unit cells with ellipsoidal, broken or debonded particles. He obtained stress–strain curves for different particle shapes, and for broken or debonded particles. It was observed that the debonding initiates at the pole of elliptical particles, and propagates toward the 'equator'. Kuna and Sun (Kuna and Sun, 1996, 1997) studied the void growth in ductile materials, using 3D hexagonal and cubic unit cells. They demonstrated that the spatial arrangement of periodic arrays of voids influences the deformation behavior only weakly, but affects strongly the plastic collapse. Mozhev and Kozhevnikova (Mozhev and Kozhevnikova, 1996, 1997) studied the mechanical behavior of elastomeric, particle reinforced composites with weak interfaces, using cylindrical unit cells with a rigid spherical inclusion and partial debonding. It was shown that the failure strain of composites decreases quickly with increase of the volume content of particles.

Steglich and Brocks (Steglich and Brocks, 1997) used axisymmetric cylindrical unit cells with spherical or ellipsoidal cavities (void), particle cracking or particle–matrix debonding to analyze the effect of the different modes of damage on the mechanical behavior of nodular iron and Al/Al_3Ti composite. The unit cell simulations were carried out to calibrate the Gurson–Tvergaard–Needleman damage model. It was observed that the critical strain increases in the following order: unit cell with cracked particle $\rightarrow$ unit cell with debonding $\rightarrow$ unit cell with void and without any particle.

Thus, the unit cell approach permits the analysis of different mechanisms of damage initiation (void growth, interfacial debonding, particle cracking) in heterogeneous materials and of their effect on material behavior. The application of the unit cell approach in modeling the damage initiation and evolution is based on a very strong assumption: namely, voids or microcracks are supposed to be uniformly distributed (i.e. no localization of microcracks) and the interaction between them is neglected.

Some boundary effects can be observed in the unit cells, due to the fact that the load is applied to the cell (periodic element), instead of the whole sample. In order to exclude the boundary effects in the vicinity of the loading points of the cells and to take into account the interaction between the cutout of microstructure and the rest of the material, the *embedded cell approach* is used. In the framework of this approach, a unit cell is embedded into a volume of the material with effective properties of the whole composite. Figure 4.18 shows unit cell models of a material with and without embedding. The properties of the embedding can be determined experimentally (Wulf, 1985) or by using homogenization methods (averaging, self-consistent procedures; Dong and Schmauder, 1995, 1996). Axelsen (Axelsen, 1995), and Axelsen and Pyrz (Axelsen and Pyrz, 1995) developed a unit cell model of a fiber reinforced composite, which consists of a sample area (with different types of random distributions of fibers) and boundary area. The boundary area interacts with the sample area, and its size is determined on the basis of 'zone of influence' calculations.

The embedded cell model developed by Dong and Schmauder (Dong and Schmauder, 1995, 1996) presents a fiber surrounded by a matrix layer, which is embedded in the squared or cubic volume of the 'equivalent composite material'. The properties of the equivalent material are determined in a self-consistent manner. The embedding allows for the effect of the rest of material and the influence of the interaction of other inclusions with a given inclusion on the behavior of the cell. One can observe the similarity between this approach and the generalized self-consistent method by Christensen and Lo (Christensen and Lo, 1979) (Figure 4.9). Dong and Schmauder used the embedded cell model to study the effect of fiber volume fraction and matrix strain hardening parameters on the limit flow stress and stress–strain behavior of Al alloys with boron fibers under transverse loading. The authors have obtained stress–strain curves for square and hexagonal fiber arrangement and for different shapes of the embedded cells. The embedded cell model allows to simulate also more complex structures of materials: Lessle *et al.* (Lessle *et al.*, 1999) and Schmauder (Schmauder, 2002) have developed the so-called 'matricity model', which allows to simulate the behavior of a material consisting of two interpercolating continuous phases with the use of the unit cell approach.

The analysis of the interaction between reinforcing inclusions in the material under loading is possible in the framework of *multi-inclusion unit cells* (Segurado *et al.*, 2003; Mishnaevsky Jr, 2004a,b). In these models, an assumption about the regular arrangement

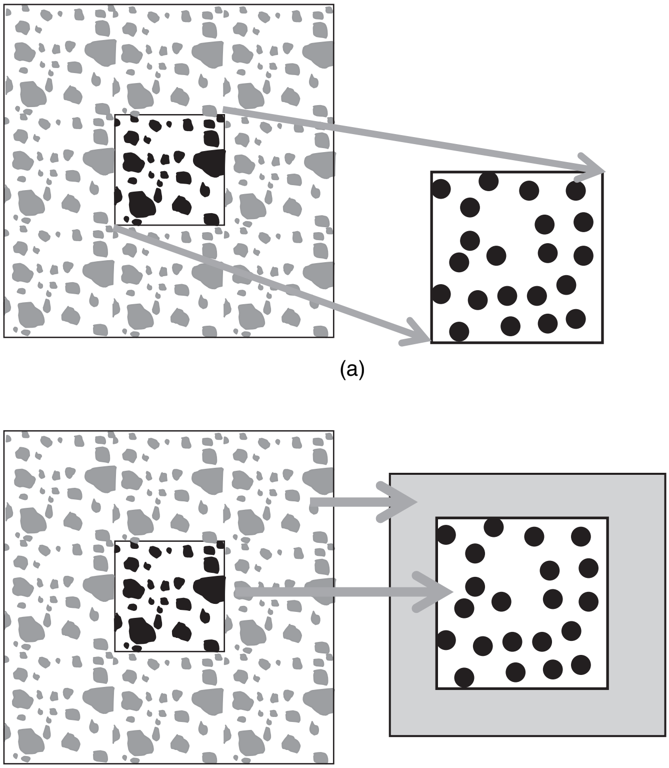

(a)

(b)

Figure 4.18 *Schematic diagram of unit cell models (a) without and (b) with embedding.*

of groups of fibers or particles instead of the regular arrangement of single reinforcing elements is used. This version of the unit cell approach allows to simulate more realistic distributions of particles or fibers than the traditional single element unit cell models. Siegmund *et al*. (Siegmund *et al*., 1993) used the unit cell consisting of an array of ideal equal-sized hexagons to simulate the plastic flow of two-phase alloys with different contiguities of phases. The hexagons represented randomly distributed grains of the alloy. The authors studied the effect of contiguity of the phases on the plastic flow of a model two-phase material with coarse structure.

Axelsen (Axelsen, 1995), and Axelsen and Pyrz (Axelsen and Pyrz, 1995) analyzed the effect of the random distribution of fibers on the mechanical properties and damage behavior of composites using multifiber unit cells with 200 fibers. In so doing, the specific parameters of random microstructures (second-order intensity function, pair distribution of fibers, etc.) have been taken into account.

The application of *3D multi-element unit cells* is limited due to the high computational costs of 3D simulations with many degrees of freedom. Therefore, the question arises of how many microstructural elements can and should be placed into a 3D unit cell in order to ensure both reliability and stability of results. Many groups sought to develop numerical techniques for the generation and numerical analysis of 3D multi-element unit cells.

Andrei Gusev (Gusev, 1997) developed a method and a program for the generation of 3D multi-element unit cell models of short fiber reinforced composites. The method, proposed by Gusev, was realized in the FE software package Palmyra (developed by MatSim GmbH, a spin-off of the Swiss Federal Institute of Technology). The program allows to design and mesh complex 3D realistic microstructures of short fiber reinforced composites, and to compute elastic constants and stiffness of composites, as well as other physical properties. Using this software package, Gusev and colleagues carried out a number of studies of the effect of the microstructure on the elastic properties of composites. Gusev (Gusev, 1997) generated 3D unit cells with elastic components and up to 64 nonoverlapping statistically distributed particles, using the Monte-Carlo method. He analyzed the overall behavior of elastic particle reinforced composites, using a 'constant-strain-tetrahedra displacement-based finite element code'.

Hine *et al.* (Hine *et al.*, 2002) determined the elastic and thermoelastic properties of short fiber reinforced composites. They generated unit cells with 100 nonoverlapping aligned spherocylinders, and compared the results of their simulations with Halpin–Tsai, Tandon–Weng and shear lag models.

Gusev *et al.* (Gusev *et al.*, 2000) generated unit cells, which consisted of 100 nonoverlapping parallel fibers with different diameters, using the Monte-Carlo procedure and taking into account the measured distribution of diameters. The microstructural parameters of unidirectional glass/epoxy composites were determined using image analysis. As a result, Gusev and colleagues determined elastic constants of the unit cell models. They demonstrated that the effect of the randomness of the composite microstructures on the elastic properties is much more significant than the effect of the distribution of the fiber diameters.

Han and Böhm (Han and Böhm, 2001), Böhm and Han (Böhm and Han, 2001) and Eckschlager *et al.* (Eckschlager *et al.*, 2002) developed FE models of unit cells with 15–20 randomly arranged spherical inclusions, and applied them to the modeling of the damage of brittle particles in composites. Meshing of the models was carried out using the preprocessor PATRAN. They used the commercial FE solver ABAQUS, which made it possible to model nonlinear component behavior and damage evolution (not realized in the FE code Palmyra). In contrast to Gusev's approach, based on the Monte-Carlo method, Böhm and colleagues used the so-called *random sequential absorption* (RSA) scheme (Rintoul and Torquato, 1997). In the framework of the RSA scheme, the coordinates of inclusions are generated using the random number generator; if the new particle overlaps with an available inclusion, its location is accepted. Otherwise, a new location of the inclusion is generated. Böhm *et al.* (Böhm *et al.*, 2002) noted that the RSA approach does not allow to generate unit cells with high volume concentrations of inclusions.

Segurado and Llorca (Segurado and Llorca, 2002) used the modified RSA algorithm to generate multiparticle unit cells with 30 nonoverlapping identical spheres and particle volume fractions of up to 50 %. The unit cells with high volume content of the particles were obtained by placing a given amount of particles in the unit cell, and then compressing the unit cells in several steps, so that the volume content of the particles reached 50 %.

The 3D multi-element unit cells can be further generated by placing nuclei of the second phases, and simulating the evolution of microstructures and the growth of nuclei according to some growth laws (Romanova *et al.*, 2005).

Zohdi *et al.* (Zohdi *et al.*, 2001) and Zohdi and Wriggers (Zohdi and Wriggers, 1999, 2001a,b) carried out finite element simulations of complex microstructures, using the domain decomposition approach. The subdomains contained from 2 up to 64 particles. Zohdi and colleagues demonstrated that a subdomain with 20 particles is large enough to calculate the effective response which is independent of the particle number, and a mesh density of 2200–3000 degrees of freedom for the vector-valued balance of momentum per particle delivers (macroscopically) mesh independent results. The responses calculated for the subdomains with 16, 32 and 64 particles differed from one another by less than 1 %.

In many cases, complex, multiscale microstructures of materials can not be analyzed in the framework of single unit cells. In these cases, *hierarchical unit cell models* or combined multiscale models of materials are used.

Geni and Kikuchi (Geni and Kikuchi, 1998) and Kikuchi and Geni (Kikuchi and Geni, 1998) developed a two-level model of the deformation and damage in Al/SiC alloys, which includes an axisymmetric (cylindrical) unit cell model with an elliptical particle (lower level), and a box-shaped 'super element' (i.e. a model, consisting of many unit cells with different particle volume fractions and shapes). The 'super element', consisting of many axisymmetric unit cells, allows both the nonregularity of the material structure and 3D effects to be taken into account. The authors studied the effects of shapes, volume content, interaction between particles and their spatial distribution on the damage formation and strength of the materials, and derived the stress–strain relationships for alloys with different particle aspect ratios, volume fractions, and uniform and nonuniform particle distributions.

In several works, unit cell models have been combined with other numerical or analytical approaches to model the behavior of materials with regular microstructure on only one scale level and without any periodicity of the microstructure on the other levels. Böhm *et al.* (Böhm *et al.*, 1993), Böhm and Rammerstorfer (Böhm and Rammerstorfer, 1993), Plankensteiner *et al.* (Plankensteiner *et al.*, 1996, 1998) and other members of their group developed several very sophisticated hierarchical models of metal matrix composites and steels. In order to study the overall response and mechanisms of local failure of high speed steels with netlike microstructures, they used the hierarchical approach, which included a discrete microstructure model, constructed on the basis of the image analysis of micrographs of the steels and the statistical averaging of properties at mesolevel, and the transformation field approach or the incremental Mori–Tanaka approach at the microscale. The authors studied the effect of progressive carbide cleavage on the stress–strain curve, and showed that the regions of high particle density are 'more highly loaded than regions with low particle volume fraction'.

Plankensteiner *et al.* (Plankensteiner *et al.*, 1996) developed the so-called 'micro–meso–macro model' of high speed steels (HSSs) with layered microstructures. In the framework of this model, each carbide string was treated as a particle reinforced matrix–inclusion composite with the use of statistical averaging techniques (multiparticle effective field method). At the mesolevel, HSS was modeled as a laminated composite. With this model, Plankensteiner and colleagues analyzed the mechanisms of damage and stress distribution in the steels.

A schema of a hierarchical model of tool steel with a layered arrangement of primary carbides is given in Figure 4.19: carbide strings are modeled as the homogeneous layers with properties of carbide rich and carbide free materials, while the material inside the strings is considered as a statistically homogeneous particle reinforced material.

Mishnaevsky Jr *et al.* (Mishnaevsky Jr *et al.*, 1999a) presented a two-level model of the damage propagation in Al/Si cast alloys. The stress–strain curves of the composite

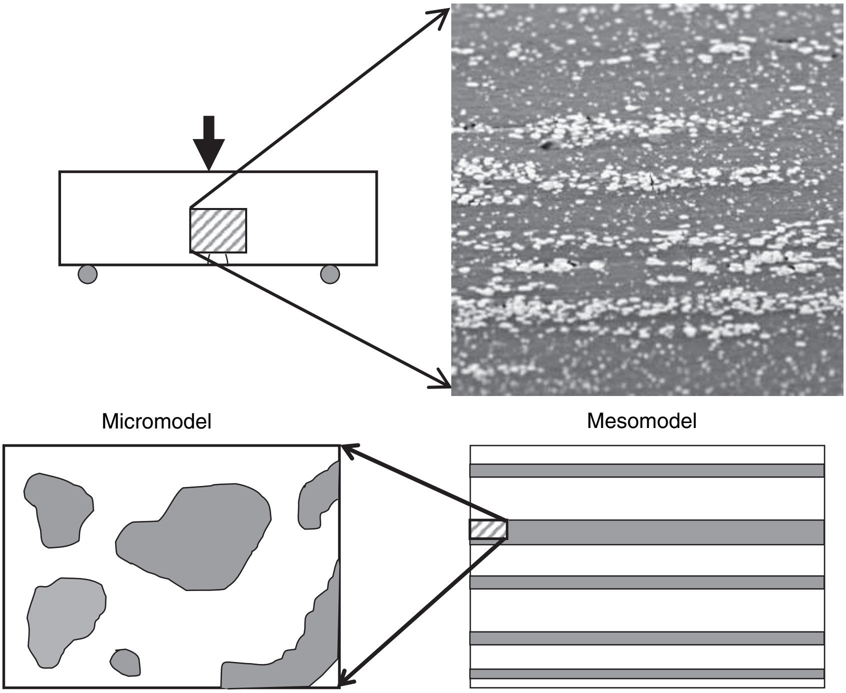

Figure 4.19 *An example of the hierarchical model of a material (after Plankensteiner* et al.*, 1996, 1998). The microstructure of a high speed steel with carbide strings is modeled as a layered material at the mesolevel and as a statistically homogeneous two-phase material inside the strings.*

with damageable Si inclusions were determined from the embedded unit cell analysis of the deformation and damage in Al/SiC cast alloys. Then, the obtained stress–strain curves were assigned to each finite element in the macromodel of a tensile specimen. Using this hierarchical model, the damage initiation and evolution, caused by the cleavage of Si particles, was simulated.

Summarizing, one may state that the unit cell approach, which was initially developed for the analysis of strictly periodic microstructures, is steadily expanded and has been generalized to deal with less regular, heterogeneous and therefore more realistic microstructures. This generalization is realized by introducing multi-element (multiparticle and multifiber), embedded, self-consistent, hierarchical unit cells. Therefore, the unit cell method is approaching the discrete microstructure simulations, with a view to the analysis of real and generic microstructures of materials.

4.4.2 How to incorporate real microstructures of materials into numerical models

The problem of the incorporation of information about microstructures into numerical models of materials is one of the challenges of computational mesomechanics of materials.

Let us look at the different methods of incorporating the microstructural information into computational models of materials.

4.4.2.1 Microgeometry-based mesh design

A finite element model of a material microstructure is designed in such a way that the element boundaries coincide with the phase boundaries. Figure 4.20 shows the microstructure-based mesh generation from a digitized image of a microstructure. The disadvantage of this method is that it can be rather difficult to align the element boundaries along complex fractal phase boundaries and interfaces, and to fill complex, interpenetrating phases with simple-shaped finite elements. However, this approach is straightforward and has been widely used to model real and generic microstructures of materials.

Ljungberg *et al*. (Ljungberg *et al*., 1986) obtained various structures of WC/Co hard alloys from micrographs, idealized them and produced 2D FE meshes from these structures. Then, Ljungberg and colleagues analyzed the growth of the plastic zone in front of a crack. To model the grain–grain interfaces, the authors used so-called 'nodal-tie dislocation elements'. It was shown that the plastic zone size in front of the crack is much larger than the single mean free path in the binder phase.

Fischmeister *et al*. (Fischmeister *et al*., 1988) studied plastic deformation of the binder in front of a crack in WC/Co hard metals with the use of an area microstructure model, embedded in a homogeneous surrounding. The authors have shown that ligaments between carbides fail by nucleation and growth of pores at the points where the crack from carbides enters the ligament. Tack (Tack, 1995) simulated the deformation of coarse two-phase materials (steels) with the use of the FE code FINEL. The areas with real structures were embedded in the coarsely meshed homogeneous surrounding. The local refinement of the FE mesh in the vicinity of hard inclusions was carried out. The effect of relationships between mechanical properties of inclusions and the matrix on the local stress concentration, and deformation in the real structure was studied.

Broeckmann (Broeckmann, 1994), Gross-Weege *et al*. (Gross-Weege *et al*., 1996) and Berns *et al*. (Berns *et al*., 1998) studied particle cracking and damage evolution in front of a large crack in ledeburitic steels. The effects of the inclusion distribution and local stress triaxiality on the stress state and fracture of these steels were investigated. The authors took into account the decohesion between carbides and the matrix, which occurs if the stresses normal to the interface reach a critical value.

One of the most efficient (and widely used) programs for the automatic microstructure-based meshing and microstructural analysis of materials is the C++-based, object-oriented FEM software OOF ('object-oriented finite element analysis'), developed by

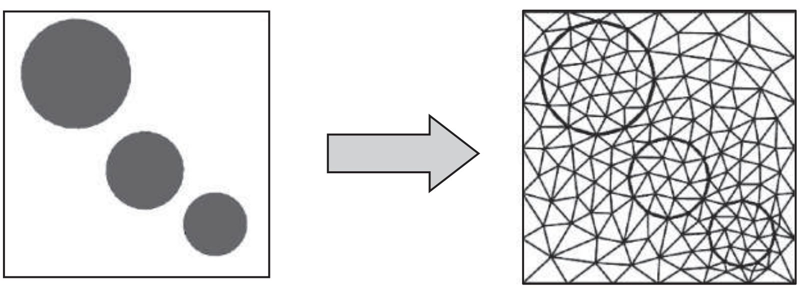

Figure 4.20 *Microstructure-based FE mesh design: from digitized micrographs to the FE mesh. Edges of FEs correspond to interfaces in the material.*

a group of scientists at NIST (USA) (Carter *et al*., 1997; Garcia *et al*., 2004). In fact, the software package includes several programs: PPM2OOF (which reads image files in the PPM format and creates automatically a FE mesh for OOF on the basis of a microstructure image), OOF solver (which calculates stress and strain distribution in the material, a recent version also includes the damage; Cannillo *et al*., 2002) and OOF2ABAQUS (which converts the geometrical information of the data files created by PPM2OOF or OOF into input files for ABAQUS). Recently, the new version of OOF (OOF2) was made available on the Website of the group. OOF2 contains a new set of C++ classes for finite elements and material properties, is more flexible and easily expandable, incorporates nonlinear solver and is scriptable in Python.

While the PPM2OOF software produces the microstructure-based FE models for the OOF solver, there exist several other programs which generate FE models from microstructural images directly to the commercial FE programs (e.g. ABAQUS).

Mishnaevsky Jr *et al*. (Mishnaevsky Jr *et al*., 2003a, 2004a) presented a program of automatic microstructure-based mesh generation, and employed the program to simulate the crack propagation in artificial microstructures of tool steels. The program reads the pgm image files of real or artificial microstructures, and produces a command file for the Pre-Processing FE software MSC/Patran, which generates the microstructural FE model. Using this technique, Mishnaevsky Jr and colleagues tested a series of generic artificial microstructures, and compared different (netlike, layered, clustered) arrangements of primary carbides in tool steels with a view to their effect on the fracture toughness of the steels.

In order to incorporate a quantitative description of real complex 3D microstructures into micromechanical models of materials, Shan and Gokhale (Shan and Gokhale, 2001) employed the *surface rendering approach*. Using serial sectioning, they generated a 3D microstructural image, which was then embedded into a FE model. The coordinates of the points on the surfaces of all the micropores from the images of sections were used as input to recreate the 3D geometry of pores in the pre-processor I-DEAS. Shan and Gokhale used this method to simulate the growth of voids in Al alloys.

Chawla *et al*. (Chawla *et al*., 2006) developed a method for the reconstruction of 3D real microstructures of materials from sectional sectioning. The 3D microstructures were reconstructed using the vectorial format software SurfDriver, and meshed using 10-node modified quadratic tetrahedral elements, with subsequent mesh refinement. Chawla and colleagues compared the 3D real microstructure models with 3D multiparticle unit cells with spherical and ellipsoidal particles, and analytical (Hashin–Shtrikman and Halpin–Tsai) estimations, and demonstrated that the 3D real microstructure models give the most accurate results compared with experiments.

4.4.2.2 Voronoi cell finite element method

Ghosh and co-workers (Ghosh *et al*., 1995; Lee *et al*., 1999) developed a very sophisticated and efficient approach to the modeling of deformation and damage initiation in MMCs, called the Voronoi cell finite element method (VCFEM). In this method, FE meshes are created by Dirichlet tessellation of real microstructures of material. Each polygon formed by such tessellation (i.e. 'Voronoi cell') contains one inclusion at most and is used as a FE. Figure 4.21 shows the Dirichlet tessellation of a microstructure and the subsequent use of each polygon as a FE. Further, Ghosh and co-workers developed a

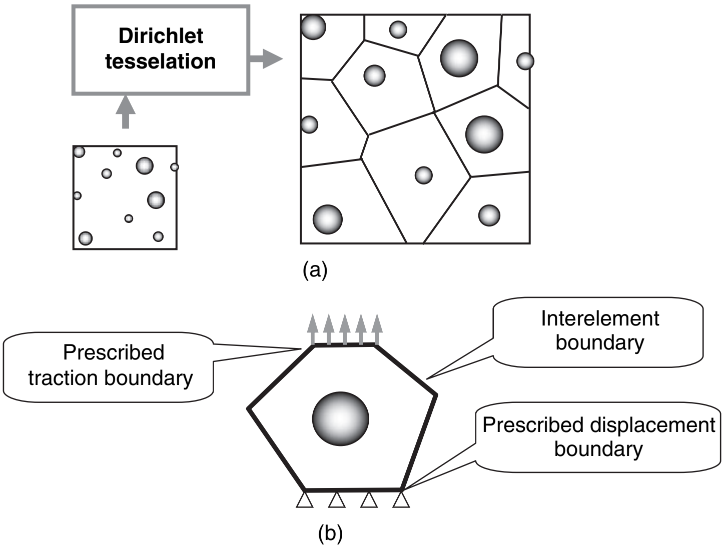

Figure 4.21 *Voronoi cell finite element method. A microstructure is divided into (a) Voronoi polygons, which are then used as (b) hybrid FEs (after Moorthy and Ghosh, 1998).*

'hierarchical multiple scale' model, which combines VCFEM (in nonperiodic microstructure subdomains) with asymptotic homogenization (in the periodic microstructure areas).

4.4.2.3 Pixel- and voxel-based mesh generation

A microstructural FE model of a composite is generated by assigning the properties of composite phases to the FEs in a regular FE mesh, consisting of squared or cubic FEs. This approach allows direct introduction of real microstructure images into FE models: taking each pixel of a digitized micrograph of a microstructure as a FE, one can transform an image of microstructure directly into a FE model. This approach has often been used with digital image based (DIB) microstructure reconstruction.

The DIB modeling technique was developed by Hollister and Kikuchi (Hollister and Kikuchi, 1994) to include the effects of microstructural morphology of bone in the FE simulations of the mechanical behavior of bones. Tareda *et al*. (Tareda *et al*., 1997) have used the DIB method together with the FEM-based asymptotic homogenization method to simulate the overall mechanical behavior of a composite, as dependent on the geometry of the microstructure and properties of the components. Tareda and colleagues have shown that the actual stress–strain curve for the unit cell model obtained with the use of DIB (and reflecting a real microstructure) is quite different from that obtained in an idealized unit cell model (elastic response more compliant, different trend of the strain hardening, etc.).

Garboczi and Day (Garboczi and Day, 1995) developed an algorithm and a model to incorporate the microstructural information into FE models using a pixel-based approach, and to determine the effective linear elastic properties of random, multiphase materials. The algorithm treats each pixel of the digital image of microstructure as a linear FE.

The authors investigated the effective Poisson's ratio of two-phase random isotropic composites numerically and compared the results with the effective medium theory estimations.

Iung *et al*. (Iung *et al*., 1996) studied the strain heterogeneity in two-phase materials (Ti alloys, dual-phase steels) on the basis of a developed FORTRAN program which automatically generates 2D FE meshes (to be used by the ABAQUS code) representing the image of a real microstructure. The mesh is generated 'in an iterative way by superimposing on the boundaries square grid of growing size', and is refined automatically at the interfaces.

Telaeche Reparaz *et al*. (Telaeche Reparaz *et al*., 1997) used their own Verborde and Digit codes to generate FE models of real structures of duplex (ferrite and austenite) steels for ABAQUS on the basis of the image analysis of micrographs. Square elements in the FE mesh were automatically associated with the corresponding materials. The authors obtained stress–strain curves of two-phase steels, and compared them with the stress–strain curves of the components.

Using the pixel/voxel based meshing, Kim and Swan (Kim and Swan, 2003a,b) developed and verified a new automated meshing technique that 'starts from a hierarchical quad-tree (in 2D) or oc-tree (in 3D) mesh of pixel or voxel elements', and then successive element splitting and nodal shifting are carried out in order to create mesh, which accurately reflects the microgeometry of the cell. The method was applied to the generation of multi-element unit cells, and verified.

A disadvantage of the simple versions of the pixel- or voxel-based approaches to the model generation is that the smooth interfaces, observed in real microstructures, are transformed into ragged interfaces in the pixel- and voxel-based models. An example of the representation of an ideal geometric figure using the voxel based method is given in Figure 4.22. One can see the ragged interface between the spherical particle and the matrix, which is not available in the input microstructure. However, in the later versions of the method, this problem is solved (e.g. by adaptive remeshing).

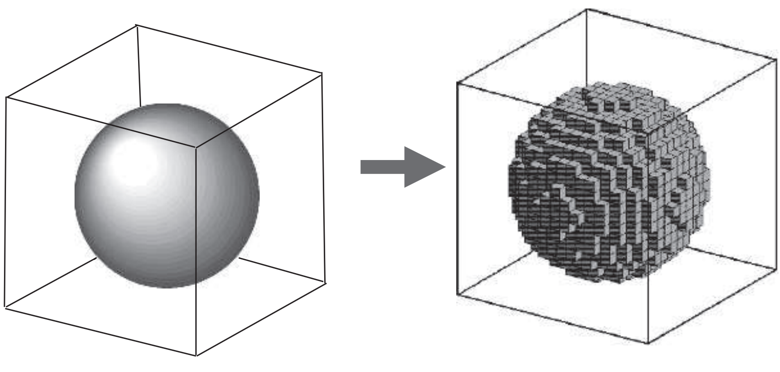

Figure 4.22 *Example of the voxel-based representation of a microstructure: ragged phase boundaries.*

4.4.2.4 Multiphase finite element method

The main idea of the multiphase finite element method is that the phase properties are assigned to individual integration points in the element independently of the phase properties assigned to other points in the element (cf. Figure 4.23). Interfaces in the material can run through the FEs in the mesh. Contrary to the microgeometry-based finite element mesh design, a FE mesh in this case is independent of the phase structure of the material, and one can use relatively simple FE meshes in order to simulate the deformation in a complex microstructure. The disadvantage of the multiphase finite element method is that it does not allow fine interface effects to be taken into account. One should note that this limitation can be even useful and could help to reflect better the local material properties in some specific cases (e.g. WC/Co hard metals, where there is no sharp interface, but a rather smooth transition from pure WC through solid solutions with different concentrations to practically pure Co is observed).

Wulf (Wulf, 1985) and Lippmann *et al.* (Lippmann *et al.*, 1996) simulated crack initiation and propagation in real structures of multiphase materials (Al-SiC composites, and AlSi cast alloy, respectively) with the use of multiphase finite elements and element elimination techniques. Wulf compared the results of the simulations with experiments, and demonstrated that the numerical and experimental results are in very good agreement.

Mishnaevsky Jr *et al.* (Mishnaevsky Jr *et al.*, 2004a) carried out micromechanical simulations of the crack growth in tool steels, using multiphase and single phase FEs. In the second case, the microstructural meshes were produced in such a way that the element boundaries were placed along the interfaces. It was demonstrated that the simulations with these methods yield very close results: a similar crack path and force–displacement curve of the model were obtained in the comparison case.

Lippmann *et al.* (Lippmann *et al.*, 1997) and Mishnaevsky Jr *et al.* (Mishnaevsky Jr *et al.*, 1999a) simulated the deformation of compact tension specimens from AlSi cast alloys, taking into account the 3D real microstructures of the alloys. In order to reconstruct 3D real microstructures of the material, serial section images of a cubic cut-out of the samples were produced, digitized and transformed into a 3D model of the

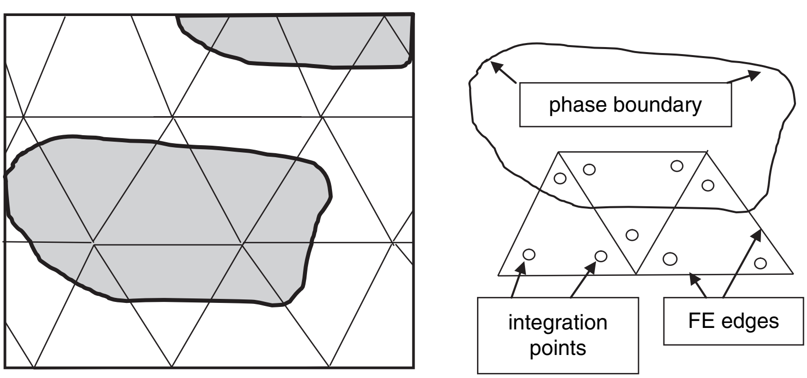

Figure 4.23 *Multiphase finite elements. The matrix–inclusion interface may run across FEs, while integration points of one and the same element can be assigned to different phases.*

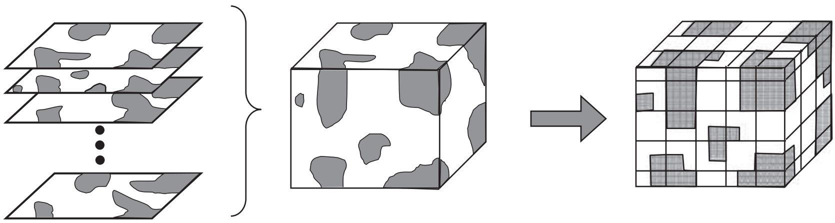

Figure 4.24 *3D reconstruction of microstructures of particle reinforced composites from serial sections, and the generation of a microstructural model in the framework of the multiphase finite element method (schema) (after Mishnaevsky Jr* et al.*, 1999a).*

composite. Figure 4.24 shows the schema of the reconstruction of a 3D multiphase FE model of a composite from serial sectioning images and the generation of the microstructural model of the material using the multiphase FE method. The 3D FE simulations were verified by Mishnaevsky Jr and colleagues by comparison with experimental results (strain distribution in the small area near the specimen notch, observed experimentally).

In the micromechanical simulations carried out by Zohdi *et al.* (Zohdi *et al.*, 2001) and Zohdi and Wriggers (Zohdi and Wriggers, 1999, 2001a,b), microstructures of the material were included in the models on the basis of the Gauss point method.

Approaches based on other discretization methods and solvers and used in micro- and mesomechanical analysis, include boundary elements (Achenbach and Zhu, 1989), discrete Fourier transforms and lattice models. In some of these methods, the microstructural information can be incorporated into numerical models more simply or more efficiently than in the framework of the FEM.

4.4.2.5 Lattice models

Ostoja-Starzewski (Ostoja-Starzewski, 2002) discussed the potential of lattice or spring network models for micromechanical simulations, and demonstrated that spring network models are an attractive alternative to the micromechanical finite element analyses. He analyzed the mechanical behavior of composites with different shapes of inclusions and ratios of the matrix/inclusion strengths (in planar case), using the spring network method. The inclusions were modeled as single pixels or as finite regions, which made it possible to take into account the anisotropy. As advantages of this method over the FEM, the author cites the lack of need of remeshing and constructing of a stiffness matrix, and the simplicity of the assignment of local material constants to the springs in the mesh.

4.4.2.6 Fast Fourier transforms

Moulinec and Suquet (Moulinec and Suquet, 1998) developed an iterative numerical method of analysis of effective properties of composites, based on fast Fourier transforms. By using the exact expression of the Green function for an elastic homogeneous comparison material, the problem is reduced to an integral equation which is solved iteratively. According to the authors, this method provides an alternative to the FEM, and is easy to parallelize. The microstructures of materials are introduced into the model using digital images of real microstructures. The rate of convergence of this method depends on the contrast of properties between phases, and becomes slow for composites with high contrast (e.g. materials with voids or rigid inclusions). To overcome the convergence problem, Michel *et al*., (Michel *et al*., 1999) extended the method to composites with high contrast of properties, using the numerical scheme for the computing response of composites by grid refinement suggested by Eyre and Milton (Eyre and Milton, 1999).

The incorporation of discrete microstructures of materials into numerical models opens the possibility of numerical testing of different discrete, real and generic microstructures of materials. The numerical testing of microstructures can serve as a basic tool for the optimization of materials, combined either with step-by-step, trial-and-error optimization procedures or a statistical genetic algorithm, as proposed by Zohdi (Zohdi, 2003).

References

Aboudi, J. (1989). Micromechanical analysis of composites by the method of cells, *Applied Mechanics Reviews*, **42**, 193–221.

Aboudi, J. (1999). *Mechanics of Composite Materials*, Elsevier, Amsterdam.

Aboudi, J. and Pindera, M.-J. (1992). Micromechanics of metal matrix composites using the generalized method of cells model (GMC), User's Guide, Report, NASA CR 190756.

Aboudi, J., Pindera, M.-J. and Arnold, S. M. (1999). Higher-order theory for functionally graded materials, *Composites: Part B (Engineering)*, **30** (8), 777–832.

Aboudi, J., Pindera, M.-J. and Arnold, S. M. (2001). Linear thermoelastic higher-order theory for periodic multiphase materials, *Journal of Applied Mechanics*, **68**, 697–707.

Aboudi, J., Pindera, M.-J and Arnold, S. M. (2003). Higher-order theory for periodic multiphase materials with inelastic phases, *International Journal of Plasticity*, **19** (6), 805–847.

Achenbach, J. D. and Zhu, H. (1989). Effect of interfacial zone on mechanical behavior and failure of fiber-reinforced composites, *Journal of the Mechanics and Physics of Solids*, **37**, 381–393.

Aifantis, E. C. (1999). Strain gradient interpretation of size effects, *International Journal of Fracture*, **95**, 299–314.

Asaro, R. J. (1983a). Crystal plasticity, *Journal of Applied Mechanics*, **50**, 921–934.

Asaro, R. J. (1983b). Micromechanics of crystals and polycrystals, in: *Advances in Applied Mechanics*, Eds J. W. Hutchinson and T. Y. Wu, Academic Press, New York, Vol. 23, pp. 1–115.

Asaro, R. J. and Rice, J. R. (1977). Strain localization in ductile single crystals, *Journal of the Mechanics and Physics of Solids*, **37** (25), 309–338.

Axelsen, M. S. (1995). Quantitative description of morphology and microdamages of composite materials, PhD Thesis, Aalborg University.

Axelsen, M. S. and Pyrz, R. (1995). Microstructural influence on the fracture toughness in transversely loaded unidirectional composites, *Proceedings of the 10th International Conference on Composite Materials*, pp. 471–478.

Bao, G. (1992). A micromechanical model for damage in metal matrix composites, in: *Damage Mechanics and Localization*, Eds J. H. Ju and K. C. Valanis, ASME, New York, pp. 1–12.

Belytschko, T., Fish J. and Bayliss, A. (1990). The spectral overlay on the finite element solutions with high gradients, *Computer Methods in Applied Mechanics and Engineering*, **81**, 71–89.

Bensoussan, A., Lions, J. L. and Papanicolaou, G. (1978). Asymptotic analysis for periodic structures, in: *Studies in Mathematics and its Applications*, Vol. 5, North-Holland, Amsterdam.

Benveniste, Y. (1987). A new approach to the application of Mori-Tanaka's theory in composite materials, *Mechanics of Materials*, **6** (2), 147–157.

Beran, M. (1965). Use of a variational approach to determine bounds for the effective permittivity of a random medium, *Nuovo Cimento*, **38**, 771–782.

Beran, M. and Molyneux, J. (1966). Use of classical variational principles to determine bounds for the effective bulk modulus in heterogeneous medium, *Quarterly of Applied Mathematics*, **24**, 107–118.

Berns, H., Melander, A., Weichert, D., Asnafi, N., Broeckmann, C. and Gross-Weege, A. (1998). A new material for cold forging tool, *Composites Materials Science*, **11** (142), 166–180.

Berryman, J. G. and Milton, G. W. (1988). Microgeometry of random composites and porous media, *Journal of Physics D: Applied Physics*, **21**, 87–94.

Bishop, J. F. S. and Hill, R. (1951). A theory of the plastic distortion of a polycrystalline aggregate under combined stresses, *Philosophical Magazine*, **42**, 414–427.

Böhm, H. J. (1998). *A Short Introduction to Basic Aspects of Continuum Micromechanics*, TU Wien, Vienna.

Böhm, H. J. and Han W. (2001). Comparisons between three-dimensional and two-dimensional multi-particle unit cell models for particle reinforced MMCs, *Modeling and Simulation in Materials Science and Engineering*, **9**, 47–65.

Böhm, H. J. and Rammerstorfer, F. G. (1993). Micromechanical models for investigating fibre arrangements in MMCs, in: *Proceedings of the International Seminar Micromechanics of Materials (MECAMAT)*, Editions Eyrolles, Paris, pp. 383–394.

Böhm, H. J., Rammerstorfer, F. G. and Weisenbek, E. (1993). Some simple models for micromechanical investigations of fiber arrangement effects in MMCs, *Computational Materials Science*, **1**, 177–194.

Böhm, H. J., Eckschlager A. and Han W. (2002). Multi-inclusion unit cell models for metal matrix composites with randomly oriented discontinuous reinforcements, *Computational Materials Science*, **25**, 42–53.

Bornert, M., Bretheau, T. and Gilormini, P. (2001). Homogeneisation en mecanique des materiaux. 1. Materiaux aleatoires et milieux periodiques, HERMES Science, Paris.

Boucher, S. (1974). On the effective moduli of isotropic two-phase elastic composites, *Journal of Composite Materials*, **8**, 82–89.

Broeckmann, C. (1994). Bruch karbidreicher Stähle – Experiment und FEM-Simulation unter Berücksichtigung des Gefüges, Dissertation, Ruhr-Universitaet Bochum.

Budiansky, B. (1965). On the elastic moduli of some heterogeneous materials, *Journal of the Mechanics and Physics of Solids*, **13**, 223–227.

Buryachenko, V. (2001). Multiparticle effective field and related methods in micromechanics of composite materials, *Applied Mechanics Reviews*, **54** (1), 1–47.

Cannillo, V., Manfredini, T., Corradi, A. and Carter, W. C. (2002). Numerical models of the effect of heterogeneity on the behavior of graded materials. *Key Engineering Materials*, **206–213**, 2163–2166.

Chaboche, J. L., Girard, R. and Schaff, A. (1997). Numerical analysis of composite systems by using interphase/interface models, *Computational Mechanics*, **20** (1–2), 3–11.

Chaboche, J. L., Kruch, S., Maire, J. F. and Pottier, J. (2001). Towards a micromechanics based inelastic and damage modeling of composites, *International Journal of Plasticity*, **17**, 411–439.

Chawla N., Sidhu, R. S. and Ganesh, V. V. (2006). Three-dimensional visualization and microstructure-based modeling of deformation in particle-reinforced composites, *Acta Materialia*, **54** (6), 1541–1548.

Christensen, R. M. (1979). *Mechanics of Composite Materials*, Wiley-Interscience, New York.

Christensen, R. M. and Lo, K. H. (1979). Solution for effective shear properties in three-phase sphere and cylinder models, *Journal of the Mechanics and Physics of Solids*, **27**, 315–330.

Cox, H. L. (1952). The elasticity and strength of paper and other fibrous materials, *British Journal of Applied Physics*, **3**, 73–79.

Dong, M. and Schmauder, S. (1995). FE modelling of continuous fiber and particle reinforced composites by self-consistent embedded cell models, in: *Computational Methods in Micromechanics*, Eds S. Ghosh and M. Ostoja- Starzewski, ASME, New York, pp. 81–86.

Dong, M. and Schmauder, S. (1996). Transverse mechanical behaviour of fiber reinforced composites – FE modelling with embedded cell models, *Computational Materials Science*, **5**, 53–66.

Drugan, W. J. and Willis, J. R. (1966). A micromechanics-based nonlocal constitutive equation and estimates of representative volume element size for elastic composites, *Journal of the Mechanics and Physics of Solids*, **44** (4), 497–524.

Dvorak, G. (1992). Transformation fields analysis of inelastic composite materials, *Proceedings of the Royal Society of London, Series A*, **437**, 311–327.

Dvorak, G. J., Bahei-El-Din, Y. A. and Wafa, A. M. (1994). The modeling of inelastic composite materials with the transformation field analysis, *Modelling and Simulation in Materials Science and Engineering*, **2** (3A), 571–586.

Eckschlager, A., Böhm, H. J. and Han, W. (2002). A Unit cell model for brittle fracture of particles embedded in a ductile matrix, *Computational Materials Science*, **25**, 85–91.

Eshelby, J. (1957). The determination of elastic field of an ellipsoidal inclusion, and related problems, *Proceedings of the Royal Society of London, Series A*, **421**, 379–396.

Estrin, Y. (1998). Dislocation theory based constitutive modelling: foundations and applications, *Journal of Material Processing Technology*, **80–81**, 33–39.

Estrin, Y. and Mecking, H. (1984) A unified phenomenological description of work-hardening and creep based on one-parameter models, *Acta Metallurgica et Materialia*, **32**, 57–70.

Eyre, D. J. and Milton, G. W. (1999). A fast numerical scheme for computing the response of composites using grid refinement, *European Journal of Applied Physics*, **6**, 41–47.

Fang, D., Qi, H. and Tu, S. (1996). Elastic and plastic properties of metal-matrix composites: geometrical effects of particles, *Computational Materials Science*, **6**, 303–309.

Feyel, F. and Chaboche, J. L. (2000). FE2 multiscale approach for modelling the elastoviscoplastic behaviour of long fibre SiC/Ti composite materials, *Computer Methods in Applied Mechanics and Engineering*, **183** (3–4), 309–330.

Fischmeister, H. F., Schmauder, S. and Sigl, L. (1988). Finite element modelling of crack propagation in WC-Co hard metals, *Materials Science and Engineering*, **A105/106**, 305–311.

Fish, J. (1992) The s-version of the finite element method, *Computers and Structures*, **43**(3), 539–547.

Fish, J. and Yu, Q. (2001). Two-scale damage modeling of brittle composites, *Composites Science and Technology*, **61**, 2215–2222.

Fish, J., Belsky, V., Pandheeradi M. (1996). Composite grid method for hybrid systems, *Computer Methods in Applied Mechanics and Engineering*, **135** (3–4), 307–325.

Fish, J., Suvorov, A. and Belsky, V. (1997a). Hierarchical composite grid method for global-local analysis of laminated composite shells, *Applied Numerical Mathematics*, **23** (2), 241–258(18).

Fish, J., Shek, K., Pandheeradi, M. and Shephard, M. S. (1997b). Computational plasticity for composite structures based on mathematical homogenization: theory and practice, *Computer Methods in Applied Mechanics and Engineering*, **148**, 53–73.

Fleck, N. A. and Hutchinson, J. W. (1997). Strain gradient plasticity, *Advances in Applied Mechanics*, **33**, 295–361.

Fleck, N. A., Muller, G. M., Ashby, M. F. and Hutchinson, J. W. (1994). Strain gradient plasticity: theory and experiment. *Acta Metallurgica et Materialia*, **42** (2), 475–487.

Gao, H., Huang, Y., Nix, W. D. and Hutchinson, J. W. (1999). Mechanism-based strain gradient plasticity - I. Theory, Journal of the Mechanics and Physics of Solids, 47(6), pp. 1239–1263.

Garboszi, E. J. and Day, A. R. (1995). An algorithm for computing the effective linear elastic properties of heterogeneous materials: 3-D results for composites with equal phase Poisson ratios, *Journal of the Mechanics and Physics of Solids*, **43**, 1349–1362.

García, R. E., Reid, A. C. E., Langer, S. A. and Carter, W. C. (2004). Microstructural modeling of multifunctional material properties: the OOF project, in *Continuum Scale Simulation of Engineering Materials: Fundamentals – Microstructures – Process Applications*, Eds D Raabe, F. Roters, F. Barlat and L.-Q. Chen, John Wiley & Sons, Ltd, Weinheim, pp. 573–585.

Geni, M. and Kikuchi, M. (1998). Damage analysis of aluminum matrix composite considering non-uniform distribution of SiC particles, *Acta Materialia*, **46** (9), 3125–3133.

Ghosh, S., Lee K. and Moorthy, S. (1995). Multiple analysis of heterogeneous elastic structures using homogenization theory and Voronoi cell finite element method, *International Journal of Solids and Structures*, **32** (1), 27–62.

Gross-Weege, A., Weichert, D. and Broeckmann, C. (1996). Finite element simulation of crack initiation in hard two- phase materials, *Computational Materials Science*, **5**, 126–142.

Gusev, A. A. (1997). Representative volume element size for elastic composites: a numerical study, *Journal of the Mechanics and Physics of Solids*, **45** (9), 1449–1459.

Gusev, A., Hine, P. J. and Ward, I. M. (2000). Fiber packing and elastic properties of a transversely random unidirectional glass/epoxy composite, *Composites Science and Technology*, **60** (4), 535–541.

Haidar, K., Dubé, J. F. and Pijaudier-Cabot, G. (2003). Modelling crack propagation in concrete structures with a two scale approach, *International Journal of Numerical and Analytical Methods in Geomechanics*, **27** (13), 1187–1205.

Han, W. and Böhm, H. J. (2001). The effects of three-dimensional multi-particle arrangements on the mechanical behavior and damage initiation of particle-reinforced MMCs, *Composites Science and Technology*, **61**, 1581–1590.

Hashin, Z. (1962). The elastic moduli of heterogeneous materials, *Journal of Applied Mechanics*, **29**, 143–150.

Hashin, Z. (1983). Analysis of composite materials, a survey, *Journal of Applied Mechanics*, **50**, 481–505.

Hashin, Z. and Rosen, B. W. (1964). The elastic moduli of fibre-reinforced materials, *Journal of Applied Mechanics*, **31**, 223–232.

Hashin, Z. and Shtrikman, S (1962a). On some variational principles in anisotropic and nonhomogeneous elasticity, *Journal of the Mechanics and Physics of Solids*, **10**, 335–342.

Hashin, Z. and Shtrikman, S. (1962b). A variational approach to the theory of the elastic behaviour of polycrystals, *Journal of the Mechanics and Physics of Solids*, **10**, 343–352.

Hashin, Z. and Shtrikman, S. (1963). A variational approach to the theory of the elastic behaviour of multiphase materials, *Journal of the Mechanics and Physics of Solids*, **11**, 127–140.

Hershey, A.V. (1954). The elasticity of an isotropic aggregate of anisotropic cubic crystals, *Journal of Applied Mechanics*, **21**, 236–241.

Hill, R. (1964). Theory of mechanical properties of fibre-strengthened materials: I. Elastic behaviour, *Journal of the Mechanics and Physics of Solids*, **12**, 199–212.

Hill, R. (1965). A self-consistent mechanics of composite materials, *Journal of the Mechanics and Physics of Solids*, **13**, 213–222.

Hine, P. J., Lusti, H. R. and Gusev, A. A. (2002). Numerical simulation of the effects of volume fraction, aspect ratio and fibre length distribution on the elastic and thermoelastic properties of short fibre composites, *Composites Science and Technology*, **62** (10–11), 1445–1453.

Hollister, S. J. and Kikuchi, N. (1994). Homogenization theory and digital imaging: a basis for studying the mechanics and design principles of bone tissue. *Biotechnology and Bioengineering*, **43** (7), 586–596.

Hori, M. and Nemat-Nasser, S. (1999). On two micromechanics theories for determining micro-macro relations in heterogeneous solids, *Mechanics of Materials*, **31**, 667–682.

Iung, I., Petitgand, H., Grange, M. and Lemaire, E. (1996). Mechanical behaviour of multiphase materials Numerical simulations and experimental comparisons, in: *Proceedings of IUTAM Symposium on Micromechanics of Plasticity and Damage in Multiphase Materials*, Kluwer, Dordrecht, pp. 99–106.

Jansson, S. (1992). Homogenized nonlinear constitutive properties and local stress concentrations for composites with periodic internal structure, *International Journal of Solids and Structures*, **29**, 2181–2200.

Kanaun, S. (1983). Elastic medium with random field of inhomogeneities, in: *Elastic Media with Microstructure*, Ed. I. A. Kunin, Springer, Berlin, Vol. 2, pp. 165–228.

Kelly, A. and Tyson, W. R. (1965). Tensile properties of fibre-reinforced metals: copper/tungsten and copper/molybdenum, *Journal of the Mechanics and Physics of Solids*, **13** (6), 329–338.

Kikuchi, M. and Geni, M. (1998). Evaluation of the interaction effects of SiC particles during damage process of MMCs, *Key Engineering Materials*, **145–149**, 895–900.

Kim, H. J. and Swan, C. C. (2003a). Voxel-based meshing and unit cell analysis of textile composites, *International Journal for Numerical Methods in Engineering*, **56** (7), 977–1006.

Kim, H. J. and Swan, C. C. (2003b). Algorithms for automated meshing and unit cell analysis of periodic composites with hierarchical tri-quadratic tetrahedral elements, *International Journal for Numerical Methods in Engineering*, **58**, 1683–1711.

Kocks, U. F. (1966). A statistical theory of flow stress and work hardening, *Philosophical Magazine*, **13**, 541–566.

Kocks, U. F. (1976). Laws for work-hardening and low temperature creep, *Journal of Engineering Materials Technology*, **98**, 76–85.

Kouznetsova, V. G. (2002). Computational homogenization for the multi-scale analysis of multi-phase materials, PhD Thesis, NIMR, Eindhoven.

Kröner, E. (1958). Berechnung der elastischen Konstanten des Vielkristalls aus der Konstanten des Einkristalls, *Zeitschrift für Physik*, **151**, 504–518.

Kuna, M. and Sun, D. -Q. (1996). Analyses of void growth and coalescence in cast iron by cell model. *Journal de Physique IV*, **6**, 113–122.

Kuna, M. and Sun, D. -Q. (1997). Three-dimensional cell model analyses of void growth in ductile materials, *International Journal of of Fracture*, **81**, 235–258.

Landis, C. M. and McMeeking, R. M. (1999). A shear-lag model for a broken fiber embedded in a composite with a ductile matrix, *Composites Science and Technology*, **59** (3), 447–457.

Lee, K., Moorthy, S. and Ghosh, S. (1999), Multiple scale computational model for damage in composite materials, *Computer Methods in Applied Mechanics and Engineering*, **172**, 175–201.

Lene, F. (1986). Damage constitutive relations for composite materials, *Engineering Fracture Mechanics*, **25**, 713–728.

Lessle, P., Dong, M. and Schmauder, S. (1999). Self-consistent matricity model to simulate the mechanical behaviour of interpenetrating microstructures, *Computational Materials Science*, **15**, 455–465.

Levin, V. (1976). Determination of thermoelastic constants of composite materials, *Transaction of the Soviet Academy of Sciences*, **6**, 137–145.

Lévesque, M. (2004). Modélisation du comportement mécanique de matériaux composites viscoélastiques non linéaires par une approche d'homogénéisation, Dr Thesis, ENSAM, Paris.

Li, S. G. (1999). On the unit cell for micromechanical analysis of fibre-reinforced composites, *Proceedings of the Royal Society of London, Series A*, **455**, 815–838.

Lippmann, N., Schmauder, S. and Gumbsch, P. (1996). Numerical and experimental study of early stages of the failure of AlSi-cast alloys, *Journal de Physique IV*, **5**, 123–131.

Lippmann, N., Steinkopff, Th., Schmauder, S. and Gumbsch, P. (1997). 3D-Finite-element-modelling of microstructures with the method of multiphase elements, *Computational Materials Science*, **9**, 28–35.

Ljungberg, A. -B., Chatfield, C., Hehenberger, M. and Sundström, B. (1986). Estimation of the plastic zone size associated with cracks in cemented carbides, in: *Proceedings of the 2nd International Conference of the Science of Hard Materials*, Adam Hilger Ltd, Rhodes, pp. 619–630.

Llorca, J., Needleman, A. and Suresh, S. (1991). An analysis of the effects of matrix void growth on deformation and ductility of metal-ceramic composites, *Acta Metallurgica et Materialia*, **39** (10), 2317–2335.

Luciano, R. and Willis, J. R. (2000). Bounds on non-local effective relations for random composites loaded by configuration-dependent body force, *Journal of the Mechanics and Physics of Solids*, **48**, 1827–1849.

Luciano, R. and Willis, J. R. (2001a). Non-local constitutive response of a random laminate subjected to configuration-dependent body force, *Journal of the Mechanics and Physics of Solids*, **49**, 431–444.

Luciano, R. and Willis, J. R. (2001b). Non-local effective relations for fibre-reinforced composites loaded by configuration-dependent body forces, *Journal of the Mechanics and Physics of Solids*, **49**, 2705–2717.

Mao, K. M. and Sun, C. T. (1991). A refined global-local finite element analysis method, *International Journal of Numerical Methods in Engineering*, **32** (1), 29–43.

Markov, K. Z. (1999). Elementary micromechanics of heterogeneous media heterogeneous media: modelling and simulation, Eds K. Z. Markov and L. Preziosi, Birkhauser, Boston, pp. 1–162.

McCoy, J. J. (1970). On the displacement field in an elastic medium with random variations in material properties, in: *Recent Advances in Engineering Sciences*, Ed. A. C. Eringen, Gordon and Breach, New York, Vol. 5, pp. 235–254.

McLaughlin, R. (1977). A study of the differential scheme for composite materials, *International Journal of Engineering Science*, **15**, 237–244.

Michel, J. C. (1993). A numerical study of the effects of particle cracking and particle debonding on matrix void growth in Al-SiC composites, in: *Proceedings of the International Seminar Micromechanics of Materials (MECAMAT)*, Editions Eurolles, Paris, pp. 395–405.

Michel, J. C., Moulinec, H. and Suquet, P. (1999). Effective properties of composite materials with periodic microstructure: a computational approach, *Computer Methods in Applied Mechanics and Engineering*, **172**, 109–143.

Milton, G. W. (1981). Bounds on the electromagnetic, elastic and other properties of two-component composites, *Physical Review Letters*, **46**, 542–545.

Milton, G. W. (2002). *The Theory of Composites*, Cambridge University Press, Cambridge.

Milton, G. W. and Phan-Thien, N. (1982). New bounds on effective elastic moduli of two-component materials, *Proceedings of the Royal Society of London, Series A*, **380**, 305–331.

Mindlin, R. D. (1964). Microstructure in linear elasticity, *Archive for Rational Mechanics and Analysis*, **16**, 51–78.

Mindlin, R. D. (1965). Second gradient of strain and surface tension in linear elasticity, *International Journal of Solids and Structures*, **1**, 417–438.

Mishnaevsky Jr, L. (2004a). Three-dimensional numerical testing of microstructures of particle reinforced composites, *Acta Materialia*, **52** (14), 4177–4188.

Mishnaevsky Jr, L. (2004b). Werkstoffoptimierung auf dem Mesoniveau, Report for the German Research Council (DFG), MPA Stuttgart.

Mishnaevsky Jr, L., Dong, M., Hoenle, S. and Schmauder, S. (1999a). Computational mesomechanics of particle-reinforced composites, *Computational Materials Science*, **16** (1–4), 133–143.

Mishnaevsky Jr, L., Lippmann, N. and Schmauder, S. (2001). Experimental-numerical analysis of mechanisms of damage initiation in tool steels, in: *Proceedings of the 10th International Conference on Fracture*, Honolulu, CD-ROM.

Mishnaevsky Jr, L., Lippmann, N. and Schmauder, S. (2003a). Computational modeling of crack propagation in real microstructures of steels and virtual testing of artificially designed materials, *International Journal of Fracture*, **120** (4), 581–600.

Mishnaevsky Jr., L., Lippmann, N. and Schmauder, S. (2003b). Micromechanisms and modelling of crack initiation and growth in tool steels: role of primary carbides, *International Journal of Materials Research*, **94** (6), 676–681.

Mishnaevsky Jr, L., Weber, U. and Schmauder, S. (2004a). Numerical analysis of the effect of microstructures of particle-reinforced metallic materials on the crack growth and fracture resistance, *International Journal of Fracture*, **125**, 33–50.

Moorthy, S. and Ghosh, S. (1998). A Voronoi cell finite element model for particle cracking in elastic-plastic composite materials, *Computer Methods in Applied Mechanics and Engineering*, **151**, 377–400.

Mori, T. and Tanaka, K. (1973). Average stress in matrix and average elastic energy of materials with misfitting inclusions, *Acta Metallurgica et Materialia*, **21**, 571–574.

Mote Jr, C. D. (1971). Global-local finite element, *International Journal of Numerical Methods in Engineering*, **3**, 565–574.

Moulinec, H. and Suquet, P. (1998). A numerical method for computing the overall response of nonlinear composites with complex microstructure, *Computer Methods in Applied Mechanics and Engineering*, **157**, 69–94.

Mozhev, V. V. and Garishin, O. K. (2005). Structural mechanics of particulate-filled elastomeric composites, *Uspehi Mechaniki*, **2**, 3–30.

Mozhev, V. V. and Kozhevnikova, L. L. (1996). Unit cell evolution in structurally damageable particulate-filled elastomeric composites under simple extension, *Journal of Adhesion*, **55**, 209–219.

Mozhev, V. V. and Kozhevnikova, L. L. (1997). Highly predictive structural cell for particulate polymeric composites, *Journal of Adhesion*, **62**, 169–186.

Mura, T. (1987). *Micromechanics of Defects in Solids*, Martinus Nghoff Publishers, Dordrecht.

Nairn, J. (1997). On the use of shear-lag methods for analysis of stress transfer in unidirectional composites, *Mechanics of Materials*, **26** (2), 63–80.

Nemat-Nasser, S. and Hori, M. (1993). *Micromechanics: Overall Properties of Heterogeneous Materials*, Elsevier, Amsterdam.

Noor, A. K. (1986). Global-local methodologies and their application to nonlinear analysis, *Finite Elements in Analysis and Design*, **2**, 333–346.

Norris, A. N. (1985). A differential scheme for the effective module of composites, *Mechanics of Materials*, **4** (1), 1–16.

Ostoja-Starzewski, M. (2002). Lattice models in micromechanics, *Applied Mechanics Reviews*, **55** (1), 35–60.

Paley, M. and Aboudi, J. (1992). Micromechanical analysis of composites by the generalized cells model, *Mechanics of Materials*, **14**, 127–139.

Plankensteiner, A. F., Böhm, H. J., Rammerstorfer, F. G. and Buryachenko, V. A. (1996). Hierarchical modelling of high speed steels as layer-structured particulate MMCs, *Journal de Physique IV*, **6**, 395–402.

Plankensteiner, A. F., Böhm, H. J., Rammerstorfer, F. G. and Pettermann H. E. (1998). Multiscale modelling of highly heterogeneous particulate MMCs, in: *Proceedings of the 2nd European Conference on Mechanics of Materials*, Otto von Guericke, Magdeburg, pp. 291–298.

Ponte Castañeda, P. (1991). The effective mechanical properties of nonlinear isotropic composites, *Journal of Mechanics and Physics of Solids*, **39** (1), 45–71.

Ponte Castañeda, P. (1992). Bounds and estimates for the properties of nonlinear heterogeneous systems, *Philosophical Transactions of the Royal Society of London, Series A*, **340** (1659), 531–567.

Ponte Castañeda, P. (1998). Three-point bounds and other estimates for strongly nonlinear composites, *Physical Review B*, **57**, 12077–12083.

Ponte Castañeda, P. and Suquet, P. (1998). Nonlinear composites, *Advances in Applied Mechanics*, **34**, 171–302.

Reuss, A. (1929). Berechnung der Fliessgrenze von Mischkristallen auf Grund der Plastizitätsbedingung für Einkristalle, *Zietschrift für Angewandte Mathematik und Mechanik (Journal of Applied Mathematics and Mechanics)*, **9**, 49–58.

Rintoul, M. D. and Torquato, S. (1997). Reconstruction of the structure of dispersions, *Journal of Colloid Interface Science*, **186**, 467–476.

Romanova, V. A., Soppa, E., Schmauder, S. and Balokhonov, R. R. (2005). Mesomechanical analysis of the elasto-plastic behavior of a 3D composite-structure under tension, *Computational Mechanics*, **36**, 475–483.

Roscoe, R. (1973). Isotropic composites with elastic or viscoelastic phases: general bounds for the moduli and solutions for special geometries. *Rheologica Acta*, **12**, 404–411.

Roters, F., Raabe, D. and Gottstein, G. (2000). Work hardening in heterogeneous alloys – a microstructural approach based on three internal state variables, *Acta Materialia*, **48** (17), 4181–4189.

Sachs, G. (1928). Zur Ableitung einer Fliessbedingung. *Zeitschrift der VDI*, **72**, 734–736.

Sanchez-Palencia, E. (1980). Non-homogeneous media and vibration theory, in: *Lecture Notes in Physics*, No. 127, Springer-Verlag, Berlin.

Schmauder, S. (2002). Computational mechanics, *Annual Review of Materials Research*, **32**, 437–465.

Seelig, Th. (2000). Mikromechanik und Homogenisierung, Kurzskript und Formellsammlung, Lecture Notes, TU Darmstadt.

Segurado, J., González, C. and LLorca, J. (2003). A numerical investigation of the effect of particle clustering on the mechanical properties of composites. *Acta Materialia*, **51**, 2355–2369.

Shan, Z. and Gokhale, A. M. (2001). Micromechanics of complex three-dimensional microstructures, *Acta Materialia*, **49** (11), 2001–2015.

Shen, Y. -L., Finot, M., Needleman, A. and Suresh, S. (1994). Effective elastic response of two-phase composites, *Acta Metallurgica et Materialia*, **42** (1), 77–97.

Shtremel, M. A. (1997). *Strength of Alloys. Part II. Deformation*, MISIS, Moscow.

Siegmund, T., Werner, E. and Fischer, F. D. (1993). Structure–property relations in duplex materials, *Computational Materials Science*, **1**, 234–240.

Silberschmidt, V. V. and Werner, E. A. (2001). Analyses of thermal stresses' evolution in ferritic-austenitic duples steels, in: *Proceedings of the 4th International Congress on Thermal Stresses*, Eds. Y.Tanigawa, R.B.Hetnarski and N.Noda, Osaka, Japan, pp. 327–330.

Søvik, O. P. (1996). Experimental and numerical investigation of void nucleation in AlMgSi alloy, *Journal de Physique*, **10** (C6), 1555–165.

Steglich, D. and Brocks, W. (1997). Micromechanical modelling of the behaviour of ductile materials including particles, *Computational Materials Science*, **9** (1), 7–17.

Suquet, P. (1987). Elements of homogenization for inelastic solid mechanics, in: *Homogenization Techniques for Composite Media. Lecture Notes in Physics No. 272*, Eds E. Sanchez-Palencia and A. Zaoui, Springer-Verlag, Berlin, pp. 193–278.

Suquet, P. (1997) (Ed.) *Continuum Micromechanics. CISM Lecture Notes No. 377*, Springer-Verlag, Berlin.

Tack, L. H. (1995). *Integration mikromechanischer Werkstoffmodelle in die Methode der finiten Elemente*, Verlag der GOM, Herzogenrath.

Takano, N., Uetsuji, Y., Kashiwagi, Y. and Zako, M. (1999). Hierarchical modelling of textile composite materials and structures by the homogenization method, *Modelling Simulations in Materials Science and Engineering*, **7**, 207–231.

Talbot, D. R. S. and Willis, J. R. (1985). Variational principles for inhomogeneous non-linear media, *IMA Journal of Applied Mathematics*, **35** (1), 39–54.

Talbot, D. R. S., and Willis, J. R. (1996). Three-point bounds for the overall properties of a nonlinear composite dielectric, *IMA Journal of Applied Mathematics*, **57** (1), 41–52.

Tareda, K., Miura, T. and Kikuchi, N. (1997). Digital image-based modeling applied to the homogenization analysis of composite materials. *Computational Mechanics*, **20**, 331–346.

Taylor, G. I. (1938). Plastic strain in metals, *Journal of Institute of Metals*, **62**, 307–328.

Telaeche Reparaz, M., Martinez-Esnaola, J. M. and Urcola, J. J. (1997). Numerical simulation of plane strain compression tests of a bimetallic composite, *Key Engineering Materials*, **127–131**, 1215–1222.

Torquato, S. (1998). Effective stiffness tensor of composite media: II. Applications to isotropic dispersions, *Journal of Mechanics and Physics of Solids*, **46**, 1411–1440.

Torquato, S. (2002a). *Random Heterogeneous Materials: Microstructure and Macroscopic Properties*, Springer-Verlag, New York.

Toupin, R. A. (1962). Elastic materials with couple stresses, *Arch. Ration. Mechanics Anal.*, **11**, 385–414.

Tvergaard, V. and Needleman, A. (1995). Effects of nonlocal damage in porous plastic solids, *International Journal of Solids and Structures*, **32**, 1063–1077.

Van der Giessen, E. and Needleman, A. (1995). Discrete dislocation plasticity: a simple planar model, *Modelling and Simulation in Materials Science and Engineering*, **3**, 689–735.

Voigt, W. (1889). Über die Beziehung zwischen den beiden Elastizitätskonstanten isotroper Körper, *Wiedmanns Annalen der Physik and Chemie*, **38**, 573–587.

Walpole, L. J. (1966). On bounds for the overall elastic moduli of inhomogeneous systems, *Journal of the Mechanics and Physics of Solids*, **14** (151–162), 289–301.

Walpole, L. J. (1969). On the overall elastic moduli of composite materials, *Journal of the Mechanics and Physics of Solids*, **17**, 235–251.

Wilkinson, D. S., Pompe, W. and Oeschner, M. (2001). Modelling of the mechanical behaviour of heterogeneous multiphase materials, *Progress in Materials Science*, **46**, 379–405.

Willis, J. R. (1977). Bounds and self consistent estimates for the overall moduli of anisotropic composites, *Journal of Mechanics and Physics of Solids*, **25**, 185–202.

Willis, J. R. (2001). Non-local micromechanical models, in: *Handbook of Materials Behaviour*, Ed. J. Lemaitre, Academic Press, New York, pp. 984–995.

Wu, T. T. (1966). The effect of inclusion shapes on the elastic moduli of a two-phase material, *International Journal of Solids and Structures*, **2**, 1–8.

Wulf, J. (1985). Neue Finite-Elemente-Methode zur Simulation des Duktilbruchs in Al/SiC, Dissertation MPI für Metallforschung, Stuttgart.

Yu, Q., and Fish, J. (2002). Multiscale asymptotic homogenization for multiphysics problems with multiple spatial and temporal scales: a coupled thermo-viscoelastic example problem, *International Journal of Solids and Structures*, **39**, 6429–6452.

Zohdi, T. I. (2003). Genetic design of solids possessing a random-particulate microstructure, *Philosophical Transactions of the Royal Society*, **361** (1806), 1021–1043.

Zohdi, T. I. and Wriggers, P. (1999). A domain decomposition method for bodies with heterogeneous microstructure based on material regularization, *International Journal of Solids and Structures*, **136**, 2507–2527.

Zohdi, T. I. and Wriggers, P. (2001a). A model for simulating the deterioration of structural-scale material responses of microheterogeneous solids, *Computer Methods in Applied Mechanics and Engineering*, **190** (22–23), 2803–2823.

Zohdi, T. I. and Wriggers, P. (2001b). Aspects of the computational testing of the mechanical properties of microheterogeneous material samples, *International Journal of Numerical Methods in Engineering*, **50**, 2573–2599.

Zohdi, T. I., Wriggers, P. and Huet, C. (2001). A method of substructuring large-scale computational micromechanical problems, *Computer Methods in Applied Mechanics and Engineering*, **190** (43–44), 5639–5656.

5

Computational experiments in the mechanics of materials: concepts and tools

5.1 Concept of computational experiments in the mechanics of materials

At one time, improvement of materials was triggered by the development of new technologies, such as the development of the Bessemer process of steel making, or the discovery of vulcanization, which led to the industrial use of rubber and rubber-based materials. Then, the progress went so far, that not only limitations of available technologies dictated the limits of the material performances, but also a predefined, required microstructure of a material could be produced (using different methods, like powder metallurgy, control of heat treatment regimes, nanotechnology, etc.). The question was raised as to which microstructures of materials could ensure the required properties.

One of the ways to determine the optimal microstructures of materials is to carry out the 'virtual testing' of different microstructures, using the micro- and mesomechanical models of the materials behaviour.

According to Mishnaevsky Jr and Schmauder (Mishnaevsky Jr and Schmauder, 2001), a possible scheme of the computational optimization/design of materials should include the following steps:

- Problem definition: definition of necessary properties to be improved on the basis of the analysis of service conditions, and the analysis of the available means of the microstructure control; analysis of the effects of the material manufacturing and processing on the microstructures (e.g., effect of the duration and temperature of sintering on the grain sizes and contiguity of hard alloys, or effect of hot working on the type of structures in high speed steel).

- Determination of the input properties for the mesomechanical simulations, in particular:
  - micrographing of cut-outs of the materials, image analysis, statistical descriptions of microstructures, determination of microstructural parameters of microstructures;
  - determination of the micromechanisms of deformation and damage in the materials (e.g. debonding, particle failure);
  - determination of the mechanical properties of the components, phases and interfaces.
- Choice of the appropriate simulation approaches: unit cell approach, multiscale simulations, real structure simulation, cohesive concepts or element elimination, etc.
- Development of numerical models of the materials with real microstructures and verification of the model by comparing the calculated and experimental results.
- Design of different artificial microstructures; virtual (computational) testing of the microstructures; comparison of the output parameters of the simulations, iterative step-by-step optimization and development of recommendations for the improvement of the microstructures of materials. By testing typical idealized microstructures of a considered material in numerical experiments, one determines the directions of the material optimization and preferable microstructures of materials under given service conditions. Such simulations should be carried out for the same loading conditions and material, as the real structure simulations, which proved to reflect adequately the material behavior.
- Producing and testing of the materials with improved microstructures in laboratory and service conditions; verification of results.

While the suggested approach can serve as a general framework for the improvement and design of structural materials, the typical path of the material improvement has been the phenomenological/experimental/analytical way: namely, some assumptions about the possibility of a material improvement are made on the basis of experiments or general physical principles, are verified experimentally, and then realized as a new material.

When designing the artificial microstructures of materials, which will be tested in the numerical experiments, it can be useful to take into account some hints on the optimal microgeometries of materials, using the analysis of biomaterials or experimental studies (cf. Chapter 2).

5.2 Input data for the simulations: determination of material properties

The correct determination of input data for the simulations is the prerequisite for the successful numerical analysis of the materials. The main challenge in this case is that the required input data represent properties of small-scale volumes, embedded and constrained by other phases, with complex geometry and some internal heterogeneity. In many cases, the properties cannot be directly measured or tested, or might be different from the properties of macrospecimens (due to the scale and size effects, constraints by other components, effects of treatment regimes, etc.). The extraction of the data for the phases from the standard or modified tests of materials can become a nontrivial problem, which requires both rather complex experiments and an inverse analysis step.

In the following, we list some methods of experimental and experimental–numerical determination of the mechanical properties of phases of multiphase materials.

5.2.1 Nanoindentation

Nanoindentation can be used to determine the elastic constants and the constitutive behavior of phases. This method was used, for instance, by Trubitz (Trubitz, 1998) to determine the Young modulus of primary carbides in cold work steels. The indentation with the Vickers indenter was carried out with simultaneous observation in the built-in microscope and recording the force–displacement (loading and uploading) curves. By analyzing the force–displacement curves for loading and unloading, the elastic constants of the constituents (primary carbides) of tool steels have been determined.

An efficient method of extraction of the required material properties from the indentation data is the application of the *neural networks* (which can be trained on the basis of experimental data or numerical simulations; Mukherjee *et al*., 1995; Huber, 2000; Huber and Tsakmakis, 2001).

5.2.2 In-situ experiments using a scanning electron microscope

In order to determine the micromechanisms and conditions of the damage and fracture in multiphase materials (Al cast alloys, tool steels), Mishnaevsky Jr *et al*. (Mishnaevsky Jr *et al*., 1999b, 2001, 2003b) carried out a series of *in-situ* experiments using a scanning electron microscope (SEM). While the small regions near the specimen notch were observed under the SEM, the force–displacement curves were recorded during the loading (Figure 5.1). The mechanisms of damage (particle cleavage, shear bands leading to the cracking) were observed in the SEM. The points on the force–displacement curve, which corresponded to the start of inelastic deformation and to the particle cracking, were

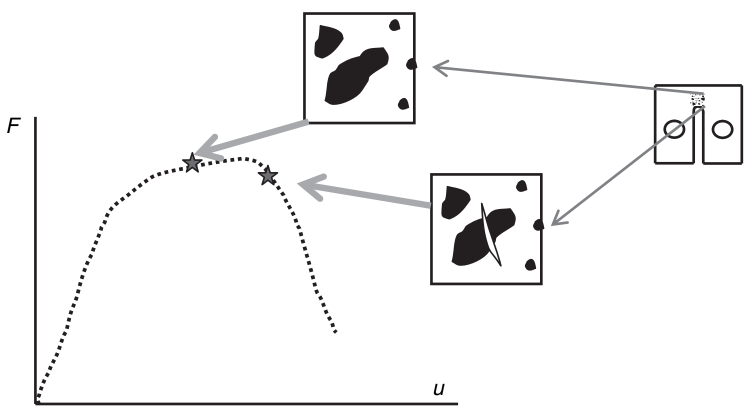

Figure 5.1 Schema of the analysis of damage mechanisms in composites by correlating the SEM observations with the force–displacement curve (Mishnaevsky Jr et al*, 2001, 2003b).*

registered. The effects of the microstructure on the strength and damage behavior have been investigated by comparing the local deformation and damage distribution, observed by the SEM, and the recorded force–displacement curves (local deviations of the curves, start of the falling branch; cf. Figure 5.1) for different materials and microstructures (tool steels, AlSi cast alloys with Si particles of globular and lamellar shapes).

5.2.3 Inverse analysis

In order to determine local properties of constituents (e.g. damage parameter, local failure condition), simulations of the damage and crack growth in real microstructures of materials are carried out and compared with the experimental observations. This technique can be applied, for instance, if all the data (microstructure of materials, expected response and crack path, boundary conditions, material properties) are known from experiments, and only the condition of the local failure of one of constituents has to be determined from the simulations. Wulf (Wulf, 1985) carried out a number of simulations of the crack path in a compact tension (CT) specimen from the Al/SiC composite using different local damage criteria. He compared the stress–strain curves and the simulated crack paths, obtained with the use of different damage criteria (critical plastic strain, parameter of triaxiality, Rice–Tracey damage criterion) with the corresponding experimental data. As a result, Wulf determined the correct damage parameter for the Al matrix in Al/SiC composites, and demonstrated that both the stress–strain curves and the simulated crack paths correspond exactly to the experimental data, if one uses the Rice–Tracey damage criterion with a critical value of 0.2.

Mishnaevsky Jr *et al.* (Mishnaevsky Jr *et al.*, 2003a) determined the failure condition of the 'matrix' of cold wok steels (i.e. the steel material without primary carbides) by carrying out the FE simulations of crack growth on real microstructures of the steels, and the inverse analysis. Figure 5.2 shows a schema of the determination of the damage condition for one phase of the material by comparing the experimental and numerical crack paths, when all the other parameters of the material (microstructure, elastic properties of the phases) are known.

Another version of the application of inverse analysis has been realized by Mishnaevsky Jr *et al.* (Mishnaevsky Jr *et al.*, 2001, 2003b) as an experimental–numerical method combined with hierarchical simulations. The authors carried out SEM *in-situ* experimental investigations of the damage evolution in tool steels, using three-point bending specimens with inclined notch. The inclined notch ensured the high localization of the stress concentration: the highest stress level was observed in only a small area, which was simple to observe under the SEM.

Mishnaevsky Jr and colleagues recorded the force–displacement curves, and photographed the areas of the specimens (in the notch), where the first microcracks were expected and appeared (in primary carbides). Then, a macroscopic FE model of the notched specimen was developed, and used to determine the local stress and strain fields in these areas. The stress and strain distributions were used as input data for a microscopic (micromechanical) FE model of the region, which incorporated the real microstructure of the material (observed in the experiments), taken from the micrographs. Simulating the deformation of the real microstructure and comparing the calculated stress and strain distributions with the experimental results, Mishnaevsky Jr *et al.* (Mishnaevsky Jr *et al.*,

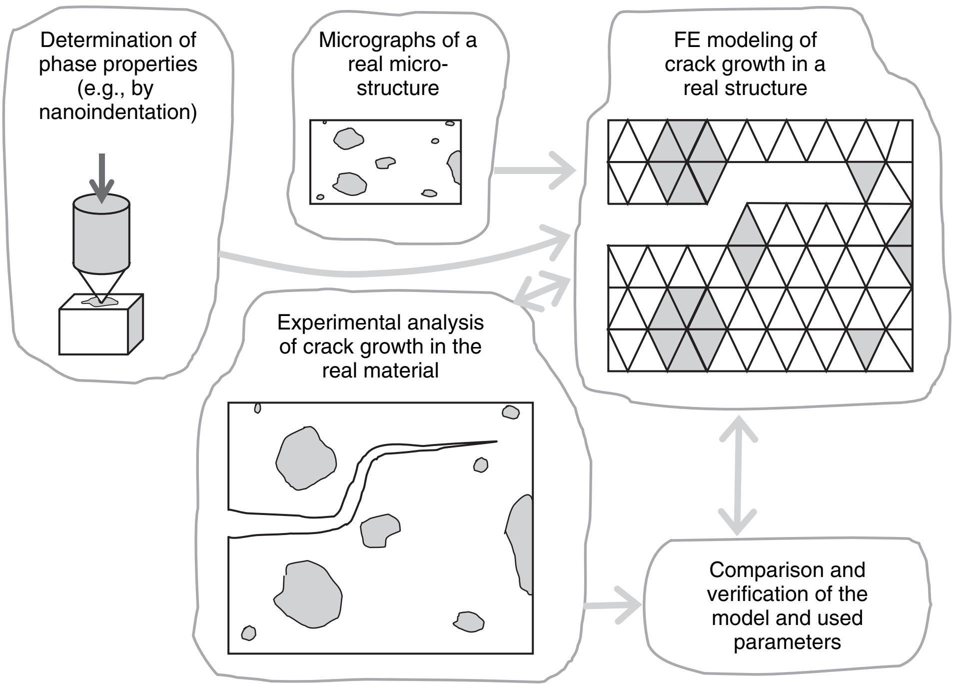

Figure 5.2 *Schema of the incorporation of microstructural parameters and local properties of composite into a FE model, and its verification by comparison with experiments.*

2001, 2003b) determined the conditions of failure of primary carbides of several types of tool steels.

An interesting approach to determine mechanical properties of a complex material (iron with secondary carbides) was employed by Muro *et al*. (Muro *et al*., 2002) (see also Balladon *et al*., 2004). The purpose of this work was to determine the averaged properties of the 'matrices' of a number of tool steels, which consist of iron and different secondary carbides and oxides. Iturriza, Rodriguez Ibabe, Muro and other scientists from the Centro de Estudios e Investigaciones Técnicas de Gipuzkoa (CEIT, Spain) produced materials, which are chemically and microstructurally identical to the 'matrix' of cold work steels, using *powder metallurgy technology*. Using hot isostatic pressing (HIP), different sintering and heat treatment technologies (as austenitizing, multitempering), they produced materials with predefined properties and microstructures. The materials were tested to determine the constitutive law and fracture toughness of the 'matrix' of multiphase materials (tool steels). As a result, the fracture toughness and constitutive law of the 'matrix' were determined, and used in mesomechanical simulations.

One can see that all the listed methods include as a step some kind of modeling of the constituents (either numerical simulations, or production of a model material using powder metallurgy methods), which helps to interpret the experimental testing data and determine from them material parameters, required for the micromechanical simulations.

5.3 Program codes for the automatic generation of 3D microstructural models of materials

The concept of the optimal design of materials on the basis of the numerical testing of microstructures can be realized if a large series of numerical experiments for different materials and microstructures can be carried out quickly, in a systematic way, automatically. This can be done, if labor costs of the numerical experiments, a significant part of which are the efforts of the generation of micromechanical models, are kept very low. To solve this problem, a series of programs was developed, which should automate the step of the generation of 3D microstructural models of materials. After a 3D microstructural model of a material with a complex microstructure is generated, the numerical testing of the microstructure is carried out with the use of commercial FE software.

In this Section, we present several recently developed programs for the automatic generation of 3D microstructural models of heterogeneous materials.

5.3.1 Program Meso3D for the automatic geometry-based generation of 3D microstructural FE models of materials

As discussed in the Chapter 4, microstructure–strength and microstructure–damage resistance relationships of composites can be analyzed numerically with the use of the unit cell approach. In particular, multiparticle unit cells make it possible to analyze the overall response, nonlinear behavior and damage evolution in composites, taking into account both the interaction between phases, between elements of each phase (e.g. particles) as well as with evolving microcracks and cracks.

In order to simplify and automate the generation of 3D multiparticle unit cell models of composite materials, a program Meso3D was developed (Mishnaevsky Jr, 2004a). The program defines the geometry, mesh parameters and boundary conditions of different multiparticle unit cell models of materials, and generates a command file (session file) for the commercial FE pre- and post-processing software MSC/PATRAN. A multiparticle unit cell model of a representative volume of a composite material is created automatically, when the session is played with MSC/Patran. Both 2D and 3D versions of the program are available. Figure 5.3 shows some examples of the generated unit cells.

The program contains the following subroutines:

- Interactive definition of the parameters of the multiparticle unit cell.
- Design of the cell: arrangement of the inclusions in the box using the random number generator.
- Writing the command file for the commercial MSC/Patran FE software.
- Statistical analysis of the generated microstructures.

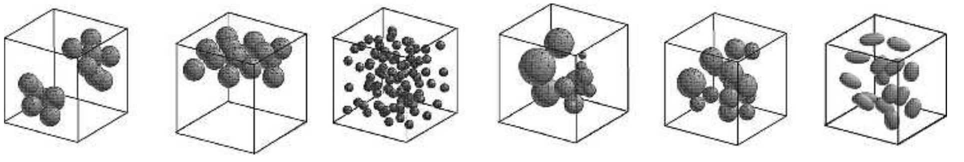

Figure 5.3 *Examples of the unit cells generated with the use of the program Meso3d.*

5.3.1.1 Definition of parameters

The geometry and parameters of the unit cell are defined during a short interactive session, in which the parameters are introduced into the program either directly or by multiple choice. The microstructures to be generated are defined by the sizes of the considered cell, the shape, volume content and amount of inclusions, the kind of the inclusion distribution (random, predefined, clustered, graded, etc.), the probability distribution of the inclusion sizes, etc. The radii, form and positions of the inclusions can be read from the input text file (for the cases of predefined or regular particle arrangements) or generated with the use of random number generators. In the latter case, there are options for the random, clustered, gradient arrangements or dense packing of particles. The model is further defined via the fineness of the meshing, availability or nonavailability and sizes of embedding, boundary conditions (uniaxial tension or triaxial loading).

Due to the fact that the models are *geometry based*, only simple shapes of the inclusions (round and ellipsoidal) can be taken into account in this model.

5.3.1.2 Design of the cell

After the main parameters of the microstructure (volume content of reinforcement, shape of reinforcement, type of the particle arrangement – random, graded, etc.) are introduced interactively, the unit cell is designed as a box containing a given amount of round or ellipsoidal particles of different sizes. Both embedded and nonembedded unit cells can be produced.

The particles in the cell with an artificial microstructure are arranged using the random sequential absorption (RSA) scheme. Each coordinate of the particle center is generated independently, using the random number generator. After the coordinates of a first particle are defined, the coordinates of each new particle are determined both by using the random number generator, and from the condition that the distance between the new particle and all available particles is no less than e.g. 0.1 of the particle radius. If this condition is not met, the seed of the random number generator is changed, and the coordinates of the new particle are determined anew. In order to avoid the boundary effects, the distance between a particle and the borders of the box is set to be no less than 0.05 of the particle radius.

In order to generate the *localized particle arrangements*, like clustered, layered and gradient particle arrangements, the coordinates of the particle centers were calculated as random values distributed by the Gauss law. The mean values of the corresponding normal distribution of the coordinates of particle centers were assumed to be the coordinates of a center of a cluster (for the clustered structure), or the y- or z-coordinate of the border of the box (for the gradient microstructures). Figure 5.4 shows schematically examples of such a design of the microstructures. The standard deviations of the distribution can be varied, allowing generation of different particle arrangements from highly clustered or highly gradient arrangements (very small deviation) to fast uniformly random particle arrangements (a deviation comparable with the box size).

Another procedure is used to create multiparticle unit cells with high volume content of particles. In this case, the dense packing algorithm is used, in which the unit cell is filled by the particles 'layer after layer' with a predefined distance between the particles. With this procedure, a volume content of particles of about 40 % can be achieved.

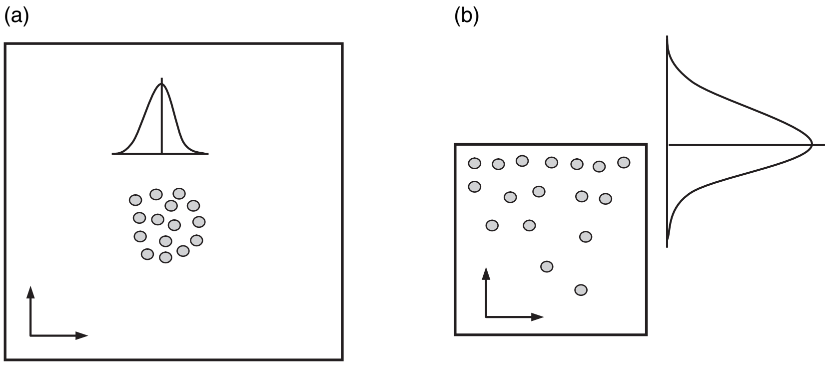

Figure 5.4 Schema of the design of artificial (a) clustered and (b) gradient microstructures.

5.3.1.3 Command file

The program writes the command file for the automatic generation of the designed model. When the command file is played with the commercial MSC/Patran software, the geometrical model is first created, and then meshed with tetrahedral elements using the free meshing technique (Thompson *et al.*, 1999) (cf. Figure 5.5). After that, the mesh is automatically improved, and finally the boundary conditions and material properties are defined. The model can be further modified or run with different commercial or noncommercial FE programs (such as ABAQUS and NASTRAN).

The FE models of both artificial and simplified real microstructures (with particles approximated, e.g. by the ellipsoids) can be generated with this program. In the case of real microstructures, either experimentally determined coordinates and radii of inclusions are given in the input file, or the experimentally determined probability distributions of these values can be used to generate quasi-real microstructures.

5.3.1.4 Statistical analysis of the generated microstructure

This subroutine carries out the statistical analysis of generated microstructures. It determines the average nearest-neighbor distances between particles, as well as the radial distribution functions and the probability distributions of the distances between particles.

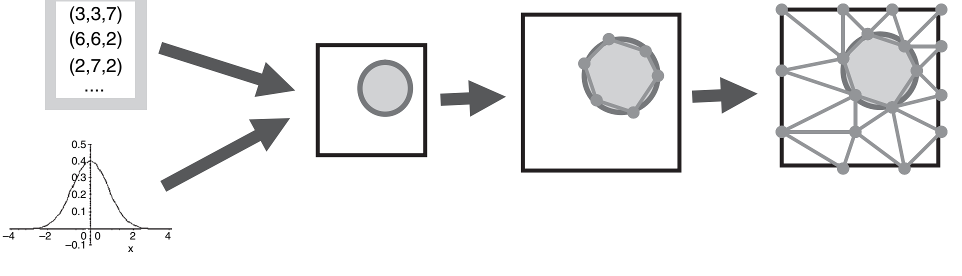

Figure 5.5 Schema of the generation and meshing of different artificial microstructures on the basis of predefined probability distribution of particle parameters.

The accurate determination of these parameters requires a much larger number of particles in a unit cell than necessary to compute the mechanical behavior. Further, the limitations on the maximum amount of degrees of freedom in a FE model, related to the hardware and software constraints, limit the amount of particles in a cell far below the level required for statistical analysis. To overcome these limitations, we followed the idea of Segurado *et al.* (Segurado *et al.*, 2003), who generated much larger unit cells than those used in their numerical experiments, using the same algorithms, and determined the statistical parameters of the microstructures with the use of the larger cells. They suggested that '. . . the cubic unit cells used for the simulation of the mechanical behavior can be understood as small representative volume elements taken at random from the larger cell.' The program generates test unit cells of size $100 \times 100 \times 100$ mm with predefined particle arrangements using the same algorithms as for the simulated cells, and calculates the statistical parameters of microstructures for these cells. Figure 5.6 shows examples of the radial distribution functions for different generated microstructures.

Lévesque *et al.* (Levesque *et al.*, 2004) compared the results of numerical simulations of the mechanical behavior of glass bead-reinforced polypropylene, carried out with the use of this program, with analytical studies, based on the homogenization approach in the affine formulation. The matrix (polypropylene) was modeled as a nonlinear viscoelastic material, using the Shapery nonlinear law. The authors observed very good agreement between the numerical and analytical results.

A version of the program Meso3D, called Meso3DFiber, generates 3D unit cells for unidirectional fiber reinforced composites. The FE meshes were generated by sweeping the corresponding 2D meshes on the surface of the unit cell (see Chapter 10).

5.3.2 Program Voxel2FEM for the automatic voxel-based generation of 3D microstructural FE models of materials

The program Meso3D, presented above, allows the automatic generation of 3D FE microstructural models of representative volumes of materials, using the exact geometric description of microstructures and the free meshing method. However, the geometry-based approach, used in this program, is applicable only for relatively simple geometrical forms of microstructural elements in composites.

In order to carry out the numerical analysis of arbitrarily complex 3D microstructures, another approach was suggested, which has to complement the program Meso3D. The approach, based on the voxel array description of material microstructures, was realized in the framework of a new program Voxel2FEM (Mishnaevsky Jr, 2005a).

The representative volume is presented as an $N_x \times N_y \times N_z$ array of points (voxels), each of them can be either black (particle) or white (matrix) (for a two-phase material).

This approach can be generalized on multiphase materials simply as well. In the interactive session, a user determines the way the microstructure information is introduced into the model: either by reading input file(s) containing the voxel array, or by generating artificial microstructures (e.g. multiparticle unit cells or 3D random chessboards), using the random number generator. Then, the parameters of the microstructure are introduced. The program defines the geometry and boundary conditions of the model, and produces a command (session) file for the commercial software MSC/PATRAN, which generates a 3D FE microstructural model of the representative volume of material. The

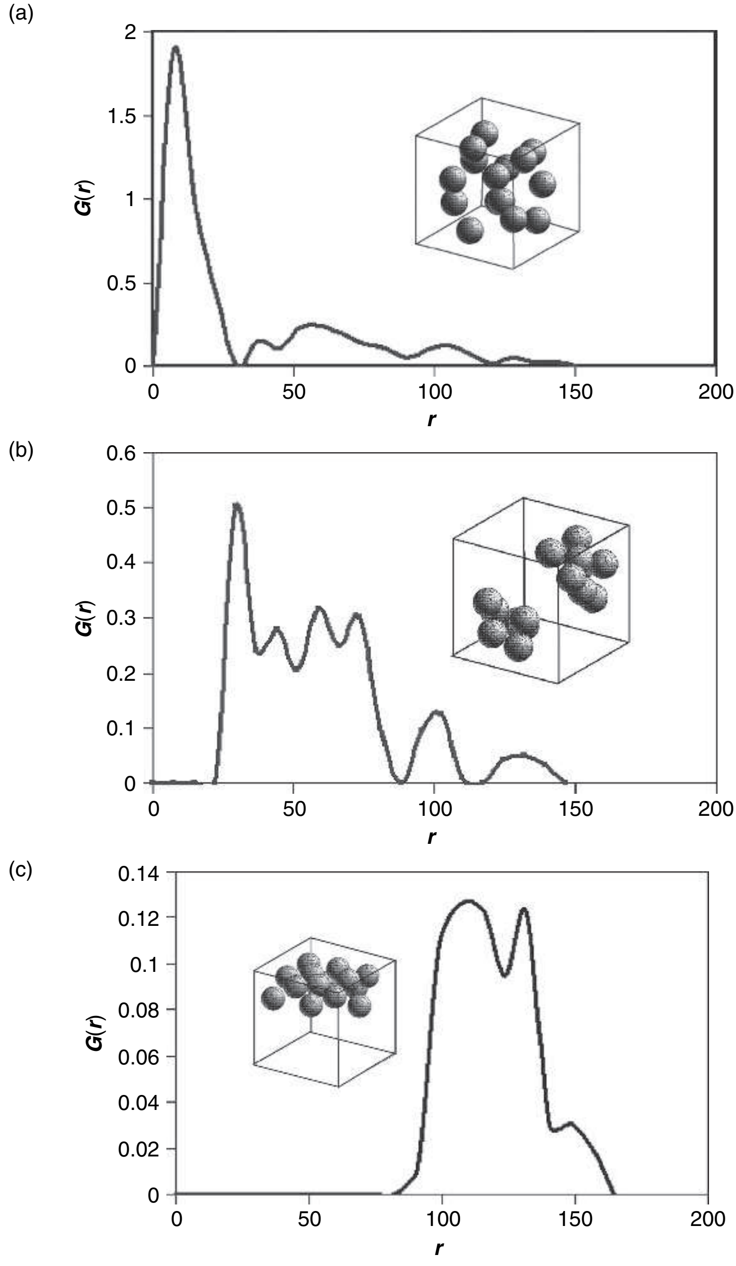

Figure 5.6 *The radial distribution functions for different microstructures: (a) random; (b) clustered and (c) graded particle arrangements.*

designed microstructures are meshed with brick elements, which are assigned to the phases automatically according to the voxel array data.

The program Voxel2FEM is applicable both for the design of artificial microstructures of materials, and for the reconstruction and analysis of real 3D microstructures (Figure 5.7). The input data (voxel array) necessary for the reconstruction of the 3D real microstructures can be obtained by using computational tomography or serial sectioning (Ljungberg *et al*., 1986; Povirk, 1994; Pyrz, 1999).

Several built-in subroutines in the program allow reading of the microstructure data from an external file (for the case of real microstructures), generation of different predefined phase arrangements, as well as the percolation theory analysis of the microstructures.

5.3.2.1 Subroutine for generating random microstructures and multiparticle unit cells

The program can generate voxel arrays for multiparticle unit cells with different arrangements of round particles in a matrix, or for the random and percolating structures (3D random chessboard). The voxel array data for 3D random microstructure models (3D random chessboards) are produced with the use of random number generators. The

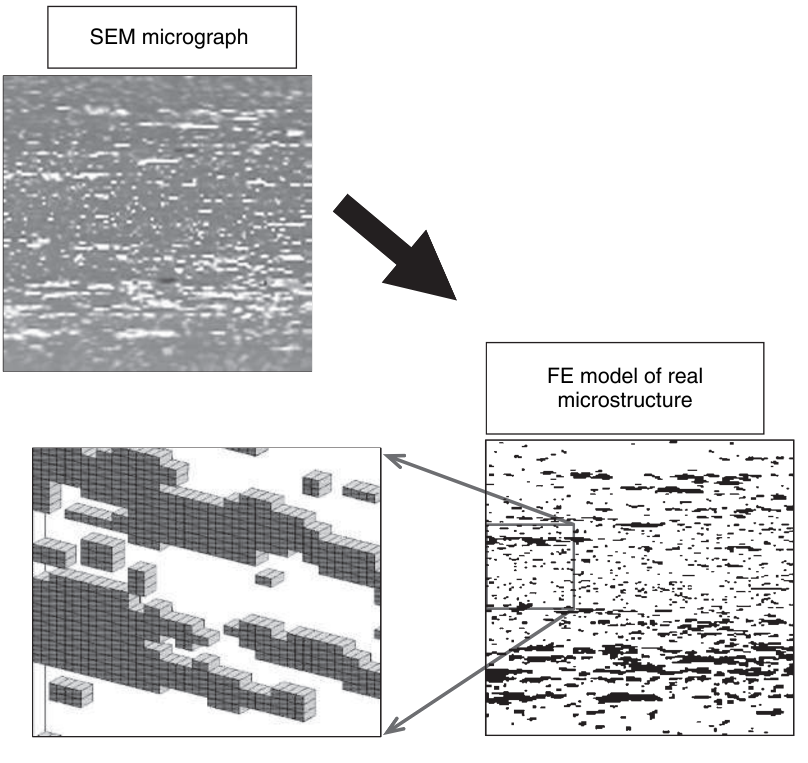

Figure 5.7 *Section of a real microstructure of a two-phase material, and a FE model, generated with the program Voxel2FEM.*

voxel arrays for multiparticle unit cells with many round particles are generated, using the algorithms described in Section 5.3.1.

5.3.2.2 Subroutine for generating graded composite microstructures

In order to analyze the effect of graded microstructures on the strength and damage in composites, a subroutine for the automated generation of random graded microstructures was included in the program Voxel2FEM.

This subroutine defines the distribution of black voxels as a random distribution both in X and Z directions, and a graded distribution in Y direction. The graded distribution of black voxels along the axis Y follows the formula:

$$vc(y) = \frac{2\ vc_0}{1+\exp(\mathrm{g}-2\ gy/L)}$$

where $vc(y)$ is the probability that a voxel is black at this point, vc_0 is the volume content of the black phase, L is the length of the cell, g is a parameter of the sharpness of the gradient interface and y is the Y coordinate (Section 7.6). This formula allows to vary the smoothness of the gradient interface of the structures (highly localized arrangements of inclusions and a sharp interface versus a smooth interface), keeping the volume content of inclusions constant.

5.3.2.3 Subroutines for the percolation theory analysis of 3D microstructures

When generating the representative unit cells, the availability of infinite percolation clusters in the generated microstructure is checked using the burning algorithm (Garboczi *et al.*, 2006). The subroutine (based on the program developed by Garboczi *et al.*) searches all three directions. The subroutine allows either periodic or hard boundary conditions. The information about the availability/nonavailability of percolation clusters for both phases and all the directions, is printed out in the session file.

Another subroutine, built-in in the program, carries out the percolation analysis of generated or reconstructed microstructures with the use of the alternative algorithm of the cluster labeling, suggested by Martín-Herrero and Peón-Fernández (Martín-Herrero and

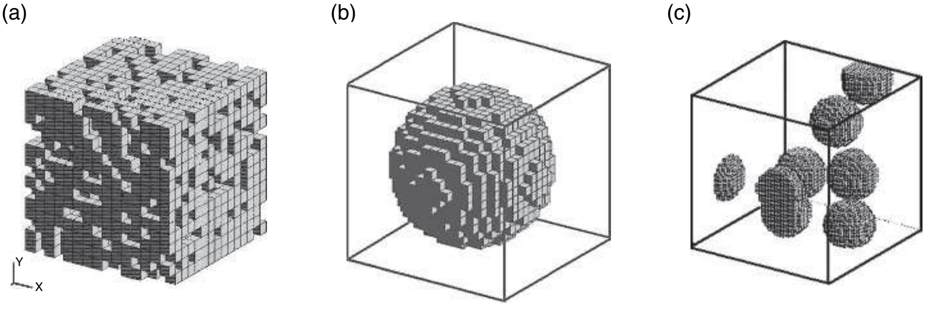

Figure 5.8 *Examples of different generated microstructures: (a) random 3D chessboard microstructure; (b) a round particle; (c) multiparticle unit cell.*

Peón-Fernández, 2000). This subroutine carries out the labeling of clusters of voxels, calculates the average and maximum cluster dimensions in all three directions and detects the existence or nonexistence of the percolation in all directions. These subroutines allow the complete percolation analysis of the microstructures to be carried out, as well as the comparison of results obtained using different techniques.

Figure 5.8 shows examples of different generated microstructures: random 3D chessboard microstructure (only one phase is shown), a round particle and a multiparticle unit cell.

(Demo versions of the programs Meso3D and Voxel2FEM are available from the author on request.)

References

Balladon, P., Ponsot, A., Lichtenegger, G., Rodriguez Ibabe, J. M., Iturriza, I., Schmauder, S. and Mishnaevsky Jr, L. (2004). Influence of micromechanical mechanisms of strength and deformation of tool steels under static and cyclic load, European Commission Technical Report, EU DG Research, 183 pp.

Garboczi, E. J., Bentz, D. P., Snyder, K. A., Martys, N. S., Stutzman, P. E., Ferraris, C. F., Bullard, J.W., and Butler, K. M. (last revision 2006). Modeling and measuring the structure and properties of cement-based materials, Part III/2, Electronic monograph, http://ciks.cbt.nist.gov/garbocz/

Huber, N. and Tsakmakis, Ch. (2001). A neural network tool for identifying the material parameters of a finite deformation viscoplasticity model with static recovery, *Computer Methods in Applied Mechanics and Engineering*, **191**, 353–384.

Huber, N. (2000). Anwendung Neuronaler Netze bei nichtlinearen Problemen der Mechanik, Wissenschaftliche Berichte, FZKA-6504, Habilitationsschrift, Universität Karlsruhe.

Lévesque, M., Derrien, K., Mishnaevsky Jr, L., Gilchrist, M. and Baptiste, D. (2004). A micromechanical model for non-linear viscoelastic particle reinforced polymeric composite materials – undamaged state, *Composites*, **35**, 905–913.

Ljungberg, A.-B., Chatfield, C., Hehenberger, M. and Sundström, B. (1986). Estimation of the plastic zone size associated with cracks in cemented carbides, in: *Proceedings of the 2nd International Conference of the Science of Hard Materials*, Adam Hilger Ltd, Rhodes, pp. 619–630.

Martín-Herrero, J. and Peón-Fernández, J. (2000). Alternative techniques for cluster labelling on percolation theory, *Journal of Physics A: Mathematical and General*, **33**, 1827–1840.

Mishnaevsky Jr, L. (2004a). Three-dimensional numerical testing of microstructures of particle reinforced composites, *Acta Materialia*, **52** (14), 4177–4188.

Mishnaevsky Jr, L. (2005a). Automatic voxel based generation of 3D microstructural FE models and its application to the damage analysis of composites, *Materials Science and Engineering*, A, **407**, (1–2), 11–23.

Mishnaevsky Jr, L. and Schmauder, S. (2001). Continuum mesomechanical finite element modeling in materials development: a state-of-the-art review, *Applied Mechanics Reviews*, **54** (1), 49–69.

Mishnaevsky Jr, L., Lippmann, N. and Schmauder, S. (2001). Experimental-numerical analysis of mechanisms of damage initiation in tool steels, in: *Proceedings of the 10th International Conference on Fracture*, Honolulu, CD-ROM.

Mishnaevsky Jr, L., Lippmann, N. and Schmauder, S. (2003a). Computational modeling of crack propagation in real microstructures of steels and virtual testing of artificially designed materials, *International Journal of Fracture*, **120** (4), 581–600.

Mishnaevsky Jr., L., Lippmann, N. and Schmauder, S. (2003b). Micromechanisms and modelling of crack initiation and growth in tool steels: role of primary carbides, *International Journal of Materials Research*, **94** (6), 676–681.

Mishnaevsky Jr, L., Lippmann, N., Schmauder, S. and Gumbsch, P. (1999b). In-situ observations of damage evolution and fracture in AlSi cast alloys, *Engineering Fracture Mechanics*, **63** (4), 395–411.

Mukherjee, A., Schmauder, S. and Rühle, M. (1995). Artificial neural networks, for the prediction of mechanical behavior of metal matrix composites, *Acta Metallurgica et Materialia*, **43** (11), 4083–4091.

Muro, P., Gimenez, S. and Iturriza, I. (2002). Sintering behaviour and fracture toughness characterization of D2 matrix tool steel, comparison with wrought and PM D2, *Scripta Materialia*, **46** (5), 369–373.

Povirk, G. L. (1994). Incorporation of microstructural information into models of two-phase materials, *Acta Materialia*, **43** (8), 3199–3206.

Pyrz, R. (1999). Prospects of x-ray microtomography for studies of composite materials, *Abstracts Image Processing Methods in Applied Mechanics* Warsaw, Poland, pp. 175.

Segurado, J., González, C. and LLorca, J. (2003). A numerical investigation of the effect of particle clustering on the mechanical properties of composites. *Acta Materialia*, **51**, 2355–2369.

Thompson, J., Soni, B. and Weatherhill, N. (1999). *Handbook of Grid Generation*, CRC Press, Boca Raton, FL.

Trubitz, P. (1998). Messung der elastischen Eigenschaften von Karbiden und der Matrix von Stahl X155CrVMo12-1, Prüfbericht, 26.11.1998, TU BA Freiberg.

Wulf, J. (1985) Neue Finite-Elemente-Methode zur Simulation des Duktilbruchs in Al/SiC, Dissertation MPI für Metallforschung, Stuttgart.

6

Numerical mesomechanical experiments: analysis of the effect of microstructures of materials on the deformation and damage resistance

As stated in Chapter 2, the subject of the mesomechanics of materials is the analysis of interrelationships between microstructures and mechanical properties of materials, taking into account not only characteristics of single elements or averaged parameters of microstructures, but also the synergistic effects and interaction between many elements of microstructures.

In this and following chapters, we carry out systematic numerical experiments to investigate the effect of the composite microstructure on the mechanical behavior, strength and damage resistance of the composite. The computational experiments are carried out, using the programs of automatic generation of microstructural models of materials, described in Chapter 5. As a test material, the aluminum matrix reinforced by ceramic (SiC) particles is considered.

First, the comparison of different types of microstructures is carried out. The following questions should be answered: how does a particle arrangement (e.g. graded, clustered, random, etc.) influence the stiffness, strength and damage resistance of the composite? Which arrangement of particles ensures the highest damage resistance?

Then, different types of microstructures are investigated in more detail. In particular, the effects of parameters of graded, clustered and interpenetrating microstructures on the deformation, stiffness and damage resistance of composites are analyzed in numerical experiments.

6.1 Finite element models of composite microstructures

A number of 3D multiparticle unit cells with different arrangements of particles were generated automatically with the use of the program Meso3D and the commercial FE code MSC/PATRAN. Unit cells with different amounts of particles, different volume contents of the inclusion phase (from 2.5 to 15 %) and different particle arrangements have been considered.

The cells were subject to a uniaxial tensile displacement loading (1 mm). The sizes of the 3D unit cells were $10 \times 10 \times 10$ mm, and of the 2D cells (considered in Chapters 7 and 8) were 10×10 mm. The micromechanical problems were solved in the framework of the embedded cell approach.

The models, considered in this Chapter, contained about 30000 elements. Each particle contained about 400 FEs. The radii of particles were calculated from the predefined volume content (VC) and the number of particles in the box, and were as follows: 1.1676 mm($\mathrm{VC} = 10\,\%, N = 15$), 0.9267 mm ($\mathrm{VC} = 5\,\%, N = 15$), 1.3365 mm($\mathrm{VC} = 10\,\%, N = 10$) and 1.0608($\mathrm{VC} = 5\,\%, N = 10$).

The embedding was $14 \times 14 \times 14$ mm. The nodes at the upper surface of the box were connected, and the displacement was applied to only one node. The simulations were done with ABAQUS/Standard.

Figure 6.1 gives the schema of the model.

6.2 Material properties used in the simulations

As a test material, SiC particle reinforced Al matrix composites were used. This material is widely used in industry (e.g. in aviation and the automobile industry). Furthermore, the deformation and damage mechanisms of this material are very well investigated, and the properties, damage criteria and conditions are well known (Wulf, 1985; Wulf *et al.*, 1993; Derrien, 1997; Baptiste, 1999; Derrien *et al.*, 1999). This allows us to omit the initial

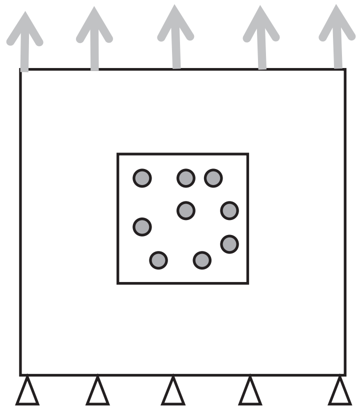

Figure 6.1 *Schema of the embedded multiparticle unit cell.*

steps of the program of the computational testing and optimization of materials, outlined in Section 5.1 (i.e., determination of components properties and damage mechanisms), and go directly to the virtual testing and comparison of microstructures.

In the simulations, the following material properties have been used. The inclusions (SiC particles) behaved as elastic isotropic damageable solids, characterized by Young modulus $E_p = 485\,\text{GPa}$ and Poisson's ratio 0.165. The Al matrix was modeled as an isotropic elastoplastic solid, with Young modulus $E_m = 73\,\text{GPa}$ and Poisson's ratio 0.345. The experimental stress–strain curve for the matrix (provided by Dr E. Soppa, personal communication) was approximated by the deformation theory flow relation (Ludwik hardening law):

$$\sigma_y = \sigma_{yn} + h\varepsilon_{pl}{}^n$$

where σ_y is the actual flow stress, σ_{yn} is the initial yield stress, ε_{pl} is the accumulated equivalent plastic strain and h and n are the hardening coefficient and the hardening exponent. The parameters of the curve for the matrix were as follows: $\sigma_{yn} = 205\,\text{MPa}$, $h = 457\,\text{MPa}$, $n = 0.20$.

The embedding zone behaved as a composite with averaged properties, i.e. as an elastoplastic material (Al/SiC), with Young modulus $E_{av} = 75.7\,\text{GPa}$ (for VC = 10%) and $E_{av} = 88.4\,\text{GPa}$ (for VC = 15%), and Poisson's ratio 0.323 taken from Wulf (Wulf, 1985) and Wulf *et al.* (Wulf *et al.*, 1993). The elastoplastic stress–strain curve for the composite (embedding) was also taken from the publications by Wulf. For the composite (embedding), the parameters of the Ludwik law were: $\sigma_{yn} = 216\,\text{MPa}$, $h = 525.4\,\text{MPa}$, $n = 0.25$.

Damage growth in the particles and in the matrix was simulated using the subroutine User Defined Field, described in the next section. In the simulations described in this Chapter (3D comparison of different types of microstructures), only the particle failure (and not the void growth in matrix or interface debonding) was considered, in order to separate out the effect of the interaction of failed particles via the stress fields, and not via the formation of microcracks in the matrix.

As output parameters of the numerical testing of the microstructures, the effective response of the materials and the amount of failed particles, the fraction of failed elements in particles and in matrix versus the far field strain, as well as the stress, strain and damage distributions in the material were determined.

6.3 Damage modeling in composites with the User Defined Fields

6.3.1 Damage mechanisms and failure conditions

Let us summarize briefly the experimental observations about the micromechanisms of damage evolution in SiC particle reinforced Al matrix composites under mechanical loading. First, some particles become damaged and fail or debond from the matrix; after that, cavities and voids nucleate in the matrix (initially, near the broken particle), grow and coalesce, and that leads to the failure of the matrix ligaments between particles, and finally to the formation of a macrocrack in a volume (Derrien, 1997; Baptiste, 1999).

The damage mechanisms in composites are strongly influenced by the particle sizes: if the SiC particles are bigger than $10\,\mu\text{m}$, particle cracking is the main damage mechanism at the early stages of loading, which leads then to void nucleation in the matrix in the vicinity of the broken particles (Mummery and Derby, 1993). Otherwise, for smaller particles, the decohesion at the particle–matrix interface becomes the main damage mechanism.

The quantitative damage criteria for the components of Al/SiC composites have been analyzed, tested and verified in many works. According to Hu *et al.* (Hu *et al.*, 1998) and Derrien *et al.* (Derrien *et al.*, 1999), the SiC particles in Al matrix become damaged and fail, if the critical maximum principal stress in the particles exceeds a critical level. The critical maximum principal stress is a random value, with an average of 1500 MPa.

Damage growth in the Al matrix occurs by the mechanism of formation and growth of voids. The void growth in the Al matrix of Al/SiC composites can be modeled with the use of different criteria: the critical equivalent plastic strain, triaxiality factor, different damage parameters and indicators, including the Gurson damage model and the nonlocal version of this model (Reusch *et al.*, 2003), as well as the Rice–Tracey damage parameters indicator. Wulf (Wulf, 1985) carried out numerical studies of mechanical behavior and the crack path in the composites with these criteria, and compared the results with experiments. The simulations with the Rice–Tracey damage indicator produced excellent results for Al/SiC composites: both the crack paths in a real microstructure of the material and the force–displacement curves were practically identical in the experiments and simulations. The damage indicator, used by Wulf, is based on the model of a spherical void growth in a plastic material in a general remote stress field with high stress triaxiality, developed by Rice and Tracey (Rice and Tracey, 1969). The local damage condition is given by:

$$D = \int_0^{\varepsilon_{pl,c}} e^{3\eta/2} d\varepsilon_{pl} = D_{cr}$$

where D is the damage indicator, ε_{pl} is effective plastic strain, $\varepsilon_{pl,c}$ is critical plastic strain, η is stress triaxiality, $\eta = \sigma_H/\sigma_V$, σ_H is hydrostatic stress, σ_V is von Mises equivalent stress and D_{cr} is the critical value of the damage indicator ($D_{cr} = 0.2$). According to Fischer *et al.* (Fischer *et al.*, 1995), the results of the FE simulations with the Rice–Tracey damage indicator were 'in surprisingly good agreement with experimental observations'.

A possible alternative to the Rice–Tracey damage indicator for the simulation of crack growth in the Al matrix is the approach based on the constitutive equations for porous plasticity developed by Gurson (Gurson, 1977) and improved by Tvergaard (Tvergaard, 1981). According to Geni and Kikuchi (Geni and Kikuchi, 1998), the simulations with the Gurson model give results which are very close to the experimental data as well. Good results can be obtained by using the nonlocal version of the Gurson model (Reusch *et al.*, 2003).

In our further simulations, we use the critical maximum principal stress as a criterion of the failure of SiC particles, and the Rice–Tracey damage indicator, as a parameter of the void growth in the Al matrix.

6.3.2 Subroutine User Defined Field

In the following numerical analysis of the microstructure–strength interrelationships of composites, we simulate the initiation and growth of damage and cracks both in ceramic inclusions and in the matrix of the composite, using the FE weakening approach.

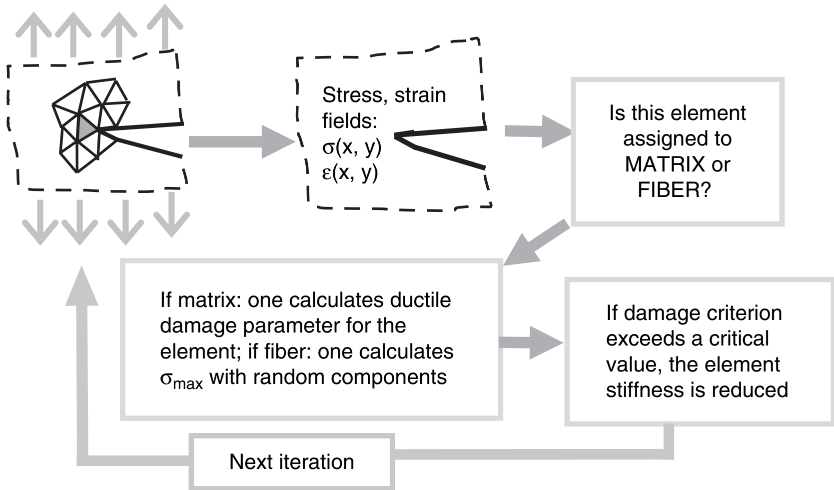

Figure 6.2 *Algorithm of the modeling of damage evolution in multiphase materials using element weakening approach (ABAQUS Subroutine User Defined Field).*

The ABAQUS Subroutine User Defined Field (USDFLD), which allows simulation of the local damage growth in both phases of Al/SiC composites as a weakening of FEs, was employed. In this subroutine, the phase to which a given FE in the model is assigned, is defined through the field variable of the element. Depending on the field variable, the subroutine calculates either the Rice–Tracey damage indicator (in the matrix) or the maximum principal stress (in particles). Another field variable characterizes the state of the element ('intact' versus 'damaged'). If the value of the damage parameter or the principal stress in the element exceeds the corresponding critical level, the second field variable of the element is changed, and the stiffness of the elements is reduced. The Young modulus of this element is set to a very low value (50 Pa, i.e. about 0.00001 % of the initial value). The critical level of the maximum principal stress can be either a constant value, or a random value with a predefined probability distribution. The number of failed elements are printed out in a file, which can be used to visualize the calculated damage distribution. Figure 6.2 gives a schema of the subroutine.

6.3.3 Interface debonding

Along with the particle cleavage and void growth in the Al matrix, the interface debonding between the SiC particles and the Al matrix plays an important role in the destruction of Al/SiC composites in many cases. According to Clyne and Withers (Clyne and Withers, 1993) and Mummery and Derby (Mummery and Derby, 1993), the interface debonding becomes the leading damage mechanism in the case of relatively small particles ($\sim<$ 10 μm).

In order to simulate the interface debonding in composites, the cohesive zone and interphase layer models are most often used. Needleman (Needleman, 1987) suggested to apply the cohesive crack model to analyze the interface decohesion. Schneider and Brocks (Schneider and Brocks, 2003) and Brocks (Brocks, 2004) implemented the cohesive zone model with the traction–separation law, as a User Element in ABAQUS. Segurado and Llorca (Segurado and Llorca, 2004) developed a 3D quadratic interface FE for the simulation of fracture in composites. The element can include any traction–separation law at the interface, and can be used to simulate both the interface decohesion and cleavage. Segurado and Llorca applied this interface element to simulate damage evolution in multiparticle unit cell models of composites.

Another approach is the *interphase layer model*, in which the interface is considered as a layer of finite thickness between two phases (Robertson and Mall, 1992; Jayaraman *et al.*, 1993). Recently, Tursun *et al.* (Tursun *et al.*, 2006) employed this approach to analyze the interface damage in Al/SiC particle reinforced composites. Chaboche *et al.* (Chaboche *et al.*, 1997) compared these two types of models (interphase layer and cohesive zone), and demonstrated that they lead to similar results, if the friction effects do not play a significant role.

Chandra and Ananth (Chandra and Ananth, 1995) proposed the spring layer model in which 'the interphase region is replaced by an interface of negligible thickness possessing the required strength'. The interface nodes are duplicated, and connected by springs, which can fail under some conditions. Chandra and Ananth modeled the interface debonding using the stress based failure theory.

In the following sections, we study Al/SiC composites with relatively large SiC inclusions and strong interfaces (Wulf, 1985). Therefore, only the particle cracking and void growth mechanisms of damage will be taken into account. In Chapter 10, we analyze the interface damage in unidirectional long fiber reinforced composites, using the interphase layer model.

6.4 Stability and reproducibility of the simulations

At this stage of the work, we seek to clarify whether the 'random' particle arrangements have peculiarities as compared with regular or localized particle arrangements, and whether these peculiarities are stable, reproducible and typical for the random arrangements.

Since the random particle arrangements were generated from a predefined random number seed parameter (idum) (which should ensure the reproducibility of the random number series), variations of this parameter lead to the generation of new microstructures. Five realizations of the random microstructures with 15 spherical particles and volume content of ceramic phase 10 % (produced with different random numbers seeds) were generated and tested.

Figure 6.3 shows the equivalent plastic strain distribution on the boundaries of the box and on the matrix–particle interfaces as well as in a vertical section in a unit cell with randomly arranged particles (VC = 5 % and 10 %).

Figure 6.4 (a) shows the tensile stress–strain curves for the five different random arrangements (15 particles, VC = 10 %). For comparison, we also included the curve for the regular and gradient particle arrangements. Figure 6.4(b) gives the amount of failed particles plotted versus the far field applied strain.

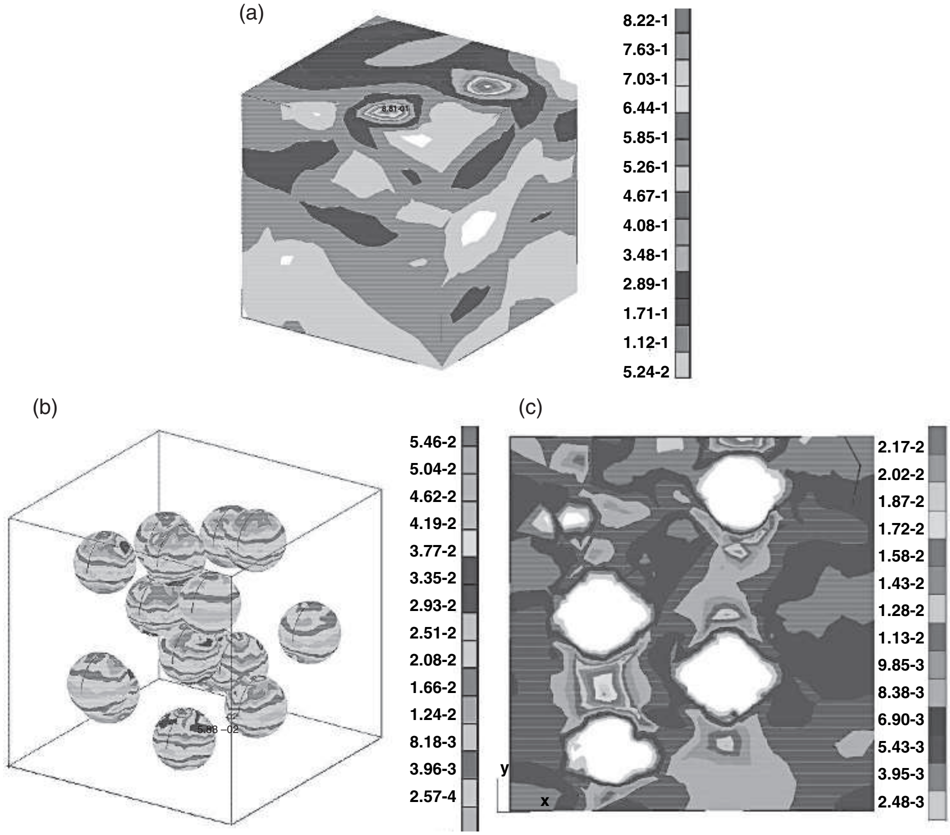

Figure 6.3 *Distribution of equivalent plastic strains (a) on the box boundary, (b) on the matrix–particle interface and (c) in a vertical section in a microstructure with random particle arrangements (15 particles,* VC = 10%*). Total strain* = 0.25. *Reprinted from* Acta Mater., **52** *(14), Mishnaevsky Jr, 'Three-dimensional…', pp.4177–4188, Copyright (2004), with permission from Elsevier. (See Plate 1)*

One can see from Figure 6.4 that the effective responses of the materials with random microstructures in different realizations lie very close to one another and differ from that for the regular or localized microstructures. However, some variations of both flow stress and damage behavior of different random microstructures are observed as well, especially after the far field strain exceeds 0.1. The difference between the stresses for different realizations of the same random structure falls in the range of 2 % even at the rather high far field strain ($\varepsilon = 0.2$). For comparison, the difference between the regular and gradient particle arrangement is about 16 % at the far field strain 0.2, and 9 % at the far field strain 0.1 (Figure 6.4). Therefore, although the stress–strain curves diverge a little when the strain is higher than 0.1, the differences between realizations of the random microstructure are still much smaller than the difference of the mechanical response between the different types of microstructures. In the following, at least three

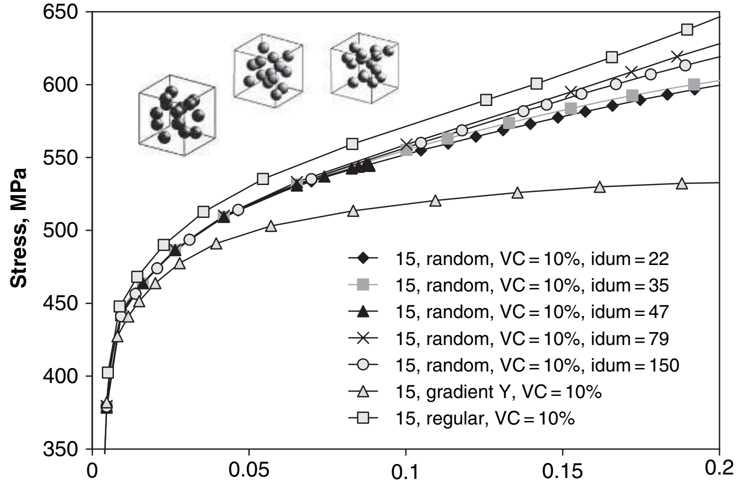

(a)

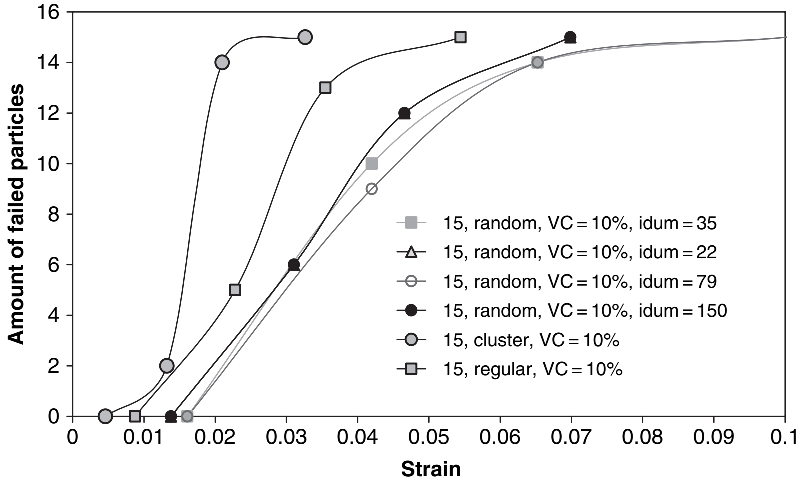

(b)

Figure 6.4 *(a) Stress–strain curves and (b) the fraction of failed particles plotted versus the far field strain for the five random arrangements (15 particles,* VC = 10 %*) and for the regular particle arrangement. Reprinted from* Acta Mater.*,* **52** *(14), Mishnaevsky Jr, 'Three-dimensional . . .', pp. 4177–4188, Copyright (2004), with permission from Elsevier.*

to five realizations of random microstructures will be simulated and averaged when a random microstructure is compared with other microstructures.

The rate of particle failure is lower for all the considered random particle arrangements than for the regular and clustered microstructures: the fraction of failed particles increases from 40 to 80 %, when the far field strain increases 2.8 times in the case of the random particle arrangement, and increases from 20 to 86 % when the far field strain increases 1.5 times for the regular particle arrangement.

One can see that the flow stress for the regular microstructure of the composite is higher than that for the random microstructures (in the following paragraphs, the regular microstructure ensures highest flow stress among all considered microstructures). It is of interest that in the simulations by Segurado *et al*. (Segurado *et al*., 2003) the flow stress for the regular BCC particle arrangement was significantly lower than for the random particle arrangement. The difference between our result and the results by Segurado and colleagues can be caused by the fact that the model, used by the authors, does not take into account the stress redistribution in the composite due to the reinforcement fracture. The varied distance between particles together with the effect of the interaction of cracks in neighboring particles in the case of the random particle arrangement can lead to the formation of weakened regions with high density of failed particles. The deformation of the weakened regions determines the low stiffness of the whole cell. This is not the case if the particles are placed equidistantly, as in the regular microstructures, and the local weakening in a particle is averaged over the entire specimen. Therefore, the constant large distance between particles, typical for the regular microstructures, can prevent the formation of weakened areas in our case, but not in the model by Segurado and colleagues.

6.5 Effect of the amount and volume content of particles on the deformation and damage in the composite

At this stage of the work, the effect of the volume content of hard phase and the amount of particles on the effective response and damage behavior of the composite were considered.

Figure 6.5 shows the tensile stress–strain curves for the random particle arrangements with varied amount of particle [VC = 5 %, amount of particles 5, 10 and 15, Figure 6.5(a), and the same for VC = 10 %, Figure 6.5(b)]. Figure 6.6 gives the tensile stress–strain curves for the regular particle arrangement with varied volume content of particles [10 particles, VC varied from 2.5 to 15 %, Figure 6.6(a), and 15 particles, VC varied from 5 to 15 %, Figure 6.6(b)]. Figure 6.7 shows the amount of failed particles in the box plotted versus the far field applied strain [10 particles, varied VC, Figure 6.7(a), and 15 particles, varied VC, Figure 6.7(b)].

In this case, the difference between the response of the composite with 5, 10 and 15 particles increases with increasing load, and the flow stress is higher for a composite with a higher amount of particles.

The curves of the amount of failed particles plotted versus the applied strain have an (almost) linear part (up to 10–12 particles of 15 fail) and an ‘asymptotic’ part (when the amount of failed particles slowly approaches the total amount of particles). Since the last part of the curve (‘asymptotic’) hardly reflects the real damage growth process, one may define a ‘critical applied strain’ as a far field applied strain at which the linear part of the curve goes into the ‘asymptotic’ part of the curve. In most cases, this takes place when approximately 80 % of particles (12 particles of 15, or 8 particles of 10) fail.

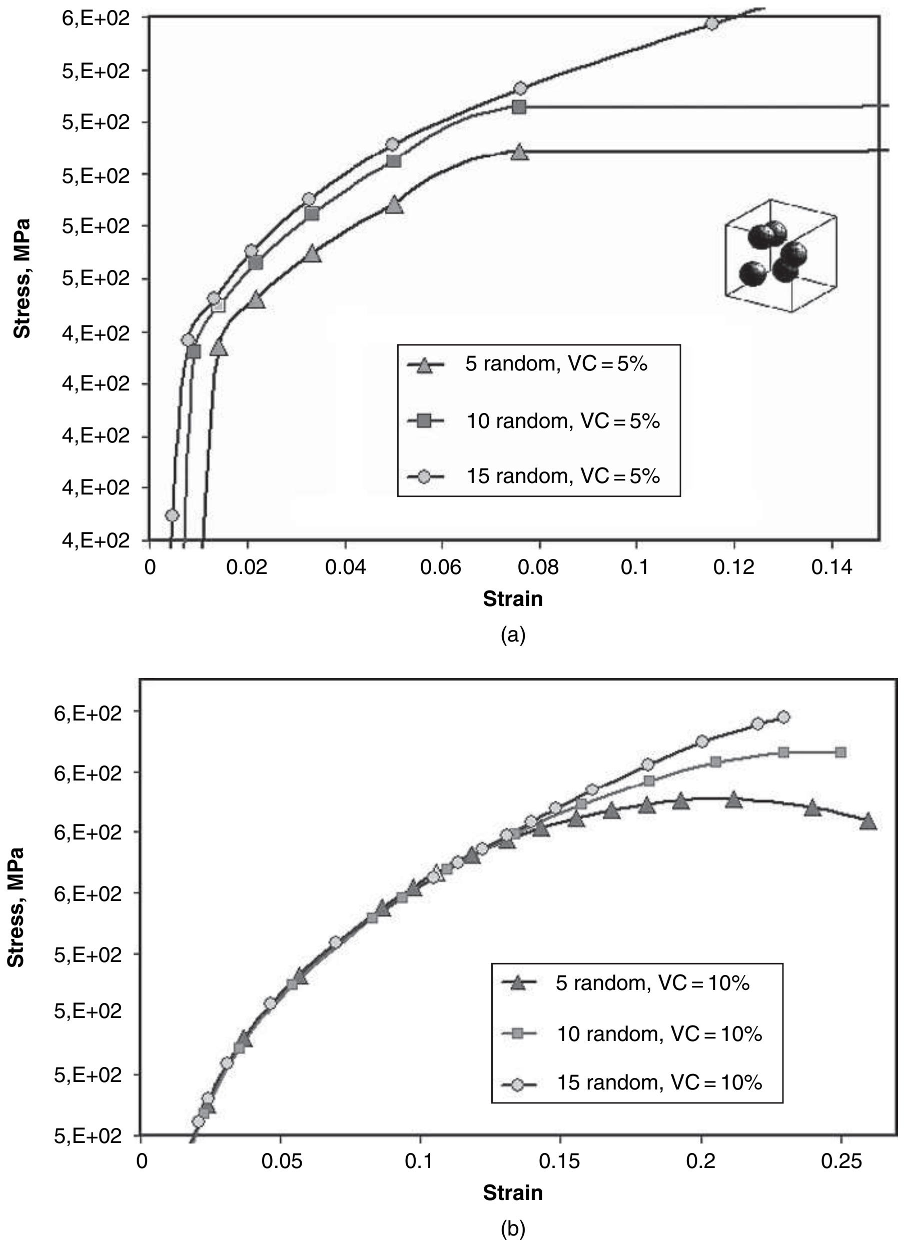

Figure 6.5 *Stress–strain curves for the random particle arrangement, [VC = 5 % (a) and 10 % (b); amount of particles 5, 10 and 15]. Reprinted from* Acta Mater., **52** *(14), Mishnaevsky Jr, 'Three-dimensional . . . ', pp. 4177–4188, Copyright (2004), with permission from Elsevier.*

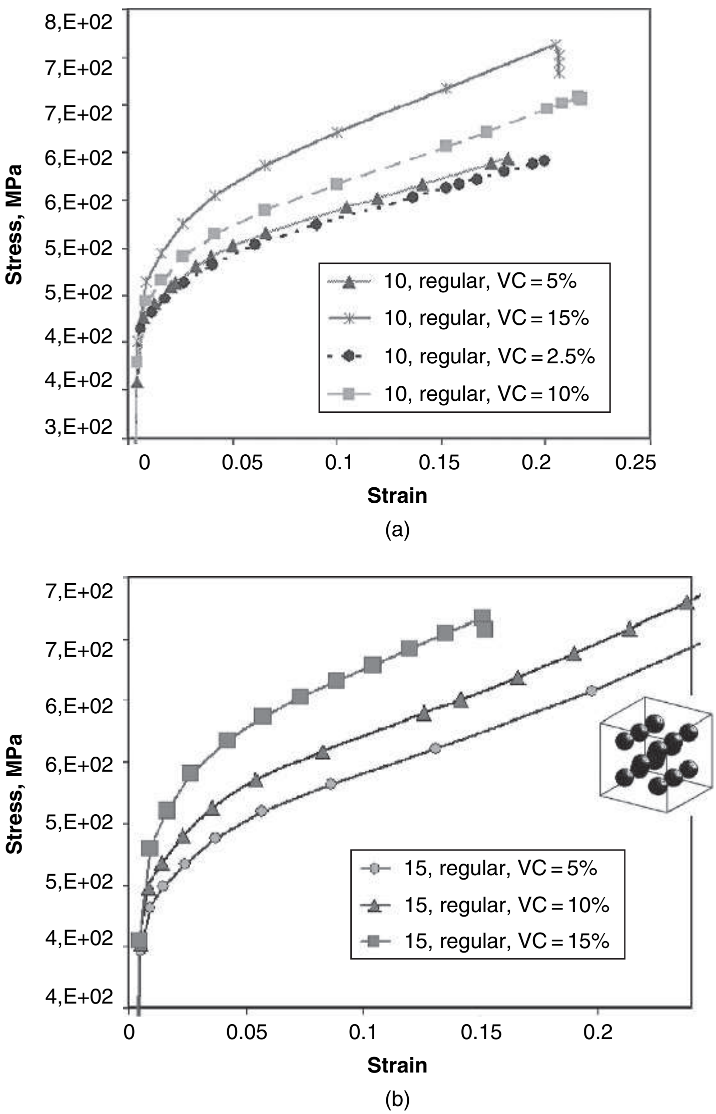

Figure 6.6 *Stress–strain curves for the regular particle arrangement: (a) 10 particles; (b) 15 particles, (varied volume content). Reprinted from* Acta Mater., **52** *(14), Mishnaevsky Jr, 'Three-dimensional . . . ', pp. 4177–4188, Copyright (2004), with permission from Elsevier.*

The critical applied strain depends on the volume content of particles as well. One can see from Figure 6.7, that the higher the volume content of particles, the lower is the critical applied strain. An increase in the volume content of particles by 5 % leads to a decrease of the critical applied strain by 4–5 %, for cells with both 10 and 15 particles.

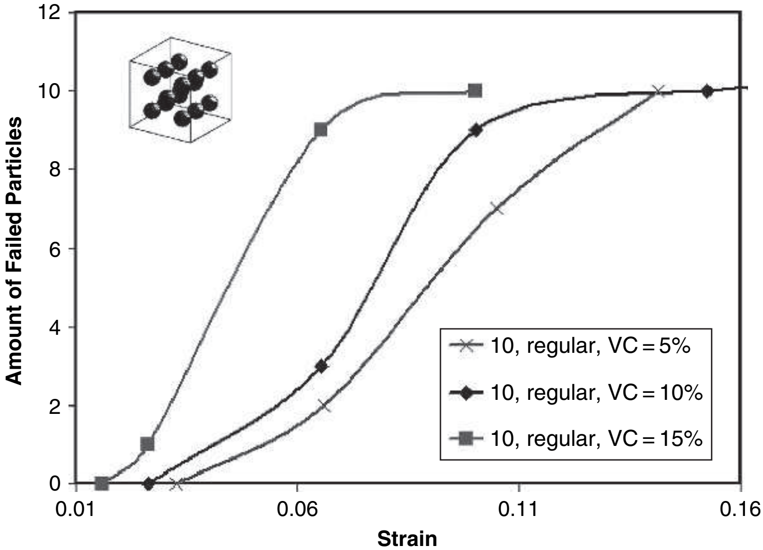

(a)

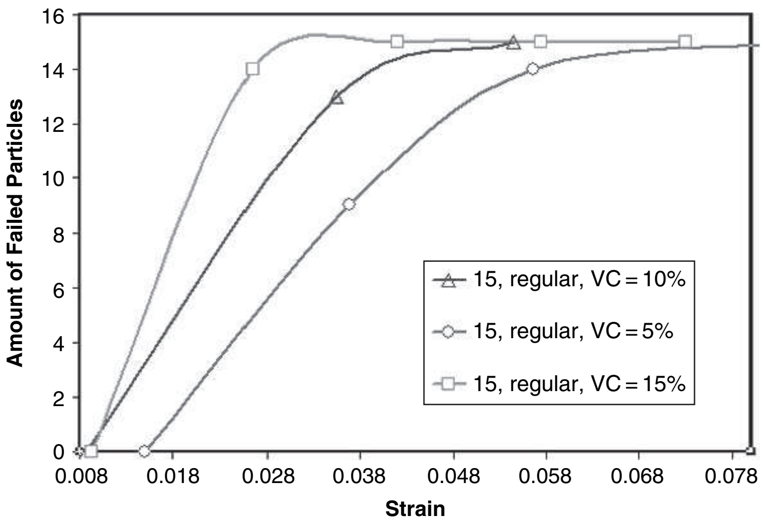

(b)

Figure 6.7 *Amount of failed particles in the box plotted versus the far field applied strain: (a) 10 particles; (b) 15 particles (varied volume content). Reprinted from* Acta Mater.*,* **52** *(14), Mishnaevsky Jr, 'Three-dimensional . . . ', pp. 4177–4188, Copyright (2004), with permission from Elsevier.*

6.6 Effect of particle clustering and the gradient distribution of particles

At this stage of the work, the effects of particle arrangement and localization on the deformation and damage evolution in the composite were considered.

Two types of gradient particle arrangements were considered: an arrangement of particles with the vector of gradient (from the high particle concentration region in the upper part of the cell to the low particle concentration region in the lower part of the cell) coinciding with the loading direction (called in the following a 'gradient Y' microstructure), and a microstructure with the gradient vector perpendicular to the loading vector (called in the following a 'gradient Z' microstructure). The standard deviations of the normal distribution of the Y or Z coordinates of the particle centers (for the Y and Z gradient microstructures, respectively) were taken as 2 mm, ensuring a rather high degree of gradient. The same standard deviations were taken for the clustered particle arrangements.

Figure 6.8 shows the tensile stress–strain curves for the random, regular and gradient microstructures [for 10 particles, VC = 5 %, Figure 6.8(a)] and for the random, regular, clustered and gradient microstructures [for 15 particles, VC = 10 %, Figure 6.8(b,c)]. Figure 6.9 shows the amount of failed particles in the box plotted versus the far field applied strain, for the same microstructures (15 particles, VC = 5 % and 10 %).

It can be seen from Figure 6.9, that the particle arrangement hardly influences the effective response of the material in the elastic area or at small plastic deformation. The influence of the type of particle arrangement on the effective response of the material becomes significant only at the load at which the particles begin to fail (cf. Figures 6.8 and 6.9). However, after the particle failure begins, the effect of particle arrangement increases with increasing applied load. (One should note here the difference with the case when only the amount of particles and neither their content nor the arrangement vary: in this case, the difference becomes sufficiently large only when most particles fail, see Figure 6.5; in the case of the different particle arrangements, the influence of the arrangement becomes strong when the first particle fails.)

After the first particle fails, the flow stress of the composite and the strain hardening coefficient increase with varying the particle arrangement in the following order:

gradient<random<clustered<regular microstructure

(see Figure 6.8).

In order to analyze the effect of particle arrangement on the strain hardening quantitatively, we determined the stress hardening coefficients for the stress–strain curves shown in Figure 6.8. The strain hardening coefficients were calculated as the power in the power-like equation for the true stress-true strain curves, using the regression analysis. Table 6.1 shows the strain hardening coefficients (n) for all the considered curves.

For all the levels of volume content, the particle failure rate is two to three times higher for the cells with 15 particles, than for the cells with 10 particles: 18–29 particles mm^{-1} (for the cells with 15 particles and regular particle arrangement) and 45–90 particles mm^{-1} (for the cells with 10 particles).

One can see from Figure 6.8 that the critical applied strain decreases in the following order: gradient (10 %)>gradient (5 %)> random (5 %)>regular (5 %), random

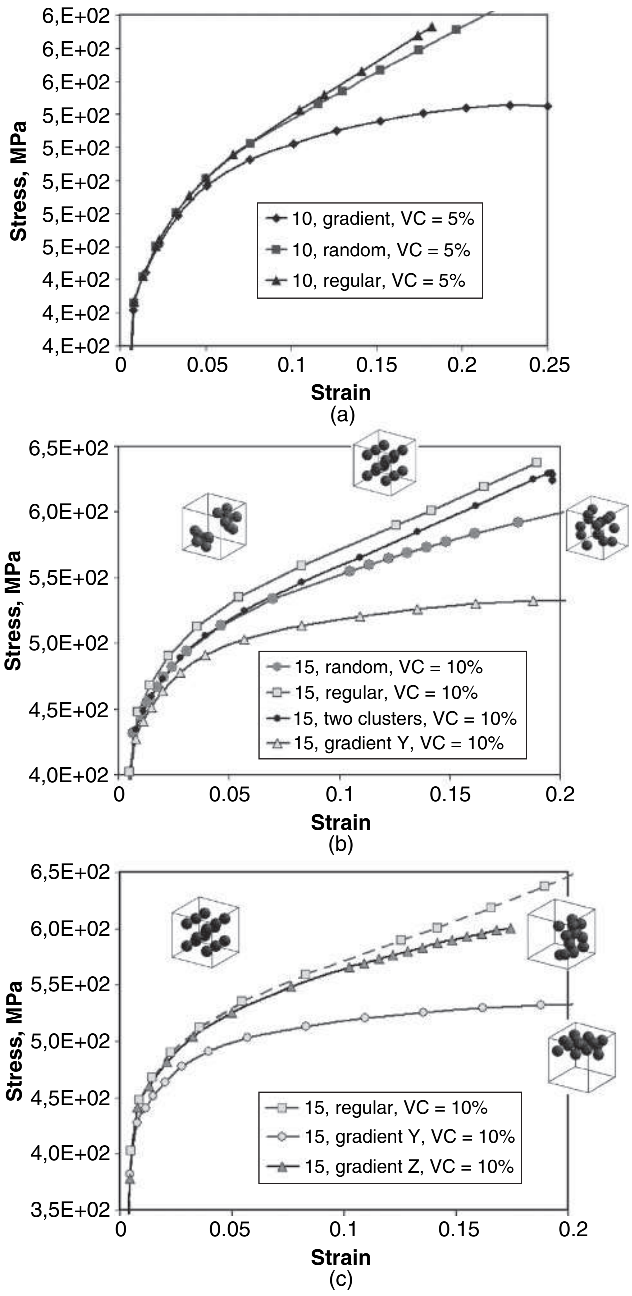

Figure 6.8 *Stress–strain curves for the unit cells with different particle arrangements: (a) 10 particles,* VC = 5%; *(b, c) 15 particles,* VC = 10%. *Reprinted from* Acta Mater., **52** *(14), Mishnaevsky Jr, 'Three-dimensional . . . ', pp. 4177–4188, Copyright (2004), with permission from Elsevier.*

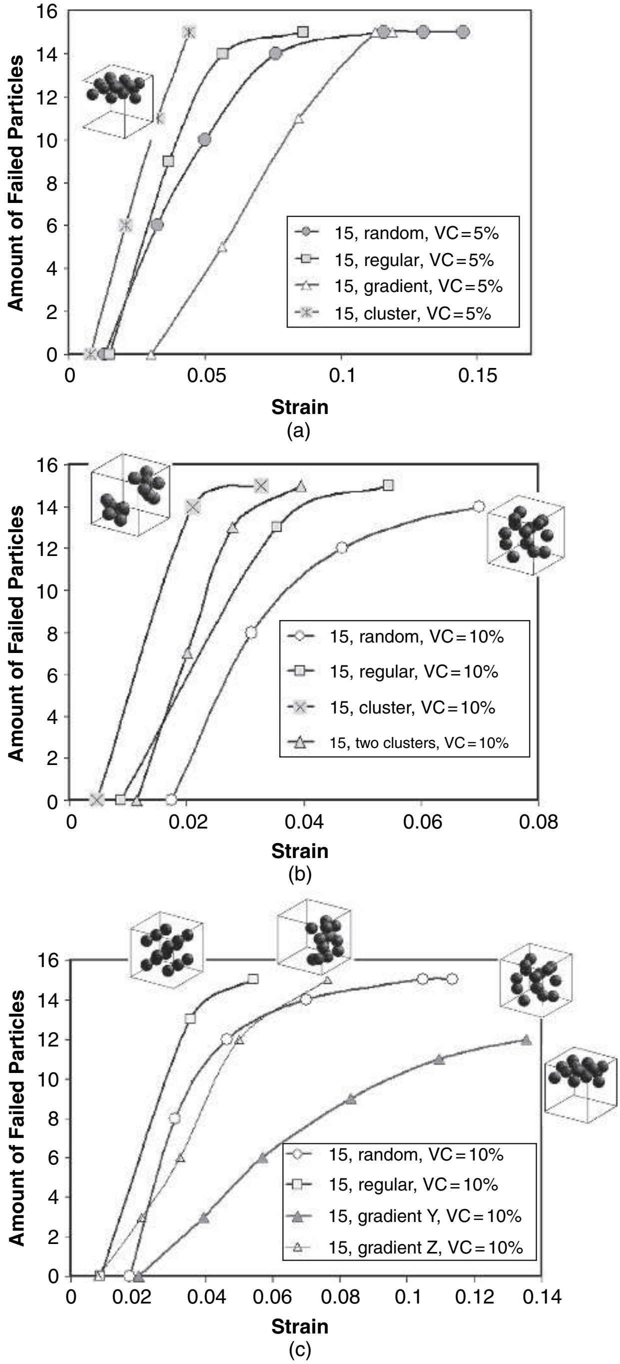

Figure 6.9 *Amount of failed particles plotted versus the far field strain: (a) 15 particles,* VC = 5 %*; (b, c) 15 particles,* VC = 10 %*. Reprinted from* Acta Mater.*,* **52** *(14), Mishnaevsky Jr, 'Three-dimensional . . . ', pp. 4177–4188, Copyright (2004), with permission from Elsevier.*

Table 6.1 *Calculated strain hardening coefficients for different particle arrangements.*

Particle arrangement	Random	Regular	Clustered	Grad. (Y)	Grad. (Z)
n	0.1284	0.193	0.1676	0.1227	0.1543

(10 %)>cluster (5 %) and regular (10 %)>clustered (10 %) (the volume contents of the SiC phase are given in parentheses).

Separating the effects of the volume content and the particle arrangements, one can see that the critical applied strain increases in the following order:

clustered regular<random<gradient particle arrangements

The strength and damage resistance of a composite with a gradient microstructure strongly depends on the orientation of the gradient in relation to the direction of loading. In the case of the 'gradient Y' microstructure, the rate of particle failure is very low (about 6.35 particles mm^{-1}) and the particle failure begins at relatively high displacement loading, 0.2 mm. In the case of the 'gradient Z' microstructure, the rate of particle failure is the same as for random microstructures.

One should note that the high gradient distributions of particles, considered here, constitute just one snapshot of many possible arrangements. Apparently, if the arrangement of particles changes from the high gradient arrangement, considered here, to the arrangements with more slow gradients, the properties of the material will be changed. This is the subject of the investigations presented in the next sections.

To characterize quantitatively the arrangements of particles and the degree of localization in different microstructures, we determined the nearest-neighbor distances (NNDs) between the particle centers, the nearest-neighbor index (NNI, ratio of observed to expected NND) and the statistical entropy of the nearest-neighbor distance (SENND).

The accurate determination of these parameters requires a much larger amount of particles than those necessary to compute the mechanical behavior and those considered in the unit cells above.

To overcome this limitation, we generated unit cells of the size $100 \times 100 \times 100$ mm with random, clustered and uniform particle arrangements using the same algorithms as for the simulated cells (s. §5.3.1.4). The values of NND, NNI and the SENND, determined from the cells, are given in Table 6.2. The scattering of the distribution of the NND, characterized by the statistical entropy of the distribution, decreases with decreasing the average value of the NND. One can see that the generated random microstructure is really close to the ideal random (NNI = 1.17 versus 1.0 in the ideal case) and that the degree of clustering/localization in the generated gradient and clustered microstructures is rather high.

From the simulations presented, one may draw the following conclusions. The arrangement of particles influences first of all the strain hardening rate and the damage behavior

Table 6.2 Nearest-neighbor distance between particle centers in the considered microstructures.

Microstructure	Average NND (mm)	SENND	NNI
Random	12.69	2.55	1.17
Clustered	2.70	1.26	0.25
Gradient	5.85	2.31	0.54

of composites. This is a remarkable difference from the effect of the volume content of inclusions, which influences the flow stress, not just its slope, i.e. strain hardening rate.

The regular particle arrangement ensures the highest flow stress of a composite, especially, after the particle failure begins. The discrepancy between our results and the results by Segurado and colleagues (Segurado *et al.*, 2003) is discussed above.

The clustered particle arrangement leads to a very high damage growth rate, and to a low critical applied strain. However, no negative effect of particle clustering on the effective response of the composite was noted. This conclusion is in agreement with the numerical conclusions by Segurado and colleagues ('the increase in strength due to clustering is almost negligible for the matrix and reinforcement properties typically found in metal matrix composites').

6.7 Effect of the variations of particle sizes on the damage evolution

At this stage of the work, the effects of the scattering of the particle sizes on the effective response and damage behavior of the composite were investigated. The radii of particles were taken as random values, following the normal probability distribution law. Microstructures with randomly arranged particles of random sizes were generated, using the program Meso3D. The degree of scattering of particle sizes, which was characterized by a standard deviation of the normal distribution law, was varied at the level of 0.1, 0.25 and 0.5 of the average particle radius (which was 1.1676 mm for the cell with 15 particles and VC = 10 %). In order to keep the volume content of particles constant, the randomly distributed radii of particles were normalized. Table 6.3 gives the maximum and minimum sizes of particles for the considered values of the standard deviations.

Table 6.3 Maximum and minimum sizes of particles for considered probability distributions of the particle radii.

Standard deviation of radii distribution/mean radius, $\Delta r/r$	Standard deviation of r, Δr	Maximum particle radius, r_{max}	Minimum particle radius, r_{min}
0.10	0.1168	1.6595	0.7021
0.25	0.2919	1.8506	0.6282
0.50	0.5838	1.9951	0.1582

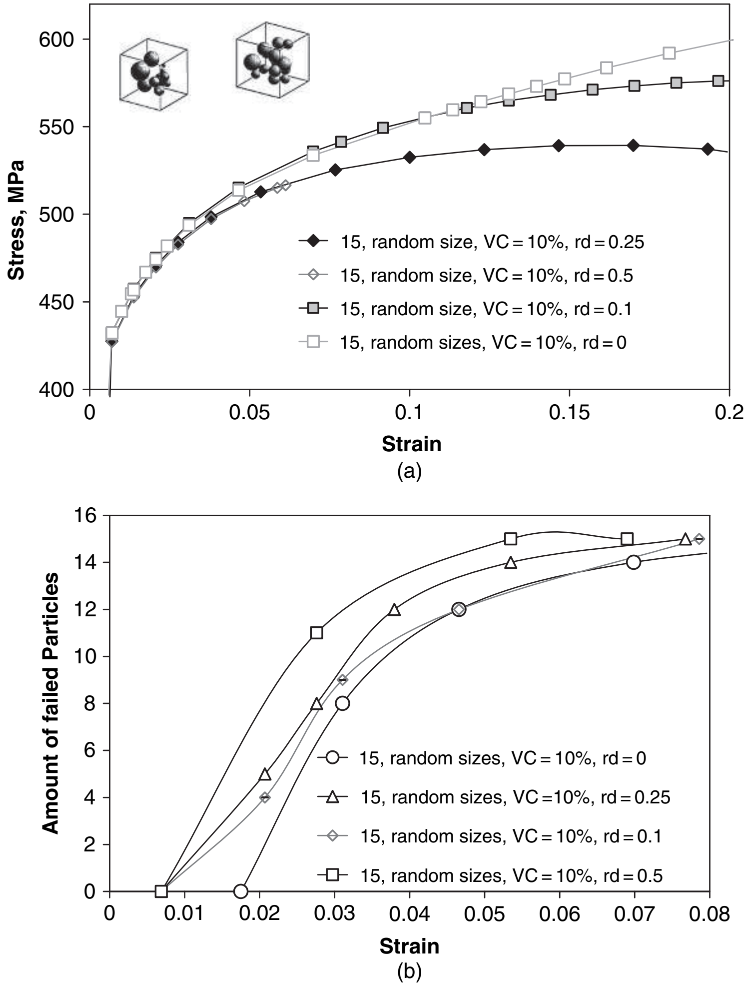

Figure 6.10 *(a) Stress–strain curves and (b) the amount of failed particles plotted versus the far field strain for the microstructures with particles of randomly distributed sizes. Reprinted from* Acta Mater.*,* **52** *(14), Mishnaevsky Jr, 'Three-dimensional . . . ', pp. 4177–4188, Copyright (2004), with permission from Elsevier.*

Figure 6.10 shows the tensile stress–strain curves and the amount of failed particles plotted versus the far field strain for these microstructures.

One can see from Figure 6.10 that the variations of the particle sizes result in a strong decrease in the strain hardening rate of the composite during the elastoplastic deformation with damage. The differences in the effective responses of the composites with different degrees of scattering of particle sizes are negligible in the elastic region, but become rather large when the particles begin to fail, and increase with increasing density of failed particles.

From Figure 6.10 it can be seen that the damage evolution in the particles begins at some lower applied strain when the particle sizes vary (0.069 mm versus 0.175 mm, when the particle radii are constant). Also, the critical applied strain is about 22 % lower for the random particle sizes with standard deviation $0.5r$, and about 60 % lower for the random particle sizes with standard deviation $0.25r$, than for the homogeneous particle radii. The difference between the cases of the constant particle radii and the randomly distributed with deviation $0.1r$ is negligible, but becomes rather large for the deviations of $0.25r$ and $0.5r$. Therefore, the scattering of particle sizes leads generally to quicker and earlier damage growth in the composites.

6.8 Ranking of microstructures and the effect of gradient orientation

Figure 6.11(a) shows values of flow stresses, corresponding to the applied displacement $u = 0.15$ mm, for all the unit cells with 15 particles and VC = 10 %. For comparison purposes, the values of flow stresses for the regular particle arrangements with VC = 5 % and 15 % are shown. The column charts of the critical applied strain, shown in Figure 6.11(b), illustrates the effect of the particle arrangement on the damage growth in the composites. Comparing Figure 6.11(a) and (b), one may see the general tendency: the higher the stiffness and the flow stress of a composite, the lower the critical failure strain. (There are, however, some deviations from this.)

Figure 6.12 shows the critical applied strain (at which the linear 'quick growth' part of the curve of the fraction of failed particles versus far-field strain goes into the 'asymptotic' part of these curves) plotted versus the flow stress of the composite at displacement 0.15 mm for all the cells with 15 particles.

Considering the ranking of the microstructures in Figure 6.11, one can see that the gradient microstructures demonstrate a very high damage resistance as compared with the isotropic (random, uniform and clustered) microstructures. The isotropic (random, uniform or clustered) microstructures are grouped in the left part (low critical strain) of the figure. From all the isotropic microstructures, the clustered microstructure ensures the lowest damage resistance.

The big difference between the mechanical behavior of the gradient Y (gradient particle arrangement with a gradient vector coinciding with the loading vector) and gradient Z (gradient particle arrangement with a gradient vector normal to the loading vector) composites is of interest. Both microstructures (gradient Z and gradient Y) show high damage resistances, but the flow stress of these structures differs. The effect of the orientation of the gradient vector on the flow stress and damage resistance of the composite can be explained by using an (oversimplified) illustrative representation of the gradient material as a bilayer material, consisting of a plastic layer (i.e. the part of the composite with a low content of particles) and a stiff layer (i.e. the part of composite with a very high content of particles). If the material is loaded along the gradient direction, the stiffness of the material is controlled by the stiffness of the high particle density region (which is rather firm, according to the results of Section 6.5). Therefore, the stiffness of the gradient Z composite is quite high, and particle failure goes rather quickly. In the case of gradient Y, the plastic flow of the material is controlled by the lower sections of the cell, with small density of particles. Therefore, the flow stress of such a material is quite

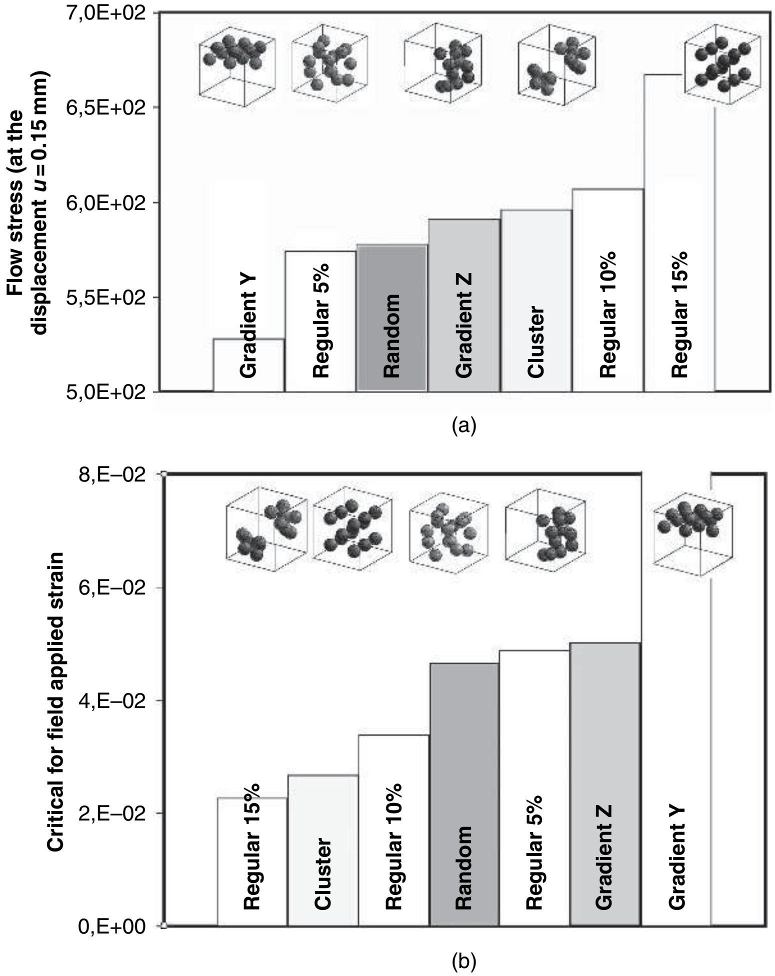

Figure 6.11 *(a) Flow stress (at the displacement u* = 0.15 mm*) and (b) critical far field applied strain for different particle arrangements. Reprinted from* Acta Mater.*,* **52** *(14), Mishnaevsky Jr, 'Three-dimensional . . . ', pp. 4177–4188, Copyright (2004), with permission from Elsevier.*

low (close to the flow stress of the pure matrix). One can draw a conclusion that if the regions of high particle density are arranged in such a way that they form a load-bearing construction (gradient Z structure) or play a role of a 'super-reinforcement' (clustered structure), that leads to a quick failure of many particles in the regions. Otherwise, if the high particle density region does not form a load-bearing construction (gradient Y microstructure), the flow stress of the material is relatively low (since the plastic flow is controlled by the regions of low particle density), yet, the intensity of damage failure is relatively low as well.

Summarizing the results of the numerical experiments presented in this chapter, one may state that:

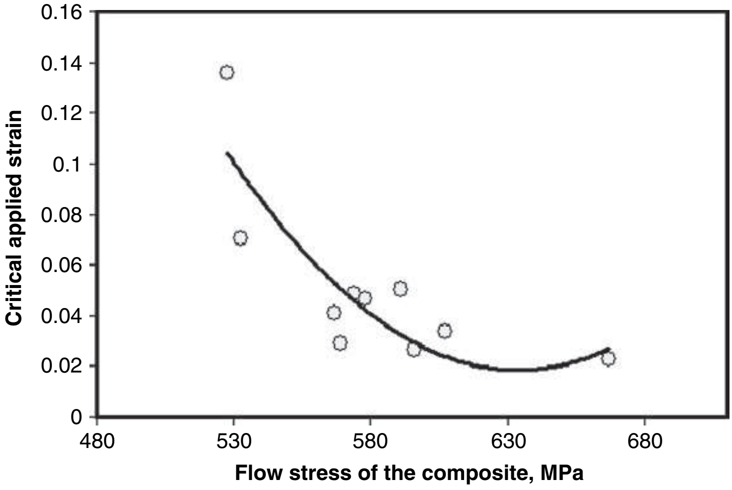

Figure 6.12 *Critical applied strain (at which 80 % of particles fail) plotted versus the flow stress of the composite (at the far field strain 0.15 mm) for all the cells with 15 particles. Reprinted from* Acta Mater.*,* **52** *(14), Mishnaevsky Jr, 'Three-dimensional . . . ', pp. 4177–4188, Copyright (2004) with permission from Elsevier.*

- The particle arrangement influences the effective response of the material only at the load at which the particles begin to fail. In this case, *the flow stress of the composite and the strain hardening coefficient increase with varying the particle arrangement in the following order: highly gradient < random < clustered < regular microstructure. The critical applied strain decreases in almost the reverse order: highly gradient > random > regular > clustered.*
- The variations of the particle sizes lead to the strong decrease in the strain hardening rate, and to the quicker and earlier damage growth in the composites.

References

Baptiste, D. (1999). Damage behaviour of composites, Cours de formation, 23–30/08, Jesi, Italy.

Brocks, W. (2004). Computational fracture mechanics, in: *Continuum Scale Simulation of Engineering Materials: Fundamentals - Microstructures - Process Applications*, Eds D Raabe, F. Roters, F. Barlat and L.-Q. Chen, John Wiley & Sons, Ltd, Wanherm, pp. 621–633.

Chaboche, J. L., Girard, R. and Schaff, A. (1997). Numerical analysis of composite systems by using interphase/interface models, *Computational Mechanics*, **20** (1–2), 3–11.

Chandra, N. and Ananth, C. R. (1995). Analysis of interfacial behavior in MMCs and IMCs by the use of thin-slice push-out tests, *Composites Science and Technology*, **54** (1), 87–100.

Clyne, T. W. and Withers, P. J. (1993). *An Introduction to Metal Matrix Composites*, Cambridge University Press, Cambridge.

Derrien, K. (1997) Modélisation par des méthodes d'homogénéisation de l'endommagement et de la rupture de composites Al/SiCp, PhD Thesis, ENSAM, Paris.

Derrien, K., Baptiste, D. Guedra-Degeorges, D. and Foulquier, J. (1999). Multiscale modelling of the damaged plastic behaviour of AlSiCp composites, *International Journal of Plasticity*, **15**, 667–685.

Fischer, F. D., Kolednik, O., Shan, G. X. and Rammerstorfer, F. G. (1995). A note on calibration of ductile failure damage indicators, *International Journal of Fracture*, **73**, 345–357.

Geni, M. and Kikuchi, M. (1998). Damage analysis of aluminum matrix composite considering non-uniform distribution of SiC particles, *Acta Materialia*, **46** (9), 3125–3133.

Gurson, A. L. (1977). Continuum theory of ductile rupture by void nucleation and growth: Part I. Yield criteria and flow rules for porous ductile media, *Journal of Engineering Materials Technology*, **99**, 2–15.

Hu, G., Guo, G. and Baptiste, D. (1998). A micromechanical model of influence of particle fracture and particle cluster on mechanical properties of MMCs, *Computational Materials Science*, **9**, 420–430.

Jayaraman, K., Reifsnider, K. L. and Swain, R. E. (1993). Elastic and thermal effects in the interphase: part II. Comments on modeling studies, *Journal of Composites Technology and Research*, **15**, 14–22.

Mummery, P. and Derby, B. (1993). Fracture behavior, in: *Fundamentals of Metal-Matrix Composites*, Eds S. Suresh, A. Mortensen, and A. Needleman, Elsevier, Boston, p 251.

Needleman, A. (1987). A continuum model for void nucleation by inclusion debonding, *Journal of Applied Mechanics*, **54**, 525–531.

Reusch, F., Svendsen, B. and Klingbeil, D. (2003). A non-local extension of Gurson-based ductile damage modeling, *Computational Material Science*, **26**, 219–229.

Rice, J. R. and Tracey, D. M. (1969). On the ductile enlargement of voids in triaxial stress fields, *Journal of the Mechanics and Physics of Solids*, **17**, 201–217.

Robertson, D. D. and Mall, S. (1992). Fiber-matrix interface effects upon transverse behavior in metal-matrix composites, *Journal of Composites Technology and Research*, **14**, 3–11.

Schneider, I. and Brocks, W. (2003). The effect of the traction separation law on the results of cohesive zone crack propagation analyses, *Key Engineering Materials*, **251–252**, 313–318.

Segurado, J. and LLorca, J. (2004). A new three-dimensional interface finite element to simulate fracture in composites, *International Journal of Solids and Structures*, **41**, 2977–2993.

Segurado, J., González, C. and LLorca, J. (2003). A numerical investigation of the effect of particle clustering on the mechanical properties of composites. *Acta Materialia*, **51**, 2355–2369.

Tursun, G., Weber, U., Soppa, E. and Schmauder, S. (2006). The influence of transition phases on the damage behaviour of an Al/10vol.%SiC composite, *Computational Materials Science*, **37** (1–2), 119–133.

Tvergaard, V. (1981). Influence of voids on shear band instabilities under plane strain conditions, *International Journal of Fracture*, **17** (4), 389–407.

Wulf, J. (1985). Neue Finite-Elemente-Methode zur Simulation des Duktilbruchs in Al/SiC, Dissertation MPI für Metallforschung, Stuttgart.

Wulf, J., Schmauder, S. and Fischmeister, H. F. (1993). Finite element modelling of crack propagation in ductile fracture, *Computational Materials Science*, **1**, 297–301.

7

Graded particle reinforced composites: effect of the parameters of graded microstructures on the deformation and damage

In Chapter 6 it has been demonstrated that particle reinforced metal matrix composites with graded particle arrangement ensure highest damage resistance, as compared with other arrangements of particles (homogeneous, random, clustered). Furthermore, it has been shown that while the damage resistance of graded composites remains the highest among all the considered microstructures independently of the orientation of the gradient vector with regard to the loading vector, the actual value of the critical applied strain does depend on the orientation.

Here we investigate the effects of the parameters of graded microstructures of composites (degree of gradient, shape and orientations of particles, etc.) on the deformation behavior and the damage resistance, using the mesomechanical FE simulations of the deformation and damage evolution in different microstructures of graded composites. In order to simplify the simulations and to take into account statistical effects (which requires models and analyses with a high amount of inclusions), the simulations have been carried out two-dimensionally.

The problems of the computational analysis of functionally gradient materials (FGMs) and the optimal numerical design of FGMs have attracted great interest from the scientific community over the last few decades. Many authors studied the deformation and strength of the gradient materials using analytical and numerical micromechanical methods. Table 7.1 gives a short overview of some of the work in this area.

On the basis of Table 7.1, one may identify the following two groups of models of strength and reliability of graded materials: one group generalizes and pushes the

Computational Mesomechanics of Composites L. Mishnaevsky Jr

Table 7.1 *Micromechanical analysis of deformation and strength of graded materials.*

Reference	Main concepts and results
Hirano *et al.*, 1990	*Rule-of-mixture*: Hirano *et al*. used the rule-of-mixture and the fuzzy set model of the transition from the region of high content of the filler to the matrix to develop an inverse design procedure for the determination of the synthesis method for required properties of FGMs
Zuiker and Dvorak, 1994a,b	*Mori–Tanaka method* of the estimation of overall properties of statistically homogeneous composites is applied to linearly variable overall and local fields. It was shown that the linear and constant field approaches 'provide different estimates of overall properties for small representative volumes, but nearly identical estimates for large volumes'
Reiter *et al.*, 1997	*Micromechanical FE model* of graded C/SiC composites consisting of up to thousands of inclusions. In the simulations, planar gradient arrangements of hexagonal inclusions with a linear volume gradient, and different transitions between the phases (i.e. microstructures with a distinct threshold between two matrix phases, with the skeletal transition zones, and mixed microstructures) were considered. Further, Reiter *et al.* presented the FGM as a number of piecewise homogeneous layers, and determined the properties of the layers using the Mori–Tanaka and self-consistent methods. It was shown that the averaging methods can be well used to characterize the graded materials in the framework of the model of piecewise homogeneous layers.
Weissenbek *et al.*, 1997	*Micromechanical numerical and analytical* (*mean-field approach* involving an incremental Mori–Tanaka analysis and the *rule-of-mixture*) models were used to analyze elastoplastic deformation due to thermal and mechanical loading of layered metal/ceramic Ni/Al_2O_3 composites with compositionally graded interfaces. Planar geometries with perfectly periodic arrangements of the constituent phases were considered using the square-packing and hexagonal-packing unit cell formulations for the graded material. Then, *unit cells*, containing large numbers of randomly placed microstructural units of two phases were used. It was found that square-packing arrangements provide the best possible bounds for the thermal strains and coefficient of thermal expansion of the graded multilayer, among the different unit cell models examined
Buryachenko and Rammerstorfer, 1998	Generalized *multiparticle effective method* (Buryachenko, 1996): FGMs were simulated as linear thermoelastic composites with elliptical inclusions, arranged in a way that the concentration of the inclusions is a function of the coordinates. Assuming that the effective field near the inclusion is homogeneous, and taking into account the binary interaction effects of the inclusions, the authors considered the joint actions of nonlocal effects, caused by the inhomogeneous inclusion number density and inhomogeneous average applied stress and temperature fields, and derived a general integral equation for the FGMs
Aboudi *et al.*, 1999	*Higher-order theory* for functionally graded materials, which explicitly couples the microstructural (local) and global effects, without using the concept of RVE, is developed on the basis of Aboudi's *method of cells*. The microstructure of the composite is discretized into a lattice of cells, which are divided in turn into subcells. The approximate solutions for temperature and displacement fields are obtained by approximating the fields in each subcell using a quadratic expansion centered at the subcell mid-point. The authors obtained the stress distributions in the FGMs and carried out the optimization of the fiber distribution in the composite

Cannillo *et al.*, 2002	FE software *OOF* and the probabilistic model of brittle fracture were used to study the crack growth in graded alumina glass. The authors analyzed the effect of stochastic placement of the second phase on the hardness and toughness of the material. The variations of the damage parameter versus applied strain curves for different random realizations of the microstructures are determined
Becker Jr *et al.*, 2002	The *nonlocal brittle fracture model* [Ritchie–Knott–Rice (RKR) fracture model], based on Weibull statistics, was used to analyze the fracture initiation ('first activated flaw') near a crack in FGMs. The dependencies of the initiation fracture toughness (i.e. the stress intensity factor that will result in a stated first failure probability) on the phase angle of crack tip as well as on the parameters of the Weibull law, were determined using FEM. Becker Jr *et al*. demonstrated numerically and analytically that the gradient in Weibull scaling stress leads to a decrease of initiation fracture toughness, and that 'gradients normal to the crack result in a crack growing toward the weaker material'. It was shown that the distribution of damage near a crack tip depends strongly on the Weibull modulus: for a high Weibull modulus, 'failure is dominated by the very near-tip parameters, and effects of gradients are minimized. With low m, distributed damage leading to toughening can be exaggerated in FGMs'
Gasik, 1995, 1998	3D model of FGMs with 'chemical' gradient as an ***array of subcells*** (local RVEs) was implemented as new software, which allows elastic and thermal properties of the composite to be calculated

limits of analytical micromechanical models, developed initially for nongradient materials (rule-of-mixture, Mori–Tanaka method, multiparticle effective method); another group is based on the methods of numerical experiments, in particular, multiparticle unit cells and FEM.

In this chapter, we use the second approach to analyze the effect of microstructures of graded composites on their strength and damage resistance.

7.1 Damage evolution in graded composites and the effect of the degree of gradient

The purpose of this part of the investigation was to clarify how the degree of gradient influences the strength and damage evolution in the composites. The deformation and damage evolution of Al/SiC composites with gradient SiC particle arrangements (with different degrees of gradient) were simulated numerically.

A number of 2D unit cells with graded arrangement of SiC inclusions have been generated, using the program Meso3D (2D version). As noted in Chapter 5, the program Meso3D controls the gradient degree of a particle arrangement by varying the standard deviation of the normal probability distribution of the distances between the Y-coordinates of the particle centers and of the upper boundary of the cell. Since the X-coordinates of particles are generated with a predefined random number seed parameter (idum) (which should ensure reproducibility of the simulations), the variation of this parameter leads to the generation of new realizations of microstructures with the same gradient.

Many graded microstructures with different standard deviations of the distributions of Y-coordinates (which ensured different gradient degrees) and with different random number seed parameter for random X-coordinates were generated, meshed and tested. At this stage of the analysis, only round particles were considered. Both the failure of SiC particles (critical maximum stress criterion) and the void growth in the Al/SiC matrix (Rice–Tracey damage criterion) were simulated, using the element weakening approach.

The generated unit cells were subject to a uniaxial tensile displacement loading (1 mm) (see Figure 7.1).

Figure 7.2 shows several examples of the generated microstructures. The degree of gradient characterized by the standard deviation (SD) of the normal distribution of distances between the particle centers and the upper rand of the cell, is denoted as follows: for instance, Grad3 means that the SD 0.3 of the cell size (= 3 mm) (Mishnaevsky Jr, 2005c, 2006). Similarly, Grad8 means SD = 0.8 of the cell size or 8 mm. In order to

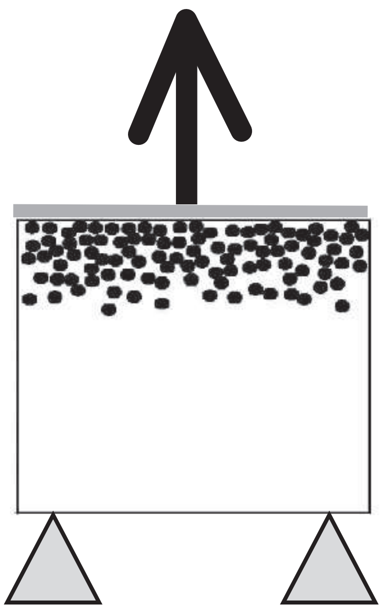

Figure 7.1 *Schema of the loading.*

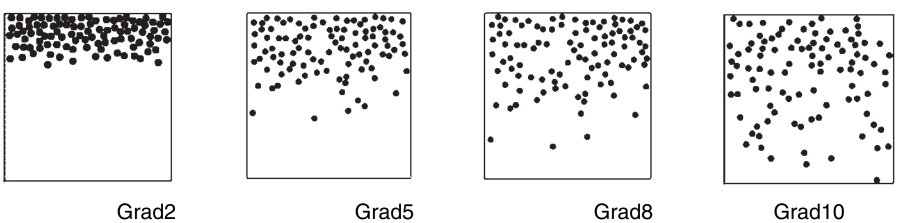

Figure 7.2 *Some examples of the generated microstructures with different degrees of gradient.*

avoid confusion (in fact, 'a high degree of gradient' means a low SD), the term 'degree of gradient' will be used for the value 1/SD.

Figure 7.3 shows some typical tensile stress–strain curves and the fraction of failed elements in the particles plotted versus the far field applied strain for the graded particle arrangements with different degrees of gradient.

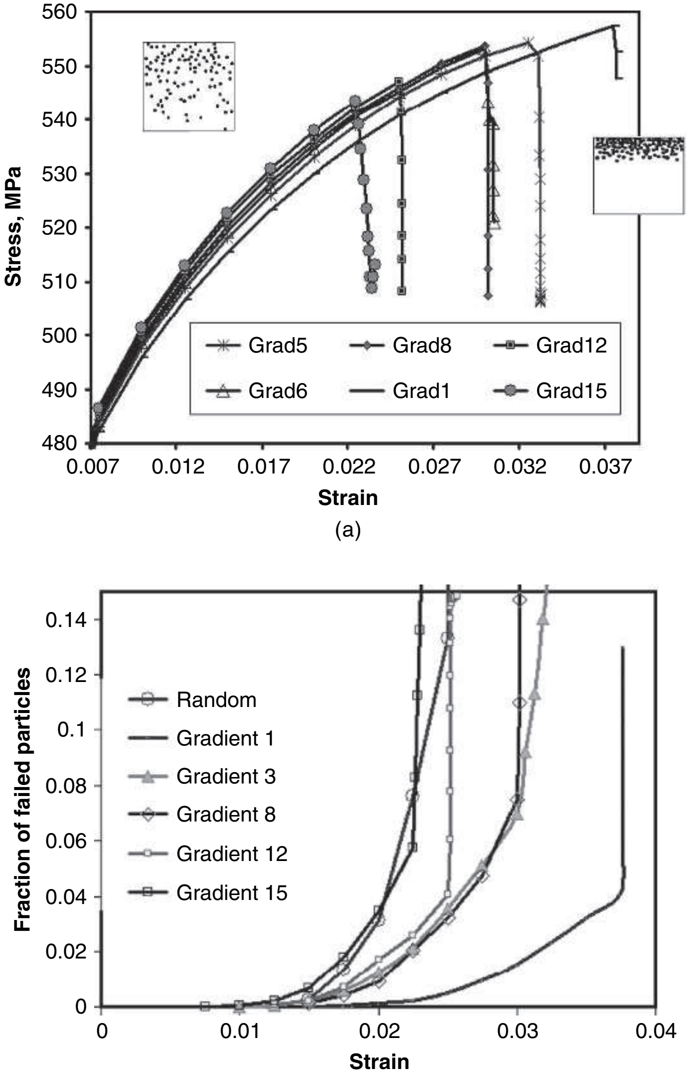

Figure 7.3 *(a) Tensile stress–strain curves and (b) the fraction of failed particles plotted versus the far field applied strain for the graded particle arrangements with different degrees of gradient. Reprinted from* Compos, Sci. Technol., ***66*** *(11–12), Mishnaevsky, Jr, 'Functionally . . . ', pp. 1873–1887, Copyright (2006), with permission from Elsevier.*

Table 7.2 *Critical (failure) strains and statistical parameters of some graded microstructures.*

Grad	Failure strain	Flow stress ($u = 0.15$ mm)	NND	SENND
1	0.038	515.49	0.44	0.83
2	0.025	515.59	0.48	0.90
3	0.028	517.07	0.49	0.36
5	0.033	518.01	0.54	0.54
6	0.030	519.01	0.55	0.54
8	0.030	520.26	0.58	0.75
12	0.025	521.66	0.58	0.43

Table 7.2 gives the critical strains, as well as statistical parameters of the microstructures (NND and SENND see Section 6.7). One can see that the gradient degree correlates with the averaged NND: the lower degrees of gradient lead to the higher average NNDs. No correlation between the degree of gradient and the SENND was found.

Figure 7.4(a) shows the failure strain (critical applied strain) plotted versus the degree of gradient in the composites. Figure 7.4(b) shows the flow stress of the composite (at the far field strain $u = 0.15$) as a function of the gradient degree.

It is of interest that the flow stress and stiffness of composites decrease with increasing gradient degree. Apparently, the more homogeneous the distribution of hard inclusions in the matrix, the stiffer the composite. If the particles are localized in one layer in the composite, the regions with low particle density determine the deformation of the material, and that leads to the low stiffness.

One can see from Figure 7.3(b) that all the microstructures have rather low damage growth rate at the initial stage of damage evolution. At some far field strain (called here 'failure strain'), intensive (almost vertical) damage growth takes place and the falling branch of the stress–strain curve begins. For all the graded microstructures, the failure strain is higher than for the homogeneous microstructures.

Thus, failure strain of the graded composites increases with increasing gradient (localization) degree of the particle arrangement.

Figure 7.5 shows the von Mises stress distribution in a highly gradient (Grad3) microstructure. One can see that the stresses are lower in the low part of the microstructure (particle-free region), than in the particle-rich regions. If two particles are placed very close to one another, the stress level in the particles is much higher than in other particles, especially if these particles are arranged along the gradient (vertical) vector. Then, the stress level is rather high in particles which are located in the transition region between the high particle density and particle-free regions. One could expect these particles to begin to fail at the later stages of loading, and that was observed in the damage simulations. Figure 7.5(b) shows the damage distribution in the particles and in the matrix (Grad3 microstructure, far field strain 0.29). That the particles begin to fail not in the region of high particle density but rather in the transition region between the particle-rich and particle-free regions, is similar to our observations for the case of clustered particle

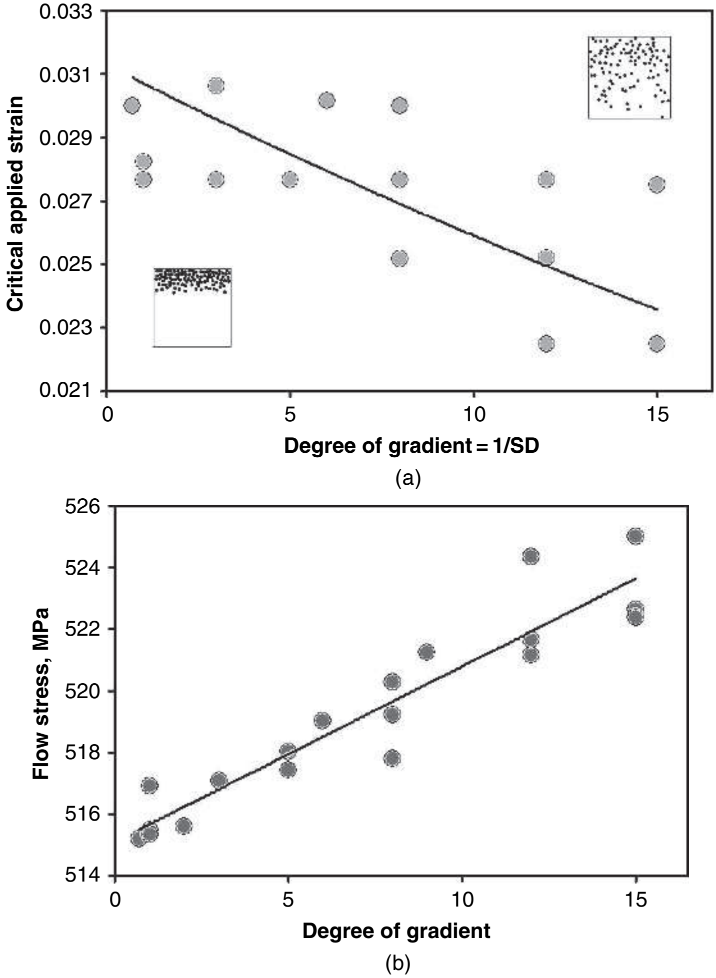

Figure 7.4 *(a) Failure strain and (b) flow stress of the composite (at the far field strain* $= 0.15$*) plotted versus the degree of gradient in the composites. SD means the standard deviation of the normal distribution of distances between the particle centers and the upper rand of the cell (see Chapter 6). Reprinted from* Compos. Sci. Technol.*,* ***66*** *(11–12), Mishnaevsky Jr, 'Functionally . . . ', pp. 1873–1887, Copyright (2006), with permission from Elsevier.*

arrangement: in the case of clustered particle arrangement, the damage begins in the particles which are placed at the outer boundaries of clusters (see Chapter 8). One can see from Figure 7.5(b) that the damage in the matrix begins near the damaged particles or between particles which are arranged closely in the direction of the gradient vector.

(a)

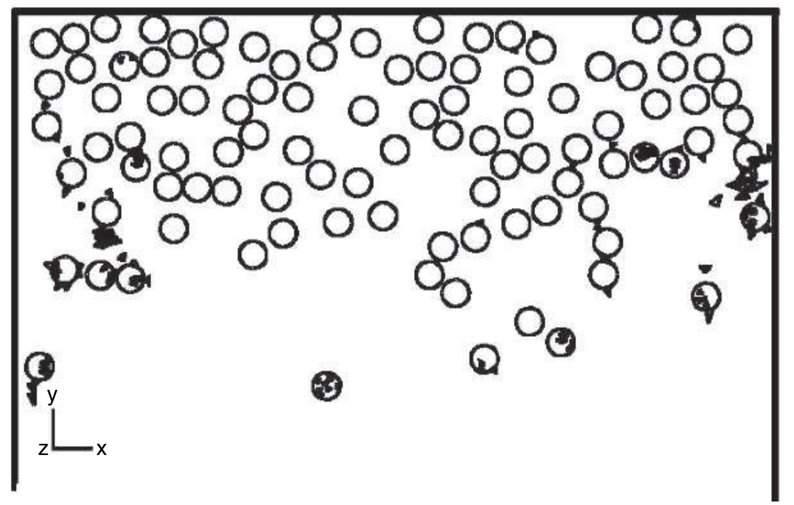

(b)

Figure 7.5 *(a) Von Mises stress distribution in a highly gradient (Grad3) microstructure and (b) damage distribution in the particles and in the matrix (Grad3 microstructure, far field strain 0.29). Reprinted from* Compos. Sci. Technol.*, **66** (11–12), Mishnaevsky Jr, 'Functionally . . . ', pp. 1873–1887, Copyright (2006), with permission from Elsevier. (See Plate 2)*

Figure 7.6 shows the mechanism of damage formation in the composite, observed in our simulations: the void growth begins near the failed particles, and the damaged area expands in the direction to the nearest damaged particle. This mechanism has been observed experimentally as well (Derrien, 1997; Derrien *et al*., 1999).

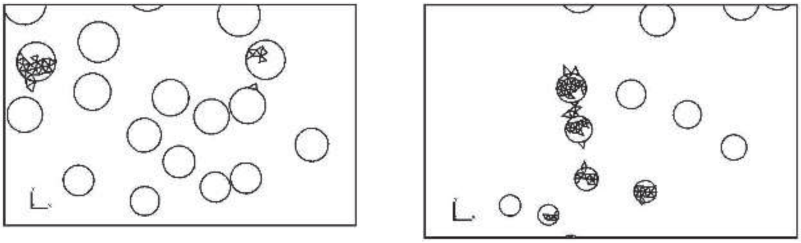

(a) (b)

Figure 7.6 *(a) Mechanism of void initiation near a failed particle and (b) of the expansion of the damaged area, observed in the simulations. Reprinted from* Compos. Sci. Technol., **66** *(11–12), Mishnaevsky Jr, 'Functionally . . .', pp. 1873–1887, Copyright (2006), with permission from Elsevier.*

7.2 'Bilayer' model of a graded composite

To verify the numerical results related to the influence of the degree of gradient on the stiffness and failure behavior and obtained in the previous section, we use the following analytical model. The gradient material is represented as a two-layer material (Figure 7.7). The Young modulus of the gradient material is calculated using the Reuss model. The upper layer, which represents the region of the gradient composite with high particle density, is taken here as a homogeneous material. The thickness of this upper layer is equal to the thickness of the region with high particle density. The lower layer represents the particle-free regions of the composite. The degree of gradient of microstructures in this model is characterized by two parameters: the thickness and the Young modulus of the upper layer (i.e. of the highly reinforced region of the gradient composite). The thinner and the stiffer the upper 'layer', the more localized are the particles in the gradient material.

A highly graded material (like Grad 1) is represented in this model as a bilayer with a thin and hard upper layer, and a lower layer with properties of the matrix, whereas a material with low gradient degree is considered as a bilayer with a thick upper layer, which has properties close to those of the matrix. Since the total amount and volume content of particles in the cell are assumed to be constant, the volume content of the SiC particles in the upper layer is inversely proportional to the layer thickness. The degree of gradient can be characterized in this model by the ratio of the cell size to the thickness of the upper layer. In Section 6.5, the effect of the volume content of SiC particles on the flow stress and stiffness of Al/SiC composites was analyzed. Approximating the results from Section 6.5, one can obtain the following relationship between the Young modulus of the composite and the volume content of SiC particles:

$$E_{\mathrm{up}} = 4.25 \times 10^4 + 242.1\mathrm{VC} \tag{7.1}$$

where E_{up} is the Young modulus of the Al/SiC composite (in this case, the 'upper layer' material) (in MPa) and VC is the volume content of the SiC particles. Assuming that the average volume content of SiC particles in the upper layer is 50 %, if the thickness of the

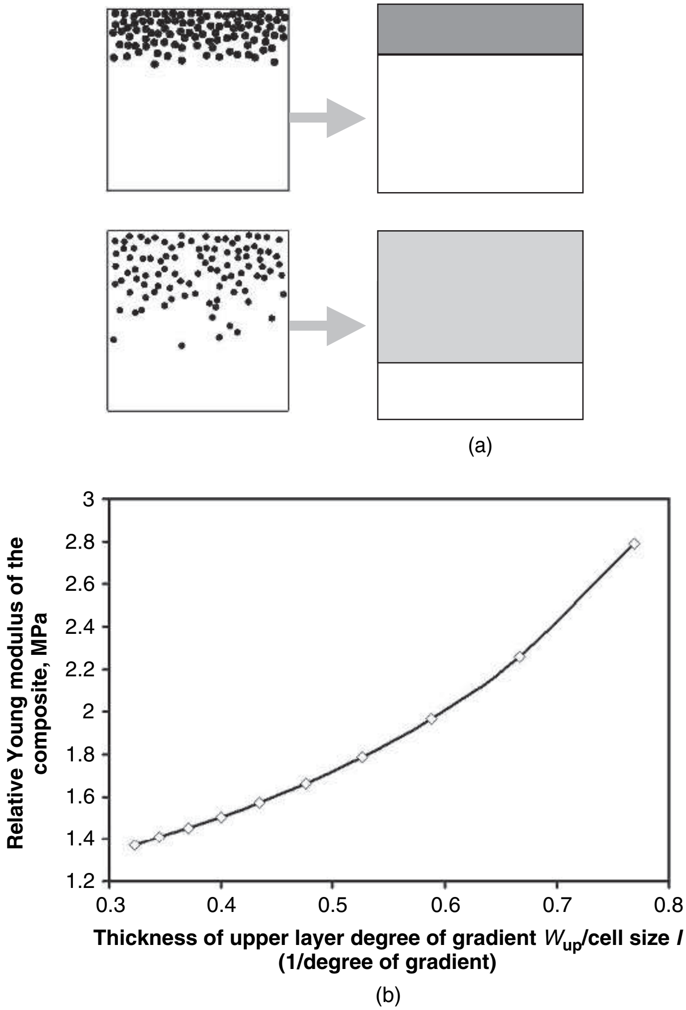

Figure 7.7 *(a) Model of a gradient material as a bilayer (highly graded and almost homogeneous composites) and (b) the normalized Young modulus of the composite plotted versus the ratio w_{up}/l.*

upper layer is 0.1 (i.e. 10 % of the total height of the cell), one obtains the relationship between the thickness of the region of the cell with high particle density (i.e. of the upper layer) and the volume content of SiC particles in this layer: $w_{up} = 0.05/\mathrm{VC}$. Substituting these formulae into the Reuss formula for the Young modulus of the bilayer:

$$E = 1/[(w_{up} \times l/E_{up}) + (l^2 - w_{up} \times l)/E_{matr}] \tag{7.2}$$

where l is the size of the cell and E_{up} and E_{matr} are the Young modulus for the highly reinforced part (upper layer) and the matrix, respectively, one can determine the Young modulus of the composite as a function of the degree of gradient (i.e. the ratio l/w_{up}).

Figure 7.7(b) shows the normalized Young modulus of the composite as a function of the degree of gradient. One can see that the stiffness of the composite decreases with increasing degree of gradient of the composite. Furthermore, as observed in Section 6.8, the failure strain of a SiC particle reinforced Al composite is inversely proportional to the stiffness of the composite. Taking into account this result and Figure 7.7(b), one can conclude that the degree of gradient has the following effect on the failure strain of composites: the failure strain increases when the gradient degree of the composite increases, and the particles are highly localized in a layer. This result, obtained with the use of a simple analytical model, confirms our results obtained in the simulations (Figure 7.4).

7.3 Effect of the shape and orientation of elongated particles on the strength and damage evolution: nongraded composites

As noted in Chapter 2, the microstructures with staggered gradient arrangement of platelets or elongated mineral particles are rather typical for many biomaterials at micro- and nanolevel, e.g. nacre, teeth and bones. The materials with such microstructures show rather high damage resistance and strength, and it has been shown that the high performances of the biomaterials can be attributed to this kind of microstructure (Mishnaevsky Jr, 2004c).

At this stage of the work, the effect of the arrangement of elongated particles, their shapes (aspect ratio) and orientations on the effective response and damage behavior of graded and homogeneous composites was studied numerically.

The following microstructures of composites were generated and tested numerically: composites reinforced with elongated ellipsoidal particles (aspect ratios 0.3 and 0.5), aligned horizontally and vertically, and oriented randomly, with graded and homogeneous arrangements. Figure 7.8 shows some examples of the designed microstructures.

First, consider nongraded microstructures with elongated reinforcing particles, with different aspect ratios and orientations of particles. Figure 7.9 shows the stress–strain curves and the damage–strain curves for nongraded microstructures with different orientations of particles (aligned vertically and horizontally, and randomly oriented).

One can see from Figure 7.9 that the failure strain of the composites with elongated particles increases in the following order:

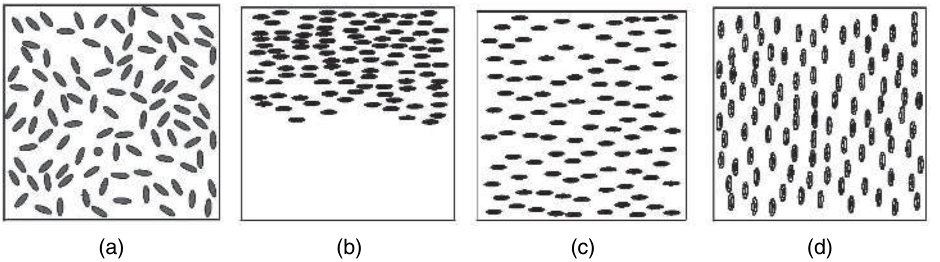

(a) (b) (c) (d)

Figure 7.8 Examples of the designed microstructures with elongated particles.

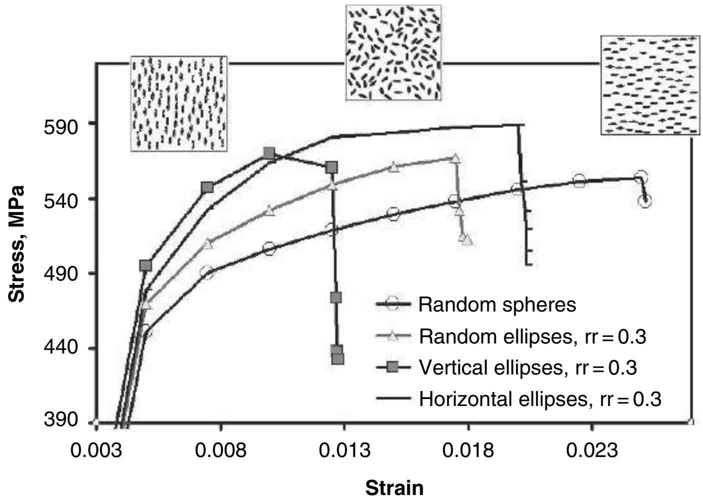

(a)

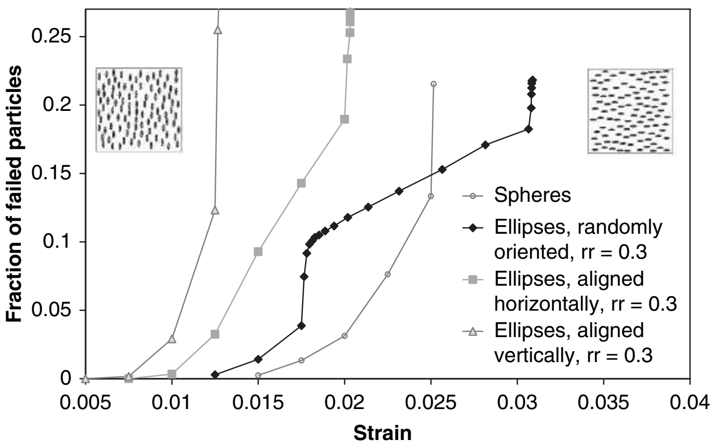

(b)

Figure 7.9 *(a) Stress–strain curves and (b) damage–strain curves for nongraded microstructures with different orientations of particles (randomly arranged spheres, and aligned vertically and horizontally, and randomly oriented ellipsoides, aspect ratio $rr = 0.3$). Ell3 means Elliptical particles with $rr = 0.3$. Reprinted from* Compos. Sci. Technol.*,* ***66*** *(11–12), Mishnaevsky Jr, 'Functionally . . . ', pp. 1873–1887, Copyright (2006), with permission from Elsevier.*

vertical aligned < randomly oriented < horizontal aligned particles

The failure strain of the microstructures with round particles is always higher than that for elongated particles.

Let us consider the effect of the aspect ratio of the particles on the strength and failure strain of the composite. Figure 7.10 shows the stress–strain curves and the damage–strain curves for the nongraded microstructures with different aspect ratios of particles (where rr = smaller particle radius divided by bigger particle radius, $rr = 0.3$, 0.5, 0.7 and 1).

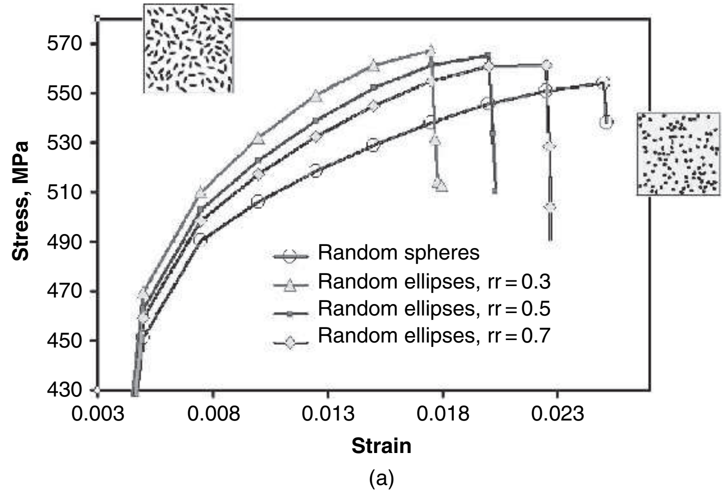

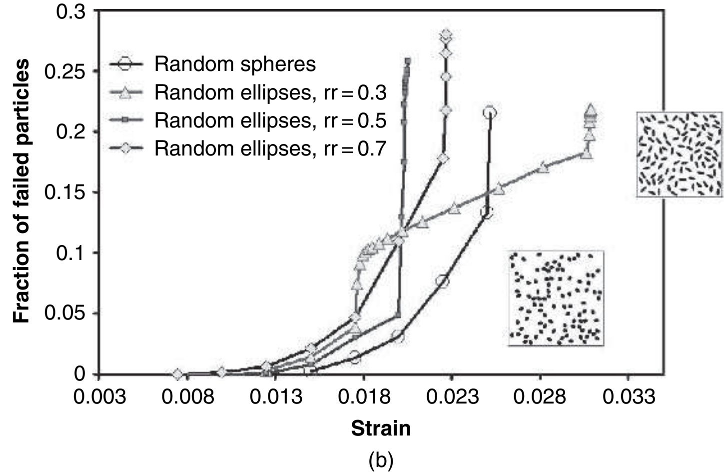

Figure 7.10 *(a) Stress–strain curves and (b) damage–strain curves for nongraded microstructures with different aspect ratios of particles. Reprinted from* Compos. Sci. Technol.*, **66** (11–12), Mishnaevsky Jr, 'Functionally . . . ', pp. 1873–1887, Copyright (2006), with permission from Elsevier.*

It can be seen that the higher the aspect ratio of particles, the higher (slightly) the flow stress and stiffness of the composites. An increase in the value of *rr* by 0.2 (0.3 to 0.5 or 0.5 to 0.7) (i.e. an increase of the aspect ratio by 40–60 %) leads to an increase of the flow stress by 1.4 %.

The failure strain increases with increasing the aspect ratio of the particles: when the value of *rr* increases by 0.2 (0.3 to 0.5 or 0.5 to 0.7, which again corresponds to an increase of the aspect ratio by 40–60 %), the failure strain increases by 13 %.

In order to analyze the mechanisms of deformation and damage evolution in the composites reinforced by elongated or platelet-like particles, one may look at the von

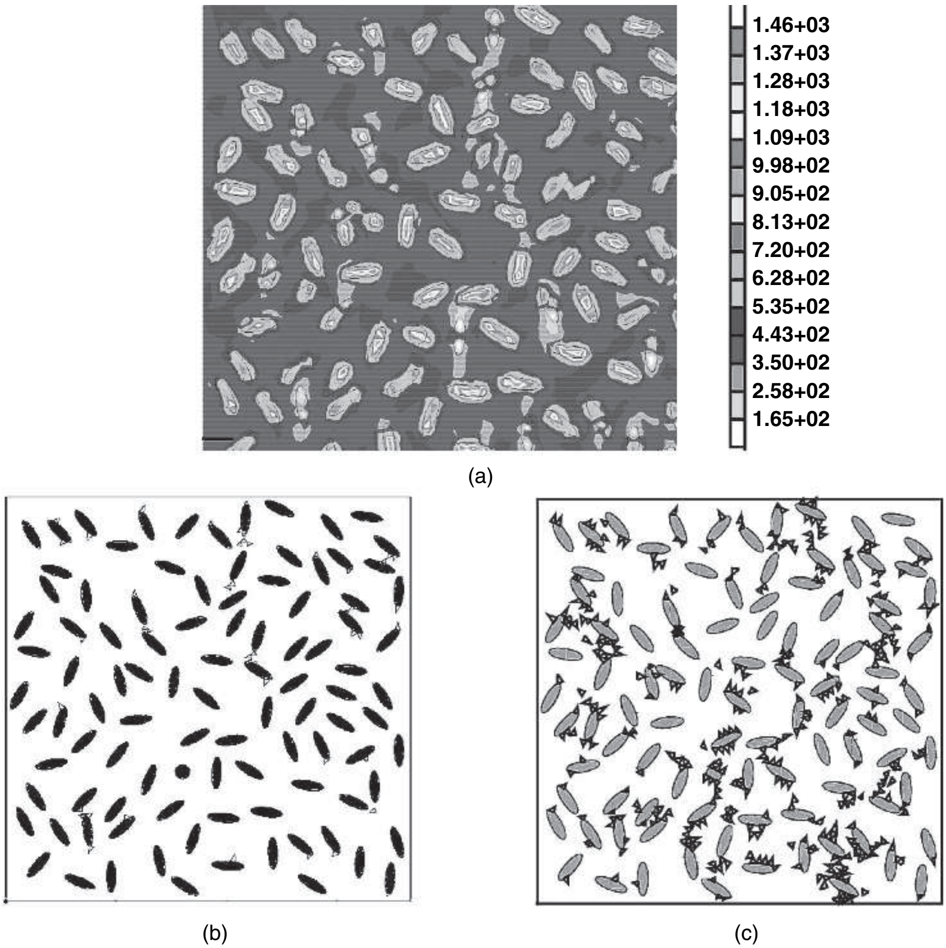

Figure 7.11 *(a) Von Mises stress ($u = 0.18$ mm) and (b,c) damage distributions in a composite with randomly oriented elongated particles ($rr = 0.3$, $u = 0.18$ mm and $u = 0.29$ mm). Repriented from* Compos. Sci. Technol.*, **66** (11–12), Mishnaevsky Jr, 'Functionally . . . ', pp. 1873–1887, Copyright (2006), with permission from Elsevier. (See Plate 3)*

Mises stress and damage distributions in a composite with randomly oriented elongated particles ($rr = 0.3$) (Figure 7.11). It can be seen that the damage in the matrix begins most often in the places between two particles which are arranged closely along the vertical direction (i.e. along the loading and gradient direction). The void growth in the matrix begins near the sharp ends of the particles. Then, the damaged areas extend and link with other voids, formed near other particles [Figure 7.11(c)], rather similar to the mechanism of the damage growth in the composites with round particles (Figure 7.5).

Figure 7.12 shows the damage distribution in microstructures with aligned (vertical and horizontal) elongated particles. One can see that the damage in the matrix often begins between closely placed particles, which are arranged one above another in the

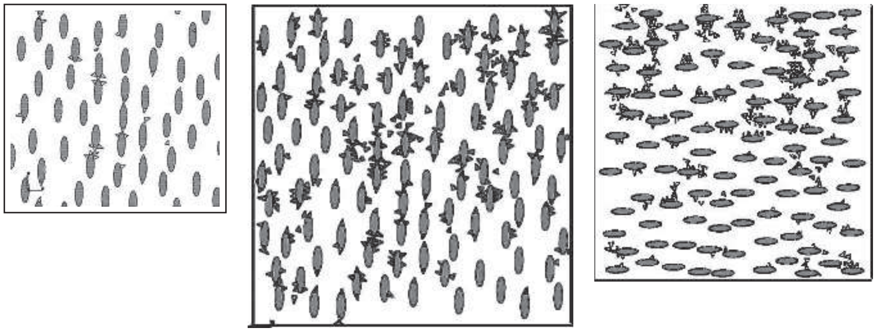

(a) (b) (c)

Figure 7.12 *Damage distribution in a composite with aligned (a, b) vertical and (c) horizontal elongated particles* (rr = 0.3, u = 0.135, 0.30 *and 0.20 mm, respectively). Reprinted from* Compos. Sci. Technol.*, **66** (11–12), Mishnaevsky Jr, 'Functionally . . . ', pp. 1873–1887, Copyright (2006), with permission from Elsevier.*

loading direction. This is similar to the mechanism observed in the case of randomly oriented particles.

7.4 Effect of the shape and orientation of elongated particles on the strength and damage evolution: graded composites

Now, we consider the effect of the graded arrangement of elongated particles on the strength and damage evolution in graded composites.

Figure 7.13 shows the stress–strain curves and the damage–strain curves for the graded and (for comparison) nongraded microstructures with different aspect ratios and orientations of particles.

The shapes of the stress–strain and damage-strain curves for graded and non–graded composites are similar. Yet, the damage growth rates, and the stiffnesses and flow stresses of the composites are much lower, and the failure strains are sufficiently higher for the graded microstructures than for the homogeneous microstructures. Whereas the damage growth rate, calculated as an increase in the fraction of failed particles divided by the increase in the far field applied strain, for a homogeneous microstructure (elongated particles, aspect ratio 0.3, randomly oriented) is 19.4, for the same but graded microstructure, it is equal to 5.3.

One can see that the failure strain for the graded composite increases in the same order, as in the case of homogeneous microstructures: vertical aligned $<$ randomly oriented $<$ horizontal aligned elongated particles. The stiffness of the composite is a little bit higher for aligned (vertical or horizontal) ellipsoids, than for the randomly oriented ellipsoids.

It is of interest that the curves of the fraction of failed elements plotted versus the far field applied strain for the random orientation of ellipsoidal particles (both graded and homogeneous arrangements) have different shape from the curves for the microstructures with aligned particles: whereas the fraction of failed particles increases monotonically with increasing applied strain for the case of aligned particle microstructures, the curves

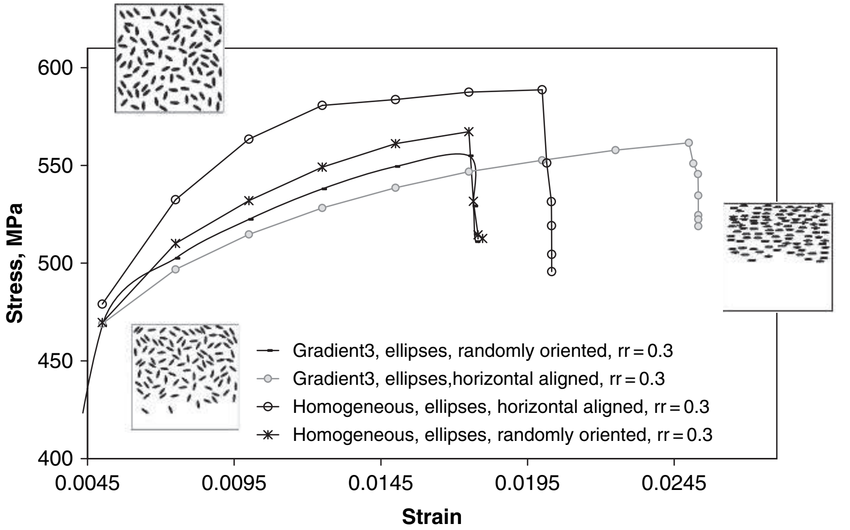

(a)

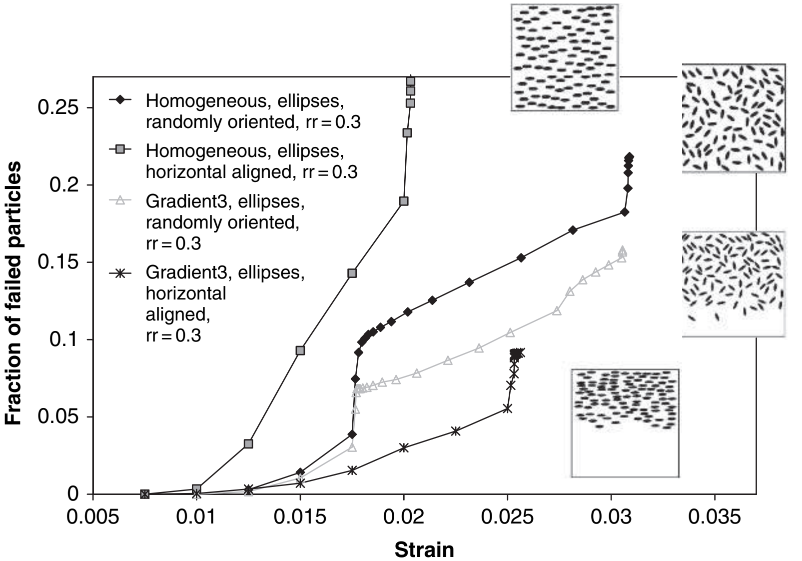

(b)

Figure 7.13 *(a) Stress–strain curves and (b) damage–strain curves for the graded and (for comparison) nongraded microstructures with different orientations of elongated particles. Aspect ratio 0.3, Gr3 and Grad3 mean the graded distribution of particles with standard deviation of the Gauss probability distribution of particle centers* = 0.3 *of the cell size. Reprinted from* Compos. Sci. Technol.*,* ***66*** *(11–12), Mishnaevsky Jr, 'Functionally . . . ', pp. 1873–1887, Copyright (2006), with permission from Elsevier.*

of the fraction of failed particles versus strain for the randomly oriented particles have plateaux. After the intensive damage evolution begins and continues for some time, it slows down and goes on at a much slower rate. At some strain level (approximately, two times the strain level of the first intensive damage growth), the intensive damage growth starts again.

It can be seen from Figure 7.13 that whereas the more localized and highly gradient microstructures have lower stiffness and higher failure strain than the homogeneous microstructures, the first critical strain (i.e. the critical strain, at which the falling branch of the stress–strain curve begins) is the same for both gradient and nongradient microstructures in the case of microstructures with randomly oriented elongated particles. After the damage growth slows down, the damage growth rate is much less for the graded microstructure than for the homogeneous microstructure. The second critical strain for these microstructures is much lower for the homogeneous than for the graded version of these microstructures.

Now let us consider the mechanism of deformation and damage in the graded composites. Figure 7.14 shows the damage distribution in the matrix in the case of a graded composite reinforced by aligned horizontal and randomly oriented ellipsoids (aspect ratio 0.3). It can be seen that both in the case of the aligned and randomly oriented ellipsoids (and similarly to the case of graded microstructure with round particles), the density of damaged particles in the area where the high particle density region passes into the particle-free region is rather high, and much higher than in the region of high particle density. Apparently, the particles which are located in the 'transition' area begin to fail first. The matrix is damaged not in the region of high particle density but rather in the area where the region of high particle density passes into the region of low particle density (similar to the mechanism of damage initiation in the graded composites reinforced by graded particles). In the case of the randomly oriented particles, the damage initiation in particles takes place rather often if the 'noses' of two or three elliptical particles are placed close to one another.

One should note that the microstructures with particles aligned along the direction normal to the loading direction, which demonstrated the highest failure strain results in our simulations, are rather similar to the microstructures of many biomaterials (see

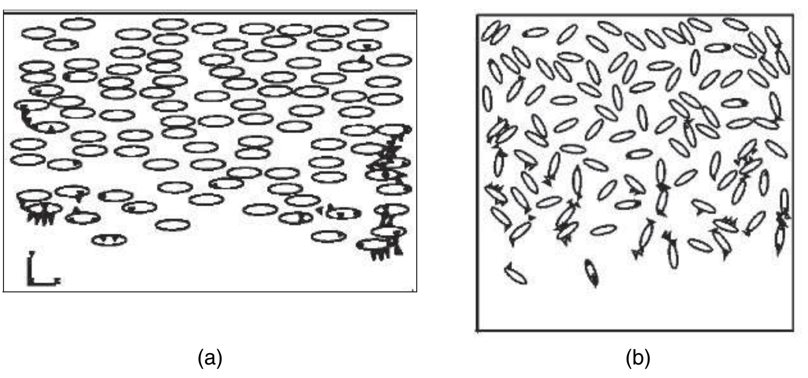

Figure 7.14 *Damage distribution in the matrix in the case of a graded composite reinforced by (a) aligned horizontal and (b) randomly oriented ellipsoids (*rr *= 0.3). Reprinted from* Compos. Sci. Technol.*,* ***66*** *(11–12), Mishnaevsky Jr, 'Functionally . . . ', pp. 1873–1887, Copyright (2006), with permission from Elsevier.*

Section 2.3), where the platelets or fibers are arranged with a gradient, and aligned normally to the expected loading direction.

On the basis of the simulations, one may draw the following conclusions. *The failure strain of the composites with elongated particles increases in the following order: vertical aligned < randomly oriented < horizontal aligned particles*. The failure strain decreases with increasing aspect ratio of the particles. The particles located in the area where the high particle density region passes into the particle-free region begin to fail first. The damage in the matrix begins most often between failed particles or between two particles which are arranged closely along the vertical direction (i.e. along the loading and gradient direction). The effect of the gradient on the flow stress, stiffness and failure strain for the microstructures with elongated particles are similar to the effect for the case of round particles: the more localized and highly gradient microstructures have lower stiffness and higher failure strain, than the homogeneous microstructures.

7.5 Effect of statistical variations of local strengths of reinforcing particles and the distribution of the particle sizes

Real reinforcing materials have always some statistical variations of the mechanical properties and strengths, which strongly influence the failure and strength of composites. At this stage of the work, we study the effect of the statistical variations of strengths of the particles in the Al/SiC graded composite on the failure behavior of the composite.

The stress–strain and fraction of failed particles versus strain curves were calculated numerically for different microstructures of the composites (random nongradient, Grad1, Grad5) with different degrees of scattering of the strength of particles. The critical maximum stress of SiC particles, which was assumed to be a constant value (1500 MPa) in all the above simulations, was a random value in these simulations. It was assumed that the critical maximum principal stress is distributed by the Gauss probability law, with mean value 1500 MPa (as above) and with standard deviations 0, 50, 200, 500 and 1000 MPa. In the simulations, the random critical maximum stress was calculated in each element and compared with the current value of maximum principal stress in the element; if the current principal stress exceeded this random critical value, the element was considered to fail, and its stiffness was reduced.

Figure 7.15(a) shows the failure strain for the different graded microstructures plotted versus the degree of scattering (standard deviation) of the local strength of particles. Figure 7.15(b) shows the damage–strain curves for the homogeneous and graded microstructures with different degrees of gradient and different standard deviations of the critical principal stress.

One can see that the failure strain of composites decreases rapidly when the degree of scattering of local strength of particles increases. However, *the negative effect of the scattering of the particle strength on the failure strain of the composite is weakened if the microstructure is graded*. The degree of reduction of the failure strain of composite due to the randomness of local strength depends on the microstructure of the composite as well: an increase of the standard deviation of the critical stress from 0 to 500 MPa leads to a 2.7 times reduction of the failure strain in the nongraded microstructure; the

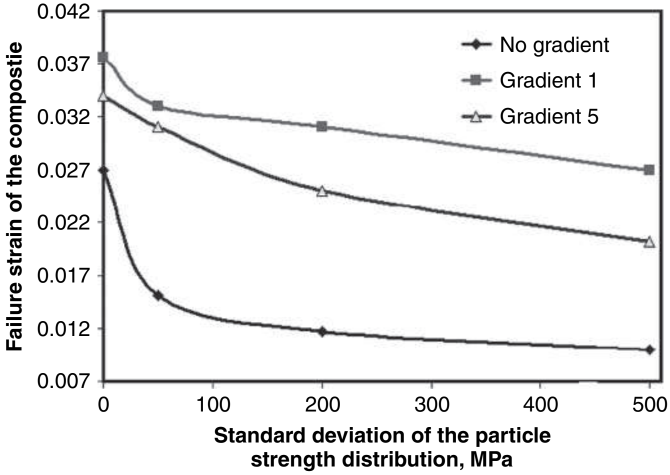

(a)

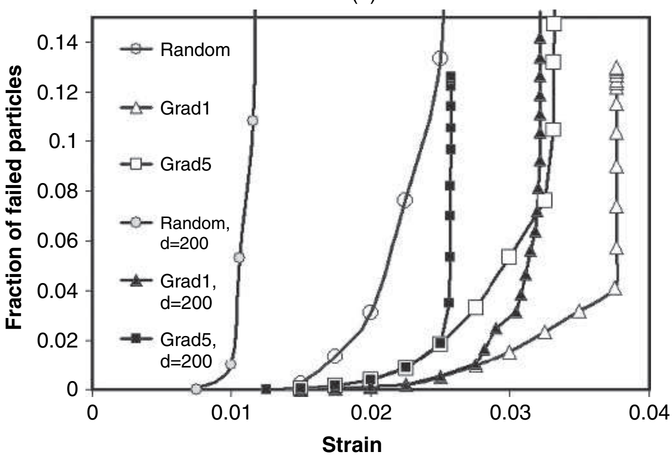

(b)

Figure 7.15 *(a) Failure strain of composites plotted versus the standard deviation of the particle strength distribution and (b) the damage–strain curves for the graded microstructures with random variations of local strength of particles. d is the standard deviation of the critical stress distribution. Reprinted from* Compos. Sci. Technol., ***66*** *(11–12), Mishnaevsky Jr, 'Functionally . . . ', pp. 1873–1887, Copyright (2006), with permission from Elsevier.*

same change leads to only 68 % and 39 % decrease in the failure strain of the graded composites (Grad5 and Grad1, respectively).

Consider now the effect of the variation of the particle sizes on the strength and failure of composites. It has been shown in Section 6.7 that composite materials with randomly distributed particle sizes have much lower failure strain than the materials reinforced with particles of a constant radius. An interesting case of a composite material with both varied sizes of reinforcing particles and the directional gradient is a composite reinforced by particles with radii that depend on the position of the particle. Figure 7.16(a)

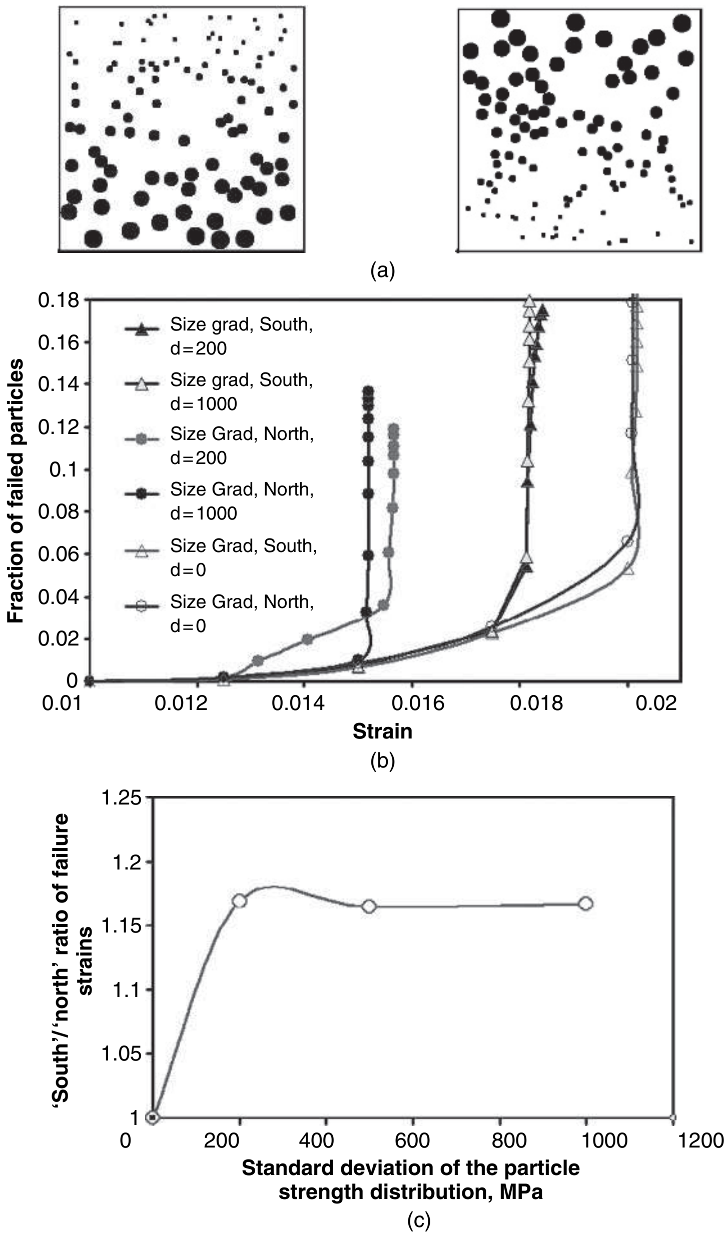

Figure 7.16 *(a) Examples of the particle size gradient 'small/big'/'big/small' microstructures, (b) fraction of failed particles plotted versus applied strain for the microstructures with random variations of the local strength of particles and (c) the ratio of failure strains for the 'small/big'/'big/small' microstructures plotted versus the standard deviation of the probability distributions of the particle strengths. Reprinted from* Compos. Sci. Technol.*, **66** (11–12), Mishnaevsky Jr, 'Functionally . . .', pp. 1873–1887, Copyright (2006), with permission from Elsevier.*

shows examples of microstructures where the radius of a particle is proportional to the Y-coordinate of the particle. Such microstructures, where the size of the particles is proportional to the vertical coordinate, will be referred to as 'particle size gradient microstructures'.

Two types of microstructures with graded distributions of sizes of reinforcing particles were considered: 'small/big' size gradient, with small round particles near the upper boundary of the cell and big particles at the lower boundary (also called 'south' microstructures, according to the location of big particles in the lower or southern part of the cell); and 'big/small' size gradient (or 'north' microstructures). The radius of the particles was taken to be proportional to the Y-coordinate of the particles, radius $\sim L$ ('north' size gradient) or radius $\sim (L\text{-Y})$, where L is the cell size ('south' size gradient). After the radii of the particles were calculated, they were normalized to keep the total volume content of the SiC particles constant.

The numerical testing of these microstructures was carried out for the constant strength of particles, as well as for the case of the random (Gaussian) distribution of the critical stress in particles, with standard deviations 200, 500 and 1000 MPa. (The average critical principal maximum stress was the same as above, 1500 MPa.)

Figure 7.16(b) shows some typical functions of the fraction of failed elements in the particles plotted versus far field applied strain for the 'small/big' and 'big/small' size gradient microstructures.

One can see that the 'small/big' and 'big/small' size gradient microstructures have very similar damage growth curves and the same failure strain, when the critical stress of particles does not vary. However, when the statistical variations of the strength of SiC particles are taken into account, the failure strain of the composite is drastically reduced: by 11 % for the 'small/big' microstructure and by 30 % for the 'big/small' microstructure. This decline hardly depends on the degree of the variation of the local strength. Figure 7.16(c) shows the ratio of the failure strains for the 'small/big' and 'big/small' size gradient microstructures as a function of the standard deviation of the probability distribution of the particle strength. Apparently, when the statistical variations of the strength of particles are included in our continuum mechanical model, the size effects of particles begin to influence the damage evolution. Therefore, the larger particles placed near the upper border of the cell in the 'big/small' gradient microstructures begin to fail earlier, and that leads to the quicker failure of the composites, whereas this effect does not take place in the 'small/big' microstructures.

On the basis of the simulations, one may draw the following conclusions. The statistical variations of the strength of particles in composites lead to the decrease of the failure strain in the composites. However, this negative effect is weakened, if the microstructures of composites are graded. In the case of the size gradient microstructures (with particles where the strength is varied randomly), the 'small/big' microstructures ensure higher failure strains than the 'big/small' microstructures.

It can be seen that the graded particle distribution has a very beneficial impact on the damage resistance of the composites: it increases the failure strain, weakens the negative effect of the heterogeneity of particles and slows down the damage growth rate in the particles. These positive effects become stronger when the degree of the particle localization increases.

7.6 Combined Reuss–Voigt model and its application to the estimation of stiffness of graded materials

In this section, a simple method to estimate the stiffness of materials with arbitrarily complex and irregular microstructures is suggested, and applied to study the effect of parameters of gradient composite microstructures on the material stiffness. This approach is based on the combined Reuss–Voigt model for the stiffness evaluation.

7.6.1 Estimation of the stiffness of materials with arbitrarily complex microstructures: combined Reuss–Voigt model

Let us consider a 2D complex microstructure of a material. The microstructure is represented as an array of white and black pixels (irregular chessboard). The color (white or black) denotes one of two phases. Let us assume that the 'black' phase represents inclusions and the 'white' phase represents matrix.

In order to calculate the stiffness (Young modulus) of the microstructure consisting of $N \times N$ pixels, we employ the combined Reuss–Voigt model. The considered microstructure is represented as a layered body consisting of N layers. In turn, each layer consists of N subcells (pixels) (Figure 7.17).

In order to estimate the Young modulus of the microstructure, one calculates first the Young modulus $E_{\mathrm{layer}=j}$ of the jth layer, using Voigt averaging:

$$E_{\mathrm{layer}=j} = (1/N)\sum\nolimits_i E(i, j) \tag{7.3}$$

where $E(i, j)$ is the Young modulus of a i, jth cell. Then, the total Young modulus of the model E_{total} is calculated as a modulus of a layered material, using the Reuss equation:

$$E_{\mathrm{total}} = 1/\left[\sum\nolimits_j 1/(NE_{\mathrm{layer}=j})\right] \tag{7.4}$$

Figure 7.17 shows the schema of the stiffness calculation. This approach was realized in the framework of the program code Microstructure Designer and Tester (or MicroDTest) (Mishnaevsky Jr, 2007).

7.6.2 Effect of the degree of gradient on the elastic properties of the composite

Let us consider the effect of the gradient microstructure of composites on their stiffness. For the sake of definiteness, we consider the glass/alumina composites. The properties of the phases were taken from Cannillo *et al.* (Cannillo *et al.*, 2002), and are as follows: alumina $E = 386\,\mathrm{GPa}$ ('black' phase) and glass $E = 72\,\mathrm{GPa}$ ('white' phase).

In order to study the effect of the interface sharpness of the stiffness of the materials, we generated different graded random microstructures (graded version of the random chessboard model of materials; see Ostoja-Starzewski, 1999) using the random number generator.

The glass inclusions (which are represented by black cells/pixels) are distributed uniformly in the X direction, and with a gradient in the Y direction. The graded distribution of black cells along the axis Y is described by:

$$vc(y) = \frac{2vc_0}{1 + \exp(g - 2gy/L)} \tag{7.5}$$

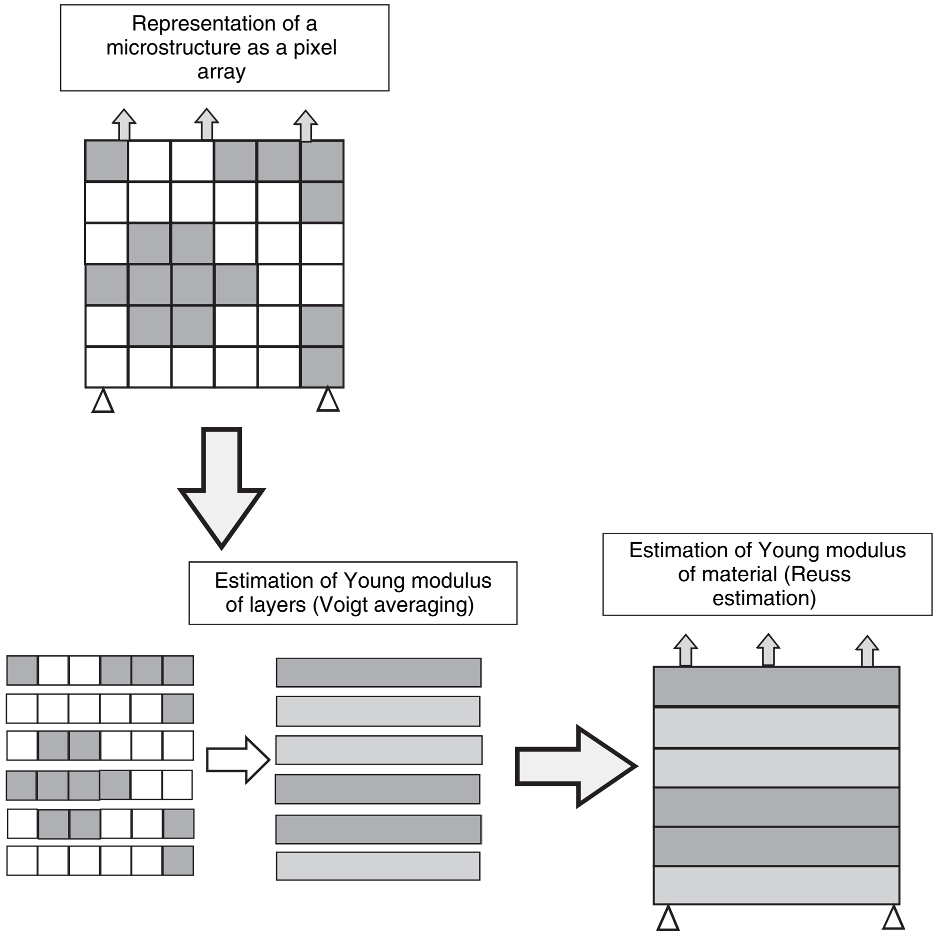

Figure 7.17 *Schema of the stiffness calculation of a lattice from pixels, using the combined Reuss–Voigt approach.*

where $vc(y)$ is the probability that a pixel is black at this point, vc_0 is the volume content of the black phase, L is the length of the cell, g is parameter of the sharpness of the gradient interface and y is the Y-coordinate. Equation (7.5) allows to vary the smoothness of the gradient interface of the structures (highly localized arrangements of inclusions and a sharp interface versus a smooth interface), keeping the volume content of inclusions constant. If $g < 2..3$ the transition between regions of high content of black or white phases is rather smooth, and if $g > 10$ the transition between the regions is rather sharp. Figure 7.18 gives the shapes of the curves for different g.

Figure 7.19 shows examples of the generated cells with different degrees of sharpness of the gradient interface.

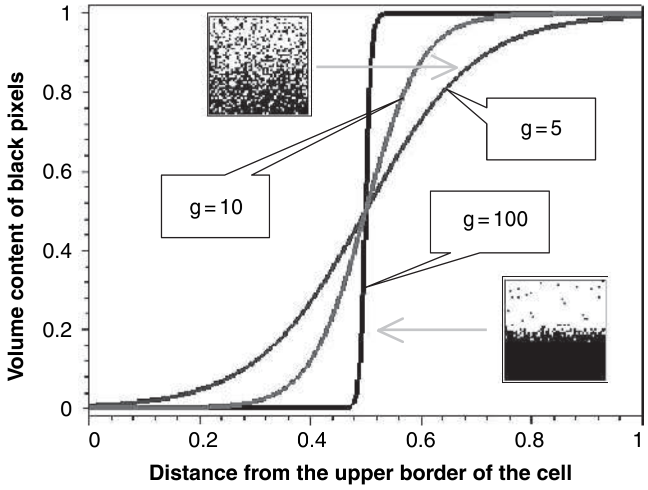

Figure 7.18 *Shapes of the curves of the distribution of the volume content of black phase in graded composites for different g. Reprinted from* Mater. Sci. Eng.*, A,* **407***, Mishnaevsky Jr, 'Automatic Voxel . . . ', pp. 11–23, Copyright (2005), with permission from Elsevier.*

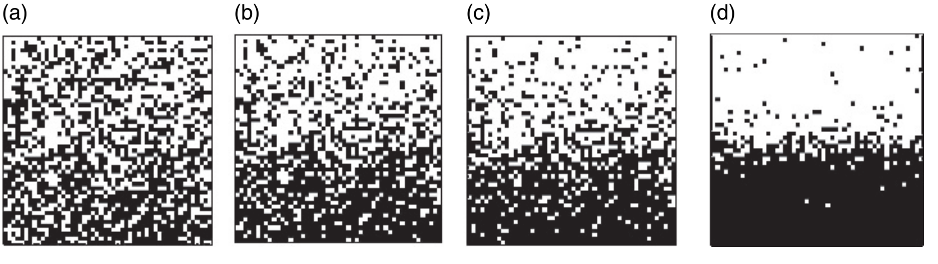

Figure 7.19 *Examples of the graded 'random chessboards' models of a material with different degrees of sharpness of the gradient interface: (a) very smooth transition (g=1); (b, c) smooth* ($g = 2,\ g = 3$)*; (d) stepwise transition* ($g = 10$)*. Reprinted from* J. Compos. Mater.*,* **41***(1), Mishnaevsky Jr, pp. 73–87, Copyright (2007), with permission from Sage Publications, Inc.*

The stiffness of the modeled materials was calculated for different g of the particle distribution, using the above approach.

Figure 7.20 gives the Young modulus of the material plotted versus the parameter g of the smoothness of the transition. One can see that the stiffness of the material increases when the transition between the black and white regions becomes smoother and decreases when this transition becomes sharp. Whereas the Young modulus of the cell is close to its Reuss estimation at $g = 1$, it decreases and approaches the Voigt estimation when g approaches 10 and the transition becomes sharp.

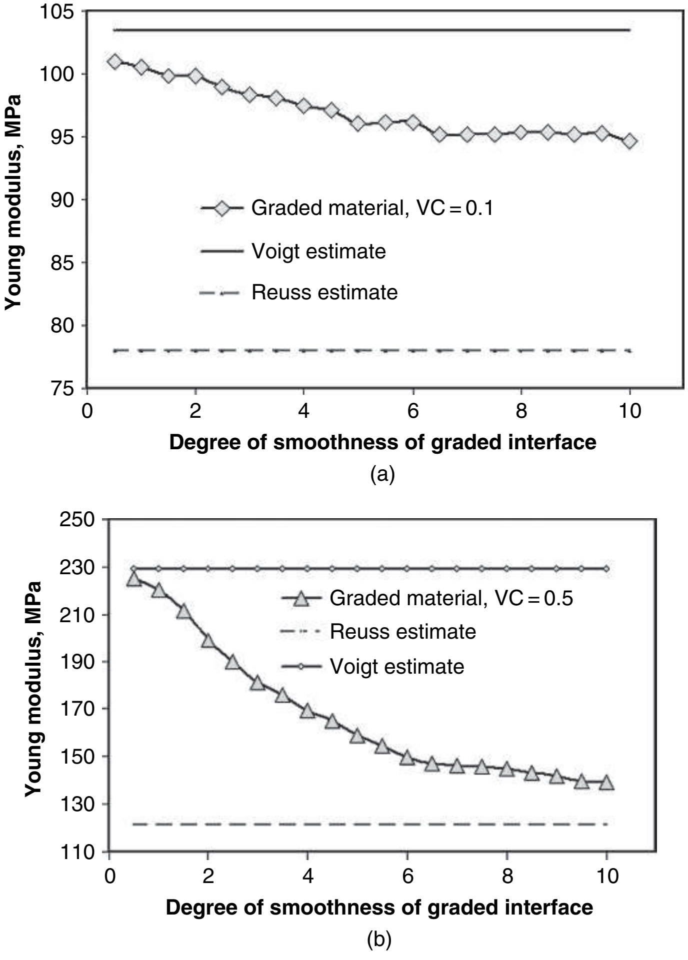

Figure 7.20 *Effect of the smoothness of the graded interface on the Young modulus of the composite (from 1, very smooth transition, to 10, almost stepwise transition). (a)* VC = 10 %; *(b)* VC = 50 %. *Reprinted from* J. Compos. Mater., ***41*** *(1), Mishnaevsky Jr, pp. 73–87, Copyright (2007), with permission from Sage Publications, Inc.*

Now, let us investigate the effect of damage in a phase of a composite on the stiffness of graded composites. The 'black' cells, which are arranged with gradient, were made randomly damaged. The density of failed cells was varied from 10 to 50 %. The damaged cells were assumed to have zero stiffness. The stiffness of the composite was calculated using the method described in Section 7.6.1. Figure 7.21 shows the Young moduli of materials with different densities of failed particles plotted versus the gradient parameter g. Figure 7.22 shows the ratio of the Young moduli of damaged and undamaged materials (with the same parameter g) plotted versus the gradient parameter g.

One can see from the Figures 7.20 and 7.21 that the *effect of damage on the stiffness of gradient materials is much stronger for the graded composites with a sharp transition, than for the composites with a smooth transition.*

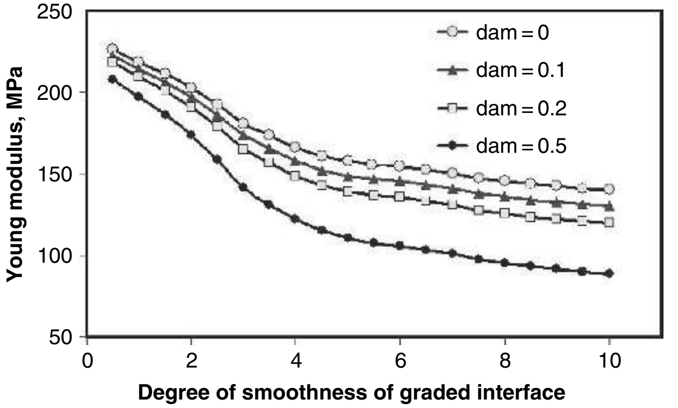

Figure 7.21 *Young moduli of materials with different densities of failed particles plotted versus the gradient parameter g. Reprinted from* J. Compos. Mater.*, **41** (1), Mishnaevsky Jr, pp. 73–87, Copyright (2007), with permission from Sage Publications, Inc.*

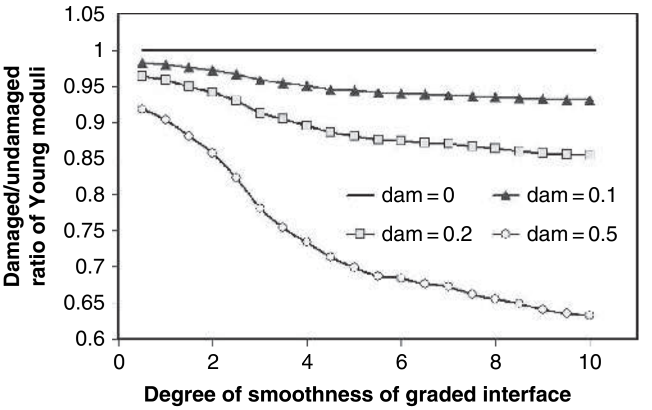

Figure 7.22 *Ratio of the Young moduli of damaged and undamaged materials (with the same parameter g) plotted versus the gradient parameter g. Reprinted from* J. Compos. Mater.*, **41**(1), Mishnaevsky Jr, pp. 73–87, Copyright (2007), with permission from Sage Publications, Inc.*

Thus, the smoother the transition between the regions of high content of each phase, the greater is the stiffness and the less the damage sensitivity of the graded composites.

7.6.3 Inclined interface: effect of the orientation of interfaces on the elastic properties

Now let us analyze the effect of the inclined interface between the materials in a bilayer on the stiffness of a two-phase composite. A two-phase cell with inclined interface is considered. The properties of the components were as in the previous section. The angle

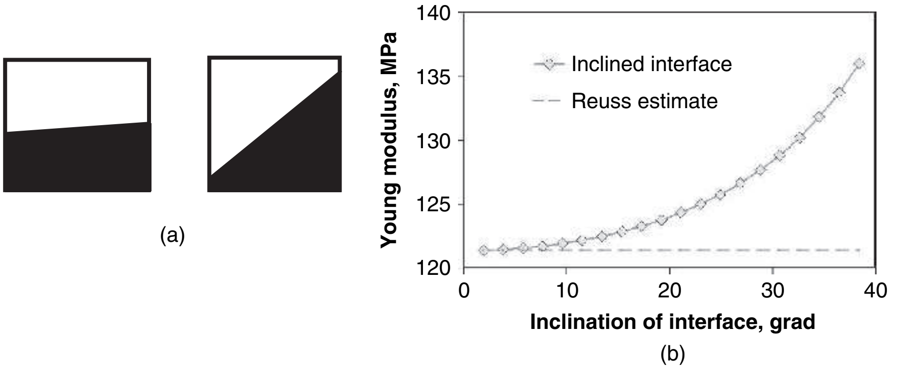

Figure 7.23 *(a) Examples of cells with inclined interface and (b) Young modulus of the cell plotted versus the angle of the interface with the horizontal line. Reprinted from* J. Compos. Mater., ***41*** *(1), Mishnaevsky Jr, pp. 73–87, Copyright (2007), with permission from Sage Publications, Inc.*

of the interface line with the horizontal was varied from 0 to 42 grad. Figure 7.23(a) gives two examples of the cell: with angle 5° and 40°. The volume content of the phases was kept constant (50 %).

The microstructures were represented as arrays of 1000×1000 subcells, with the black subcells placed below the interface, and white subcells above it. The Young moduli of the cells with different inclinations of the straight interface were calculated using the approach described in Section 7.6.1.

Figure 7.23(b) gives the Young modulus of the cell plotted versus the angle of the interface with the horizontal line. One can see that the stiffness of the material increases when the angle between the interface and horizontal line increases. At the angle 40°, the stiffness of the material is 12 % higher than for the case of the horizontal interface.

Practically, that means that the stiffness of a composite, reinforced by fibers or whiskers, can be increased just by reorienting the elongated particles or whiskers: if the whiskers are arranged not normal to the load (which corresponds to the horizontal interface in our case), but at some angle to the load (inclined interface), that can lead to the higher stiffness of the material. This result is confirmed also by the results of FE analysis in Section 7.3.

References

Aboudi, J., Pindera, M.-J. and Arnold, S. M. (1999). Higher-order theory for functionally graded materials, *Composites: Part B (Engineering)*, **30** (8), 777–832.

Becker, Jr, T. L., Cannon, R. M. and Ritchie, R. O. (2002). Statistical fracture modeling: crack path and fracture criteria with application to homogeneous and functionally graded materials, *Engineering Fracture Mechanics*, **69**, 1521–1555.

Buryachenko, V. (1996). The overall elastoplastic behavior of multiphase materials with isotropic components, *Acta Mechanica*, **119**, 93–117.

Buryachenko, V. and Rammerstorfer, F. G. (1998). Micromechanics and nonlocal effects in graded random structure matrix composites, in: *Proceedings of the IUTAM–Symposium on Transformation Problems in Composite and Active Materials*, Eds Bahei-el-Din and G. J. Dvorak, Kluwer Academic Dordrecht, pp. 197–206.

Cannillo, V., Manfredini, T., Corradi, A. and Carter, W. C. (2002). Numerical models of the effect of heterogeneity on the behavior of graded materials. *Key Engineering Materials*, **206–213**, 2163–2166.

Derrien, K. (1997). Modélisation par des méthodes d'homogénéisation de l'endommagement et de la rupture de composites Al/SiCp, PhD Thesis, ENSAM, Paris.

Derrien, K., Baptiste, D. Guedra-Degeorges, D. and Foulquier, J. (1999). Multiscale modelling of the damaged plastic behaviour of AlSiCp composites, *International Journal of Plasticity*, **15**, 667–685.

Gasik, M. M. (1995). Principles of functional gradient materials and their processing by powder metallurgy, Acta Polytechnica Scandinavica, Helsinki.

Gasik, M. M. (1998). Micromechanical modelling of functionally graded materials, *Computational Materials Science*, **13** (1–3), 42–55.

Hirano, T., Teraki, J. and Yamada, T. (1990). One design of functionally gradient materials, in: *Proceedings of the 1st International Symposium on FGM*, Eds M. Yamanouchi *et al.*, FGM, Sendai, pp. 5–10.

Mishnaevsky Jr, L. (2004c). Computational design of bioinspired composite materials: an approach based on numerical experiments, in: *Proceedings of the 3rd Materials Processing for Properties and Performance Conference*, Vol. 3, Eds K. A. Khor, R. V. Ramanujan, C. P. Ooi and J. H. Zhao, Institute of Materials East Asia, Singapore, pp. 226–232.

Mishnaevsky Jr, L. (2005c). Functionally graded lightweight composites: effect of the microstructure on the damage resistance, in: *Proceedings of the 4th International Conference Numerical Analysis in Engineering*, Yogyakarta, Indonesia, CD-ROM.

Mishnaevsky Jr, L. (2006). Functionally gradient metal matrix composites: numerical analysis of the microstructure-strength relationships, *Composites Science and Technology*, **66** (11–12), 1873–1887.

Mishnaevsky Jr, L. (2007). A simple method and program for the analysis of the microstructure–stiffness interrelations of composite materials, *Journal of Composite Materials*, **41** (1), 73–87.

Mishnaevsky Jr, L., Derrien, K. and Baptiste, D. (2004b). Effect of microstructures of particle reinforced composites on the damage evolution: probabilistic and numerical analysis, *Composites Science and Technology*, **64** (12), 1805–1818.

Ostoja-Starzewski, M., (1999). Microstructural disorder, mesoscale finite elements and macroscopic response, *Proceedings of the Royal Society of London, Series A*, **455**, 3189–3199.

Reiter, T., Dvorak, G. J. and Tvergaard, V. (1997). Micromechanical models for graded composite materials, *Journal of Mechanics and Physics of Solids*, **45**, 1281–1302.

Weissenbek, E., Pettermann, H. E. and Suresh, S. (1997). Numerical simulation of plastic deformation in compositionally graded metal-ceramic structures, *Acta Materialia*, **45** (8), 3401–3417.

Zuiker, J. R. and Dvorak, G. J. (1994a). On the effective properties of functionally graded composites-I. Extension of the Mori–Tanaka method to linearly varying fields, *Composite Engineering*, **4**, 19–35.

Zuiker J. R. and Dvorak G. J. (1994b). On the effective properties of composite materials by the linearly field, *ASME Journal of Engineering Materials Technology*, **116**, 428–437.

8

Particle clustering in composites: effect of clustering on the mechanical behavior and damage evolution

8.1 Finite element modeling of the effect of clustering of particles on the damage evolution

The effect of reinforcement clustering on the strength, damage and fracture of composites has been studied by many researchers. Table 8.1 gives a brief overview of some works in this area. Apparently, there are some contradictions in the results on the effect of particle clustering on the strength and mechanical behavior of composites. Whereas Berns *et al*. (Berns *et al*., 1998) demonstrated both theoretically and experimentally that replacing the large primary carbides by clusters of small carbides in tool steels leads to the increase of the fracture resistance and strength of materials, Geni and Kikuchi (Geni and Kikuchi, 1998) have shown that the particle clustering decreases the failure strain of composites as compared with the uniform particle distribution case.

In this section, we analyze the effects of the parameters of the clustered microstructures on the deformation and damage resistance of composites, using the numerical experiments approach.

Computational Mesomechanics of Composites L. Mishnaevsky Jr

Table 8.1 *Effect of reinforcement clustering on the strength, damage and fracture resistance of composites.*

Author; materials, method	Main results
Srensen and Talreja, 1993; unidirectionally fiber reinforced ceramic matrix composites subject to cool down from stress-free temperature FEM, 3D unit cell models	The effect of nonuniformity of fiber distribution on the residual stresses is studied. It was demonstrated that the stresses around the fibers show significant dependence on the nonuniformity of fiber distribution. The radial compressive stress is very sensitive to the nonuniformity, and is maximum, when fibers are in contact. The enhancement of the stress increases with increasing the amount of fibers in contact
Bush, 1997; elastic analysis of Al/SiC composite, BEM (dual boundary integral method)	The interaction between a crack and a particle cluster is investigated numerically. It was shown that the energy release rate (ERR) is reduced, when a crack approaches the cluster (increasing the effective fracture toughness), and amplified, when the crack leaves the cluster (reducing the toughness). The pre-existing interface flaws can attract the crack, and increase the ERR
Llorca and Gonzalez, 1998; Al/SiC composite, FEM	The authors have shown that the vertical clustering of whiskers lowers the overall flow strength and promotes a slower rate of void growth as compared with the uniform arrangement. Vertical clustering leads to the smaller hardening exponent and larger ductility as well, but the difference with the case of the uniform arrangement is smaller. The influence of reinforcement clustering is significantly less pronounced for particulate and sphere reinforced composites, than for the whiskers reinforced composites
Geni and Kikuchi, 1998; Kikuchi and Geni, 1998; Al/SiC composites, 3D FEM	The fracture strain of composites is much higher when the particle are distributed uniformly than when they are clustered
Berns *et al*., 1998; tool steels, FEM, experiments	A new material, in which clusters of small primary carbides replace large carbides ('double dispersion' microstructure), ensures sufficiently higher fracture toughness and lifetime, than the usual steels
Mishnaevsky Jr *et al*., 2003a, 2004a; tool steels, FEM	The fracture toughness of tool steels with clustered microstructures is much higher than that for the steels with uniform or random microstructures
Segurado *et al*., 2003; model MMC, FEM model (3D multiparticle cubic cells)	The influence of the reinforcement clustering on the macroscopic composite behavior is weak, but the average maximum principal stresses in the particles are appreciably higher in the inhomogeneous materials. The presence of clustering greatly increased (by a factor of 3–6) the fraction of broken spheres, leading to a major reduction of the composite flow stress and ductility

8.1.1 Numerical models of clustered microstructures and statistical characterization of the microstructures

A number of 2D unit cells with random uniform and clustered arrangements of SiC particles have been generated automatically, using the 2D version of the program Meso3D. The volume content (VC) of inclusions was taken as 6, 10 and 18 %. The microstructure with VC = 10 % and amount of particles $N = 100$ was taken as a basic microstructure. The microstructures with VC = 6 and 18 % were designed on the basis of one of two rules: either keeping the amount of particles constant ($N = 100$) but varying the particle radius, or keeping the particle radius constant ($r = 0.178$ mm) but varying the amount of particles. Therefore, we were able to consider separately the effects of the amount and the volume content of particles in the materials with clustered microstructures.

The mechanical properties of the materials used in these models correspond to the properties described in Section 6 (AL matrix reinforced with SiC particles).

Table 8.2 gives the amount and radii of particles for the considered microstructures.

To characterize quantitatively the arrangements of the particles and the degree of localization in different microstructures, we determined the radial distribution function of sphere centers as well as the nearest neighbor distances (NNDs) between the particle centers and the nearest neighbor index (NNI, ratio of observed to the expected NND) for the considered microstructures. The scattering of the distribution of the NNDs between particles was characterized by the statistical entropy of the NND (SENND). The entropy was calculated by:

$$H = -\Sigma p(L) \ \log p(L) \tag{8.1}$$

where $p(L)$ is the probability distribution of the NNDs between particles.

Figure 8.1 shows the FE meshes in the microstructure areas with the uniform (random) and clustered particle arrangements.

Figure 8.2 gives examples of the determined radial distribution functions of particle centers for the clustered and uniform (random) particle arrangements. The radial distribution functions for the random particle distributions have one wide peak, and then the curve falls slowly, demonstrating the large scattering of distances. The distribution functions for the clustered microstructure have two peaks: the first peak corresponds to the distance between the particles in a cluster, and the second peak corresponds to the distance between particles from different clusters.

The values of NND, NNI and SENND, determined for the generated microstructures, are given in Table 8.3

Table 8.2 *Amount (N) and radii (r) of particles for the considered microstructures.*

	VC				
	10 %	6 %		18 %	
		N = const.	r = const.	N = const.	r = const.
N	100	100	60	100	180
r	0.178	0.138	0.178	0.24	0.178

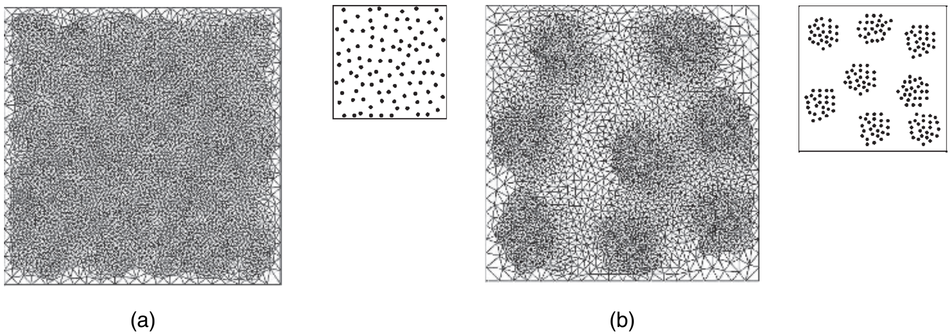

Figure 8.1 *Examples of (a) the uniform (random) and (b) clustered particle arrangements and FE meshes. Reprinted from* Compos. Sci. Technol.*,* **64***, Mishnaevsky Jr et al., 'Effect of Microstructures . . . ', pp. 1805–1818, Copyright (2004), with permission from Elsevier.*

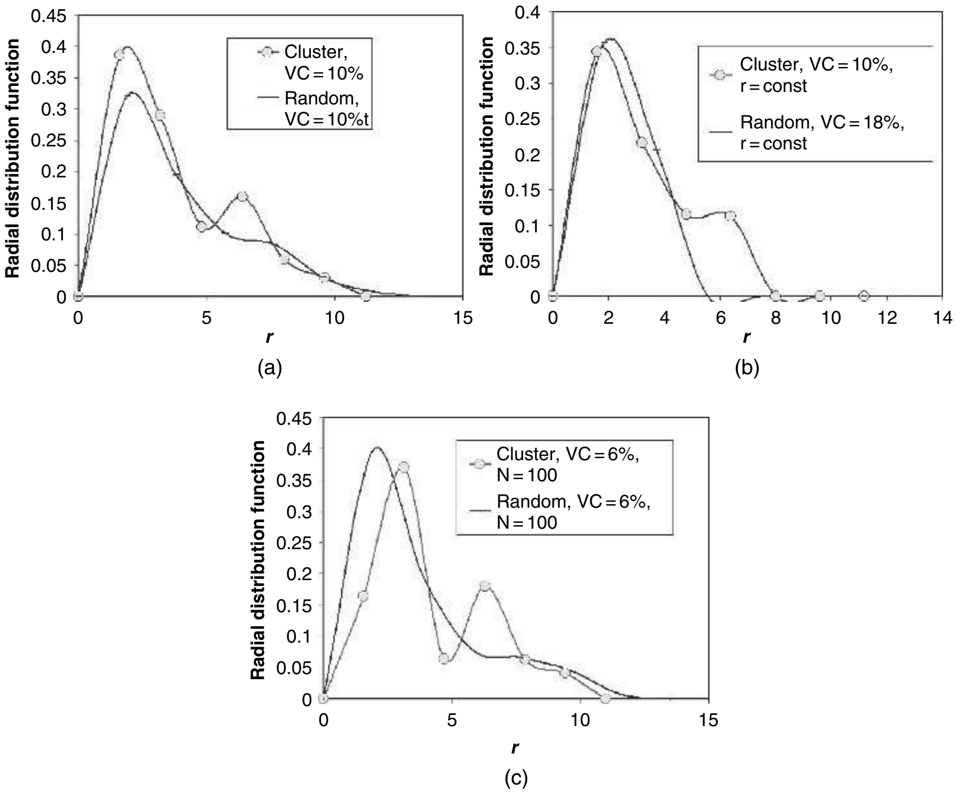

Figure 8.2 *Radial distribution functions of sphere centers for the clustered and uniform (random) particle arrangements. (a)* VC = 10 %*, 100 particles,* $r = 0.178\,\mathrm{mm}$*; (b)* VC = 18 %*, 180 particles,* $r = 0.178\,\mathrm{mm}$*; (c)* VC = 6 %*, 100 particles,* $r = 0.138\,\mathrm{mm}$*. Reprinted from* Compos. Sci. Technol.*,* **64***, Mishnaevsky Jr et al., 'Effect of microstructures . . . ', pp. 1805–1818, Copyright (2004), with permission from Elsevier.*

Table 8.3 NND between particle centers for the considered microstructures.

Microstructure	Parameter	VC				
		10 %	6 %		18 %	
			N = const.	r = const.	N = const.	r = const.
Random	NND	0.807	0.702	0.937	0.614	0.55
	SENND	0.895	1.15	0.8	0.613	0.9
	NNI	1.614	1.404	1.09	1.23	1.48
Clustered	NND	0.417	0.339	0.419	0.411	0.319
	SENND	0.607	0.652	0.574	0.531	0.374
	NNI	0.83	0.68	0.65	0.82	0.86

One can see from Table 8.3, that the NND, SENND and the NNI are much higher for the random particle arrangement than for the clustered particle arrangement.

8.1.2 Simulation of damage and particle failure in clustered microstructures

The deformation and damage evolution in composites with clustered and uniform particle distributions were simulated, using the above described models. Figure 8.3 gives the von Mises stress distributions for composites with clustered and uniform particle arrangements. The damage in the phases was simulated using the ABAQUS subroutine described in Section 6.3.

One can see from Figure 8.3 that the stresses in particles are much higher in the case of the clustered than in the case of the uniform particle arrangement. The stress distribution in the matrix is more homogeneous in the uniform than in the clustered microstructure. The stresses between clusters are typically lower than inside the clusters. One may expect therefore that after some particles fail, the ductile failure of ligament between particles inside clusters proceeds at relatively low load, yet, the propagation of cracks between clusters will require much higher energy than in the case of the uniform particle distribution. Figure 8.4 shows the elements which were weakened in the clustered microstructure as a result of damage initiation. From the simulations, one can see that the particles placed at the outer boundary of clusters (and not the particles inside clusters) become damaged at the beginning of the damage evolution. After a particle becomes damaged (i.e. an element from the particle is removed), other elements from the same particle are removed further. Simultaneously, other (mostly neighboring) particles become damaged (including the particles inside clusters).

Figure 8.5 shows the tensile stress–strain curves for composites with clustered and uniform (random) particle arrangements. Figure 8.6 shows the fraction of failed particles plotted versus the far field applied strain.

One can see from the Figures 8.5 and 8.6 that the clustered particle arrangement leads to a small increase in the flow stress and stiffness of the composite as compared with the uniform (random) particle arrangement. The difference between the flow stress for the clustered and uniform (random) particle arrangements is no more than 2–3 %. Such a small difference lies apparently in the limits of the experimental error, and therefore can not be observed in experiments (Derrien, 1997).

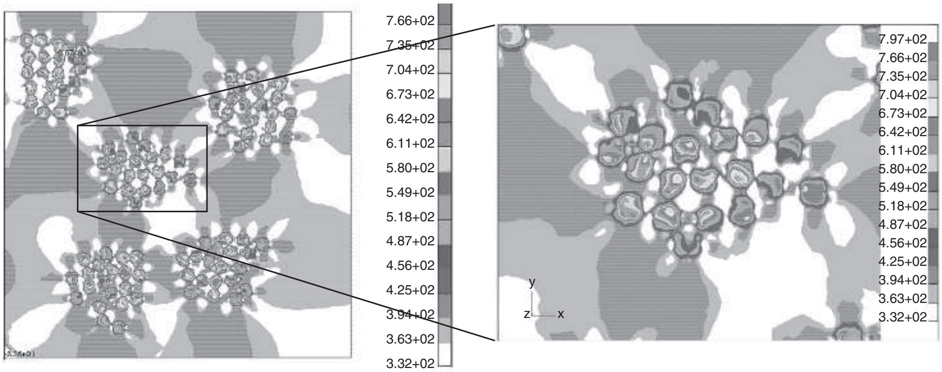

(a)

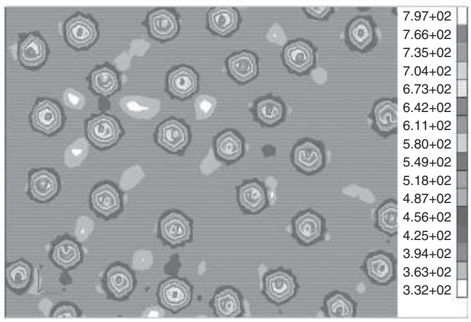

(b)

Figure 8.3 *Von Mises stress distributions for composites with (a) clustered and (b) uniform particle arrangements. Reprinted from* Compos. Sci. Technol.*,* **64***, Mishnaevsky Jr* et al.*, 'Effect of microstructures . . . ', pp. 1805–1818, Copyright (2004), with permission from Elsevier. (See Plate 4)*

The failure strain of the composite with the cluster particle arrangement is significantly lower than that for the uniform arrangement. These results correspond to the results from the 3D FE analysis in Section 6.6.

From Figure 8.6 it can be seen that many particles fail at almost the same external load, which is characteristic of the type of microstructure (clustering, volume content of particles). For instance, for the clustered particle arrangement ($\mathrm{VC} = 18\,\%,\ N = \mathrm{const.}$), the fraction of failed particles increases from 0.2 to 1 %, when the far field applied strain is about 0.02 mm. This can be explained by the fact that the particle failure occurs due to the plastic energy accumulated in the matrix during the previous deformation, and not just as a quick response to the load. Many particles in the matrix are subject to the similar local loads due to the high deformation energy in the matrix, and, therefore, many particles fail at the same load.

Table 8.4 gives the failure strains for the different microstructures of the composites, and the relations of the failure strains for random/clustered microstructures.

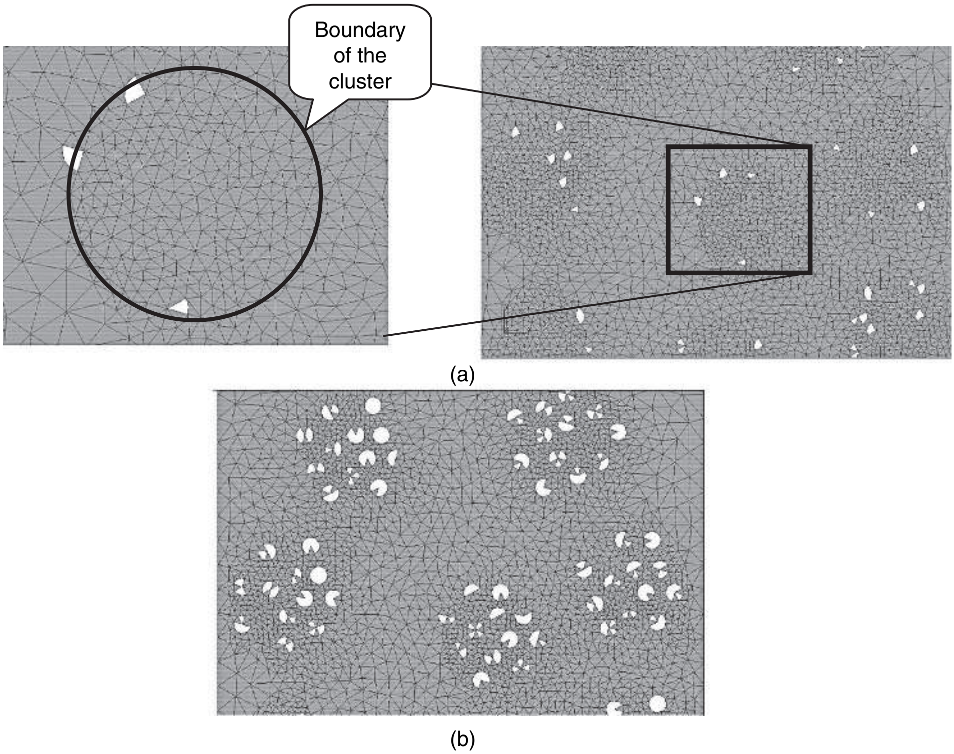

Figure 8.4 *Weakened finite elements in the particles: (a) scattered microcracks formed in the particles, mostly at the outer boundaries of the particle clusters; (b) intensive particle failure. Reprinted from* Compos. Sci. Technol.*,* **64***, Mishnaevsky Jr* et al.*, 'Effect of microstructures . . . ', pp. 1805–1818, Copyright (2004), with permission from Elsevier.*

Now, we can analyze the effect of the microstructure on the strength, stiffness and failure behavior of the composites with clustered microstructures.

The values of the failure strains are presented in Figure 8.7 as a column chart, in order to illustrate the effect of microstructures on the failure strain. From Figure 8.7 it can be seen that the random arrangement of particles ensures much higher failure strain than the clustered microstructure for all cases. Only the clustered microstructure with a very low volume content (6 %) and small amount of particles ($N = 60$) gives a failure strain comparable with that of the random microstructures.

The ratio of the random versus clustered arrangement failure strains depends strongly on the volume content of the particles. The effect of an increased amount of particle in a cluster on the failure strain is much stronger than the effect of particle radius: While an increase of the particle number, corresponding to an increase of SiC volume content from 6 to 18 %, leads to a reduction of the failure stress by 50 %, a similar increase in the particle radius leads to a reduction of the failure stress by 3–20 %.

Figure 8.8 gives the failure strain of the composites, determined in the simulations, plotted versus the average NND (nearest neighbor distance) between the particles in the composites. The trend line shows that the higher the values of the average NND, the higher the failure strain of the composite. An increase in the NND by 35 % leads to a decrease of the probability of failure by 40 %.

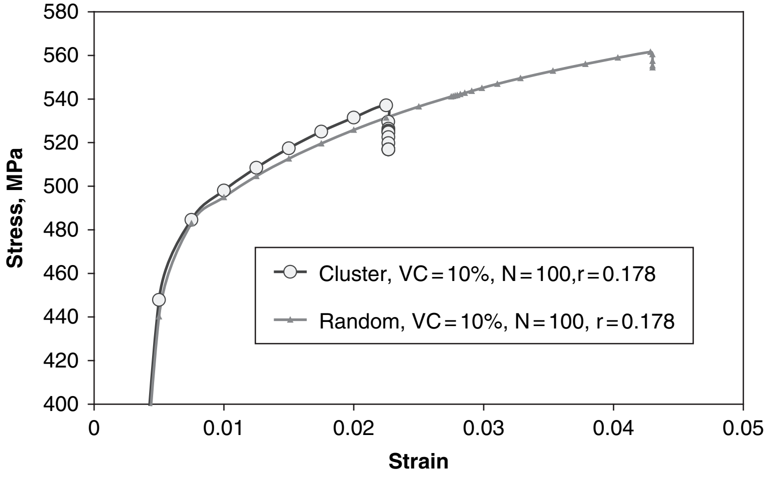

(a)

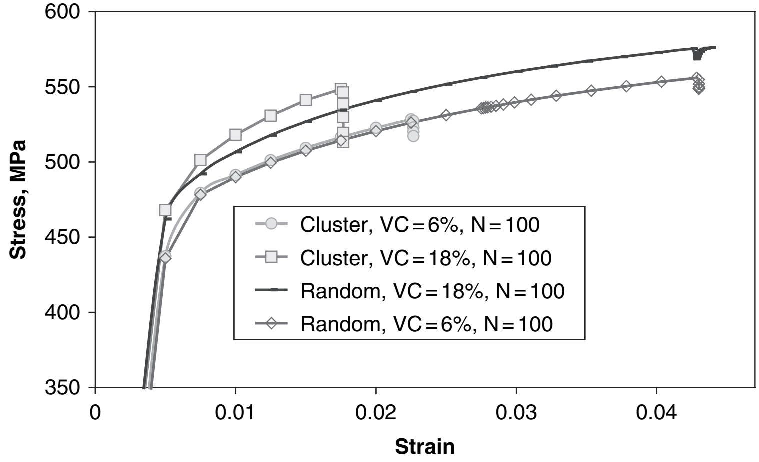

(b)

Figure 8.5 *Tensile stress–strain curves for composites with uniform (random) and clustered arrangements of particles: (a)* VC = 10 %, *N* = 100, *r* = 0.178 mm*; (b) N* = 100*, varied volume content (6 % and 18 %) and particle radii; (c) r* = 0.178 mm *and varied volume content and amount of particle. Reprinted from* Compos. Sci. Technol.*,* **64***, Mishnaevsky Jr* et al.*, 'Effect of microstructures . . . ', pp. 1805–1818, Copyright (2004), with permission from Elsevier.*

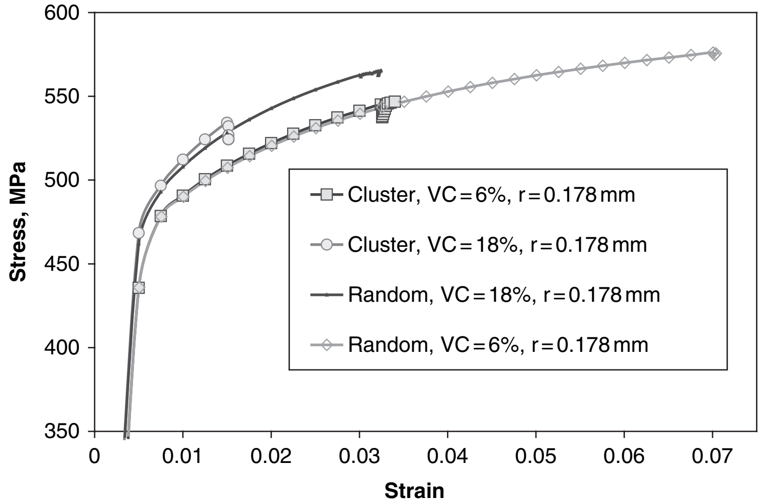

(c)

Figure 8.5 *(Continued)*

8.2 Analytical modeling of the effect of particle clustering on the damage resistance

8.2.1 Cell array model of a composite

Let us consider the damage accumulation in composites with uniform (random) and clustered particle arrangements. For the sake of definiteness, we consider the SiC particle reinforced Al matrix composite again. The composite material may be presented as an array of cells (Mishnaevsky Jr. *et al*., 2004b), each the size of a particle cluster. Figure 8.9 shows such a material representation. If N is the amount of particles in the material, M the amount of cells in the model and K the amount of clusters in a model, the total amount of particles in each cell is $m = N/M$ for the case of the uniform particle arrangement, and $m = N/K$ (in a cell with particle cluster) and $m = 0$ (in a cell without a cluster) for the case of the clustered microstructure.

The probability of macroscopic fracture in a clustered microstructure can be defined as a probability of the formation of a crack of the size of a cluster (Baptiste, 1999).

Let us determine the probability of the failure of a cell. Failure in Al/SiC composites proceeds as follows (see Chapter 6): first, some particles fail; after that, cavities and microvoids nucleate in the matrix near the broken particles, grow and coalesce, and that leads to the failure of the matrix ligaments between particles, and finally to the formation of a macrocrack (Hu *et al*., 1998; Derrien *et al*., 1999). Derrien *et al*. (Derrien *et al*., 1999) considered the failure of matrix ligament between failed particles. They demonstrated that the growth rate of cavities in the ligament between particles is a decreasing function of the distance between particles. A ligament fails, when the growth rate of cavities in the ligament exceeds some critical value. Figure 8.10 shows this mechanism of damage in the composite. Using the model of the formation of a plastic zone between two broken particles, developed by Evensen and Verk (Evensen and Verk, 1981), Derrien *et al.* (Derrien *et al.*, 1999) derived a formula for the critical distance between neighboring failed particles, at which the matrix ligament between them fails by the mechanism of the progressive void growth:

$$l_1 = l_{cr} = a(\sqrt{2\pi/3f} - \sqrt{8/3}) \tag{8.2}$$

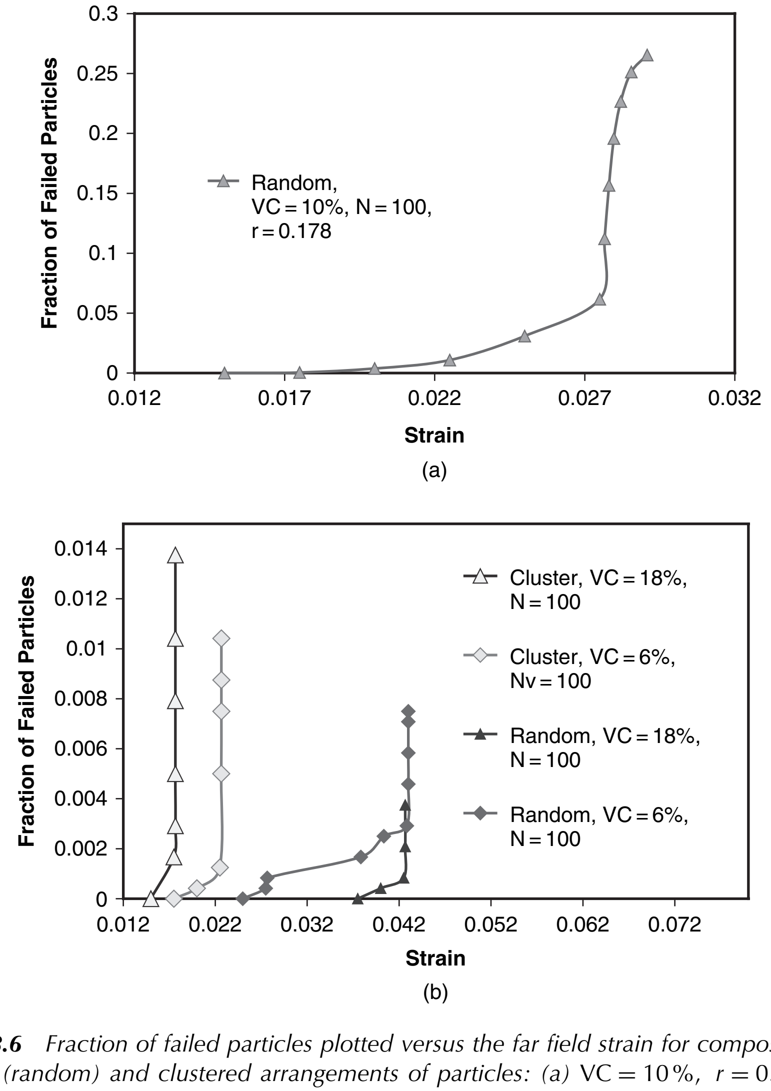

Figure 8.6 *Fraction of failed particles plotted versus the far field strain for composites with uniform (random) and clustered arrangements of particles: (a)* VC = 10 %, *r* = 0.178 mm, *random particle arrangement; (b) N* = 100*, varied volume content and particle radii; (c) r* = 0.178 mm *and varied volume content and amount of particle. Reprinted from* Compos. Sci. Technol.*,* **64***, Mishnaevsky Jr* et al.*, 'Effect of microstructures . . . ', pp. 1805–1818, Copyright (2004), with permission from Elsevier.*

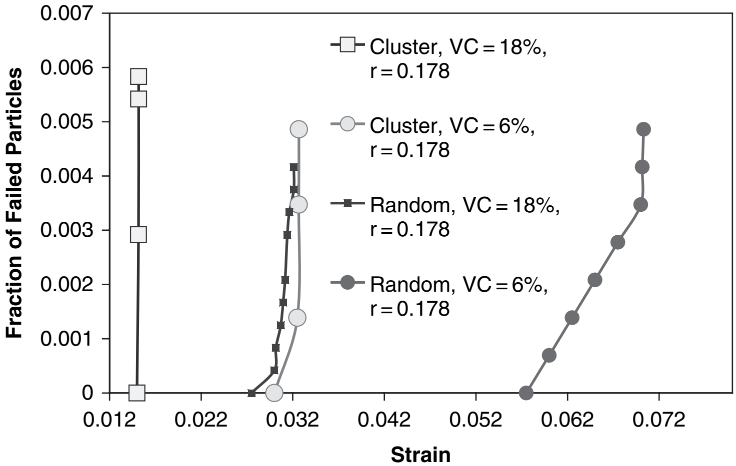

(c)

Figure 8.6 *(Continued)*

Table 8.4 *Failure strains for the different microstructures of the composites.*

Microstructure		VC(%)	Random	Clustered	Ratio of failure strains (random /clustered)	Ratio of failure strains (18 %/6 %)	
N	*r*					Random	Clustered
100	0.178	10	0.042	0.022	1.90		—
100	0.138	6	0.043	0.022	1.95	0.97	0.8
	0.24	18	0.042	0.0176	2.39		
60	0.178	6	0.062	0.032	1.94	0.51	0.47
180		18	0.032	0.015	2.13		

where a is particle radius, f is particle volume content, l_l and l_{cr} are the length and critical length of the ligament (i.e. the distance between particles). When some amount n particles in a cell fail, the average distance between failed particles is:

$$l_{av} = 0.5\sqrt{v/n} \tag{8.3}$$

where v is the volume of a cell. The condition of the cell failure can be stated as a condition that the average distance between failed particles l_{av} exceeds the critical distance, calculated by Equation (8.2):

$$l_{av} = l_l \tag{8.4}$$

and

$$\mathrm{Prob_F} = \mathrm{Prob}\{l_{av} = l_l\} \tag{8.5}$$

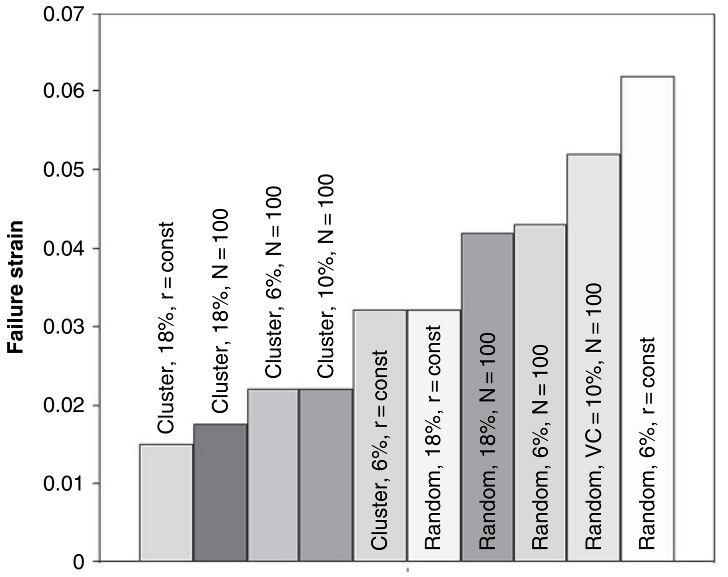

Figure 8.7 *Failure strains for different microstructures. Reprinted from* Compos. Sci. Technol.*,* **64***, Mishnaevsky Jr* et al.*, 'Effect of microstructures . . . ', pp. 1805–1818, Copyright (2004), with permission from Elsevier.*

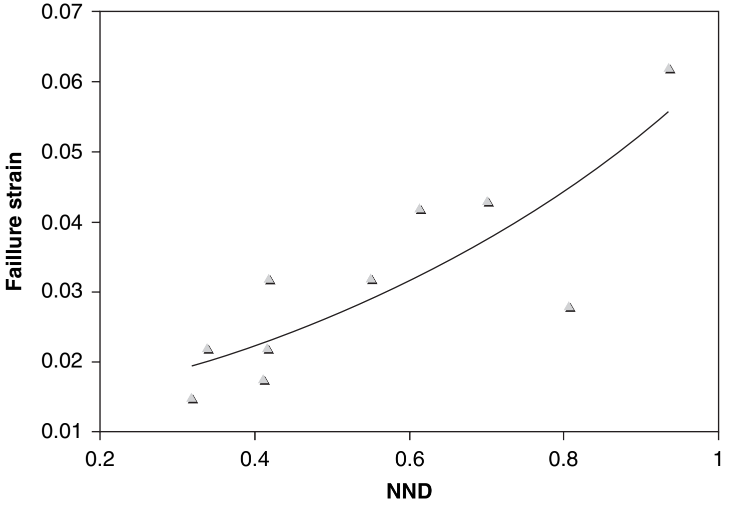

Figure 8.8 *Failure strain plotted versus the average NND (nearest neighbor distance) between particles. Reprinted from* Compos. Sci. Technol.*,* **64***, Mishnaevsky Jr* et al.*, 'Effect of microstructures . . . ', pp. 1805–1818, Copyright (2004), with permission from Elsevier.*

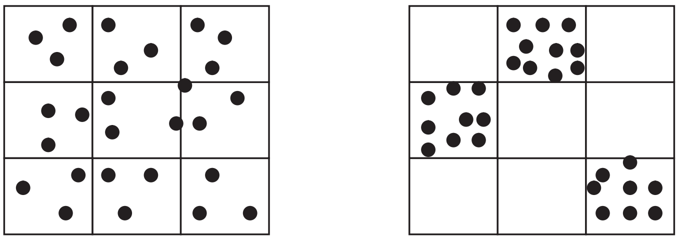

Figure 8.9 Schema of a clustered material presented as an array of cells.

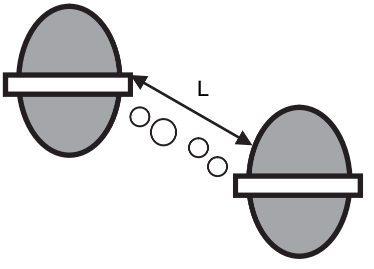

Figure 8.10 Mechanism of damage in the Al/SiC composites: failure of matrix ligaments between the damaged SiC particles.

where Prob_F is the probability of the specimen failure.

The critical amount of failed particles in a cell, at which the average distance between failed particles is equal to the critical length of the ligament between particles, can be calculated by:

$$n_{cr} = \frac{v}{4a(\sqrt{2\pi/3f} - \sqrt{8/3})^2} \tag{8.6}$$

Thus, the condition (8.4) is met if the amount of failed particles in a cell is equal to n_{cr}.

8.2.2 Probabilistic analysis of damage accumulation in a cell

Consider the density of failed particles in a cell. The probability, that n_{cr} particles fail in a cell (which is considered here as the probability of the cell failure) can be determined as a probability of realizing this event (i.e. particle failure) n_{cr} times in m independent repeated trials, where $m = N/K$ for the clustered microstructure and $m = N/M$ for the random microstructure. Assuming that the particles fail independently with a probability p, one may describe such a probability distribution by the binomial law:

$$\mathrm{Prob}_F = \mathrm{Prob}(n = n_{cr}) = C_m^{n_{cr}}\ p^{n_{cr}}\ (1-p)^{m-n_{cr}} \tag{8.7}$$

where p is the the probability of particle failure (or the density of failed particles). The probability of particle failure can be determined, for instance, by the equation suggested by Maire *et al*. (Maire *et al*., 1997):

$$p = 1 - \exp\{-(a/a_0)^3[(\sigma - \sigma_{cr})/\sigma_0)^h\} \tag{8.8}$$

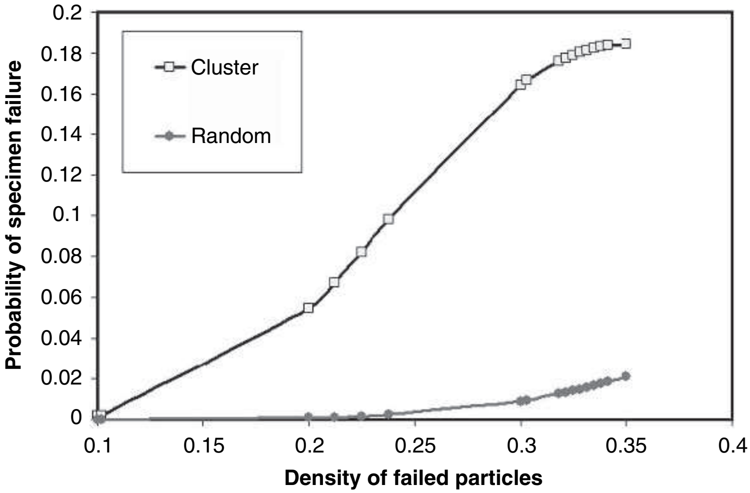

Figure 8.11 *Probability of the formation of a crack calculated by Equations (8.7) and (8.8) as a function of the density of failed particles Reprinted from* Compos. Sci. Technol.*,* **64***, Mishnaevsky Jr* et al.*, 'Effect of microstructures. . . ', pp. 1805–1818, Copyright (2004), with permission from Elsevier.*

where σ is stress on a particle, a is particle size, σ_{cr} is stress below which no particle failure occurs, σ_0, a_0 and h are material constants, i.e. representative stress, representative dimension and Weibull modulus, respectively.

Figure 8.11 shows the probability of the formation of a crack calculated by Equations (8.7) and (8.8) as a function of the density of failed particles. The calculations were made for the following parameters: $N = 100$, $M = 10$, $K = 5$, $n_{cr} = 7$. The parameters of the material were taken from Maire *et al.* (Maire *et al.*, 1997), and are as follows: $\sigma_{cr} = 580\,\text{MPa}$, $\sigma_0 = 1700\,\text{MPa}$, $a_0 = 11.5\,\mu\text{m}$, $h = 3.8$.

One can see that the density of failed particles must be three times higher for the random, than for the clustered particle arrangement, to ensure equal failure probability. Similarly, the stress on a particle must be 15–16 % higher for the random, than for the clustered particle arrangement, to ensure equal failure probability. For the same density of failed particles, the failure probability for the clustered particle arrangement is 10–100 times higher than for the random particle arrangement, depending on the density of failed particles and their strength. The ratio between the probability of failure for clustered and uniform microstructures is very high for relatively strong particles (i.e. low density of failed particles). For the weaker particles, the ratio decreases.

Now, consider the effect of the degree of clustering on the probability of a crack formation. The degree of particle clustering can be characterized in our model by the ratio M/K (i.e. the total amount of cells divided by the amount of cells with clusters). The higher M/K, the more particles are located in one cell, and the bigger the volume of the particle-free material in the composite.

Figure 8.12 shows the ratio of the probabilities of specimen failure for random and clustered arrangements plotted versus the degree of particle clustering M/K. The

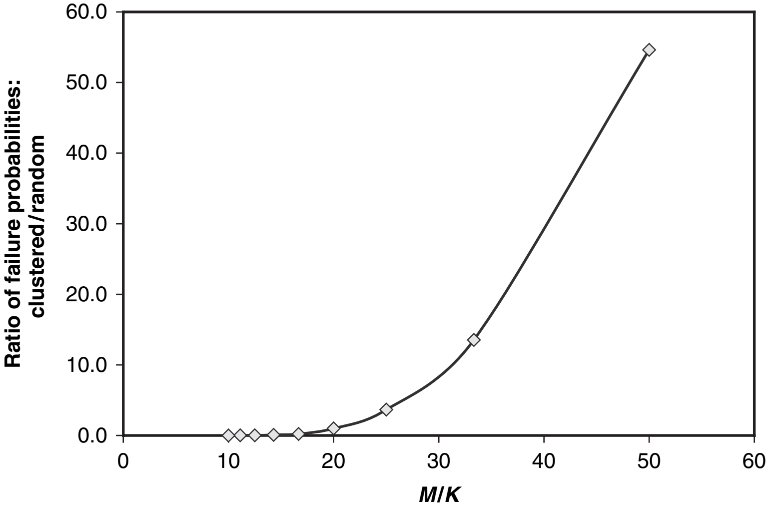

Figure 8.12 *Ratio of the probabilities of macrocrack formation for random and clustered arrangements plotted versus the degree of particle clustering M/K. Reprinted from* Compos. Sci. Technol.*,* **64***, Mishnaevsky Jr* et al.*, 'Effect of microstructures . . .', pp. 1805–1818, Copyright (2004), with permission from Elsevier.*

probabilities were calculated for the average density of failed particles $p = 0.1$, and $N = 100$, $M = 10$, K varied from 10 (no clustering) to 2 (very high clustering). One can see that the probability of failure of a composite with clustered particle arrangement increases with increasing the degree of particle clustering.

The curve in Figure 8.12 can be interpreted also as a relationship between the ratio of the probabilities of macrocrack formation and the NND (nearest neighbor distance) between particle centers. The average NND for the clustered microstructure can be calculated by:

$$l_{\mathrm{NND}} = 0.5\sqrt{vK/M} \tag{8.9}$$

One can see from Figure 8.12, that the decrease in the NND between particle centers by 50 % (from 0.15 for $K = 9$ to 0.1 for $K = 4$ and $v = 0.5$) leads to the increase of the ratio of the failure probabilities of clustered/random microstructures from 0.01 to 3.66.

A similar result was obtained numerically in Section 8.1.2. One can draw a conclusion from the above analysis that the clustered arrangement of particles leads to a much higher likelihood of crack formation, as compared with the uniform (random) particle arrangement (for the same density of failed particles and the same applied load).

8.2.3 Effect of particle clustering on the fracture toughness

The conclusion drawn from the above analysis, is that the critical strain, at which the intensive damage growth begins and a first crack forms, decreases if the damageable particles in the composite are arranged in clusters, as compared with uniform and random particle arrangement. This conclusion is confirmed by the experimental results by Derrien (Derrien, 1997), Derrien *et al.* (Derrien *et al.*, 1999) and by the numerical results by Geni and Kikuchi (Geni and Kikuchi, 1998) and Segurado *et al.* (Segurado *et al.*, 2003).

It is of interest to discuss here the difference between these results, and the results by Berns *et al.* (Berns *et al.*, 1998) and Mishnaevsky Jr *et al.* (Mishnaevsky Jr *et al.*, 2003a, 2004a), who have shown that the clustering of particles ensures higher fracture toughness of brittle particle reinforced materials as compared with homogeneous microstructures. One should note that the deformation and damage evolution in the model presented here are considered up to the point, where the falling branch of the force–displacement curve begins. This corresponds to the point, when a mesoscale crack (i.e. a crack of the size of a cluster) forms, or the density of failed particles exceeds some critical value. This approach is natural for the materials used in the automobile and aviation industry, for instance. If we however look at the specimen failure defined as a formation of a percolating macrocrack in the specimen (running both through the particle clusters and the particle-free zone), the fracture resistance of the material becomes dependent on the toughness of the particle-free regions of the material (which is much higher than the toughness of the composite with particles). In this case, the specific fracture energy can be calculated in the framework of the cell model of the material as follows:

$$G_{\text{av}} = \sqrt{K/M}\ G_{\text{clust}} + (1 - \sqrt{K/M})G_{\text{matrix}} \tag{8.10}$$

where G_{av} is the specific fracture energy of the material, G_{clust} and G_{matrix} are the specific fracture energies of the formation of a new surface in a particle cluster and in the matrix, respectively, M is the amount of the cells (with or without clusters) in the model and K is the amount of clusters in the model. Denoting $\psi = G_{\text{clust}}/G_{\text{matrix}}$, one can rewrite Equation (8.10) in the form:

$$G_{\text{av}} = G_{\text{matrix}}[1 - \sqrt{K/M}\ (1 - \psi)] \tag{8.11}$$

The ratio M/K characterizes the degree of the particle clustering: $M/K = 1$ for a homogeneous material, and increases with increasing localization of particles for a clustered particle arrangement. For a ductile metal matrix composite with brittle damageable particles, $G_{\text{clust}} << G_{\text{matrix}}$ and $\psi < 1$. One can see from Equation (8.11) that the specific fracture energy increases with increasing the degree of the particle clustering M/K. Thus, *whereas the strain, at which the critical density of failed particles in the material is achieved, is much higher for the material with the uniform particle arrangement than for the clustered arrangement, the total fracture toughness of the materials increases with increasing the degree of particle clustering*. This conclusion is supported by the numerical and experimental results by Berns *et al.* (Berns *et al.*, 1998) and Mishnaevsky Jr *et al.* (Mishnaevsky Jr *et al.*, 2004a).

Summarizing, one may state that the clustered arrangement of brittle particles in a ductile matrix leads to lower failure strain than that in the case of a homogeneous inclusion arrangement. It is shown that the higher the values of the average NND, the higher the failure strain of the composite. However, the total fracture toughness of the composites increases with increasing the degree of particle clustering.

References

Baptiste, D. (1999). Damage behaviour of composites, Cours de formation, 23–30/08, Jesi, Italy.

Berns, H., Melander, A., Weichert, D., Asnafi, N., Broeckmann, C. and Gross-Weege, A. (1998). A new material for cold forging tool, *Composites Materials Science*, **11** (142), 166–180.

Bush, M. B. (1997). The interaction between a crack and a particle cluster, *International Journal of Fracture*, **88** (3), 215–232.

Derrien, K. (1997) Modélisation par des méthodes d'homogénéisation de l'endommagement et de la rupture de composites Al/SiCp, PhD Thesis, ENSAM, Paris.

Derrien, K., Baptiste, D. Guedra-Degeorges, D. and Foulquier, J. (1999). Multiscale modelling of the damaged plastic behaviour of AlSiCp composites, *International Journal of Plasticity*, **15**, 667–685.

Evensen, J. D. and Verk, A. S. (1981). The influence of particle cracking on the fracture strain of some Al-Si alloys, *Scripta Metallurgica*, **15**, 1131–1133.

Geni, M. and Kikuchi, M. (1998). Damage analysis of aluminum matrix composite considering non-uniform distribution of SiC particles, *Acta Materialia*, **46** (9), 3125–3133.

Hu, G., Guo, G. and Baptiste, D. (1998). A micromechanical model of influence of particle fracture and particle cluster on mechanical properties of MMCs, *Computational Materials Science*, **9**, 420–430.

Kikuchi, M. and Geni, M. (1998). Evaluation of the interaction effects of SiC particles during damage process of MMCs, *Key Engineering Materials*, **145–149**, 895–900.

Llorca, J. and Gonzalez, C. (1998). Microstructural factors controlling the strength and ductility of particle reinfoced metal matrix composites, *Journal of the Mechanics and Physics of Solids*, **46** (1), 1–28.

Maire, E., Embury, J. D. and Wilkinson, D. S. (1997). Modelling of damage in particulate metal matrix composites, *Key Engineering Materials*, **127–131**, 1167–1174.

Mishnaevsky Jr, L., Lippmann, N. and Schmauder, S. (2003a). Computational modeling of crack propagation in real microstructures of steels and virtual testing of artificially designed materials, *International Journal of Fracture*, **120** (4), 581–600.

Mishnaevsky Jr, L., Weber, U. and Schmauder, S. (2004a). Numerical analysis of the effect of microstructures of particle-reinforced metallic materials on the crack growth and fracture resistance, *International Journal of Fracture*, **125**, 33–50.

Mishnaevsky Jr, L., Derrien, K. and Baptiste, D. (2004b). Effect of microstructures of particle reinforced composites on the damage evolution: probabilistic and numerical analysis, *Composites Science and Technology*, **64** (12), 1805–1818.

Segurado, J., González, C. and LLorca, J. (2003). A numerical investigation of the effect of particle clustering on the mechanical properties of composites. *Acta Materialia*, **51**, 2355–2369.

Sϕrensen, B. F. and Talreja, R. (1993). Effects of nonuniformity of fiber distribution on thermally-induced residual-stresses and cracking in ceramic-matrix composites. *Mechanics of Materials*, **16**, 351–363.

9

Interpenetrating phase composites: numerical simulations of deformation and damage

In Chapters 4–8, composites with relatively low volume content of reinforcement were considered. In such materials, the reinforcing elements are surrounded by the matrix phase, and interact via stress and strain fields. However, with increasing volume content of the reinforcing elements, the reinforcing particles start to touch each other and to form aggregates. At some density of reinforcement, the particles form interconnected networks (finite or infinite percolation clusters), which strongly influence mechanical properties and strength of composites.

The materials, in which one or both phases forms an interconnected network, present a rather large and important group, and many of the materials are widely used industrially. This group of materials includes, for instance, various biomaterials, tool materials (e.g. WC/Co cemented carbides with the WC skeleton, compare Figure 9.1) (Loshak, 1984; Mishnaevsky Jr, 1995a), other sintered composites (Purohit and Sagar, 2001), porous materials and foams, polymer composites, containing conducting filler particles (e.g. graphite), as well as other dielectric composites. Some graded composite materials have regions with interpercolating phases between the regions of high concentration of each of the phases.

If both phases of a composite form completely interconnected networks (infinite percolation clusters), the material is referred to as *interpenetrating phase composite* (IPC) (Clarke, 1992).

The interest in the modeling of materials with interpenetrating phases has increased in the last few years, as a result of the development of new materials: nanocomposites with nanoscale reinforcement, which forms percolating networks (Buxton and Balazs, 2004), foams and porous materials, etc.

Computational Mesomechanics of Composites L. Mishnaevsky Jr

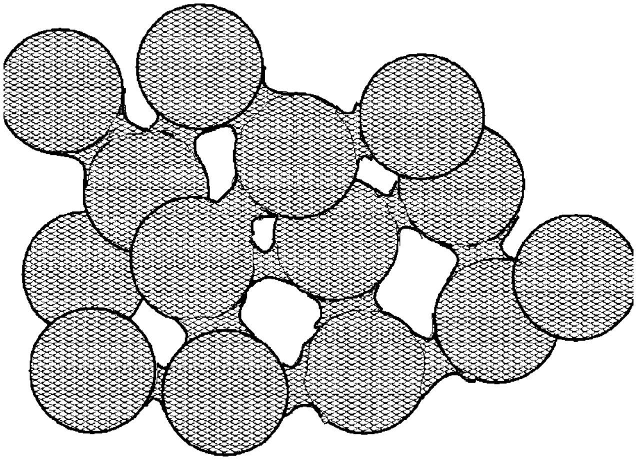

Figure 9.1 *Schema of a skeleton from carbide particles in a sintered composite.*

The oldest approach to the analysis of materials with a skeleton is based on the parameters of continuity and contiguity (see Chapter 2). The *contiguity* parameter was introduced by Gurland (Gurland, 1958) to characterize microstructures of cemented carbides with a skeleton, and is defined as a ratio of the grain–grain boundary surface area to the total interface area. Chermant and Osterstock (Chermant and Osterstock, 1979) have shown that the yield stress of WC/Co hard alloys increases if the contiguity of the skeleton from WC particles in the material increases. Using a probabilistic model of joining particles in sintering, Mishnaevsky Jr (Mishnaevsky Jr, 1995a, 1998a) calculated the continuity of the skeleton of a hard alloy as a function of the sintering conditions. Using a probabilistic model of damage accumulation in intergrain necks in the wolfram carbide skeleton of the hard alloys, Mishnaevsky Jr demonstrated that the yield strength of the composite is proportional to the contiguity of the skeleton.

Fan *et al.* (Fan *et al.*, 1992) expanded the concept of contiguity, and introduced several other parameters of microstructure (the degree of separation of the phases, numbers of intercepts of interfaces). Further, Fan and colleagues developed a method of estimation of the young modulus of composites, based on the topological transformation of a two-phase microstructure into a three-phase microstructural element body. Aldrich *et al.* (Aldrich *et al.*, 2000) applied this model to the analysis of nickel/alumina interpenetrating phase composites, and demonstrated that the estimations of Young modulus, based on this model, are in good agreement with experiments.

Several micromechanical unit cell models have been developed for the analysis of the mechanical behavior of materials with percolating/interpenetrating microstructures.

Ravichandran (Ravichandran, 1994) proposed a simple cubic unit cell model of interpenetrating microstructures and employed it to study the deformation of composites with two ductile phases. The 3D simple cubic model [Figure 9.2(a)] was used by Daehn *et al.* (Daehn *et al.*, 1996) to analyze the deformation behavior of the C^4 materials (interpenetrating mixture of elastic perfectly plastic Al and elastic Al_2O_3; see Breslin *et al.*, 1994).

Lessle *et al.* (Lessle *et al.*, 1999) introduced the 'matricity' parameter which is defined as 'the fraction of the skeleton lines of one phase S, and the length of the skeleton lines of

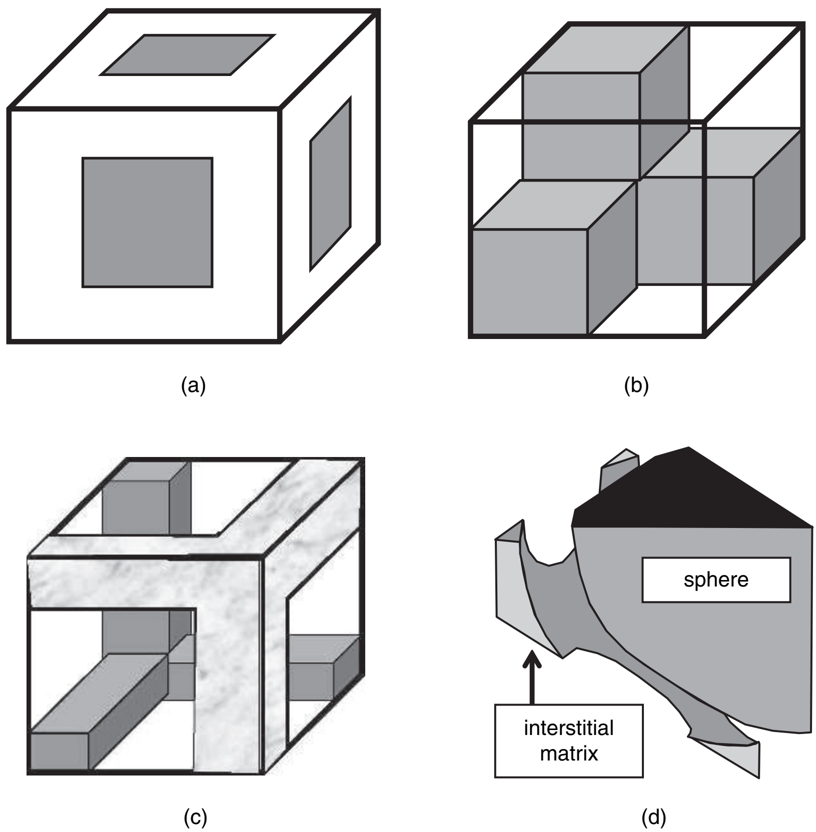

Figure 9.2 *Unit cell models of interpenetrating phase composites: (a) 3D cubic model by Daehn* et al. *(Daehn* et al.*, 1996); (b) and (c) two- and three–phase models by Feng* et al. *(Feng* et al.*, 2003, 2004); (d) triangular prism unit cell model by Wegner and Gibson (Wegner and Gibson, 2000). (a) Reprinted from* Acta Mater.*,* ***44*** *(1), Daehn* et al.*, 'Elastic and plastic behavior . . . ', pp. 249–261, Copyright (1996), with permission from Elsevier. (b,c) Reprinted from* Comput. Mater. Sci.*,* ***28*** *(3–4), Feng* et al.*, 'A micromechanical model for . . . ', pp. 496–493, Copyright (2003), with permission from Elsevier. (d) Reprinted from* Int. J. Mech. Sci*,* ***42*** *(5), Wegner and Gibson, 'The mechanical behavior . . . ', pp. 943–964, Copyright (2000), with permission from Elsevier.*

the participating phases'. Using the approach, based on the combination of two unit cell models, Lessle and colleagues incorporated the matricity parameter into the embedded cell model, developed by Dong and Schmauder (Dong and Schmauder, 1996). In the models, each phase is considered as an inclusion, surrounded by a layer of another phase, so that the length of this layer corresponds to the length of the skeleton line of the phase.

Feng *et al*. (Feng *et al*., 2003, 2004) developed unit cell models for the estimation of elastic moduli of interpenetrating multiphase composites, and considered special cases of interpenetrating two- and three-phase composites. The unit cells for n phases are decomposed into series and parallel subcells, and their elastic moduli are determined using the Mori–Tanaka method, and the Reuss and Voigt estimations. Figure 9.2(b) and (c) shows the unit cells, used by Feng and colleagues for the analysis of two- and three-phase composites.

Wegner and Gibson (Wegner and Gibson, 2000) modeled an interpenetrating phase composite as a hexagonal array of intersecting spheres. The volume between the spheres is filled with another material. The triangular prism unit cell model was designed by analyzing symmetries of the close-packed array of spheres. Wegner and Gibson demonstrated that the composites with interpenetrating phases have improved Young modulus, strength and thermal expansion, as compared with composites with noninterpenetrating microstructures.

The lattice models can be efficiently used for the analysis of composites with interpenetrating microstructures. Using the analogy between the electrical conductivity of resistor networks and stiffness of phases in composite, Moukarzel and Duxbury (Moukarzel and Duxbury, 1994) simulated the failure of composites with interpenetrating phases as failure of random resistor networks on cubic lattices.

Another group of approaches is based on the methods of statistical physics and percolation theory, utilized to determine scaling properties and critical exponents of percolating composite materials (Bergman, 1978, 2002; Barta, 1994; Sarychev and Brouers, 1994).

In this Chapter, we seek to analyze the effect of the formation of interpenetrating structures (percolation clusters) on the strength and mechanical behavior of composites. In order to model the near-percolating and percolating microstructures, we use the voxel array based representation of microstructures of materials (realized in the program Voxel2FEM, see Section 5.3). The advantage of this method (as compared with the unit cell models, listed above) is that it allows to analyze both interpenetrating microstructures, locally (gradient) interpenetrating microstructures and transition microstructures (close to the percolation threshold) in the framework of one and the same approach. Further, it allows to take into account the random arrangement of microstructural elements in the interpenetrating microstructures. In the following, we carry out numerical simulations of the deformation and damage behavior in several groups of materials with percolating microstructures:

- interpenetrating phase composites with random distribution of phases (‘3D random chessboards’);
- graded interpenetrating phase composites, where the regions of interpenetrating microstructures are available between the regions of high content of each phase;
- porous ductile materials.

Results of simulations carried out with the use of the geometry-based and voxel array based methods of the FE model generation are compared, in order to verify the compatibility of results in this and previous chapters. Further, we consider here the same materials as in previous chapters to ensure the compatibility and comparability of the results.

9.1 Geometry-based and voxel array based 3D FE model generation: comparison

Now, we seek to verify the compatibility of results obtained with the use of the geometry-based and voxel-based methods of the model generation. Two multiparticle unit cell models for identical ideal 3D microstructures were generated using the program Meso3D (i.e. exact geometrical shape based model generation plus free meshing) and the program Voxel2FEM (voxel-based model generation). The cells ($10 \times 10 \times 10$ mm) with five spherical particles and volume content of particles 5 % were considered in both cases. The FE analysis of deformation and damage in a composite was carried out, and the results of simulations were compared.

In total, the geometry-based model contained 7800 elements, and the voxel-based model 15625 brick elements. Each particle contained 370 FEs in the geometry-based model, and 156 FEs in the voxel-based model.

Figure 9.3 shows the considered unit cells, as well as the stress–strain curves and the fraction of failed elements plotted versus applied strain curves, obtained numerically.

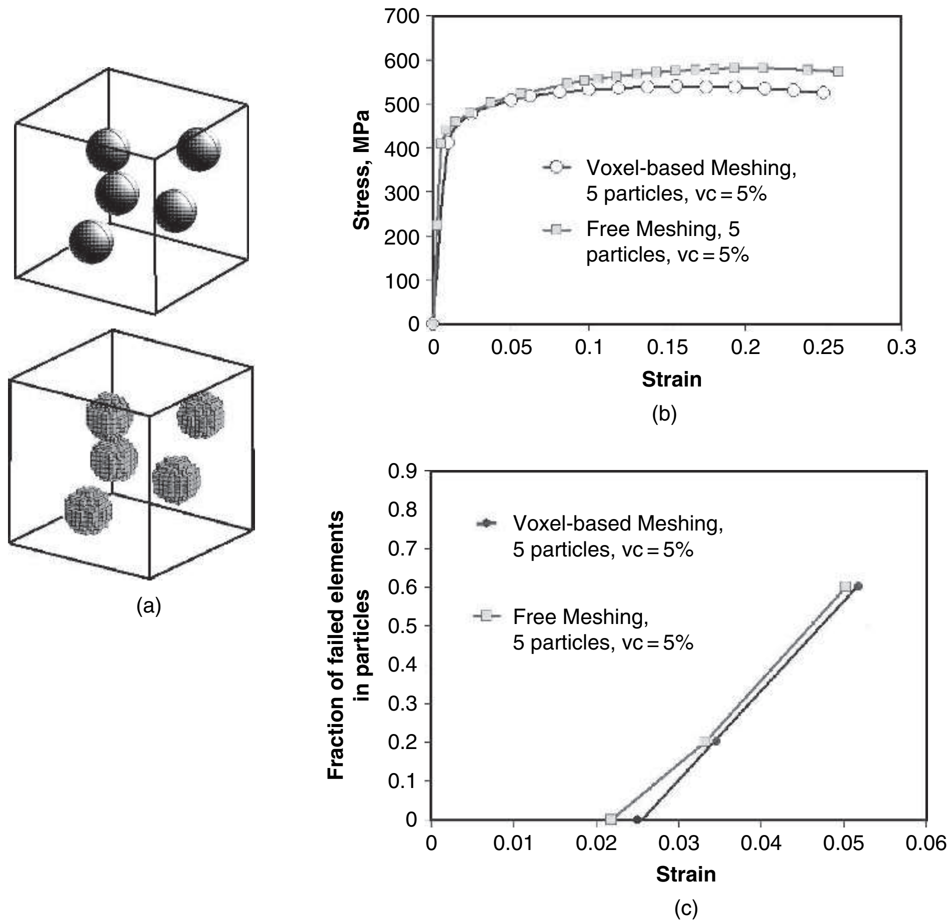

Figure 9.3 *(a) Considered unit cells, as well as (b) the stress–strain curves and (c) the fraction of failed elements versus applied strain curves, obtained numerically. Reprinted from* Mater. Sci. Eng., A*, **407**, Mishnaevsky Jr, 'Automatic voxel . . . ', pp. 11–23, Copyright (2005), with permission from Elsevier.*

One can see that the results obtained from the models, generated from the voxel data arrays and from the exact geometrical description of microstructures, are very close: the stress–strain curves differ only by 5 %, and the damage–strain curves only by 3–4 %.

Let us compare our conclusions with the results of similar investigations carried out in other groups. Guldberg *et al.* (Guldberg *et al.*, 1998) tested the accuracy of digital image based FE models in 2D and 3D cases, and concluded that the 'solution at digital model boundaries was characterized by local oscillations, which produced potentially high errors within individual boundary elements'. The solution, however, oscillated about the theoretical solution, and was improved by averaging the results over the region of several elements. The observed absolute errors in different simulations were of the order of 1–4 %. Niebur *et al.* (Niebur *et al.*, 1999) investigated the convergence behavior of FE models depending on the size of elements used, the element polynomial order, and on the complexity of the applied loads, and concluded that differences in apparent properties at different resolutions were always less than 10 %, when the ratio of mean trabecular thickness to element size was greater than four. Therefore, our conclusions are rather close to the results of other authors.

9.2 Gradient interpenetrating phase composites

In this section, we analyze the effect of microstructures of gradient composites on the deformation and damage resistance. In contrast to the analysis in Chapter 7, we consider the case of graded composite microstructures with high volume content of inclusions (and, therefore, with regions of interpenetrating phases). In this case, the gradient of the hard phase distribution can not be described by the probability distribution of the distances between the particle centers and the upper border of the cell. Instead, we use the more general approach to the generation of artificial microstructures of the materials, based on the distribution of the volume content of hard phase and realized in the program Voxel2FEM. Taking the volume content of the black voxels (hard phase), as a function of the Y coordinate, proportional to $1/[1+\exp(g-2^{*}g^{*}\mathrm{Y}/L)]$ (where L is cell length and g the gradient parameter, see §7.6.2), we generated a series of 3D FE models of graded random arrangements of hard phase (with different gradient parameter g and different volume contents of the inclusions).

Figure 9.4 shows some examples of the designed gradient interpenetrating phase microstructures. The deformation and damage in the materials were simulated numerically. The material properties were the same as in the above simulations. Figure 9.5 shows the stress–strain curves of composites with volume content of hard phase of 10 % and 20 %, and with various values of the gradient parameter g.

One should note here that in the models, which are used in this section, the grains of phases are represented as single bricks/voxels. While the brick model is a rather rough approximation of the grain shape, the widely used representation of particles or inclusions in materials as spheres is as far from the real shapes of particles as the brick model. However, the analysis of statistical parameters of microstructures and their effects on the damage resistance and strength of composites is possible only on the basis of relatively big cutouts (windows) of materials. Given the available constraints on the numerical analysis of complex systems, we opted for the larger material model at the expense of the resolution of the modeling.

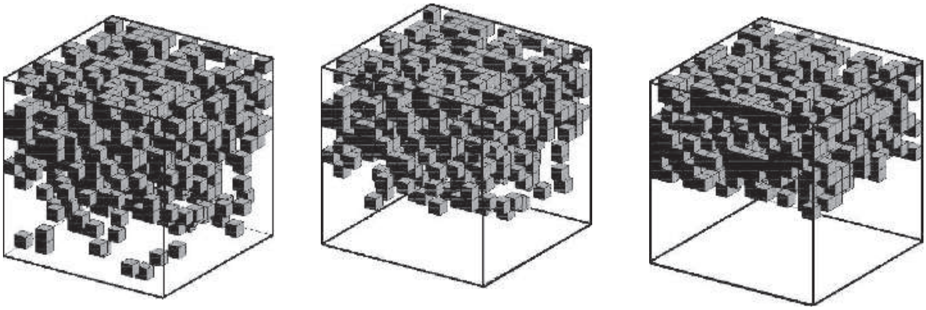

Figure 9.4 *Examples of the considered graded microstructures of the material: (a)* $g = 3$*; (b)* $g = 6$*; (c)* $g = 100$.

One can see from Figure 9.5 that the critical strain, at which the damage growth begins in the material, does not depend on the parameter of the volume fraction gradient g. Whether the transition from the region of the high density of the hard phase to the region of low density is sharp or smooth, the critical applied strain remains constant. However, the stiffness of the composite and the peak stress of the stress–strain curve increase with increasing sharpness of the transition between the regions. A reduction of g from 20 to 1 can lead to a decrease of the peak stress by 6 %.

Figure 9.6 shows the peak stress of the stress–strain curves plotted versus the parameter g of sharpness of the transition between the regions of high and low content of hard phase.

In order to analyze the observed relationship between the peak stress and stiffness of the composite and the degree of localization of hard phase grains, let us apply the bilayer model of a gradient composite, described in Section 7.2. In the framework of this model, the Young modulus of the upper layer (highly reinforced region in the 'bilayer' model of a graded composite, which is assumed to be homogeneous in the first approximation) can be calculated by ('rule-of-mixture'):

$$E_{\mathrm{up}} = E_{\mathrm{p}} vc \frac{L}{w_{\mathrm{up}}} + E_{\mathrm{m}} (1 - vc \frac{L}{w_{\mathrm{up}}}) \tag{9.1}$$

where E_{up}, E_{p}, E_{m} are Young moduli of the 'upper (highly reinforced) layer' of the gradient composite, of hard and ductile phases, respectively, L is the cell size, vc is the total volume content of the hard phase and w_{up} is the thickness of the highly reinforced region of the composite. The ratio w_{up}/L characterizes the function of the volume fraction gradient: if $g > 20$ (sharp transition), $w_{\mathrm{up}}/L = 0.5$, and if $g < 5$ (smooth transition), $w_{\mathrm{up}}/L = 0.6$–0.9.

The gradient degree of microstructures in this model is characterized by two parameters: the thickness and the Young modulus of the upper layer (i.e. of the highly reinforced region of the gradient composite) (see Section 7.2). Using the Reuss formula for the Young modulus of a bilayer, one can calculate the total Young modulus of the gradient material as a function of the degree of gradient (i.e. the ratio L/w_{up}):

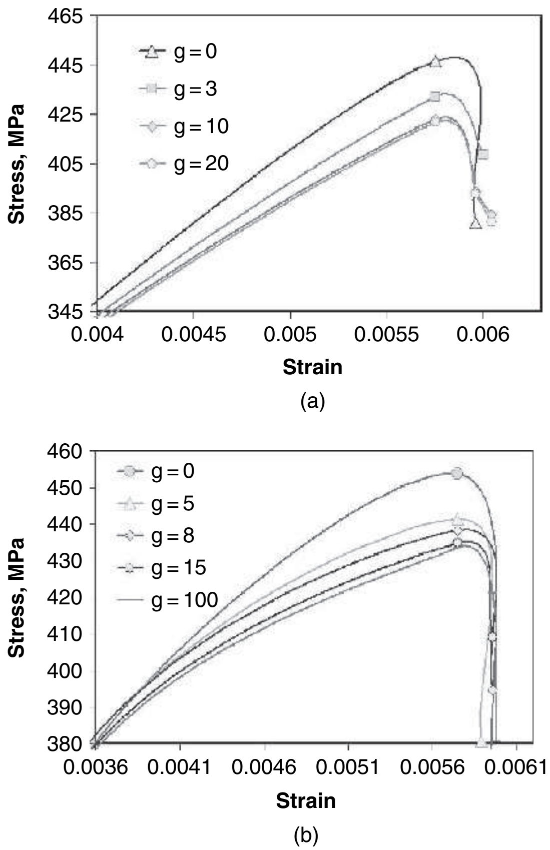

Figure 9.5 *Typical tensile stress–strain curves for the different gradient degree of the composite: (a)* VC = 10 %, *(b)* VC = 20 %. *Reprinted from* Mater. Sci. Eng., A*, **407**, Mishnaevsky Jr, 'Automatic voxel . . . ', pp. 11–23, Copyright (2005), with permission from Elsevier.*

$$E = \left(\frac{w_{\mathrm{up}}}{LE_{\mathrm{up}}} + \frac{L - w_{\mathrm{up}}}{LE_{\mathrm{m}}} \right)^{-1} \tag{9.2}$$

where L is the size of the cell and E_{up} and E_{m} are Young modulus for the highly reinforced part (upper layer) and the matrix.

Figure 9.7 shows the Young modulus of the composite, calculated with the use of the simplified model, as a function of the smoothness of the interface between the regions w_{up}/L. One can see that the increase in the width of the highly reinforced region in the composite (even at a sacrifice of the stiffness of the region) leads to a proportional increase in the stiffness of the whole composite. i.e. the stiffness of the composite increases with increasing the smoothness of the transition from the highly reinforced region of the composite to the hard phase free region. This result, obtained with the use of the simple analytical model, confirms our numerical results (Figure 9.5).

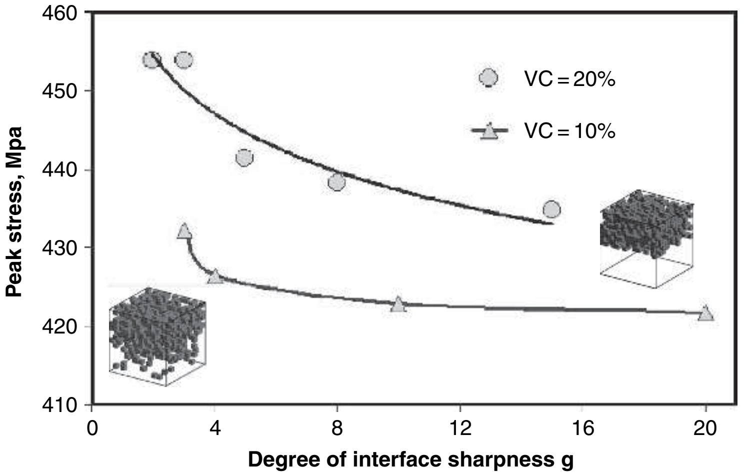

Figure 9.6 *Peak stress of the stress–strain curves plotted versus the degree of gradient (smooth versus sharp interface) for the graded composites with different volume content of hard phase (10 % and 20 %). Reprinted from* Mater. Sci. Eng., A, ***407****, Mishnaevsky Jr, 'Automatic voxel . . . ', pp. 11–23, Copyright (2005), with permission from Elsevier.*

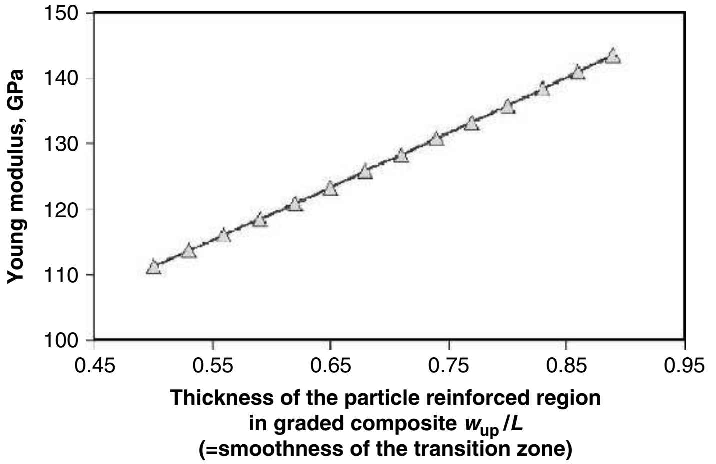

Figure 9.7 *Young modulus of a graded composite as a function of the width of the highly reinforced region (=smoothness of the transition from the region of high density of hard phase grains to the particle-free region).*

Thus, the *stiffness of graded interpenetrating phase composites can be improved by making the transition region between the highly reinforced and reinforced free regions smoother.*

It is of interest to compare this conclusion with the results from Chapters 6 and 7. In Section 6.6, it was shown that the graded arrangement of hard particles in composites ensures much higher damage resistance but lower stiffness than composites with random and homogeneous particle arrangements. Furthermore, the more localized is the particle arrangement, the higher is the damage resistance of the composite (see Section 7.1). Taking into account the result above, one may summarize that *graded composites with high gradient degree and smooth transition between the highly reinforced and particle-free regions can ensure both high damage resistance and relatively high stiffness*. The idea of the graded composite with both high localization of hard phase and smooth transition between the regions is shown schematically in Figure 9.8.

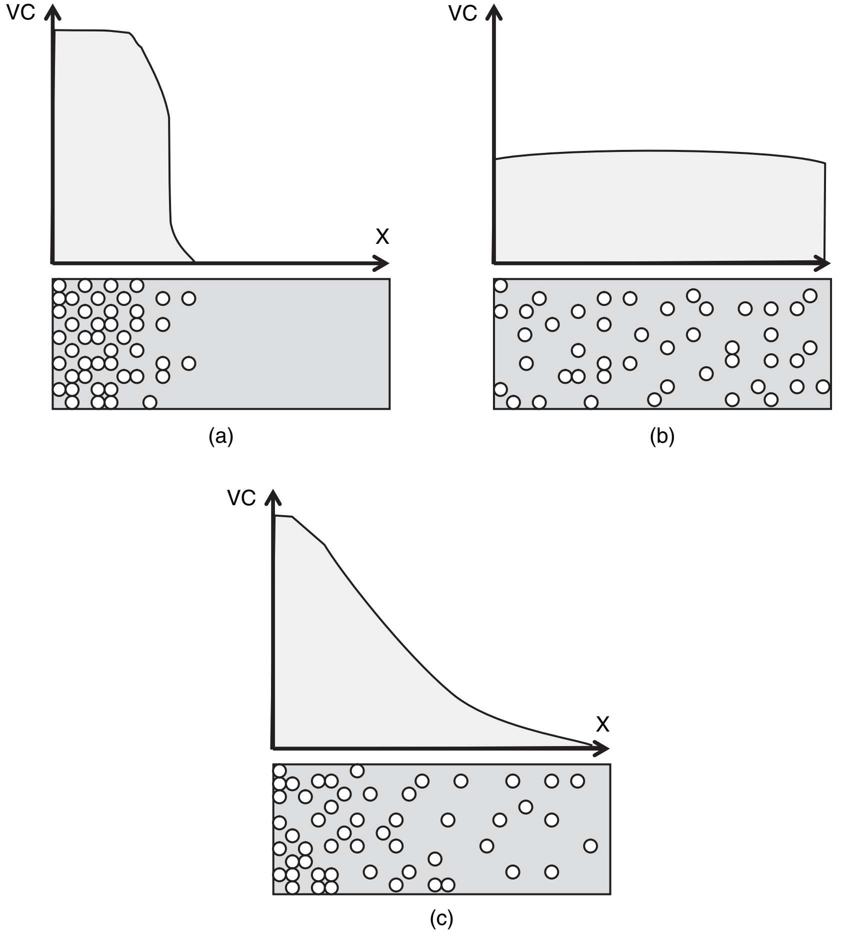

Figure 9.8 *Schema of the graded composite with both high localization of the hard phase and smooth transition between the regions: (a) graded composite with highly localized hard phase arrangement (high damage resistance, low stiffness); (b) nongraded particle arrangement; (c) graded composite with smooth transition between the regions of high and low density of particles.*

9.3 Isotropic interpenetrating phase composites

9.3.1 Effect of the contiguity of interpenetrating phases on the strength of composites

At this stage of the work, we seek to analyze the effect of microstructures of isotropic IPCs on their strength and damage resistance. In particular, the effect of the availability and the size of contiguous (percolation) clusters of hard phase on the deformation, strength and damage in the composites should be clarified. In order to solve this problem, a series of 3D FE models of composites with random distribution of the hard phase grains and different volume content of the inclusions (3D 'random chessboards') were generated using the program Voxel2FEM. Cubic unit cells ($10 \times 10 \times 10$ mm) were subject to uniaxial tensile displacement loading, 1.0 mm.

Figure 9.9 shows some typical tensile stress–strain curves and the fraction of failed elements in the hard phase plotted versus the far field applied strain for the different volume contents of the hard phase. The falling branches of the stress–stress curves begin, when the intensive failure of the hard phase occurs. After some part of the hard material fails, the damage growth slows down, and the stiffness of the materials is not reduced further. The damage growth in the ductile matrix proceeds much more slowly than the damage growth in the hard grains.

Apparently, the constant stress branches of the curves correspond to the stage of the material behavior, when many hard grains failed and ceased to bear any load, while the matrix remains almost intact, and only slow damage accumulation in the matrix occurs.

Figure 9.10 shows the critical applied strain (at which the falling branches of the stress–strain curves and the intensive damage growth in the hard phase begin) plotted as a function of the volume content of hard phase. One can see that the critical strain, at which the falling branches of the stress–strain curve begin, decreases with increasing volume content of the hard phase.

It is of interest to correlate the strength, deformation and damage resistance of the composites with the formation of a contiguous, interpenetrating network of the hard phase. When generating the FE models, the percolation analysis for all three directions (X, Y, Z) and for both phases (hard grains, matrix) was carried out, and the availability or nonavailability of the infinite percolation clusters of the hard grains and the matrix in each direction in the considered representative volume was tested. As expected (Stauffer and Aharony, 1992), infinite percolation clusters of hard phase do not form at the volume content of hard phase below 31 %, but were detected (in one direction) at VC = 32 %. Infinite clusters of hard phase form in all three directions at VC = 70 %, but infinite clusters of matrix can be detected only in two directions at this volume content. If the volume content is between 32 % and 69 %, the microstructure is interpenetrating, and both phases form infinite clusters.

Comparing these data with the results shown in Figure 9.9, one can draw a conclusion that *metal matrix composites (normally, elastoplastic damageable materials) start to behave as an elastic-brittle material (i.e. the linear stress–strain dependence up to the peak stress and then vertical falling branch of the stress–strain curve), when the infinite percolation cluster from the hard phase is formed* (i.e. at VC > 32 %).

Figure 9.11 shows the peak stresses of the stress–strain curves plotted versus the maximum size of a percolation cluster of hard phase. The linear sizes of all the hard phase

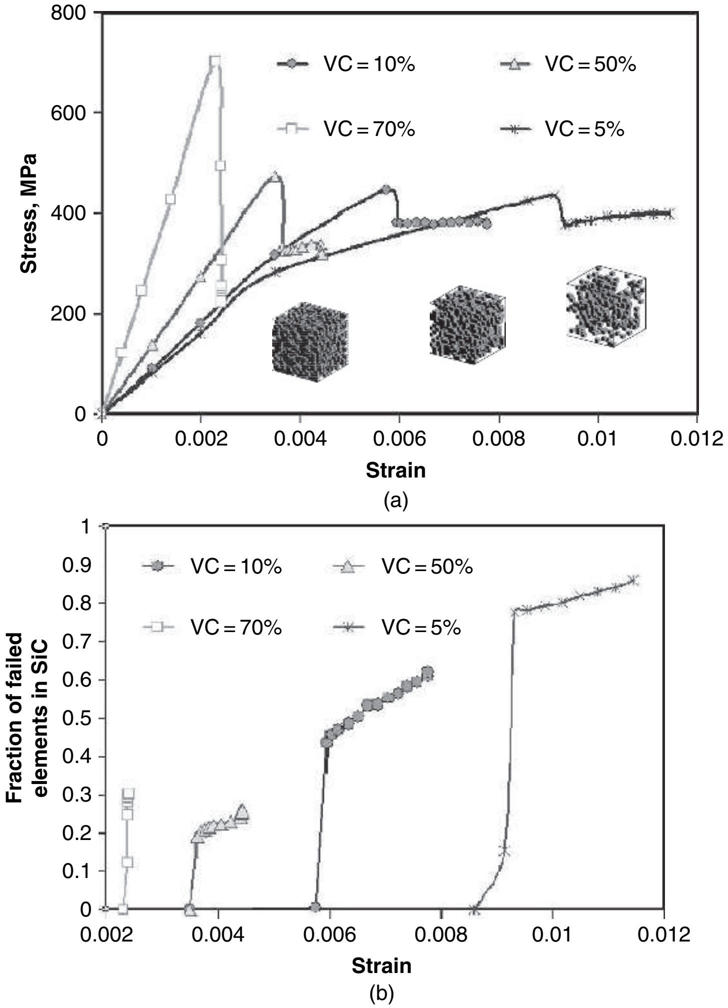

Figure 9.9 *(a) Typical tensile stress–strain curves and (b) the fraction of failed elements in the hard phase plotted versus the far field applied strain for the different volume contents of the hard phase. Reprinted from* Mater. Sci. Eng., A, ***407****, Mishnaevsky Jr, 'Automatic voxel . . .', pp. 11–23, Copyright (2005), with permission from Elsevier.*

clusters have been calculated for the generated 3D FE models, using the built-in percolation analysis subroutine in the program Voxel2FEM. One can see from Figure 9.11 that the stiffness and the peak stress of a composite increase almost linearly with increasing the linear size of the largest hard phase cluster up to the percolation threshold. The formation of clusters of hard grains therefore plays an important role in the stiffness and strength of composites.

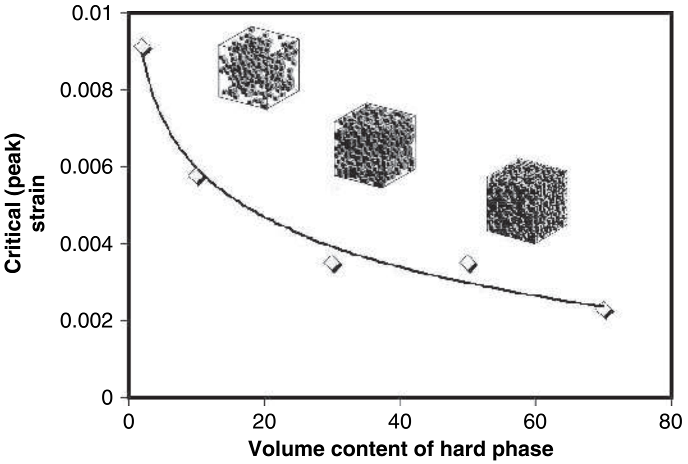

Figure 9.10 *Critical applied strain, at which the intensive damage growth in hard phase begins and goes on, plotted as a function of the volume content of hard phase. Reprinted from* Mater. Sci. Eng., A, **407**, *Mishnaevsky Jr, 'Automatic voxel . . . ', pp. 11–23, Copyright (2005), with permission from Elsevier.*

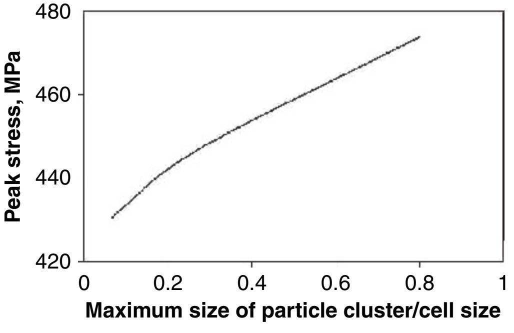

Figure 9.11 *Peak stress plotted versus the maximum size of a cluster of hard phase. Reprinted from* Mater. Sci. Eng., A, ***407***, *Mishnaevsky Jr, 'Automatic voxel . . . ', pp. 11–23, Copyright (2005), with permission from Elsevier.*

Summarizing, one can formulate the following conclusions. The increase in the volume content of hard phase leads, as expected, to the proportional increase in the Young modulus of the composites, and to the strong increase in the peak stress of the stress–strain curves. However, it leads to the decrease in the critical applied strain, at which the falling branch of the stress–strain curve begins. The stiffness and the yield stress of a composite increase almost linearly with increasing the linear size of the largest hard grain cluster up to the formation of an infinite percolation cluster of hard phase. After an infinite percolation cluster of hard phase is formed, the material (consisting of the ductile matrix and hard grains) starts to behave as a brittle material (i.e. linear stress–strain dependence up to the peak stress and then vertical falling branch of the stress–strain curve).

9.3.2 Porous plasticity: open form porosity

In this part of the work, we seek to investigate numerically the effect of the void/pore density and the formation of percolation clusters of voids in the material on the deformation, stiffness and strength of ductile voided/porous materials in the 3D case.

3D numerical models of porous material with different porosity and random distributions of pores were generated using the program Voxel2FEM. The relative porosity (volume content of voids) was varied from 10 to 70 %. The properties (constitutive law, Young modulus, Poisson's ratio) of the matrix of the porous material corresponded to the properties of the aluminum in the above simulations. The location of each pore was determined using the random number generator (random values in all three directions).

Figure 9.12 shows examples of the considered representative volumes of the material. The calculated tensile stress–strain curves for the porous Al with different volumes of porosity are given in Figure 9.13.

When generating the FE models, the percolation analysis for all three directions (X, Y, Z) and for both phases (pores, matrix) was carried out. The probability of the formation of infinite clusters of the pores in each direction in the considered representative volume was calculated, as described above. There were the following critical points in the material: VC = 32 % (formation of a first infinite percolation cluster of pores) and VC = 69 % (infinite clusters of pores are available in all three directions, however, the infinite clusters of matrix are available only in two directions X and Z). At the volume content of pores between 32 % and 68 %, both infinite percolation clusters of matrix and of pores are available in all three directions. The volume content of pores, at which the percolation of matrix is lost (i.e. 69 %), corresponds to the formation of a crack along the Z axis (the material was loaded along the Y axis). At this volume content of pores, there is no percolation of matrix phase, and the material does not bear any load. Practically, it means that the volume consists of two unconnected parts.

The yield stress (at far field applied strain $\varepsilon = 0.03$) was plotted versus the porosity (Figure 9.14). As expected, the yield stress of the porous material decreases with increasing porosity. However, looking at the points of formation of percolation clusters, one can conclude that even a formation of a percolation cluster of pores (in one

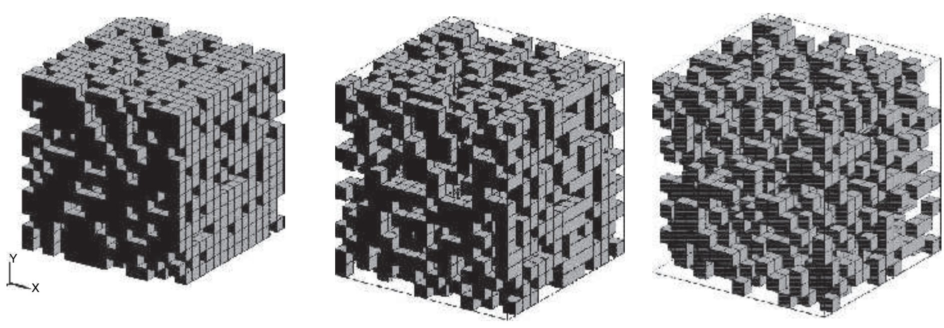

(a) (b) (c)

Figure 9.12 *Examples of the considered representative volumes of the porous material: (a) porosity 30 %; (b) 50 %; (c) 70 %. Reprinted from* Mater. Sci. Eng., A*, **407**, Mishnaevsky Jr, 'Automatic voxel . . . ', pp. 11–23, Copyright (2005), with permission from Elsevier.*

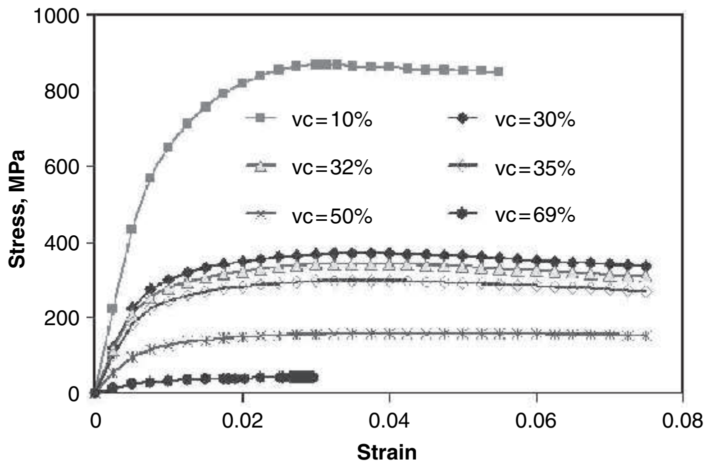

Figure 9.13 *Tensile stress–strain curves for porous Al with different volumes of porosity. Reprinted from* Mater. Sci. Eng., A, **407**, *Mishnaevsky Jr, 'Automatic voxel . . . ', pp. 11–23, Copyright (2005), with permission from Elsevier.*

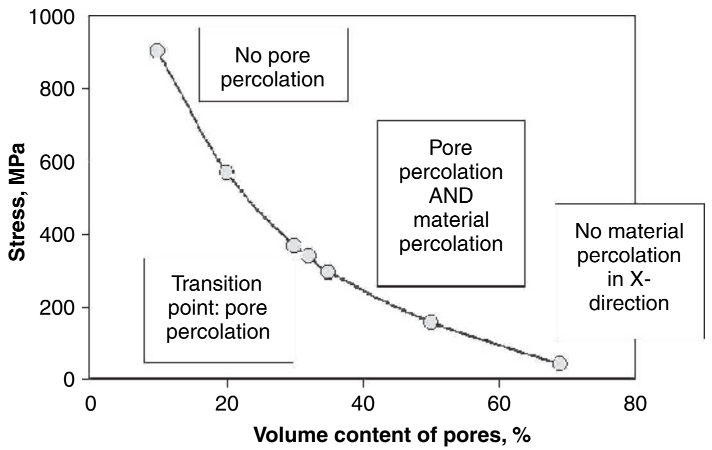

Figure 9.14 *Yield stress (at far field applied strain* $\varepsilon = 0.03\,\mathrm{mm}$*) plotted versus the porosity. Reprinted from* Mater. Sci. Eng., A, ***407***, *Mishnaevsky Jr, 'Automatic voxel. . . ', pp. 11–23, Copyright (2005), with permission from Elsevier.*

or two directions) in a ductile material does not lead to the stepwise loss of stiffness of the material. Only the nonavailability of the infinite percolation cluster of matrix phase corresponds to a stepwise loss of stiffness. Apparently, whereas clusters of connected pores may serve as sites of crack initiation, the formation of a cluster of pores does not necessarily correspond to the formation of a crack in the material.

The results of the simulations presented in this chapter, can be summarized as follows. The stiffness and the yield stress of a composite containing infinite percolation clusters of hard phase, increases almost linearly with increasing linear size of the largest cluster up to the formation of an infinite percolation cluster of hard phase. After an infinite percolation cluster of hard phase is formed, the material (consisting of the ductile matrix and hard damageable grains) starts to behave as a brittle material (i.e. linear stress–strain dependence up to the peak stress and then vertical falling branch of the stress–strain curve).

It was shown that the stiffness of a graded interpenetrating phase composite and the peak stress of the stress–strain curve increase with increasing smoothness of the transition from the region of high density of hard phase to the region of low density.

References

Aldrich, D. E., Fan, Z. and Mummery, P. (2000). Processing, microstructure and physical properties of interpenetrating Al_2O_3/Ni composites, *Materials Science and Technology*, **16**, 747–752.

Barta, S. (1994). Effective Young's modulus and Poisson's ratio for the particulate composite, *Journal of Applied Physics*, **75** (7), 3258–3263.

Bergman, D. (1978). The dielectric constant of a composite material – a problem in classical physics, *Physical Reports*, **43** (9), 377–407.

Bergman, D. (2002). Exact relations between critical exponents for elastic stiffness and electrical conductivity of two-dimensional percolating networks, *Physical Reviews E*, **65** (2), 026124.

Buxton, G. A. and Balazs, A. C. (2004). Predicting the mechanical and electrical properties of nanocomposites formed from polymer blends and nanorods, *Molecular Simulation*, **30** (4), 249–257.

Chermant, J. L. and Osterstock, F. (1979). Elastic and plastic characteristics of WC-CO composite materials, *Powder Metallurgy International*, **11** (3), 229–235.

Clarke, D. R. (1992). Interpenetrating phase composites, *Journal of American Ceramic Society*, **75**, 739–759.

Daehn, G. S., Starck, B., Xu, L., Elfishawy, K. F., Ringnalda J. and Fraser H. L. (1996). Elastic and plastic behavior of a co-continuous alumina/aluminum composite, *Acta Materialia*, **44** (1), 249–261.

Dong, M. and Schmauder, S. (1996). Transverse mechanical behaviour of fiber reinforced composites – FE modelling with embedded cell models, *Computational Materials Science*, **5**, 53–66.

Fan, Z. G., Tsakiropoulos, P. and Miodownik, A. P. (1992). Prediction of the Young's modulus of particulate composites, *Materials Science and Technology*, **8**, 922–929.

Feng, X.-Q., Mai, Y.-W. and Qin, Q.-H. (2003). A micromechanical model for interpenetrating multiphase composites, *Computational Materials Science*, **28**, 486–493.

Feng, X.-Q., Tian, Z., Liu Y.-H. and Yu, S.-W. (2004). Effective elastic and plastic properties of interpenetrating multiphase composites, *Applied Composite Materials*, **11**, 33–55.

Guldberg, R. E., Hollister, S. J. and Charras, G. T. (1998). The accuracy of digital image-based finite element models, *Journal of Biomechanical Engineering*, **120**, 289–295.

Gurland, J. (1958). The measurement of grain contiguity in two-phase alloys, *Transactions of the American Institute of Mining, Metallurgical and Petroleum Engineers*, **212**, 452–455.

Lessle, P., Dong, M. and Schmauder, S. (1999). Self-consistent matricity model to simulate the mechanical behaviour of interpenetrating microstructures, *Computational Materials Science*, **15**, 455–465.

Loshak, M. G. (1984). *Strength and Durability of Hard Alloys*, Naukova Dumka, Kiev.

Mishnaevsky Jr, L. (1995a). A new approach to the analysis of strength of matrix composites with high content of hard filler, *Applied Composite Materials*, **1**, 317–324.

Mishnaevsky Jr, L. (1998a). *Damage and Fracture in Heterogeneous Materials*, Balkema, Rotterdam.

Moukarzel, C. and Duxbury P. M. (1994). Failure of three-dimensional random composites, *Journal of Applied Physics*, **76** (7), 4086–4094.

Niebur, G. L., Yuen, J. C., Hsia, A. C. and Keaveny, T. M. (1999). Convergence behavior of high-resolution finite element models of trabecular bone, *Journal of Biomechanical Engineering*, **121**, 629–635.

Purohit, R. and Sagar, R. (2001). Fabrication of a cam using metal matrix composites, *International Journal of Advanced Manufacturing Technology*, **17** (9), 644–648.

Ravichandran, K. S. (1994). Deformation behavior of interpenetrating phase composites, *Composites Science and Technology*, **52**, 541–549.

Sarychev, A. K. and Brouers F. (1994). New scaling for ac properties of percolating composite material, *Physical Review Letters*, **73**, 2895–2898.

Wegner, L. D. and Gibson, L. J. (2000). The mechanical behaviour of interpenetrating phase composites. I: Modeling. II: A case study of a three-dimensionally printed material, *International Journal of Mechanical Sciences*, **42** (5), 925–942, 943–964.

10

Fiber reinforced composites: numerical analysis of damage initiation and growth

In previous chapters, the mechanical behavior and strength of particle reinforced, gradient and interpenetrating phase composites have been analyzed. Here, we consider the methods of modeling and simulation of deformation and damage evolution of unidirectional fiber reinforced composite (FRCs).

10.1 Modeling of strength and damage of fiber reinforced composites: a brief overview

10.1.1 Shear lag based models and load redistribution schemas

The *shear lag model*, developed by Cox in 1952 (Cox, 1952) is one of the most often used approaches in the analysis of strength and damage of FRCs. This model is often employed to analyze the load redistribution in FRCs, resulting from failure of one or several fibers. This redistribution is described in the framework of various *load sharing rules*. In the fiber bundle model, developed by Daniels (Daniels, 1945), the *global load sharing* (GLS) *schema* was assumed: i.e. the load, which was born by a broken fiber, is equally redistributed over all the remaining intact fibers in the cross-section of the composite. As noted by Zhou and Wagner (Zhou and Wagner, 1999), the GLS model is applicable only to a loose fiber bundle, with no matrix between the fibers. In the case of fibers which are bound together by the matrix, other models of the load sharing should be used.

Computational Mesomechanics of Composites L. Mishnaevsky Jr

For the qualitative description of the load redistribution after the fiber failure, the *stress concentration factor* (SCF) is introduced:

$$\mathrm{SCF} = \frac{\sigma_{\text{local}}}{\sigma_{\text{applied}}} = 1 + \frac{\sigma_{\text{extra}}}{\sigma_{\text{applied}}} \tag{10.1}$$

where σ_{local} and σ_{applied} are the local stress in an intact fiber and applied stress, and $\sigma_{\text{extra}} = \sigma_{\text{local}}{}^{-}\sigma_{\text{applied}}$ is the overload at the fiber related to the fiber break (Zhou and Wagner, 1999).

Harlow and Phoenix (Harlow and Phoenix, 1978) proposed the *local load sharing* (LLS) *model*, in which the extra load, related to the failed fiber(s), is transferred to two nearest neighbors of the fiber(s). In this case, the stress concentration factor is determined by:

$$\mathrm{SCF} = 1 + \frac{k}{2} \tag{10.2}$$

where k is the amount of failed fibers. Figure 10.1 shows schematically the GLS and LLS models, as well as the power law based model of load sharing, discussed below.

Hedgepeth (Hedgepeth, 1961) was first to apply the shear lag model to a multifiber system. He studied the stress distribution around broken fibers in 2D unidirectional composites with infinite array of fibers. Hedgepeth and van Dyke (Hedgepeth and van Dyke, 1967) generalized the elastic model by Hedgepeth to the 3D case and included the elastic-plastic matrix behavior into the model. Considering an array of parallel fibers, bonded to the matrix and subject to axial loading, they determined the average SCF in a fiber after the failure of k adjacent fibers:

$$\mathrm{SCF} = \prod_{i=1}^{k} \frac{2i+2}{2i+1} \tag{10.3}$$

Curtin (Curtin, 1991) noted that the problem of independent and successive fiber fractures under GLS condition is reduced to the problem of failure of single fiber in the matrix.

Determining the cumulative number of defects in fibers from the Weibull distribution of fiber strengths, he estimated the ultimate strength of the composite as:

$$\sigma_{\mathrm{F}} = \frac{(m+1)}{(m+2)} \left[\frac{2\sigma_0^m \tau L_0}{(2+m)r} \right]^{\frac{1}{m+1}} \tag{10.4}$$

where m is Weibull modulus, τ is sliding resistance, r is fiber diameter, L_0 and σ_0 are parameters of the Weibull distribution of the fiber strengths and σ_0 is defined as 'the stress required to cause one failure on average, in a fiber of length L_0'.

The shear lag model was used by Wagner and Eitan (Wagner and Eitan, 1993) to study the redistribution of stress from a failed fiber to its neighbors. They determined SCF and derived the following formula for the case of load redistribution after one single fiber in a 2D unidirectional composite is broken:

$$\mathrm{SCF} = 1 + \frac{\varphi}{\pi} \frac{\sinh[\beta(\lambda/2 - z)]}{\sinh(\beta\lambda/2)} \tag{10.5}$$

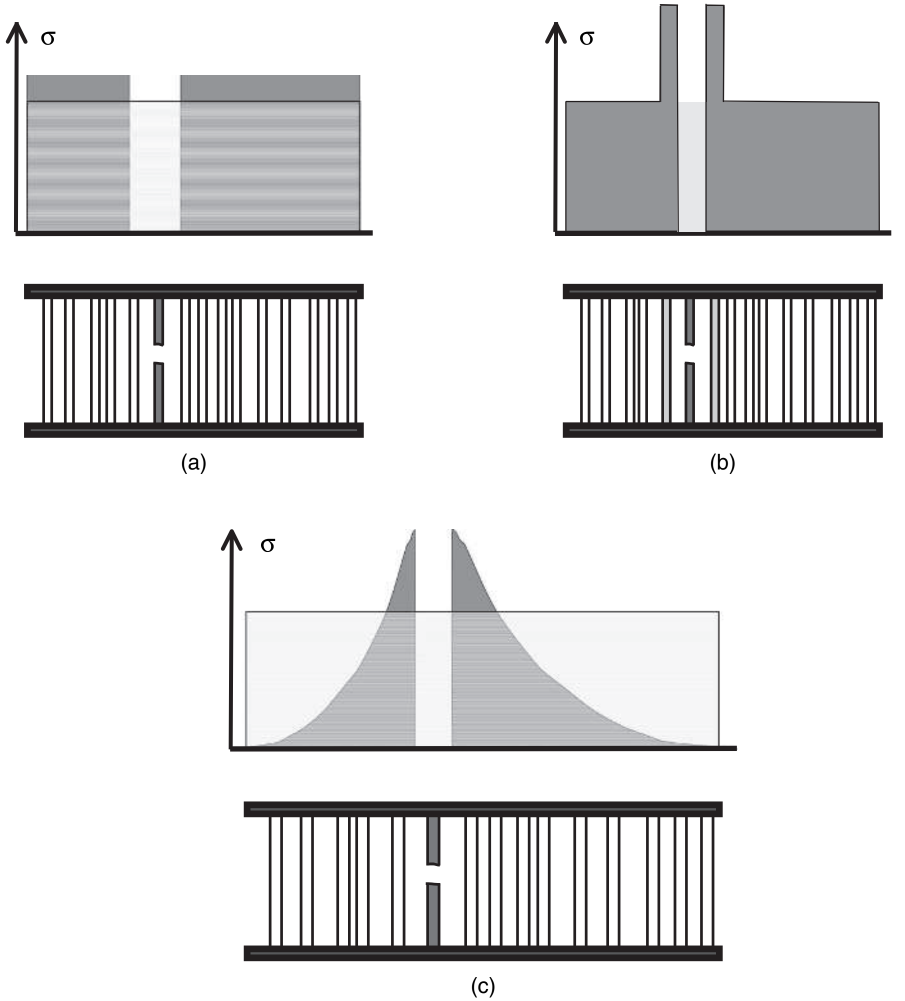

Figure 10.1 Schemas of the stress redistribution in a fiber bundle model: (a) global load sharing; (b) local load sharing; (c) power law of the load sharing.

where β is the Cox shear lag parameter, z is the distance from break along the fiber, λ is the shear transfer length, $\varphi = \sin^{-1}(r/d)$, r is the fiber radius and d is the center-to-center interfiber distance. On the basis of their model, Wagner and Eitan demonstrated that the 'local effect of a fiber break on the nearest neighbors is much milder than previously calculated, both as a function of the interfiber distance and of the number of adjacent broken fibers'.

Zhou and Wagner (Zhou and Wagner, 1999) proposed a model of stress redistribution after the fiber failure, which incorporated the effects of fiber/matrix debonding and fiber/matrix interfacial friction. The interfacial friction in the debonding region was calculated as proportional to the far field longitudinal stress in the fiber. It was observed that SCF can reach a maximum value of 1.33 for the case of one broken fiber.

The effects of multiple fiber breaks and their interaction on the stress distribution and strength of composites can be analyzed with the use of the *break influence superposition* (BIS) *technique*. The BIS technique was developed by Sastry and Phoenix (Sastry and Phoenix, 1993) on the basis of the Hedgepeth approach. In the framework of this technique, an infinite lamina with N aligned breaks, each subject to the unit compressive load, is considered. The fiber and matrix loads and displacement at an arbitrary point are determined as weighted sums of the influences of N single breaks. The weighting factors are calculated from a system of N equations. The unit tensile load is then superimposed on the solution (Beyerlein *et al.*, 1996).

This technique was employed and expanded in a series of works by Phoenix, Beyerlein, Landis and colleagues (Beyerlein *et al.*, 1996; Landis *et al.*, 2000). Beyerlein and Phoenix (Beyerlein and Phoenix, 1996) generalized the break influence superposition technique, and developed the quadratic influence superposition (QIS) technique. The quadratic influence superposition technique allows to analyze the deformation and damage of elastic fibers in an elastic-plastic matrix, taking into account the interface debonding. Using this method, Beyerlein and Phoenix studied stress distribution around arbitrary arrays of fiber breaks in a composite subject to simple tension. The authors demonstrated that the size of the matrix damage region increases linearly with applied tensile load. Using Monte-Carlo method and shear lag based models, Beyerlein *et al.* (Beyerlein *et al.*, 1996) and Beyerlein and Phoenix (Beyerlein and Phoenix, 1997) studied the effects of the statistics of fiber strength on the fracture process. They assigned randomly (Weibull) distributed strengths to individual fibers, and simulated the evolution of random fiber fractures. It was observed that variability in fiber strength can lead to a nonlinear deformation mechanism of the composite.

Landis *et al.* (Landis *et al.*, 1999) developed a 3D shear lag model, in which matrix displacements were interpolated from the fiber displacements, and analyzed the stress distributions around a single fiber break in square or hexagonal fiber arrays. The FE equations were transformed into differential equations and solved using Fourier transformations and the influence function technique. Further, Landis *et al.* (Landis *et al.*, 2000) combined this approach with the Weibull fiber statistics and the influence superposition technique, and applied it to analyze the effect of statistical strength distribution and size effects on the strength of composites.

The BIS technique has been combined with FEM by Li *et al.* (Li *et al.*, 2006). Li and colleagues modeled the stress transfer from broken to unbroken fibers in fiber reinforced polymer matrix composites. The damage evolution in composites, including the fiber fracture, damage cracking and interface debonding, was simulated using FEM combined with the Monte-Carlo technique. The special FE code was written on the basis of the break influence superposition technique, to analyze multiple breaks. The authors observed in the numerical experiments, that while both low and high interface sliding strengths lead to the decrease of the composite strength (due to the large scale debonding and matrix cracking), the moderate interface sliding strength weakens the negative effect of the fiber fracture on the composite strength.

An approach to the analysis of the interaction between multiple breaks in fibers, based on *Green's function model* (GFM), was proposed by Curtin and colleagues (Ibnabdeljalil and Curtin, 1997a,b; Xia *et al.*, 2001, 2002a,b). Stating that the axial stress σ_i in an undamaged *i*th fiber can be determined as a product of the axial applied stress p_j across the *j*th cross-section of the fiber and a Green's function G_{ij}, Curtin and colleagues determined the σ_i–p_j relationships for the case of many broken fibers, transferring the stress on the remaining unbroken fibers. The Green's function G_{ij} determines the stress concentration factors at the remaining intact fibers. In this model, the stress state around a single fiber break (which can be obtained from any micromechanical solution) is used to determine the stress distribution in a composite with multiple fiber breaks.

Ibnabdeljalil and Curtin (Ibnabdeljalil and Curtin, 1997a,b) employed the 3D lattice Green's function model to determine the stress distribution and to simulate damage accumulation in titanium matrix and ceramic matrix FRCs under LLS (local load sharing) conditions. They analyzed the size effects and other statistical aspects of the failure of composites, using the weakest link statistics. Further, Ibnabdeljalil and Curtin considered damage evolution in FRCs with a cluster of initial fiber breaks. Using the Monte Carlo technique, they determined the stress distribution, and simulated the damage evolution in the composite. It was shown that the tensile strength decreases with increasing the size of the initial cluster of broken fibers.

Xia and Curtin (Xia and Curtin, 2001), and Xia *et al.* (Xia *et al.*, 2001) employed 3D FE micromechanical analysis to study the deformation and stress transfer in FRCs. The results of FEM (stress distribution around the broken fibers and the average axial stress concentration factor on fibers around the break) were used to extract the appropriate Green's function in a larger scale model of stochastic fiber damage distribution. Xia *et al.* (Xia *et al.*, 2002a,b) compared the shear lag and 3D FE micromechanical models of stress transfer in composites. In the 3D FE model, they assumed the same hexagonal geometry and other microstructural parameters as in the shear lag model. Taking into account the symmetry, they reduced the model to the 30° wedge. The stress distribution, fiber stress concentration factor and other parameters have been compared. Xia and colleagues demonstrated that the shear lag model is accurate for the high fiber/matrix stiffness ratios in high fiber volume fractions, but not for the low volume fractions of fibers.

10.1.2 Fiber bundle model and its versions

A group of models of damage and failure of FRCs is based on the *fiber bundle model* (FBM). The classical FBM, proposed by Daniels in 1945 (Daniels, 1945), as well as some early modifications of this model are discussed in Chapter 3. Recently, a number of FBM-based models were developed, which take into account the roles of the matrix and interfaces, nonlinear behavior of fibers and the matrix and the real micromechanisms of composite failure.

The continuous damage fiber bundle model (CDFBM) as well as versions of this model with creep rupture and interfacial failure were developed by Kun *et al.* (Kun *et al.*, 2000). In the CDFBM, the multiple failure of each fiber (i.e. continuous damage) is included in the model. Using this approach, Kun, Herrmann and colleagues investigated the scaling behavior of the composites, and observed that the multiple failures of brittle fibers can lead to the ductile behavior of the composite.

In the creep rupture model, they described the fiber behavior by Kelvin–Voigt elements, consisting of springs and dashpots in parallel. The failure condition was analyzed using the strain failure criterion, with randomly distributed failure thresholds. The interfaces between fibers were described as arrays of elastic beams, which may be stretched and bent, and fail, if the load exceeds some critical level. With this model, Kun, Herrmann and colleagues investigated further the lifetime of the bundle as a function of the distance to the critical stress point, and demonstrated that the scaling laws in the creep rupture are analog to those in second order phase transitions.

Using the power law of stress redistribution in the form:

$$\sigma_{\text{add}} \propto r^{-\gamma} \tag{10.6}$$

Hidalgo *et al.* (Hidalgo *et al.*, 2002) analyzed the effect of the range of interaction between failed fibers on the fracture of material. (Here r is the distance from the crack tip, σ_{add} is the stress increase due to the fiber failure at a distance r and γ is the power coefficient). The power law (10.6) is reduced to the case of global load sharing, if $\gamma \to 0$, and to the local load sharing, if $\gamma \to \infty$. Hidalgo and colleagues observed in their numerical experiments that the transition from the mean field regime of the load redistribution (i.e. when the strength of the material does not depend on the system size) to the short range behavior regime (when the correlated growth of clusters of broken fibers goes on) takes place at $\gamma = 2.0$.

Raischel *et al.* (Raischel *et al.*, 2006) extended the FBM further for the case when failed fibers carry a fraction of their load (i.e. the plasticity of fibers is included into the model). Using the plastic fiber bundle model, they have shown that the failure behavior of the material is strongly dependent on whether failed fibers still bear load: the macroscopic composite response can become plastic, if the fibers are plastic and the loads are redistributed according to GLS (global load sharing) schema.

Hemmer and Hansen (Hemmer and Hansen, 1992) analyzed the occurrence, statistics and dynamics of bursts in the fiber bundle model with global load sharing. (A burst event takes place when several fibers break simultaneously.) Considering statistical distribution of burst events, they demonstrated that the histogram of burst events can be described in the very general case by:

$$D(\Delta) = \Delta^{-2.5} \tag{10.7}$$

where Δ is the number of fibers that break simultaneously during a burst event. This law is independent of the strength distribution of the individual fibers, and the value 5/2 is therefore a universal critical exponent. Further, this law holds even if the load redistribution does not follow the global load sharing schema, but the load is redistributed to the neighboring fibers according to a power law. If, however, the load from a failed fiber is distributed only to the two nearest neighbors, the burst histogram does not follow the power law anymore. Hansen (Hansen, 2005) noted that the availability of universal critical exponents should be considered as an argument supporting the assumption about the fracture process as a self-organizing system.

10.1.3 Fracture mechanics based models and crack bridging

In connection with the development of ceramic and other brittle matrix composites, the problem of material toughening by crack-bridging fibers gained in importance. In the cracked composite with bridging fibers, the fiber/matrix bonding (frictional bonding

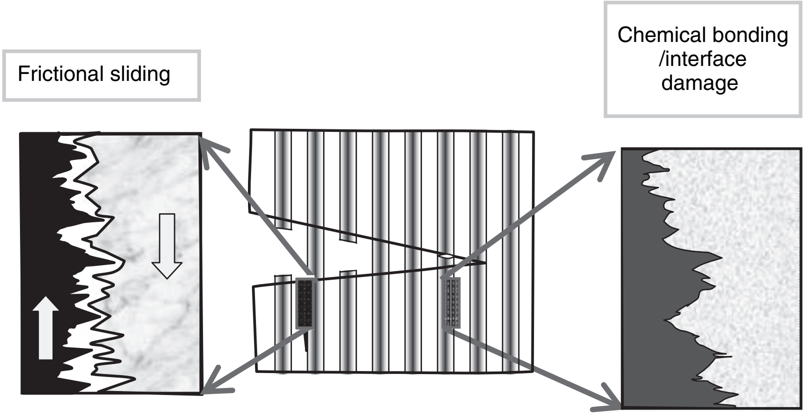

Figure 10.2 *Mechanisms of the interface bonding in fiber bridged composites (interface sliding and chemical/physical bonding).*

or chemical bonding) determine the fracture resistance of the composite. Figure 10.2 schematically shows the frictional and chemical bonding of bridging fibers in the composite.

The classical fracture mechanics based model of matrix cracking was developed by Aveston and colleagues in 1971 (Aveston *et al.*, 1971). (The model is often referred to as *ACK*). Assuming that the fibers are held in the matrix only by frictional stresses, Aveston and colleagues carried out an analysis of the energy changes in a ceramic composite due to matrix cracking. On the basis of the energy analysis, they obtained the condition of matrix cracking in composites.

Budiansky and colleagues (Budiansky *et al.*, 1986) considered the propagation of *steady state matrix cracks* in composites, and generalized some results of the ACK theory, including the results for the initial matrix stresses. Considering the energy balance and taking into account the frictional energy and potential energy changes due to the crack extension, Budiansky and colleagues determined the matrix cracking stress for composites with unbonded (frictionally constrained and slipping) and initially bonded, debonding fibers.

In several works, *continuum models of a bridged matrix* crack are used. In these models, the effect of fibers on the crack faces is smoothed over the crack length and modeled by continuous distribution of tractions, acting on the crack faces. The schema of the nonlinear spring bridging model, used by Budiansky *et al.* (Budiansky *et al.*, 1995), is shown in Figure 10.3. The relationships between the crack bridging stresses and the crack opening displacement (*bridging laws*) are used to describe the effect of fibers on the crack propagation. For the case of the constant interface sliding stress τ, the crack opening displacement u can be determined as a function of the bridging stress σ (Aveston *et al.*, 1971; Zok, 2000):

$$u = \lambda\sigma^2 \tag{10.8}$$

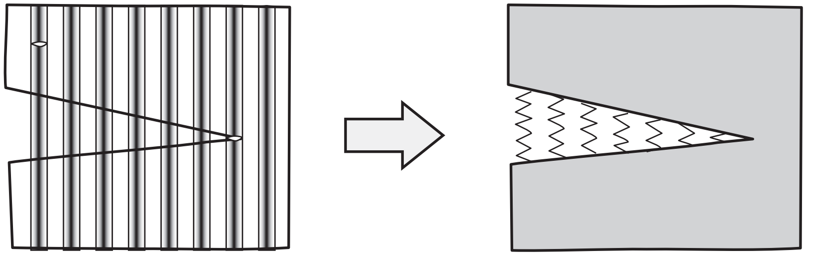

Figure 10.3 *Spring bridging model: the crack bridging by fibers is represented by continuously distributed nonlinear springs (after Budiansky* et al.*, 1995).*

where

$$\lambda = \frac{2r(1 - V_f)^2 E_m^2}{4V_f^2 \tau E_f E^2}$$

E is the composite Young's modulus, r is the fiber radius and indices f and m relate to the fibers and matrix, respectively, V is the volume content of a phase, τ is the sliding stress.

Marshall and colleagues (Marshall *et al.*, 1985) and Marshall and Cox (Marshall and Cox, 1987) used the *stress intensity approach* to determine the matrix cracking stress in composites. The bridging fibers were represented by the traction forces connecting the fibers through the crack. It was supposed that the fibers are held in the matrix by frictional bonding. The matrix cracking stress was determined by equating the composite stress intensity factor, defined through the distribution of closure pressure on the crack surface, to the critical matrix stress intensity factor. Further, Marshall and Cox studied the conditions of the transitions between failure mechanisms (matrix vs fiber failure) and the catastrophic failure and determined the fracture toughness of composites as functions of the normalized fiber strength.

McCartney (McCartney, 1987) used the continuum model of a bridged matrix crack, in order to derive the ACK-type matrix cracking criterion on the basis of the crack theory analysis. McCartney considered the energy balance for continuum and discrete crack models, and demonstrated that the Griffith fracture criterion is valid for the matrix cracking in the composites. He determined further the effective traction distribution on the crack faces resulting from the effect of fibers, and the stress intensity factor for the matrix crack.

Hutchinson and Jensen (Hutchinson and Jensen, 1990) used an axisymmetric cylinder model to analyze the fiber debonding accompanied by the frictional sliding (both constant and Coulomb friction) on the debonded surface. Considering the debonding as mode II interface fracture, Hutchinson and Jensen determined the debonding stress and the energy release rate for a steady-state debonding crack.

Slaughter (Slaughter, 1993) developed a self-similar model for calculation the equivalent spring constant (i.e. the proportionality coefficient between the far field stress and the part of the axial displacement related to the crack opening) (Budiansky and Amazigo, 1989) in the crack bridging problem. His approach is based on the load transfer model by Slaughter and Sanders (Slaughter and Sanders, 1991), in which the effect of an embedded fiber on the matrix is approximated by a distribution of axial forces and dilatations along the fiber axis.

Pagano and Kim (Pagano and Kim, 1994) studied the damage initiation and growth in fiber glass-ceramic matrix composites under flexural loading. Assuming that an annular crack surrounding a fiber (and lying in the plane normal to the fiber) extends only to the neighboring fibers of the hexagonal array, they developed the axisymmetric damage model and calculated the energy release rate as a function of the volume fraction of fibers. Pagano (Pagano, 1998) employed the axisymmetric damage model to analyze the failure modes of glass matrices reinforced by coated SiC fibers.

Using the shear lag model and the continuously distributed nonlinear springs model, Budiansky and colleagues (Budiansky *et al.*, 1995) determined the stresses in the matrix bridged by intact and debonding fibers, and derived an equivalent crack-bridging law, which includes the effect of debonding toughness and frictional sliding.

Zok *et al.* (Zok *et al.*, 1997) studied the deformation behavior of ductile matrix composites with multiple matrix cracks. Substituting the bridging law into the equation of the crack opening profile and integrating, Zok and colleagues obtained an approximate analytical solution for the COD profile for short and steady-state long cracks. For the long cracks, it was demonstrated that 'the crack area scales with the square of the stress'.

González-Chi and Young (González-Chi and Young, 1998) applied the partial-debonding theory by Piggott (Piggott, 1987) to analyze the crack bridging. In the framework of this theory (based on the shear lag model and developed for the analysis of the fiber pull-out tests), the fiber/matrix interface is assumed to consist of a debonded area (where the stress changes linearly along the fiber length) and the fully bonded, elastically deforming area (Piggott, 1987). Considering each fiber and surrounding matrix as a single pull-out test, González-Chi and Young determined stresses in the fiber and on the interface. The model was compared with the experimental (Raman spectroscopy) analysis of the stress distribution in the composites.

10.1.4 Micromechanical models of damage and fracture

In a series of works, the composite deformation and crack growth *under transverse loading* was simulated using micromechanical FE models.

Brockenborough *et al.* (Brockenborough *et al.*, 1991) used unit cell models for different (square edge-packing, diagonal-packing and triangle-packing) periodic fiber arrangements to study the effect of the fiber distribution and cross-sectional geometry on the deformation (stress–strain response and stress distribution) in Al alloy reinforced with boron fibers. Considering the random, triangle and square edge and square diagonal packing of fibers, and different fiber shapes, they demonstrated that the fiber arrangement influences the constitutive response of composites much more than the fiber shape.

Böhm and Rammerstorfer (Böhm *et al.*, 1993) suggested a modified unit cell with an off-center fiber, which enables the application of the unit cell model to composites with nonstrict regularity of the fiber arrangement. Using this model, they studied the effect of fiber arrangement and clustering on the stress field and damage initiation in Al alloy reinforced by boron fibers, and computed microscale stress and strain fields for periodic, modified periodic and clustered periodic fiber arrangements. Böhm *et al.* (Böhm *et al.*, 1993) used the unit cell approach with the perturbing periodic square array of fibers to model deterministic but less ordered fiber arrangements in FRCs.

Asp *et al.* (Asp *et al.*, 1996a,b) studied numerically the failure initiation (yielding and cavitation-induced brittle failure) in the polymer matrix of composites subject to transverse loading. They considered unit cells with different fiber arrangements (square, hexagonal, diagonal), and determined the zones of yielding and cavitation-induced brittle fracture, using the von Mises yield criterion and the dilatational energy density criterion, respectively. It was shown that failure by cavitation-induced cracks occurs earlier than the matrix yielding. Further, Asp and colleagues studied the effect of the interphase layer properties on the transverse failure of fiber reinforced epoxy. They demonstrated that the transverse failure strain increases with increasing the thickness of the interphase layer and Poisson's ratio of the interphases.

Trias *et al.* (Trias *et al.*, 2006a) simulated the transverse matrix cracking in FRCs. Real microstructures of carbon fiber reinforced polymers were determined with the use of the digital image analysis, introduced into FE models and simulated in the framework of the embedded cell approach. In so doing, they used the results from Trias *et al.* (Trias *et al.*, 2006b), who determined the critical size of a statistical RVE for carbon fiber reinforced polymers, taking into account both mechanical and statistical (point pattern) criteria. Trias *et al.* obtained probability density functions of the stress, strain components and the dilatational energy density in the loaded composites.

Vejen and Pyrz (Vejen and Pyrz, 2002) modeled the transverse crack growth in long fiber composites. The criteria of pure matrix cracking (strain density energy), fiber/matrix interface crack growth (bimaterial model) and crack kinking out of a fiber/matrix interface were implemented into the automated crack propagation module of the FE package. As a result, Vejen and Pyrz obtained numerically the crack paths for different fiber distributions. The numerical results (crack paths) were compared with experimental data.

Micromechanical unit cell models have been widely applied to the analysis of the composite failure under *tensile loading along the fiber direction*, or off-axis loading.

Megnis *et al.* (Megnis *et al.*, 2004) employed the continuum damage mechanics to develop thermodynamically consistent formulation for damageable FRCs. Fiber fracture was included into the model by determining the corresponding internal state variable. The damage tensor was determined using a unit cell model of a cracked fiber in the matrix. The stiffness degradation of the composite as a function of the applied strain was simulated numerically, and the results were compared with the experimental data.

Zhang *et al.* (Zhang *et al.*, 2004) studied toughening mechanisms of FRCs using a micromechanical model ('embedded reinforcement approach'), taking into account both fiber bridging and matrix cracking. They defined the cohesive law for the matrix cracking as a linearly decreasing function of the separation. Bilinear traction–separation laws were taken for fiber–matrix debonding and the following interfacial friction. For different traction–separation laws of interfaces, *R*-curves were obtained. Zhang and colleagues demonstrated that the strong interfaces can lead to the lower toughness of the composites.

Zhang *et al.* (Zhang *et al.*, 2005) simulated unidirectional fiber reinforced polymers under off-axis loading, using a 3D unit cell with nonlinear viscoelastic matrix and elastic fibers. In order to model the matrix cracking, the smeared crack approach was used. The matrix damage growth in the form of two 'narrow bands' near the interface and along the fiber direction were observed in the numerical experiments.

González and LLorca (González and LLorca, 2006) developed a multiscale 3D FE model of fracture of FRCs. The notched specimens from SiC fiber reinforced Ti matrix composites subject to three-point bending were considered. Three damage mechanisms, namely, plastic deformation of the matrix, brittle failure of fibers and frictional sliding on the interface were simulated. The fiber fracture was modeled by introducing interface elements randomly placed along the fibers. The interface elements incorporated the cohesive crack model (with random strengths). The fiber/matrix interface sliding was modeled using the elastic contact model in ABAQUS. It was assumed that the interface strength is negligible, and that the fiber/matrix interaction is controlled by friction. The simulation results were compared with experiments (load–crack mouth opening displacement curve), and a good agreement between experimental and numerical results was observed.

Other important directions of the micromechanical analysis of the strength and failure of FRCs are the compressive failure (controlled by different mechanisms, like kinking, buckling, kink band formation, etc.) as well as fatigue damage. The overviews of the compressive and fatigue damage mechanisms in FRCs and methods of their modeling are given in the literature (Talreja, 1987; Budiansky and Fleck, 1993, 1994; Sutcliffe *et al.*, 1996; Fleck, 1997; Niu and Talreja, 2000).

Summarizing the short overview in this section, one may see that the main approaches used in the analysis of the strength and damage of FRCs are based on the shear lag model, fiber bundle model as well as micromechanical unit cell models. When analyzing the strength, damage and fracture of FRCs, one has to overcome some challenges, among them the problem of the correct representation of the load transfer and redistribution between fibers and matrix, taking into account the interaction between multiple fiber cracks, matrix and interface cracks, modeling the interface bonding mechanisms and their effects on the composite behavior. The load transfer from failed fibers to the matrix is modeled most often with the use of the shear lag model and its versions, direct micromechanical analysis or phenomenological load redistribution laws. In many works, micromechanical FE simulations are used to complement, verify or test the studies, carried out with the use of other methods (Xia *et al.*, 2001; Li *et al.*, 2006). One can observe that the points of interests of the mechanics of strength and failure of FRCs lie in the area of mesomechanics (rather than micromechanics): the interactions between many microstructural elements, and many microcracks/cracks play leading roles for the strength of the FRCs.

In this chapter, several examples of 3D mesomechanical simulations of the deformation and damage in unidirectional FRCs are given. With these models, we seek to demonstrate some peculiarities of the modeling of unidirectional FRCs as compared with particle reinforced composites (e.g. constant stress distribution along the fiber length, leading to the special role of the variability of fiber strengths for the composite failure; effects of interfaces; direct load transfer between the microstructural elements of the material rather than via stress fields).

10.2 Mesomechanical simulations of damage initiation and evolution in fiber reinforced composites

The purpose of this part of the investigation was to simulate the damage evolution in FRCs, as well as to analyze the interaction between different damage modes.

10.2.1 Unit cell model and damage analysis

A number of 3D multifiber unit cells were generated automatically with the use of the program Meso3DFiber and the FE code MSC/PATRAN (see Chapter 5). The fibers in the unit cells were placed randomly in X and Y directions. The dimensions of the unit cells were $10 \times 10 \times 10$ mm. The cells were subject to a uniaxial tensile displacement loading, 1 mm, along the axis of fibers (Z axis). Figure 10.4 shows an example of a multifiber unit cell with 50 fibers and random fiber radii. The FE meshes were generated by sweeping the corresponding 2D meshes on the surface of the unit cell.

In order to model the fiber cracking, we employed the idea of predefined fracture planes, suggested by González and Llorca (González and Llorca, 2006). González and LLorca proposed to simulate the fiber fracture in composites by placing damageable (cohesive/interface) elements along the fiber length and creating therefore potential fracture planes in the model. The random arrangement of the potential failure planes in this case reflects the statistical variability of the fiber properties. Following this idea, we introduced damageable planes (layers) in several sections of fibers. The locations of the damageable layers in the fibers were determined using a random number generator (uniform distribution). These layers have the same mechanical properties as the fibers (except that they are damageable). The damage evolution in these layers was modeled using the subroutine User Defined Field, described in Chapter 6. The failure condition of fibers (in the damageable layers) was the maximum principal stress, 1500 MPa. Figure 10.5 shows a micrograph of the fracture surface of a unidirectional carbon fiber reinforced polyester matrix composite (with failed fibers), and multifiber unit cells with 20 fibers, in which the layers of potential cracking have been removed.

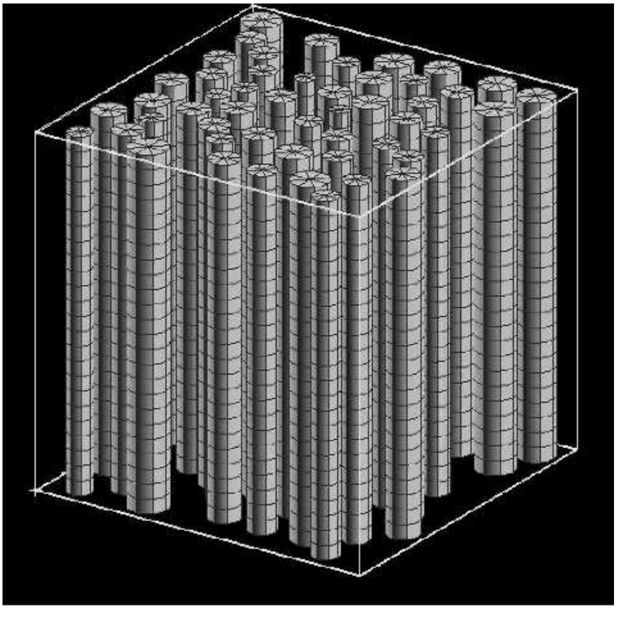

Figure 10.4 *3D unit cell model of a composite with 50 fibers.*

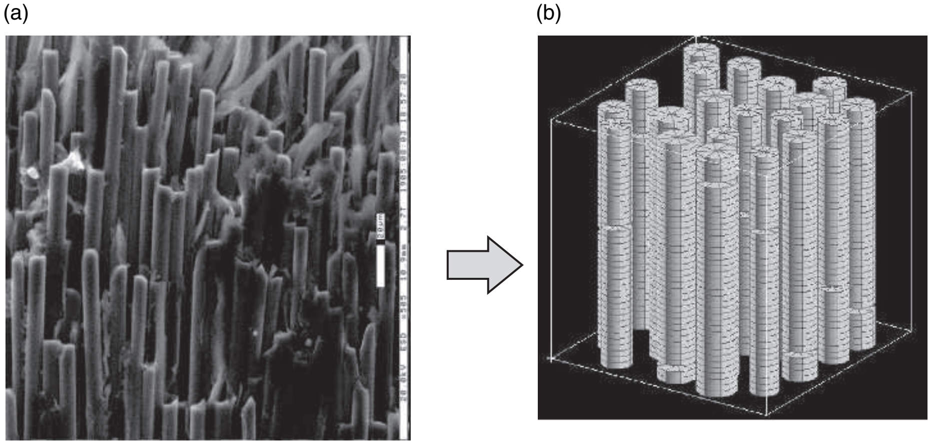

Figure 10.5 *(a) Micrograph of the fracture surface of a unidirectional FRC (with failed fibers) and (b) an example of the generated FE models with 20 fibers, and removed layers of potential fracturing. (a) Carbon fibers in the polyester matrix. (Courtesy of Dr S. Goutianos, Risø National Laboratory, Denmark.)*

In order to simulate the interface cracking of composites, the model of the interface as a third material (interphase) layer is employed. The idea of the *interface layer model* is based on the following reasoning. The surfaces of fibers are usually rather rough, and that influences both the interface debonding process and the frictional sliding. The interface regions in many composites contain interphases, which influence the debonding process as well (Huang and Petermann, 1996; Downing *et al*., 2000). Thus, the interface debonding does not occur as a 2D opening of two contacting plane surfaces, but is rather a 3D process in some layer between the homogeneous fiber and matrix materials. In order to take into account the nonplaneliness (but rather fractal or 3D nature) of the debonding surfaces and the debonding process, the interface damage and debonding are modeled as the damage evolution in a thin layer between two materials (fiber and matrix). This idea was also employed by Tursun *et al*. (Tursun *et al*., 2006), who utilized the layer model to analyze damage processes in interfaces of Al/SiC particle reinforced composites. Figure 10.6 schematically shows the idealization of the rough interface as a thin layer.

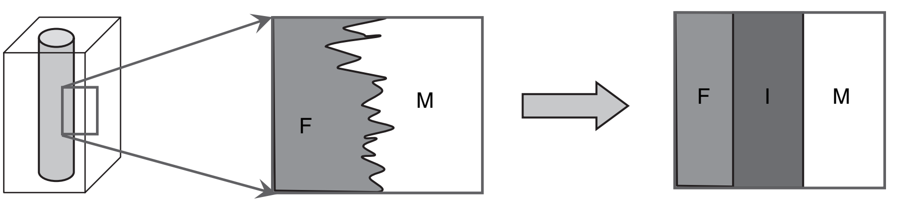

Figure 10.6 *Model of the rough interface as a third material layer. F, fiber; I, interface; M, matrix.*

10.2.2 Numerical simulations: effect of matrix cracks on the fiber fracture

In this section, we investigate the effect of cracks in the matrix on the fiber fracture. Unit cells with 20 fibers and VC = 25% have been generated. Further, three versions of the unit cells were generated, with introduced matrix cracks (notches). The cracks were oriented horizontally, normal to the fiber axis and loading vector. The lengths of the cracks were taken as 1.6 (1/6 of the cell size), 4.1 (5/12 of the cell size) and 6.6 mm (8/12 of the cell size). The crack opening was taken as 1/12 of the cell size (0.8 mm). Figures 10.7 and 10.8 show the lengths of the cracks and the general appearance of the cells with matrix cracks, respectively. At this stage of the work, the very strong fiber/matrix interface bonding was assumed, and only the effect of the matrix cracks on the fiber fracture was studied.

The damage evolution (fiber cracking) in the unit cells was simulated, using the damage subroutine User Defined Field.

Figure 10.9 shows the von Mises stress distribution in the fibers (in the unit cell with the matrix crack) after the fiber cracking. The stresses are rather low in the fiber regions close to the cracks, but increase with distance from the cracks (apparently, due to the load transfer via the shear stresses along the interface).

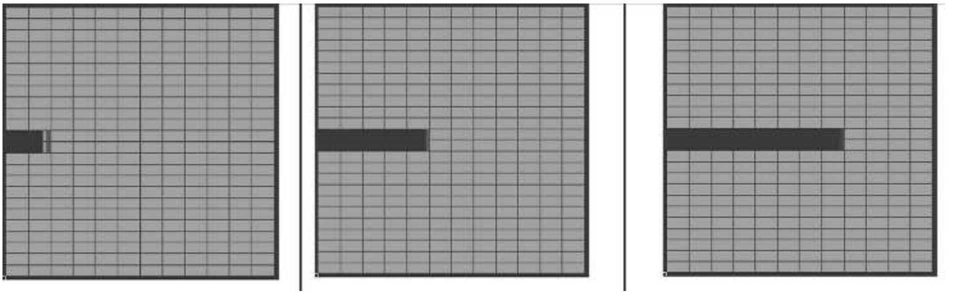

Figure 10.7 *Relative lengths of the matrix cracks in the unit cells.*

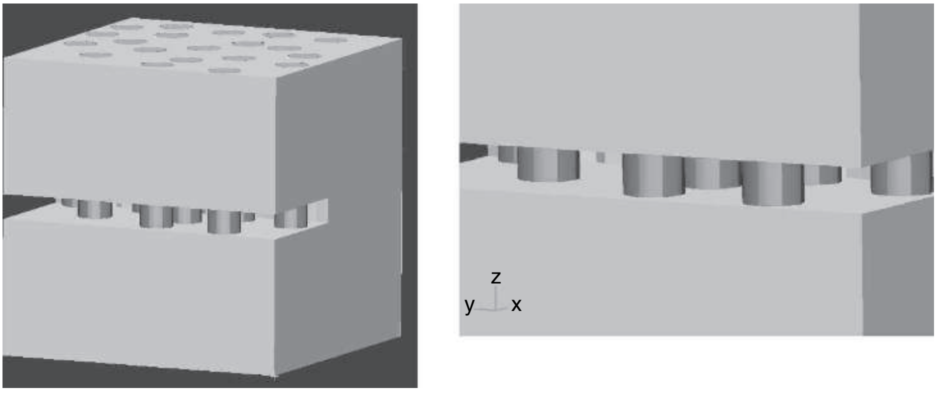

Figure 10.8 *Unit cells with cracks in the matrix and bridging fibers.*

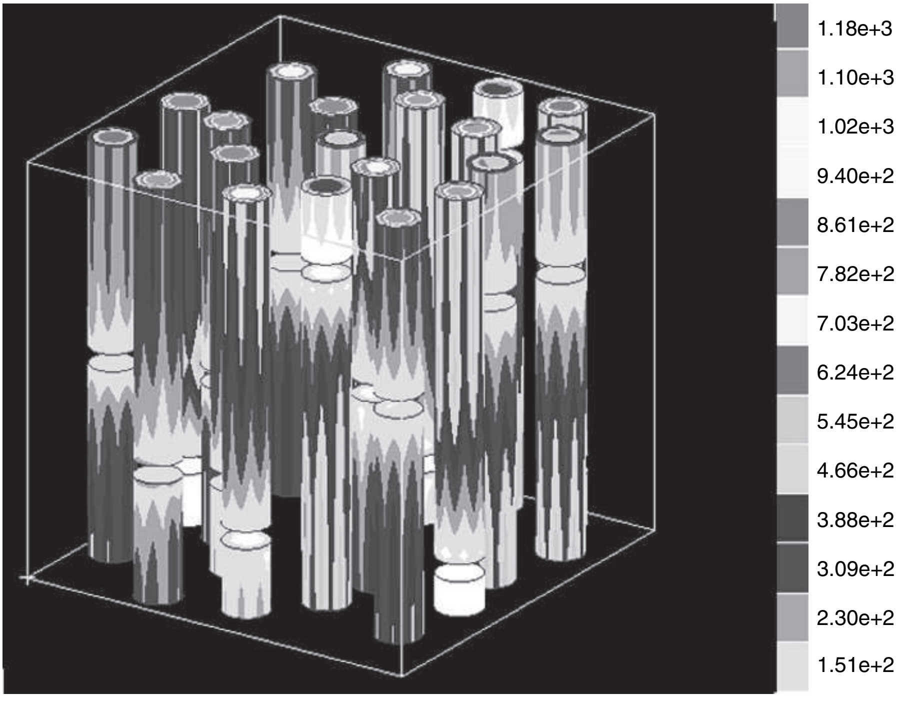

Figure 10.9 *Von Mises stress distribution in the fibers after the fiber cracking. (See Plate 5)*

Figure 10.10 shows the von Mises strain distribution in the matrix after the fiber failure. It is of interest to observe the shear bands, which tend to form in the matrix, connecting the regions of high stress concentration near the fiber cracks.

Figures 10.11 and 10.12 give the stress–strain curves of the models (initial part) and the damage (fraction of damaged elements in the damageable sections of the fibers) versus strain curves. One can see that the fiber cracking begins much earlier in the composites with matrix cracks, than in noncracked composites (apparently, due to the higher load in the bridging fibers, than in the fibers embedded in the matrix). The fiber failure leads to the much greater loss of stiffness in the composites with cracked matrix, than in noncracked composites.

Figure 10.13 shows the von Mises strain distribution in the matrix with a long crack after fiber failure. The regions of high strain level are seen along the surfaces of the potential debonding (between the matrix crack and the fiber fractures).

10.2.3 Numerical simulations: interface damage initiation and its interaction with matrix cracks and fiber fractures

Let us consider the interaction between all three damage modes in composites: matrix cracks, interface damage and fiber fracture.

In order to model the interface damage, the model of the interface as a 'third layer' was used (Downing *et al.*, 2000). The interface layer was assumed to be a homogeneous

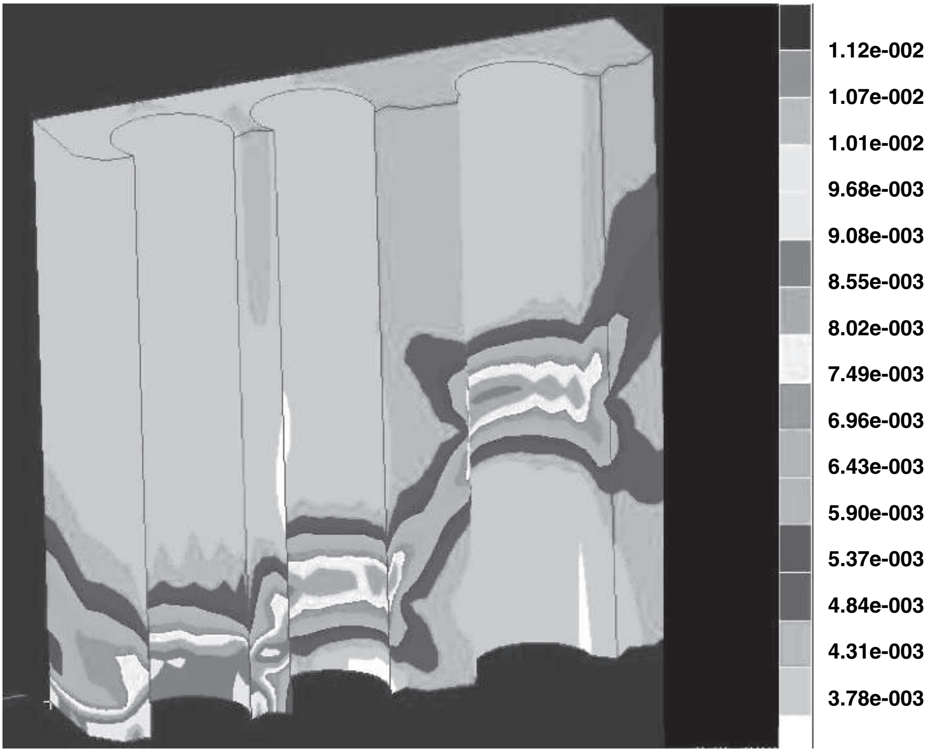

Figure 10.10 *Von Mises strain distribution in the matrix after the fiber failure. (See Plate 6)*

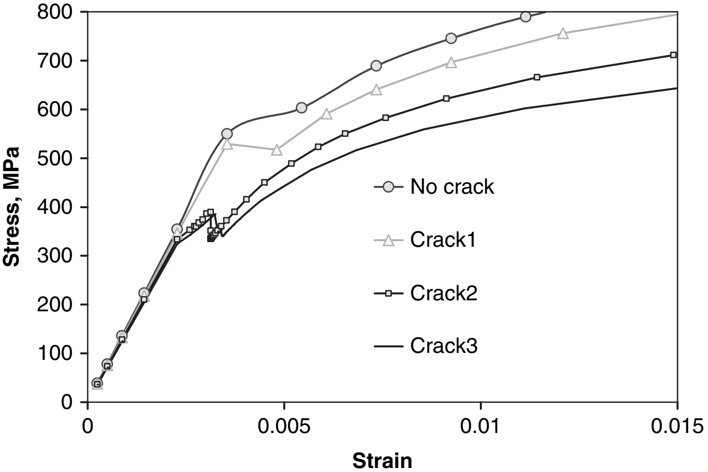

Figure 10.11 *Stress–strain curves for the unit cells with and without matrix cracks (initial part). The lengths of the cracks are as follows: Crack1, 1/6 of the cell size; Crack2, 5/12 of the cell size; Crack3, 8/12 of the cell size.*

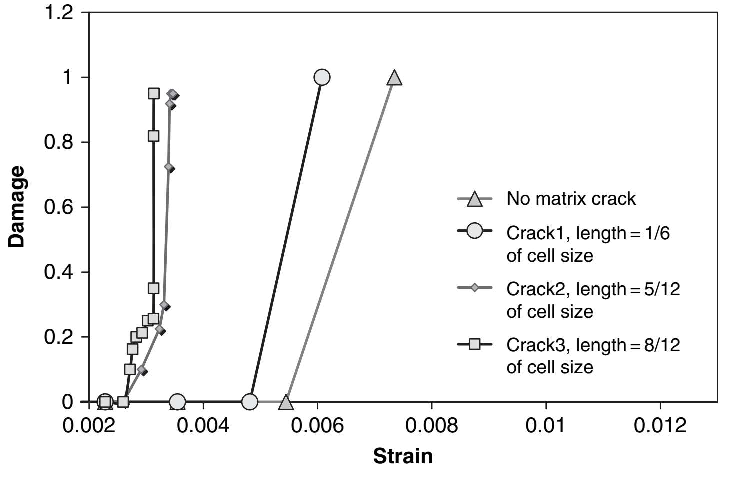

Figure 10.12 *Damage (fraction of damaged elements in the damageable sections of the fibers) versus strain curves for unit cells with and without matrix cracks.*

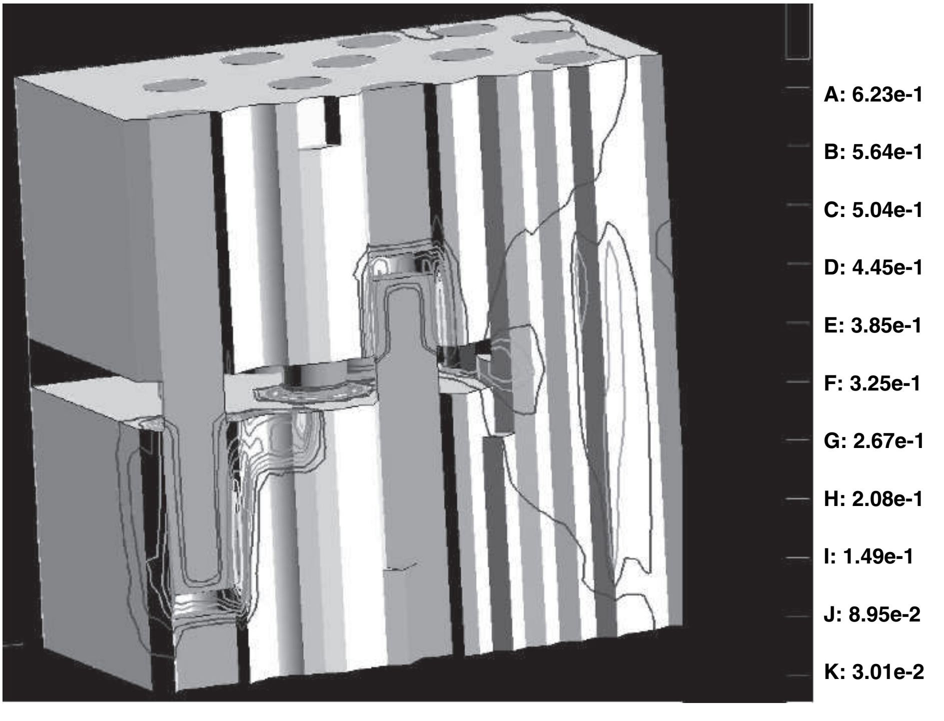

Figure 10.13 *Von Mises strain distribution in the matrix of a unit cell with a matrix crack after fiber failure. (See Plate 7)*

isotropic material, with Young modulus 273 MPa (i.e. the mean value of the Young moduli of fiber and matrix) and Poisson's ratio of the matrix. The thickness of the layer was taken as 0.2 mm. Following Tursun *et al.* (Tursun *et al.*, 2006), we chose the maximum principal stress criterion for the interface damage (therefore, assuming rather brittle interface). Two values of the critical stress were taken: 2000 MPa (i.e. strong, but still damageable interface) and 1000 MPa (weak interface). While the interface layer is considered as a homogeneous material in the first approximation, the model can be further improved if the graded material model is used to represent the interface layer, with properties to be determined from the inverse analysis.

Unit cells (with 15 fibers and 25 % fiber volume content) were generated, and tested (with different strengths of interface layers). The unit cells without matrix cracks as well as with matrix cracks (notches) of 0.3 (short crack) and 0.58 (long crack) of the cell size were analyzed. The fiber arrangement in the cells with and without matrix cracks was the same.

Figure 10.14 shows von Mises stress distribution in the fibers and in the interface layer before and after fiber cracking (the case of the longer matrix crack, and of the strong damageable interface). One can see that the fiber cracking leads to high stress concentration at the interfaces of the composite in the vicinity of the fiber cracks.

Figure 10.15 gives stress–strain curves for the unit cells with and without the matrix cracks, and with stronger (failure stress 2000 MPa) and weaker (failure stress 1000 MPa) interfaces. It can be seen that the stress–strain curves in the unit cells without matrix cracks are in fact identical for the cases of stronger and weaker interfaces. Thus, the interfaces are subject to very low stresses in the composites under axial tensile loading in the fiber direction, as long as both the fibers and matrix remain intact. For the case of the cracked matrix, the interface properties do influence the stiffness and strength of the composite: the stiffness of the composite decreases much quicker under loading if the interface between the fiber and matrix is weak.

Figure 10.16 shows the damage (fraction of failed elements) in fibers and in the interface plotted versus the applied strain, for the case of strong and weak interfaces, and the cracked matrix (long crack). In the case of the strong interface, the interface damage growth starts at a higher strain than the fiber cracking, and begins in the vicinity of the fiber cracks. Apparently, the interface damage growth is triggered by the fiber cracking. In the case of the weaker interface, the interface damage is not triggered by the fiber cracking, but precedes the fiber cracking: while in the unit cells with the stronger interfaces the interface damage begins only after the fibers fail (at strain 0.00543), in the unit cells with weak interfaces the interface damage begins at strain 0.0026.

Thus, the interface properties influence the bearing capacity and damage resistance of fibers: in the case of the weak fiber/matrix interface, fiber failure begins at much lower applied strains than in the case of the strong interface.

Comparing the simulations presented in this section, with the conclusions of the overview in the previous section, one can see that the mesomechanical FE simulations can efficiently complement other methods in the analysis of strength and damage of FRCs, mechanisms of the damage evolution and interaction between different damage modes. In contrast to the analytical methods of the analysis of multiple fiber cracking (e.g. BIS), the FE mesomechanical models make it possible to simulate the nonlinear behavior of phases

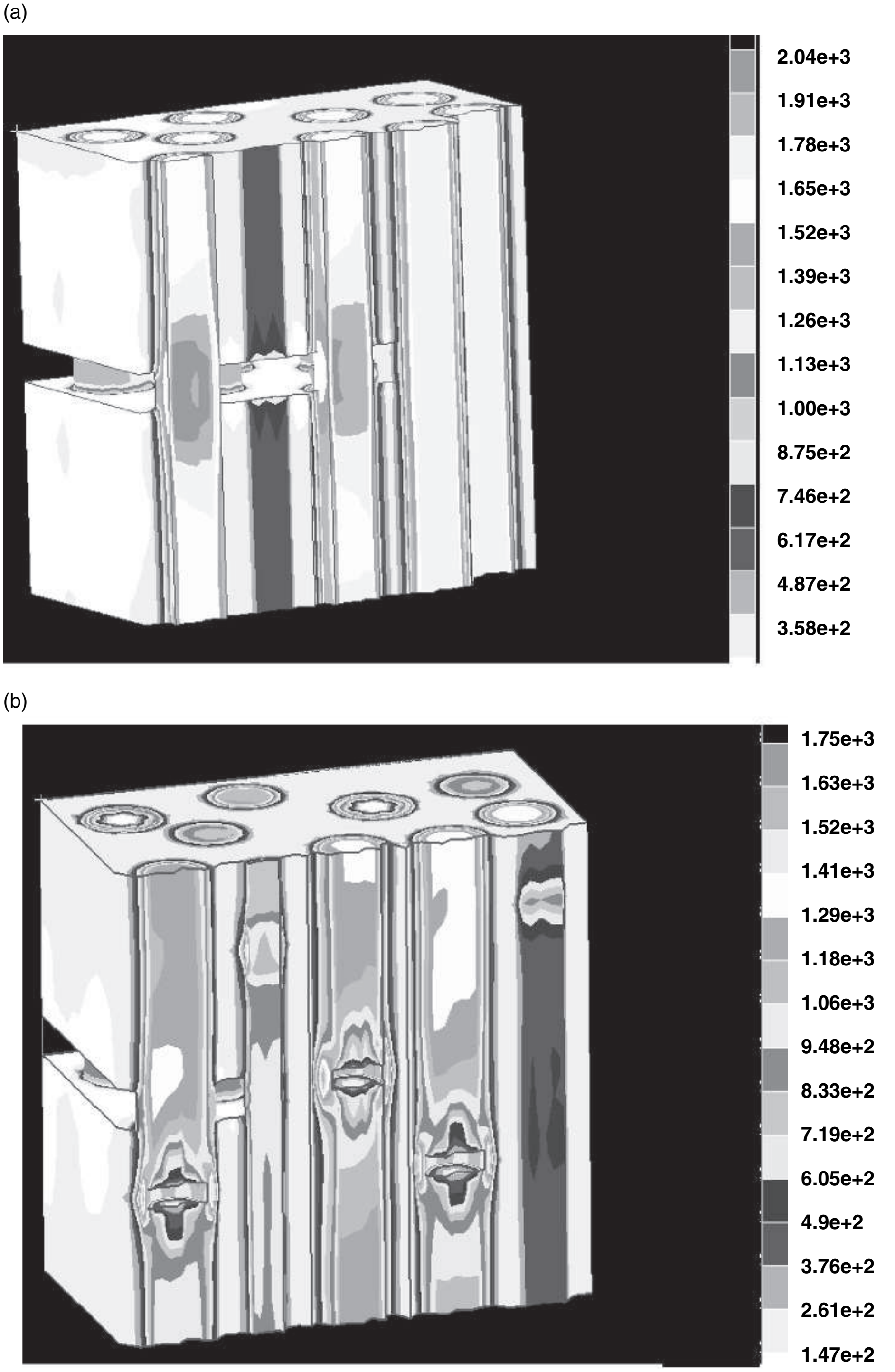

Figure 10.14 *Von Mises stresses in the unit cell with the matrix crack and the interface layer: (a) before and (b) after the fiber failure.*

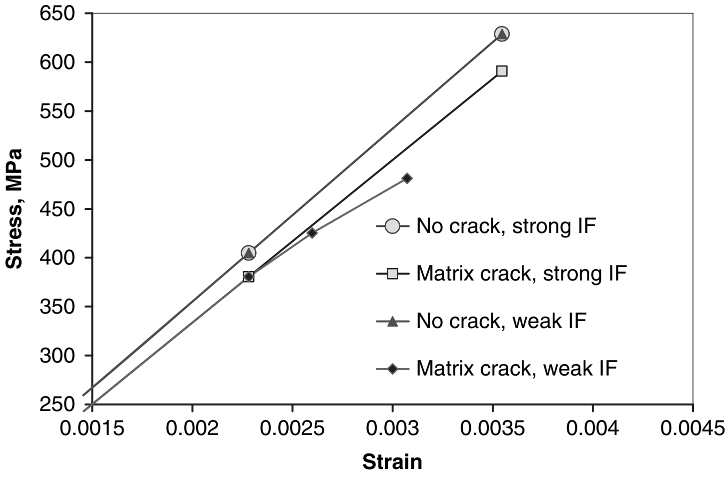

Figure 10.15 Stress–strain curves for unit cells with strong and weak interfaces. IF means 'interface'.

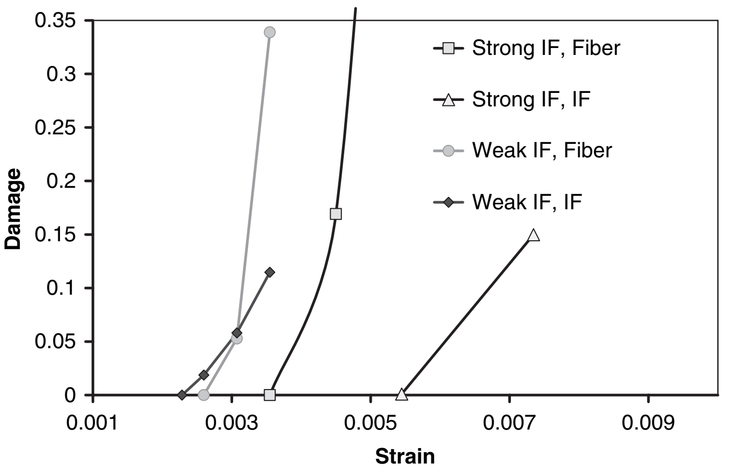

Figure 10.16 Damage–strain curves for fibers and interface damage for the strong (failure stress 2000 MPa) and weak (failure stress 1000 MPa) interfaces. The unit cell with the longer matrix crack (0.58 of the cell size) is considered.

(e.g. elastic-plastic matrix) and its effect on the damage in the composites. In some cases (e.g. transverse loading of composites), 2D models can be successfully applied to the analysis of the damage and fracture of FRCs. The results of 2D modeling of gradient and clustered composites, presented in Chapters 7 and 8, are applicable to unidirectional FRCs composites under transverse loading.

References

Asp, L. E., Berglund L. A. and Talreja R. (1996a). Effects of fiber and interphase on matrix-initiated transverse failure in polymer composites, *Composites Science and Technology*, **56** (6), 657–665.

Asp, L. E., Berglund L. A. and Talreja R. (1996b). Prediction of matrix-initiated transverse failure in polymer composites, *Composites Science and Technology*, **56** (9), 1089–1097.

Aveston, J., Cooper, G. A. and Kelly, A. (1971). Single and multiple fracture, in: *The Properties of Fibre Composites*, IPC Science and Technology Press, Surrey, pp. 15–26.

Beyerlein, I. J. and Phoenix, S. L. (1996). Stress concentrations around multiple fiber breaks in an elastic matrix with local yielding or debonding using quadratic influence superposition, *Journal of the Mechanics and Physics of Solids*, **44** (12), 1997–2039.

Beyerlein, I. J. and Phoenix, S. L. (1997). Statistics of fracture for an elastic notched composite lamina containing Weibull fibers – Part I. Features from Monte-Carlo simulation, *Engineering Fracture Mechanics*, **57** (2–3), 241–265.

Beyerlein, I. J., Phoenix, S. L. and Sastry, A. M. (1996) Comparison of shear-lag theory and continuum fracture mechanics for modeling fiber and matrix stresses in an elastic cracked composite lamina, *International Journal of Solids and Structures*, **33** (18), 2543–2574.

Böhm, H. J. and Rammerstorfer, F. G. (1993). Micromechanical models for investigating fibre arrangements in MMCs, in: *Proceedings of the International Seminar Micromechanics of Materials (MECAMAT)*, Editions Eyrolles, Paris, pp. 383–394.

Böhm, H. J., Rammerstorfer, F. G. and Weisenbek, E. (1993). Some simple models for micromechanical investigations of fiber arrangement effects in MMCs, *Computational Materials Science*, **1**, 177–194.

Brockenborough, J. R., Suresh, S. and Wienecke, H. A. (1991). Deformation of metal-matrix composites with continuous fibers: geometrical effects of fiber distribution and shape, *Acta Metallurgica et Materialia*, **39** (5), 735–752.

Budiansky, B. and Amazigo, J. C. (1989). Toughening by aligned, frictionally constrained fibers. *Journal of the Mechanics and Physics of Solids*, **37** (1), 93–109.

Budiansky, B. and Fleck, N. A. (1993). Compressive failure of fibre composites, *Journal of the Mechanics and Physics of Solids*, **41** (1), 183–211.

Budiansky, B. and Fleck, N. A. (1994). Compressive kinking of fibre composites: a topical review, *Applied Mechanics Reviews*, **47** (6), Part 2, S246–S250.

Budiansky, B., Hutchinson, J. W. and Evans, A. G. (1986). Matrix fracture in fiber-reinforced ceramics, *Journal of the Mechanics and Physics of Solids*, **34** (2), 167–189.

Budiansky, B., Evans, A. G. and Hutchinson, J. W. (1995). Fiber-matrix debonding effects on cracking in aligned fiber ceramic composites, *International Journal of Solids and Structures*, **32** (3), 315–328.

Cox, H. L. (1952). The elasticity and strength of paper and other fibrous materials, *British Journal of Applied Physics*, **3**, 73–79.

Curtin, W. A. (1991). Theory of mechanical properties of ceramic-matrix composites, *Journal of American Ceramic Society*, **74** (11), 2837–2845.

Daniels, H. E. (1945). The statistical theory of the strength of bundles of threads, *Proceedings of the Royal Society of London*, **183** (A995), 405–435.

Downing, T. D., Kumar R., Cross, W. M., Kjerengtroen, L. and Kellar, J. J. (2000). Determining the interphase thickness and properties in polymer matrix composites using phase imaging atomic force microscopy and nanoindentation, *Journal of Adhesion Science and Technology*, **14** (14), 1801–1812.

Fleck, N. A. (1997). Compressive failure of fibre composites, *Advances in Applied Mechanics*, **33**, 43–119.

González, C. and LLorca, J. (2006). Multiscale modeling of fracture in fiber-reinforced composites, *Acta Materialia*, **54**, 4171–4181.

González-Chi, P. I. and Young, R. J. (1998). Crack bridging and fibre pull-out in polyethylene fibre reinforced epoxy resins, *Journal of Materials Science*, **33** (24), 5715–5729.

Hansen, A. (2005), Physics and fracture, *Computing in Science and Engineering*, **7** (5), 90–95.

Harlow, D. G. and Phoenix, S. L. (1978). Chain-of-bundles probability model for strength of fibrous materials .1. Analysis and conjectures, *Journal of Composite Materials*, **12**, 195–214.

Hedgepeth, J. M. (1961). Stress concentrations in filamentary structures, NASA TND-882.

Hedgepeth, J. M. and van Dyke, P. (1967). Local stress concentrations in imperfect filamentary composite materials, *Journal of Composite Materials*, **1**, 294–309.

Hemmer, P. C. and Hansen, A. (1992). The distribution of simultaneous fiber failures in fiber bundles, *Journal of Applied Mechanics*, **59** (44), 909–914.

Hidalgo, R. C., Moreno, Y., Kun, F. and Herrmann, H. J. (2002). Fracture model with variable range of interaction, *Physical Review E*, **65**, 046148.

Huang, Y. and Petermann, J. (1996). Interface layers of fiber-reinforced composites with transcrystalline morphology, *Polymer Bulletin*, **36** (4), 517–524.

Hutchinson, J. W. and Jensen, H. M. (1990). Models of fiber debonding and pullout in brittle composites with friction, *Mechanics of Materials*, **9** (2), 139–163.

Ibnabdeljalil, M. and Curtin, W. A. (1997a). Strength and reliability of fiber-reinforced composites: Localized load-sharing and associated size effects, *International Journal of Solids and Structures*, **34** (21), 2649–2668.

Ibnabdeljalil, M. and Curtin, W. A. (1997b) Strength and reliability of notched fiber-reinforced composites, *Acta Materialia*, **45** (9), 3641–3652.

Kun, F., Zapperi, S. and Herrmann, H. J. (2000). Damage in fiber bundle models, *European Physical Journal*, **B17**, 269–279.

Landis, C. M., Beyerlein, I. J. and McMeeking, R. M. (2000). Micromechanical simulation of the failure of fiber reinforced composites, *Journal of the Mechanics and Physics of Solids*, **48** (3), 621–648.

Landis, C. M., McGlockton, M. A. and McMeeking, R. M. (1999). An improved shear lag model for broken fibers in composites, *Journal of Composite Materials*, **33**, 667–680.

Li, H., Jia, J. X., Geni, M., Wei, J. and An, L. J. (2006). Stress transfer and damage evolution simulations of fiber-reinforced polymer-matrix composites, *Materials Science and Engineering, A*, **425** (1–2), 178–184.

Marshall, D. B. and Cox, B. N. (1987). Tensile properties of brittle matrix composites: influence of fiber strength, *Acta Metallurgica et Materialia*, **35**, 2607–2619.

Marshall, D. B., Cox, B. N. and Evans, A. G. (1985). The mechanics of matrix cracking in brittle-matrix fiber composites, *Acta Metallurgica et Materialia*, **33**, 2013–2021.

McCartney, L. N. (1987). Mechanics of matrix cracking in brittle-matrix fiber-reinforced composites, *Proceedings of the Royal Society of London, Series A*, **409**, 329–350.

Megnis, M., Brϕndsted, P. and Mikkelsen, L. P. (2004). Damage evolution in laminated composite materials, in: *Materaleopførsel og skadesanalyse. Dansk Metallurgisk Selskabs vintermϕde*, Ed. M. A. J. Somers, DMS, Lyngby, pp. 33–42.

Niu, K. and Talreja, R. (2000). Modeling of compressive failure in fiber-reinforced composites. *International Journal of Solids and Structures*, **37** (17), 2405–2428.

Pagano, N. J. (1998). On the micromechanical failure modes in a class of ideal brittle matrix composites. Part 1. Coated-fiber composites. Part 2. Uncoated-fiber composites, *Composites Part B: Engineering*, **29** (2), 93–119, 121–130.

Pagano, N. J. and Kim, R. Y. (1994). Progressive microcracking in unidirectional brittle matrix composites, *Mechanics of Composite Materials and Structures*, **1**, 3–29.

Piggott, M. R. (1987). Debonding and friction at fibre-polymer interfaces. I: Criteria for failure and sliding, *Composites Science and Technology*, **30** (4), 295–306.

Raischel, F., Kun, F. and Herrmann, H. J. (2006). Failure process of a bundle of plastic fibers, *Physical Review E*, **73**, 066101–12.

Sastry, A. M. and Phoenix, S. L. (1993). Load redistribution near non-aligned fibre breaks in a two-dimensional unidirectional composite using break-influence superposition, *Journal of Materials Science Letters*, **12** (20), 1596–1599.

Slaughter, W. S. (1993). A self-consistent model for multi-fiber crack bridging, *International Journal of Solids and Structures*, **30** (3), 385–398.

Slaughter, W. S. and Sanders Jr, J. L. (1991). A model for load-transfer from an embedded fiber to an elastic matrix, *International Journal of Solids and Structures*, **28** (8), 1041–1052.

Sutcliffe, M. P. F., Fleck, N. A. and Xin, X. J. (1996). Prediction of compressive toughness for fibre composites, *Proceedings of the Royal Society of London, series A*, **452**, 2443–2465.

Talreja R. (1987). *Fatigue of Composite Materials*, Technomic, Lancaster.

Trias, D., Costa, J., Mayugo, J. A. and Hurtado, J. E. (2006a). Random models versus periodic models for fibre reinforced composites, *Computational Materials Science*, **38** (2), 316–324.

Trias, D., Costa, J., Turon, A. and Hurtado, J. E. (2006b). Determination of the critical size of a statistical representative volume element (SRVE) for carbon reinforced polymers, *Acta Materialia*, **54** (13), 3471–3484.

Tursun, G., Weber, U., Soppa, E. and Schmauder, S. (2006). The influence of transition phases on the damage behaviour of an Al/10vol. %SiC composite, *Computational Materials Science*, **37** (1–2), 119–133.

Vejen, N. and Pyrz, R. (2002). Transverse crack growth in glass/epoxy composites with exactly positioned long fibres. Part II: numerical, *Composites: Part B (Engineering)*, **33** (4), 279–290.

Wagner, H. D. and Eitan, A. (1993). Stress concentration factors in two-dimensional composites – Effects of material and geometrical parameters, *Composites Science and Technology*, **46** (4), 353–362.

Xia, Z. H. and Curtin, W. A. (2001). Multiscale modeling of damage and failure in aluminum-matrix composite, *Composites Science and Technology*, **61** (15), 2247–2257.

Xia, Z. H., Curtin, W. A. and Peters, P. W. M. (2001). Multiscale modeling of failure in metal matrix composites, *Acta Materialia*, **49** (2), 273–287.

Xia, Z. H., Okabe, T. and Curtin, W. A. (2002a). Shear-lag versus finite element models for stress transfer in fiber-reinforced composites, *Composites Science and Technology*, **62** (9), 1141–1149.

Xia, Z., Curtin, W. A. and Okabe, T.(2002b). Green's function vs. shear-lag models of damage and failure in fiber composites, *Composites Science and Technology*, **62** (10–11), 1279–1288.

Zhang, X., Liu, H. Y. and Mai, Y. W. (2004). Effects of fibre debonding and sliding on the fracture behaviour of fibre-reinforced composites, *Composites A*, **35** (11), 1313–1323.

Zhang, Y., Xia, Z. and Ellyin, F. (2005). Nonlinear viscoelastic micromechanical analysis of fibre-reinforced polymer laminates with damage evolution, *International Journal of Solids and Structures*, **42** (2), 591–604.

Zhou, X. -F. and Wagner, H. D. (1999). Stress concentrations caused by fiber failure in two-dimensional composites, *Composites Science and Technology*, **59**, 1063–1071.

Zok, F. W. (2000). Fracture and fatigue of continuous fiber-reinforced metal matrix composites, in: *Comprehensive Composite Materials*, Eds A. Kelly and C. Zweben, Pergamon, Oxford, Vol. 3, pp. 189–220.

Zok, F. W., Begley M. R., Steyer T. E. and Walls D. P. (1997). Inelastic deformation of fiber composites containing bridged cracks, *Mechanics of Materials*, **26** (2), 81–92.

11

Contact damage and wear of composite tool materials: micro–macro relationships

In this chapter, some ideas on the mesomechanical analysis of the surface damage and the wear of composite materials under contact loading are discussed.

The wear and the volume damage evolution in composites have many common features, including similar micromechanisms of damage initiation and growth. For instance, the crack initiation by the inclusion failure, followed by the interface debonding and by the damage and destruction of the matrix, adjacent to the inclusion, is observed both in the volume fracture and in the surface wear of composites.

However, there are also many differences between the destruction processes under volume and surface loading. In the volume loading, the stiffness of the specimen is reduced due to the damage evolution; in the wear, shapes of the contacting bodies are changed, whereas the physical parameters (overall stiffness) remain constant. The damage accumulation under volume loading leads ultimately to the failure of the specimen. In the case of wear, the damage accumulation on the surface of a tool may lead to the dulling of the tool, which will make its further utilization impossible. However, the preferable, and rather often observed situation, is when the wear becomes a stable dynamic process, and leads to the self-sharpening of the tool.

The complex, multiscale and multiphysics nature of wear requires either a correspondingly complex multilevel modeling approach or combining different techniques for the analysis of different aspects of the process. In this chapter, we seek to analyse the aspects of the wear of composites which are relevant to the mesomechanics of composites, namely:

Computational Mesomechanics of Composites L. Mishnaevsky Jr

- damage and failure of surface particles under contact loading (which is the leading wear mechanism in many applications, such as diamond grinding or cutting with cemented carbide tools);
- dynamic macro–micro relationships for the surface damage and wear of materials;
- interrelationships between the scattering of the mechanical properties of contacting bodies at the micro level, and their damage resistance and shape stability at the macro level.

11.1 Micromechanical modeling of the contact wear of composites: a brief overview

According to Khrushchov and Babichev (Khrushchov and Babichev, 1970) and Garkunov *et al.* (Garkunov *et al.*, 1969), the mechanisms of wear can be classified as follows:

- mechanical wear: abrasive wear (roughnesses of contacting surfaces are cut, squeezed out or failed in friction), erosion, wear due to the plastic deformation of surface layers, wear due to the embrittlement of surface layers, fatigue wear (fatigue destruction of surface layers);
- 'molecular-mechanical' wear: adhesion of contacting surfaces which leads to the destruction of surface layers of the weaker material;
- corrosion wear, oxidation, fretting, etc.

For the case of the low sliding speed, the abrasive and other mechanical mechanisms of wear control the rate of wear (Tjong *et al.*, 1997; Kwok and Lim,1999). In turn, these mechanisms include a number of interactions between elements (particles, matrix, debris, etc.), and different micromechanisms of damage, which are in some cases very similar to the mechanisms of damage in composites under volume loading: cracking in particles and on interfaces, delamination, damage, related to the dislocation accumulation and hardening, but also plowing and scratching of grains.

Numerically, the contact wear of materials is simulated by *introducing some wear laws* into numerical models, complemented by some kind of the geometry or mesh update algorithms. The phenomenological law, relating the wear rate, applied load and sliding distance, was suggested by Archard (Archard, 1953). Assuming that the wear of materials is controlled by the adhesion mechanisms, which cause the detachment of small volumes of materials, Archard demonstrated that:

$$W \propto \frac{Fx}{h} \tag{11.1}$$

where W is wear rate, F is normal load, x is sliding distance and h is hardness of the soft surface.

Molinari *et al.* (Molinari *et al.*, 2001) developed a FE model of dry sliding wear in metals, which uses the generalized Archard's law. In the framework of the generalized Archard's law, the hardness of the soft material is assumed to be a function of temperature. The temperature dependence of the hardness incorporates indirectly the oxidation and other chemistry effects by employing the idea of Lancaster (Lancaster, 1963) that the transition from severe to mild wear is related to the level of oxidation of the contacting metals. This allows the transition from severe wear to mild wear at a critical sliding speed to be described. This model takes into account the surface evolution due to wear by using the continuous adaptive remeshing algorithm.

Archad's model was implemented by Hegadekatte *et al.* (Hegadekatte *et al.*, 2005) in FE post-processor software. The wear on the interacting contact surfaces was computed using the contact pressure distributions, which were determined in a series of static FE simulations of the deformation of contact bodies. The wear simulations were carried out in a loop, and the surface geometries were updated and refreshed after each simulation.

A formula for adhesive wear, similar to Archard's law, was suggested by Shaw (Shaw, 1984). Usui *et al.* (Usui *et al.*, 1978) introduced the analytical formula for the rate of crater wear, derived from Shaw's equation of adhesive wear, into a numerical (finite difference) analysis of stress and temperature fields in cutting, and calculated the crater wear of a cutter. Xie (Xie, 2004) implemented the Usui tool wear model into a FE model of turning and milling, which included the numerical analysis of chip formation and temperature distribution in the cutting tool. On the basis of calculated nodal tool wear rates, the tool geometry was updated and the next tool wear calculation cycle was started.

Along with the numerical implementation of phenomenological material models, questions about the *effect of the microstructures* on the wear and numerical analysis of the micromechanisms of wear attracted growing interest from researchers.

In their book, Khrushchov and Babichev (Khrushchov and Babichev, 1970) suggested the inverse rule of mixture to analyze the effect of the microstructures on the wear:

$$\frac{1}{W} = \frac{vc_{\mathrm{A}}}{W_{\mathrm{A}}} + \frac{vc_{\mathrm{B}}}{W_{\mathrm{B}}} \tag{11.2}$$

where W is wear rate of the composite, $W_{\mathrm{A,B}}$ are the wear rates of each phase (A, B) and $vc_{\mathrm{A,B}}$ are the volume fractions of phases A and B. Other formulae, in which the contribution of each phase of a composite to the wear rate is supposed to be proportional to the volume content of this phase, were suggested by Zum Gahr (Zum Gahr, 1987) and Axen and Jacobson (Axen and Jacobson, 1994a,b).

Lawn (Lawn, 1975b) employed the approach of the indentation fracture mechanics to analyze the abrasion wear of brittle materials. Taking into account the volume removal from both the lateral chip-forming cracks and 'plastic' deformation track, and carrying out the summation over the microchips from all the inclusions at the contact surface, Lawn derived a formula for the macroscopic abrasion wear rate of brittle solids. In his formula, the wear rate is independent of the apparent contact area and number of contacting particles, and determined uniquely by the material hardness.

Cho *et al.* (Cho *et al.*, 1989) analyzed the grain size effect in the abrasive wear of brittle ceramics (alumina). Considering the equilibrium condition of a flaw in a grain in terms of stress intensity factors, they determined the stress necessary to cause wear-associated grain spalling: $\sigma \sim d^{-1/2} + \text{constant}$, where d is grain size. Cho and colleagues concluded that the wear resistance increases with decreasing grain sizes and reducing internal stresses in the ceramics.

Lee *et al.* (Lee *et al.*, 2002) developed a micromechanical model for the abrasive wear of composite (ductile matrix reinforced by brittle particles) materials, based on the 'equal wear rate assumption', used by Khruschchov and Babichev. In the framework of this model, a triangular abrasive medium particle acts on the composite material, containing rectangular hard reinforcements. The motion of the grain causes the plowing, cracking on the matrix/reinforcement interface and in the reinforcement, as well as the particle removal. The acting micromechanisms of wear are taken into account by analyzing the ratio between the fracture toughnesses of the reinforcement/matrix interface and the reinforcing material. Assuming that any portion of the reinforcement that is removed as wear debris cannot contribute to the wear resistance of the matrix material, the authors analyzed the influence of the parameters of the reinforcement, such as the relative size, fracture toughness and the nature of the matrix/reinforcement interfaces, on the wear of composites.

Another example of the micromechanical modeling of wear is given in the work by Yan *et al.* (Yan *et al.*, 2000). Yan *et al.* applied a multiscale micromechanical approach to analyze the sliding wear of coated components. The authors used unit cell models to study the localized deformation patterns at the mesoscale (scale of the coating thickness) and calculated the rate of material removal due to the repeated sliding contact. Assuming that the wear is controlled by the accumulation of plastic deformation in the coating subsurface, Yan and colleagues proposed a wear equation, and carried out parametric studies on the effect of the loading conditions on the wear rate.

A series of publications deals with the effect of microstructures of unidirectional fiber reinforced composites (FRCs) on their wear resistance. On the basis of a number of experiments, Tsukizoe and Ohmae (Tsukizoe and Ohmae, 1983) proposed an empirical formula for the wear rate of polymer FRCs:

$$W \sim (1/I)(\mu P/E)^{\beta} \tag{11.3}$$

where β is an empirical constant, μ is the coefficient of friction, P is load, E is Young's modulus of the composite and I is the interlaminar shear strength.

Lhymn *et al.* (Lhymn *et al.*, 1985) and Lhymn (Lhymn, 1987) analyzed the effect of fiber orientations on the tribological properties of unidirectional polymer FRCs. They derived several phenomenological equations for specific wear rates of composites on the basis of the analysis of crack propagation, delamination physics and bond rupture in the composites. In some cases, the Lhymn equations can be reduced to the empirical formula by Tsukizoe and Ohmae (Tsukizoe and Ohmae, 1983).

Friedrich *et al.* (Friedrich *et al.*, 2002) developed a series of micromechanical FE models of wear of FRCs. Friedrich and colleagues used the displacement coupling technique to link micro- and macrolevel models. On the basis of the micromechanical modeling, dominant wear mechanisms in different cases were identified. It was shown that fiber/matrix debonding as a result of shear stresses at the interface, shear failure in the matrix and fiber thinning are the dominant sliding wear mechanisms in the case of the parallel fiber orientation. In the case of the anti-parallel fiber orientation, matrix shear, tension/compression type fiber/matrix debonding and fiber thinning, associated with fiber cracking events, are the dominant wear mechanisms.

A special case in the analysis of the abrasive wear of composite materials is the *wear of grinding wheels*, in particular, the diamond and cubic boron nitride (CBN) metal-bond or polymer-bond grinding wheels (Mishnaevsky, 1982; Malkin, 1989). Schemas of the main physical mechanisms of the wear of grinding wheels (chemical wear and dulling, grain fracture and interface debonding) are shown in Figure 11.1.

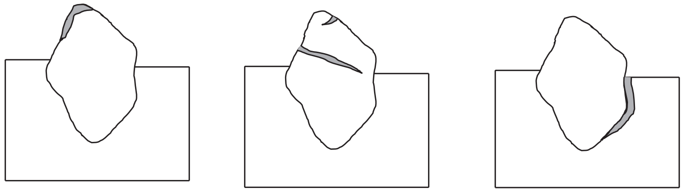

Figure 11.1 *Schemas of some micromechanisms of the wear of the grinding wheels: (a) chemical/oxidation wear and particle dulling; (b) grain cracking; (c) interface cracking, leading to the grain falling out.*

Mishnaevsky (Mishnaevsky, 1982, 1985) applied the methods of fracture mechanics and the theory of reliability to the analysis of failure of diamond grains in grinding. On the basis of the analysis of probability distributions of the reliability indices of diamond and CBN grains on the surface of a grinding wheel, he derived a formula for the optimal strength of grains for a given grinding condition. Considering the effect of the grain shapes on their strength, he determined the failure conditions of the grains and the wear rate of grinding wheels.

A comprehensive model of the grinding process, which includes the wear, was developed by Chen and Rowe (Chen and Rowe, 1996, 1998). They simulated the wear of ceramic grinding wheels, taking into account the attrition of the peaks of grains ('attritious wear') as well as the failure of grains and the bonds. The attritious wear was represented as a local reduction of the wheel radius. The grain failure was simulated by changing the grain shapes in grinding: the grain peaks were replaced by plane areas with two to three small sinusoidal peaks. The bond failure was simulated by considering the critical ratio between the cutting force and the bond strength. Using this model, Chen and Rowe analyzed the effect of the grinding wheel wear on the efficiency of grinding.

Summarizing, one may state that main challenges in the numerical modeling of wear are the complex interacting micromechanisms, multiscale and multiphysical nature of wear processes, and the interaction between changing shapes and changing loading conditions.

11.2 Mesomechanical simulations of wear of grinding wheels

One of the areas where the analysis of wear is of great importance for industrial applications is the modelling and optimization of machining of materials. The wear resistance of machining (turning, grinding, etc.) tools determines their life span and the costs of machining to a large extent.

In this section, the mesomechanical simulations of the wear of diamond grinding wheels were carried out using the numerical tools presented in Chapters 5 and 6.

We consider here straight grinding wheels with synthetic diamonds and bronze copper bond. Such wheels are often used for machining ceramics. 3D FE models of cut-outs of the work surface of a grinding wheel have been generated automatically using the program Meso3D. On the contact surface 10×10 mm, 15 diamond grains were randomly placed. The FE model is shown in Figure 11.2. The radius of grains was 1.16 mm (therefore, 63 % of the contact surface was taken by the diamond grains).

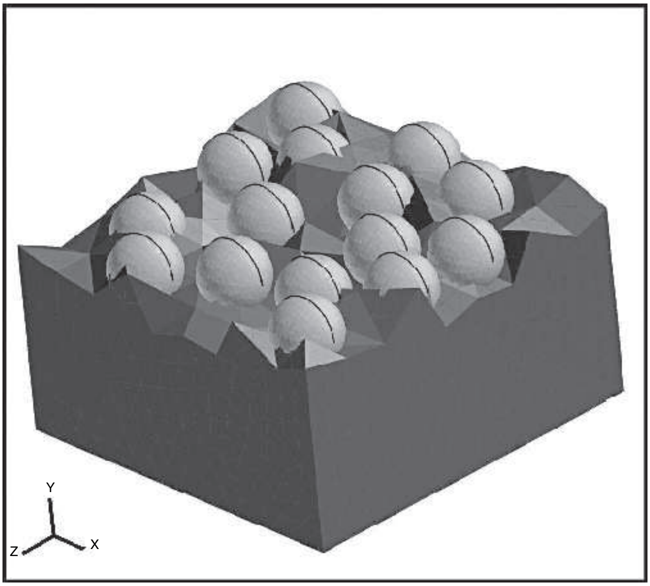

Figure 11.2 Mesomechanical FE model of a cut-out of the surface of a grinding wheel.

The material properties were as follows: diamond: Young modulus $E = 900\,\text{GPa}$, Poisson's ratio $v = 0.2$, compressive yield strength 5 MPa; bond: $E = 93\,\text{GPa}$, tensile yield stress 125 MPa, yield strain 0.2%, ultimate tensile strength 255 MPa (Bauccio, 1994). The failure stress of the diamond grains was taken to be 20 GPa (Mishnaevsky, 1982). The grain tips have been loaded by the inclined force, 70 N grain^{-1}. The force was oriented at a 60° angle to the horizontal line. The temperature effect was neglected in the first approximation, following the results of Mishnaevsky (Mishnaevsky, 1982), who demonstrated that local heating up to 200–300 °C (i.e. the local temperatures observed on the grain surfaces at relatively low cutting speeds) does not change the mechanisms and critical parameters of the grain destruction. The damage in the diamond grains was modeled using the subroutine User Defined Field, presented in Section 6.3. The critical maximum stress was taken as a criterion of the FE failure.

The schema of the loading is shown in Figure 11.3.

Figure 11.4 shows von Mises strain distribution in the diamond grains and in the metal bond in grinding. Figure 11.5 shows the fraction of FEs in the grains versus applied force.

One can see from Figure 11.4 that the high strains are localized near the peaks of the diamond grains. This corresponds to the experimental observations made by Mishnaevsky (Mishnaevsky, 1982): the damage in diamond grains in grinding has been observed in a small region near the grain peaks.

It can be seen from Figure 11.5 that the damage growth in the diamond grains starts at a force of 24 N and becomes very intense at a force of about 45 N.

The results, presented in this section, demonstrate the applicability of the computational mesomechanics approach and the numerical tools developed in Chapter 5 to the analysis of the wear of diamond grinding wheels.

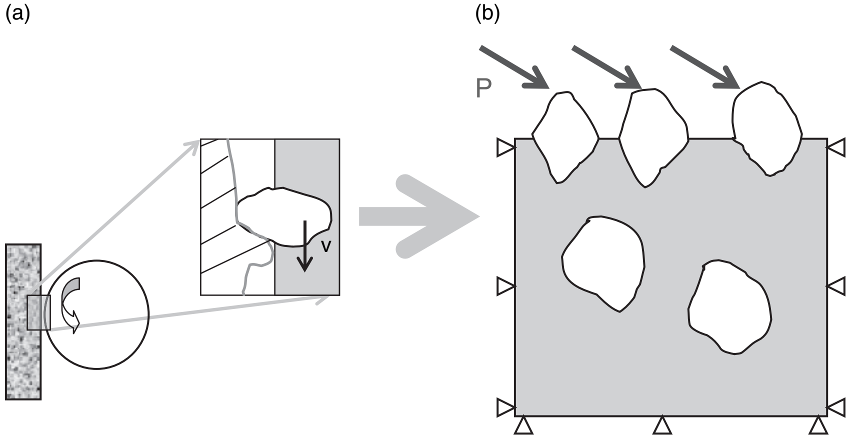

Figure 11.3 *Schema of (a) the loading of diamond grains, in the diamond wheel/workpiece contact zone and (b) the idealized model of the grain loading.*

11.3 Micro–macro dynamical transitions for the contact wear of composites: 'black box modeling' approach

11.3.1 Model of the tool wear based on the 'black box modeling' approach

In this section, we analyze the dynamical variations of the wear rate, contact stresses and tool shapes, caused by the tool wear.

Let us consider the following case, which is rather important for a number of industrial applications: a tool from a composite material, cutting another heterogeneous material (Mishnaevsky Jr, 1994). The tool material consists of hard particles and a ductile matrix: for example, metal bond diamond grinding wheels or drilling tools from WC/Co hard alloys. Figure 11.6 shows a schema of a composite tool in cutting a sample of a heterogeneous material.

The mechanisms of the material removal from the tool contact surface in the mechanical wear can be described as follows (Khrushchov and Babichev, 1970; Mishnaevsky, 1982): The particles on the tool surface interact with the work material, plow, deform, cut it, and are subject to the loading by the work material. The cyclic loading and damage accumulation in the particles lead to their failure, debonding along the interface and/or grains falling out. While the matrix on the tool surface does not contact with the work material, it interacts with and is worn out by the debris (chips, failed grains, etc.), which are accumulated between two contacting surfaces. The wear of the matrix speeds up the grains falling out. However, at the high density of grains on the surface, the rate of the matrix wear in the vicinity of a grain remains rather low, as long as the grain is intact. After a particle fails or comes out, the ductile matrix is worn out quickly by the debris. Thus, the rate of the wear of the tool is in fact controlled by the rate of the failure and falling out of hard grains on the working surface. (One should note that the described mechanisms can change drastically depending on the properties of materials and friction conditions.)

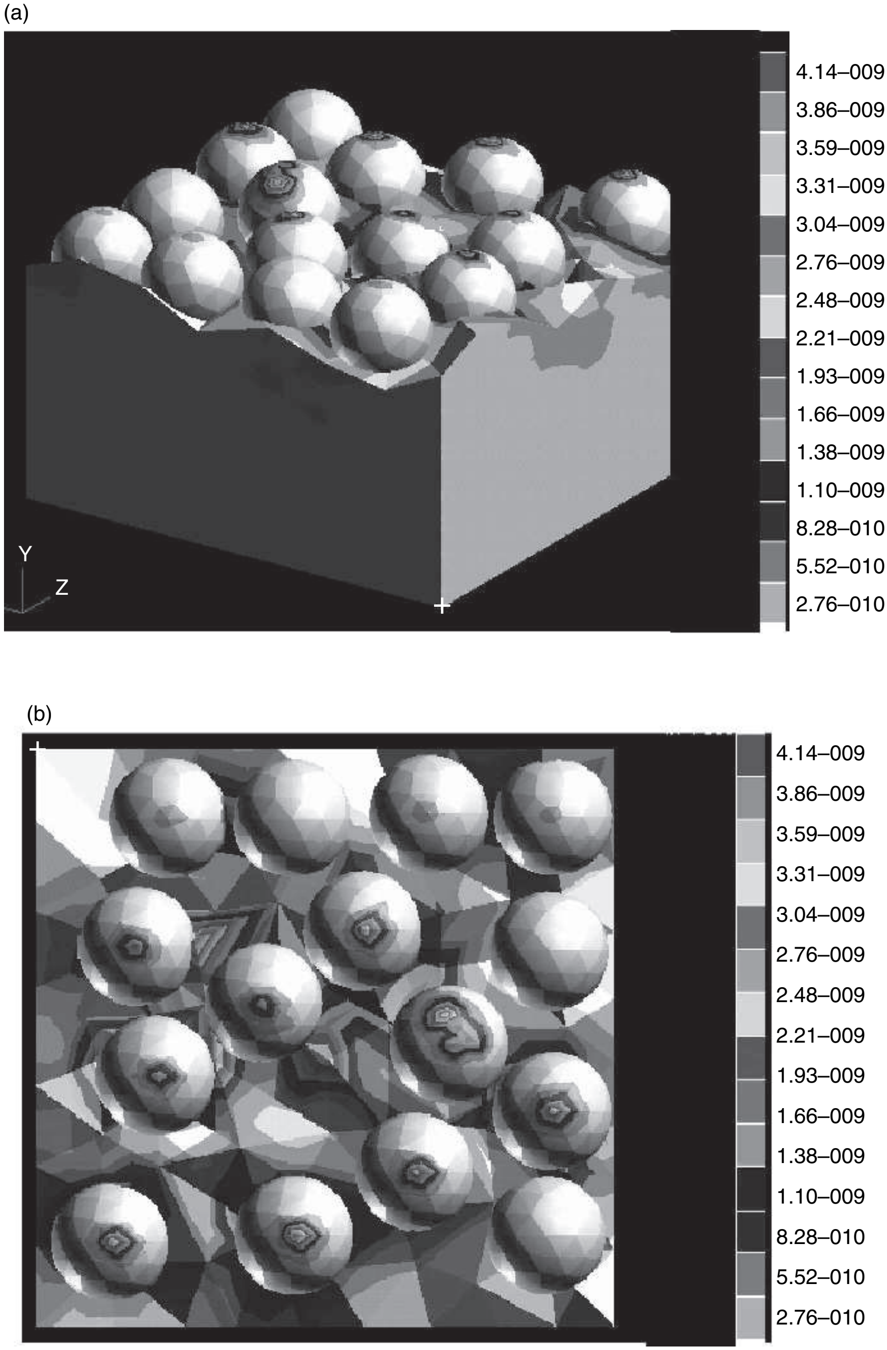

Figure 11.4 *Von Mises strain distribution in the diamond grains and in the metal bond in grinding: (a) isometric; (b) top view. (See Plate 8)*

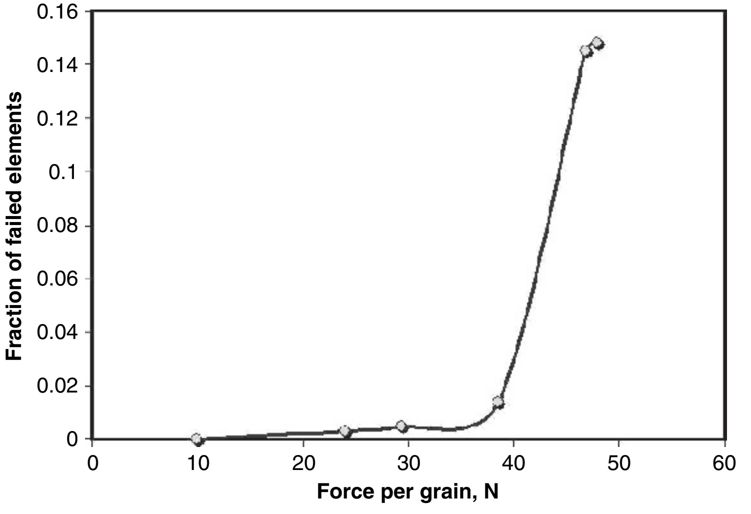

Figure 11.5 *Fraction of failed elements in the grains versus applied force.*

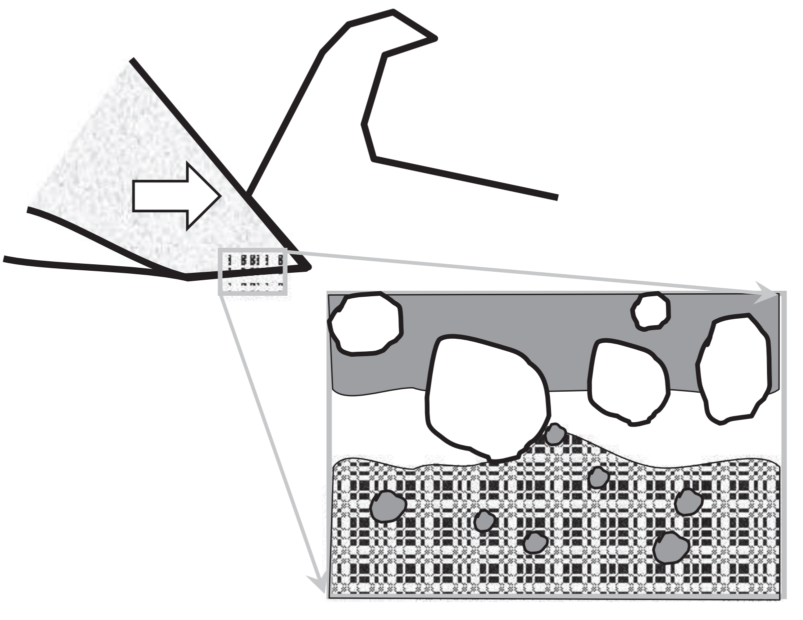

Figure 11.6 *Schema of a cutting tool from cemented carbide in cutting a work material.*

As a result of the failure of grains and grains falling out on the contact surface, and the following abrasion of the matrix layers, the tool shape is changed, the contact stress redistribution takes place, and the wear rate changes as well. This can be considered as a transient in a dynamical system with a feedback: the tool shape determines the distribution of wear rates over the contact surface, and this distribution in turn influences the tool shape.

In order to model such a dynamical, transient process, the methods of the control system theory can be applied. In the framework of the 'black box modeling' approach to the analysis of complex systems or processes (Mishnaevsky Jr, 1998a), a system or process is described as a combination of several elementary physical processes/subsystems. The acting physical mechanisms/elementary processes are represented as signal transformation units ('black boxes'), characterized by their input and output 'signals'. As 'signals', variations of the wear rate, contact stresses or the tool shape can be considered. The relations between input and output signals of the units are determined by considering the physical mechanisms of the 'signal' transformation.

In the framework of the 'black box modeling' approach, the tool is represented as a dynamical system in the form of a block diagram (Van der Bosch and Van den Klauw, 1994). The system is presented in Figure 11.7. It is made up of three units which take into account the following factors:

- the influence of the local wear rate on the tool shape (unit 1);
- the influence of the contact stress on the rate of local wear (unit 2);
- the influence of the tool shape on the contact stress distribution (unit 3).

A unit ('black box') can be characterized with the use of transfer functions. A transfer function is defined as the Laplace transform of an output signal of the box, divided by the Laplace transform of the input signal:

$$W(q) = \frac{L[\text{output\_signal}(t)]}{L[\text{input\_signal}(t)]} \tag{11.4}$$

where $L()$ is the Laplace transform, q is the parameter of the Laplace transform and t is time.

Let us determine the transfer functions of the system, presented in Figure 11.7. First, consider 'input–output relations' of each of the units.

11.3.1.1 Unit 1 (input signal, local wear rate; output signal, shape variations of the contacting bodies)

Let us describe the tool surface by the equation:

$$\mathrm{Z} = f(\mathrm{X},\ \mathrm{Y}) \tag{11.5}$$

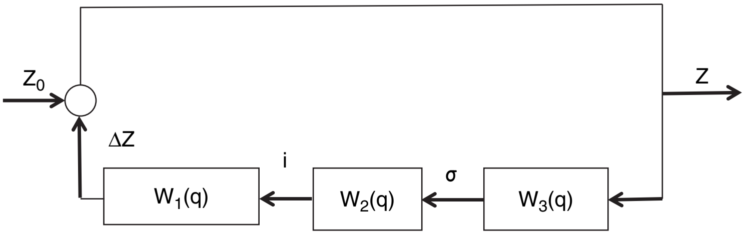

Figure 11.7 *Block diagram of the 'black box model' of the tool wear system. Here: $W_i(q)$ is the transfer function of i-th unit, q is the parameter of the Laplace transform Z_0 and Z are the coordinates of the point at the initial moment of contact and in time t, $\triangle Z = Z - Z_0$, i is the local rate of wear, σ is the contact stress.*

where X, Y, Z are the Cartesian coordinates. Let the axis Z be directed so that the function $f(\mathrm{X}, \mathrm{Y})$ is convex up.

The change in the Z-coordinate of a given surface point due to the wear can be calculated by:

$$\mathrm{Z}(t) = \mathrm{Z}_o - v \int_0^t i \mathrm{d}t \tag{11.6}$$

where Z_o is the Z-coordinate of the point at the initial moment of contact and v is the sliding/cutting rate. From Equation (11.6) it is seen that unit 1 can be considered as integrating (Van der Bosch and Van den Klauw, 1994).

The transfer function of unit 1 (integrating) presents the Laplace transform of function $\mathrm{Z}(t)$, which is given by Equation (11.6):

$$W_1(q) = L[\mathrm{Z}(t)] = v/q \tag{11.7}$$

11.3.1.2 Unit 2 (input signal, contact stress σ; output signal, local wear rate i)

In order to describe the local wear rate versus contact stress relationship, we may use the analytical equation from Mishnaevsky Jr (Mishnaevsky Jr, 1995b, 1998a):

$$i = \frac{0.78}{\mathrm{A} v n_{\mathrm{p}}^{3/2}} \exp\left(\frac{\mathrm{B}\sigma}{\mathrm{k}T}\right) \tag{11.8}$$

where A,B are kinetic constants of the reinforcement material, n_{p} is the mean number of reinforcement particles per unit contact area of the tool material, k is the Boltzmann constant, T is temperature and v is the sliding (cutting) rate.

As a first approximation, unit 2 can be taken to be a proportional one (Mishnaevsky Jr, 1998a). In this case, its transfer function $W(q) = L[i(\sigma)]/L(\sigma)$ is a constant value, which is equal to $\mathrm{d}i(\sigma)/\mathrm{d}\sigma$ (i.e. the proportionality coefficient in a piecewise linear approximation of the function (11.8)). We have:

$$W_2(q) = L[i(\sigma)]/L(\sigma) = \mathrm{d}i(\sigma)/\mathrm{d}\sigma = C_i \tag{11.9}$$

where C_i is the coefficient proportionality, depending on the physical properties of the materials. The parameter $C_i = \mathrm{d}i(\sigma)/\mathrm{d}\sigma$ can be calculated on the basis of Equation (11.8):

$$C_i \sim \frac{0.78B}{\mathrm{A}v\mathrm{k}Tn_{\mathrm{p}}^{3/2}} \exp(\frac{\mathrm{B}\sigma_{\mathrm{m}}}{\mathrm{k}T}) \tag{11.10}$$

where σ_{m} is the mean contact stress over the contact surface.

11.3.1.3 Unit 3 (input signal, the shape of the contacting bodies; output signal, contact stress)

Presenting the stress-strain relation of the work material as piecewise linear, one can write: $\mathrm{d}\sigma = (\sigma_{\mathrm{m}}/\mathrm{Z}_{\mathrm{m}})\mathrm{dZ}$, where Z_{m} is the mean Z-coordinate over the contact surface.

The transfer function of the proportional unit 3 can be determined as the proportionality coefficient between σ_m and Z_m:

$$W_3(q) = \sigma_m / Z_m \tag{11.11}$$

With the scheme of Figure 11.7, we can obtain the transfer function of all the system. The tool shape which is given by the equation of tool surface $Z_o = f(X, Y)$ is supposed to be the input signal of the system in Figure 11.7. A function $Z(t) = f(X, Y, Z_o, t)$ characterizes the tool shape after a time t, and can be taken as an output signal. The transfer function of the system can be written as:

$$W(q) = \frac{1}{1 + W_1 W_2 W_3} \tag{11.12}$$

where $W_1,\ W_2,\ W_3$ are the transfer functions of units 1, 2, 3, respectively.

After some rearrangements, we have:

$$W(q) = 1/(1 + C_i \sigma_m v q / Z_m) \tag{11.13}$$

Knowing the transfer function (11.12), one can determine a function, which describes the variations of the tool shape due to the wear. Taking the reverse Laplace transform of the product of the transfer function (11.12) by the Laplace transform of the input signal ($Z_o = \text{constant},\ W(q) = Z_o/q$), we obtain:

$$Z(t) = Z_o \exp(-2C_i \sigma_m Z_o v t / {Z_m}^2) \tag{11.14}$$

where $Z(t)$ is the Z-coordinate of a given point of the contact surface at instant t.

From Equation (11.14) it follows that the greater the initial height of a point on the tool surface, the greater is the wear rate in this point.

11.3.2 Effect of the loading conditions on the tool wear

In order to demonstrate the possible areas of application of the 'black box modeling' method, we consider the influence of the cutting conditions on the tool wear. Consider two regimes of cutting: approach cutting (when the applied load increases linearly with time) and steady state cutting (with constant applied load) (Figure 11.8). The approach cutting corresponds usually to the initial stage of machining processes, whereas the steady state regime corresponds to the 'main' part of the processes.

If the rate of increase of the applied load in the approach cutting is constant, one can write:

$$\sigma_m = ut \tag{11.15}$$

where u is the rate of the increase of the load in the approach cutting. To analyze the effect of the variations of the cutting force on the tool wear, the block diagram model of the system (Figure 11.7) is represented as shown in Figure 11.9. Here, the input signal is the mean contact stress over the contact surface, and the output signal is the wear rate. In order

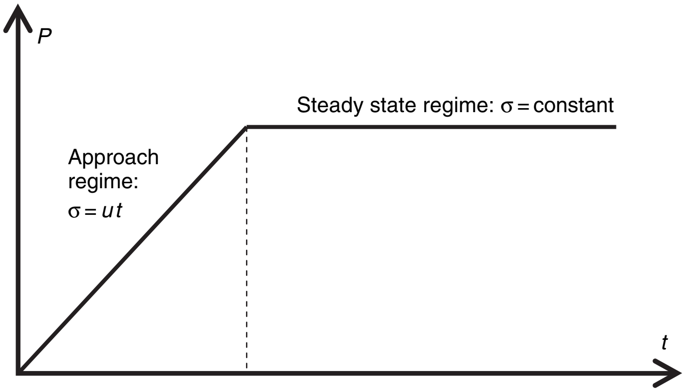

Figure 11.8 *Approach and steady state cutting regimes: cutting force plotted versus time.*

to obtain the wear rate versus time relation, we have to determine the transfer function of the system shown in Figure 11.9. The wear rate versus time relation is determined as follows:

$$i(t) = L^{-1}[W(q)L(\sigma)] \tag{11.16}$$

where L() and L^{-1}() are Laplace transform and inverse Laplace transform, respectively. Substituting Equations (11.12)–(11.14) into (11.16), we have (for the case of the applied load which increases in proportion to time, see Equation (11.15):

$$i_1(t) = \frac{uZ_\mathrm{m}}{v\sigma_\mathrm{m}}[1 - \exp(-\frac{C_i v\sigma_\mathrm{m}}{Z_\mathrm{m}}t)] \tag{11.17}$$

This function describes the time dependence of the wear rate in approach cutting.

In steady state cutting, the cutting force is assumed to be constant: σ_m = constant. The manipulations, similar to those above, give:

$$i_2(t) = C_i\sigma_\mathrm{m}\exp\left(-\frac{C_i v\sigma_\mathrm{m}}{Z_\mathrm{m}}t\right) \tag{11.18}$$

From Equations (11.17) and (11.18) it follows that:

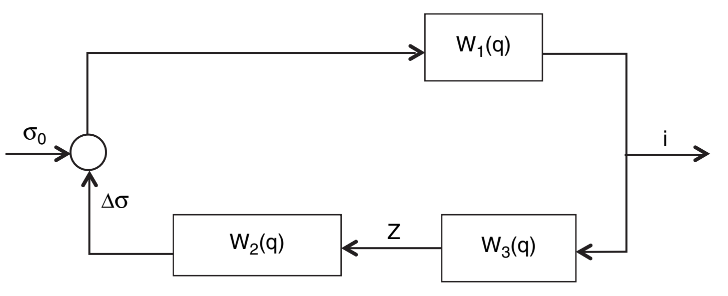

Figure 11.9 *Block diagram of 'black box model' of variations of the wear rate, depending on the applied load.*

- when the applied (cutting) force increases in proportion to time, the wear rate is increasing as well;
- when the applied force is constant, the wear rate decreases slowly with time.

Thus, the *tool wear can be controlled by varying the contact force in cutting*.

On the basis of the model, we can further investigate the influence of tool-to-work vibrations on the tool wear. Let the variations of the load be given in the following form:

$$\sigma_{\rm m}(t) = \sigma_{\rm m0} + \Delta\sigma \sin \omega t \tag{11.19}$$

where $\Delta\sigma$ and ω are the amplitude and the frequency of the tool vibrations. Taking this function as the input signal of the system in Figure 11.9, we obtain after some manipulations:

$$i(t) = i_1(t) + \frac{C_i \Delta\sigma\omega}{\xi + \omega^2/\xi}[\exp(-\xi t) + (\xi/\omega)\sin \omega t - \cos \omega t] \tag{11.20}$$

where $\xi = C_i v_{\sigma \rm m}/Z_m$. From Equation (11.20) it follows that the lower the amplitude and the greater the frequency of the vibrations, the lower is the tool wear rate.

11.3.3 Experimental verification: approach and steady state cutting regimes

In order to verify the results from this section, we use the experimental data by Vulf (Vulf, 1973). Vulf studied the cutting tool wear in interrupted cutting of steels. The following experiments were carried out. Specimens from steel X8CrNiMo15.4 were machined by hard alloy tools (hard alloy with 5 % TiC and 10 % Co), with the depth of cut 0.5 mm, cutting rate 150 m min^{-1}, and feed 0.21 m rev^{-1}. The cutting process was interrupted every 1, 5 and 10 min (first, second and third sets of experiments, respectively). Thus, the total durations of approach cutting for the second and third sets of experiments were 5 and 10 times smaller, respectively, than for the first one. The total time of cutting in each set of experiments was 30 min. The flank wear of the tools was measured after every period of cutting. To compare the experimental data with the above theoretical results, we determined the dimensionless values of the tool wear. These values were calculated as the tool wear, measured in the first and second series of experiments (duration of cutting period 1 and 5 min, respectively) divided by the tool wear, measured in the third series (10 min period):

$$\int_0^{t_{\rm A}} i_1(t){\rm d}t \Big/ \int_0^{t_0} i_1(t){\rm d}t \tag{11.21}$$

where $t_{\rm A}$ is the duration of approach cutting when the process is interrupted every 1 or 5 min, t_0 is the same, when the process is interrupted every 10 min. Using dimensionless values makes it possible to apply Equations (11.17) and (11.18) without calculating the coefficient C_i, which depends on the physical mechanisms of wear. The values of tool wear obtained experimentally and calculated with Equations (11.17) and (11.18) are presented in Figure 11.10.

The difference between theoretical and experimental results is within limits of 20 %. Thus, although only a simple phenomenological model was used, the theoretical results are in good qualitative agreement with the experiments.

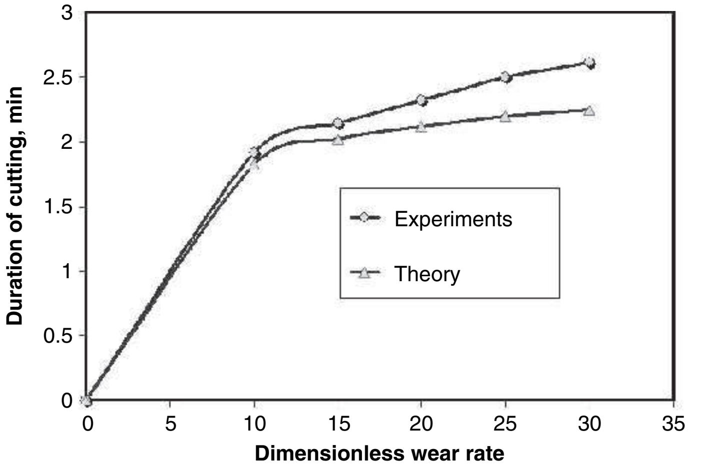

(a)

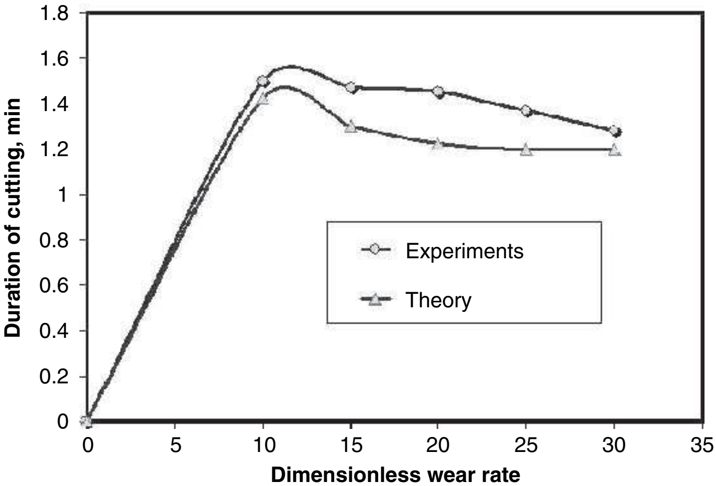

(b)

Figure 11.10 *Variations of the wear rate in interrupted cutting of steels: experiments (Vulf, 1973) and simulations. Cutting interrupted (a) every 1 min and (b) every 5 min.*

11.4 Microscale scattering of the tool material properties and the macroscopic efficiency of the tool

In this section, we consider the effect of the scattering of local properties of contacting bodies (e.g. strengths, wear resistances, shape parameters) on the damage and wear resistances. First, we analyze the effect of the indenter shape on the damage growth and fragmentation of materials under indentation, and demonstrate that shapes of tools that destroy, fragment or fracture a material can be characterized by a statistical parameter of the probability distributions of contact stresses.

Then, we analyze the effect of statistical variations of local properties of the tool material on the damage growth in the work material under indentation. Generalizing the results of the studies, we will be able to formulate some ideas on the optimal design of tools that destroy, fragment or fracture a material (e.g. drilling tools).

11.4.1 Statistical description of tool shapes

Now, we consider the effect of indenter shapes on the damage growth in the material under indenter. Let us look at the three simplest forms of indenters: spherical, conical and cylindrical ones (Figure 11.11). Although the shapes of indenters differ and the peculiarities of destruction for each of the indenters have been well investigated, there is no quantitative parameter ('input' or a priori characteristic) which can characterize the form, serve as a criterion for their comparison and which may be generalized for more complex cases of the tool/material interaction.

The experiments on the indentation of differently shaped indenters in rock specimens, described by Zhlobinsky (Zhlobinsky, 1970), have shown that the volume of craters of spalled rock is maximal for conical, minimal for spherical and medium for cylindrical indenters (the ratio was about 2.1:1:1.56). If one compares the result with the contact stress distributions for these cases (Galin, 1961), one can see that the maximal volume of the indentation crater corresponds to the most sharp curve of contact stress distribution, whereas the minimal volume corresponds to the most homogeneous contact stress distribution.

One can suppose that the degree of 'sharpness' (i.e. nonhomogeneity) of the contact stress distribution can be taken as a parameter which determines the intensity of rock fragmentation (in this case, the volume of crater). Mishnaevsky Jr (Mishnaevsky Jr, 1996a, 1998a,b) suggested to characterize the 'sharpness' of this distribution quantitatively by the *statistical entropy of the contact stress distribution*.

Let us suppose that the contact stress distribution function is given in the following general form:

$$\sigma_c = F(x,\ y,\ z) \tag{11.22}$$

where σ_c is the contact stress in a point and x, y, z are the coordinates of a contact point. The function (11.22) is determined by the tool shape and properties of contacting materials. Peaks of this function correspond to stress concentrators on the tool (indenter)

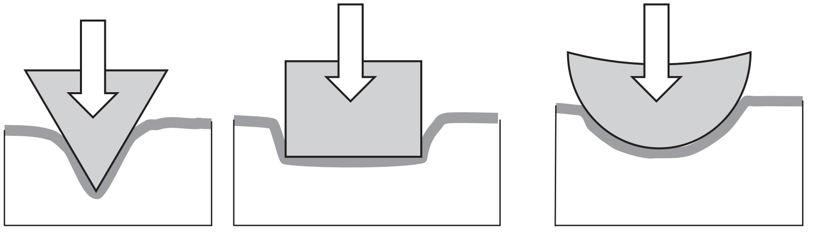

Figure 11.11 *Forms of indenters.*

surface. Discretizing the range of the contact stress variation, one can obtain from Equation (11.22) the probability distribution of contact stresses over the contact surface:

$$p(\sigma_c) = \frac{1}{N_L} \sum_j Y\,[F(x, y, z); \sigma_c] \tag{11.23}$$

where $p\ (\sigma_c)$ is the probability that the contact stress in a point is equal to the value σ_c, N_L is the amount of the discretization levels of σ_c, j is the number of contact points, $Y\,[]$ is the step function, $Y\,[X_1; X_2] = 1$, when $X_l = X_2$ and is equal to 0, otherwise.

The statistical entropy of the contact stress distribution can be calculated by:

$$H_c = -\sum_{\sigma_c} p(\sigma_c)\ \ln\ p(\sigma_c) \tag{11.24}$$

The greater the parameter H_c, the less homogeneous the contact stress distribution. This value characterizes the 'sharpness' (nonhomogeneity) of contact stress distribution for arbitrary function F, and thus, for arbitrary tool shape. Table 11.1 shows the interrelations between the tool shape, probability distributions of the contact stresses and the statistical entropies of these distributions on a few examples.

Consider now the relation between the degree of the heterogeneity of the contact stress distribution H_c and the damage in the work material. Let us suppose that some volume V of a material is loaded by an intricately shaped tool. The damage growth under contact loading of many (first of all, brittle) materials proceeds as follows: first, the defects (microcracks) form at the contact surface, in the vicinity of stress concentrators, and then the microcracks begin to grow, microcracks deeply under the contact surface form, they coalesce, and that leads to spalling and to the fragmentation of the volume (Mishnaevsky Jr, 1995c, 1998a). We assume that the initial defects are formed in the points on the contact surface when the normal contact stress in the contact point exceeds some critical level. Then, one can calculate the initial damage as follows:

$$R_o = \int_{\sigma_{cr}}^{\infty} p(\sigma_c) \mathrm{d}\sigma_c \tag{11.25}$$

Table 11.1 *Examples of the interrelation between the indenter shape and the probability distribution of the contact stresses.*

Shape of an indenter	Type of the probability distribution	H_c	Meaning
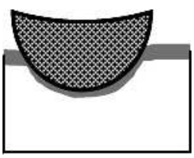	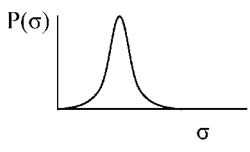	low	The stress is almost constant over all the contact surface
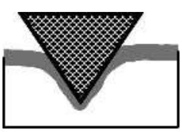	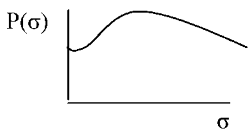	high	The stress distribution is very heterogeneous on the contact surface

where R_o is the initial defect density on the contact surface and σ_{cr} is the critical contact stress.

As a first approximation, one can suppose that the function $p(\sigma_c)$ is given by the exponential function (more general cases will be considered below). For this case, the statistical entropy and the expectation of the probability distribution are related by a linear function (Wilson, 1970; Stratonovich, 1975). Substituting the formula of exponential distribution into Equation (11.24) and taking into account the relation between the entropy and expectation of the exponential distribution, one can obtain the following relation between the surface damage R_o in the material and the statistical characteristics of tool shape:

$$R_o \sim \exp(\text{constant}^* H_c) \tag{11.26}$$

During the initial stage of the tool/material interaction, the surface damage R_o is equal to the damage parameter in the material.

Consider now damage evolution in material. Using any appropriate damage evolution law, one may determine the damage parameter (defect density in the material) from the initial damage parameter (R_o). For instance, integrating Lemaitre's damage evolution law (Lemaitre, 1992) (an oversimplification in this case), one can obtain after some manipulations:

$$R = 1 - [(1 - R_o)^3 - 3W]^{1/3} \tag{11.27}$$

where $W = (1/E)\int_t C\sigma^2 \mathrm{d}t$ is a function of loading conditions, E is the Young modulus, C is a coefficient which includes the triaxility function, the damage threshold function, strain rate and material constants. Apparently, R will be an increasing function of R_o in the framework of any damage model.

Equations (11.25)–(11.27) relate the shape of a tool, which is characterized by the statistical entropy of contact stress distribution, and the damage (defect density) in the work material. From these equations it follows that the *greater the statistical entropy of the contact stress distribution over the contact surface, the greater the microcrack density in the work material (at the same load), and therefore the greater the ability of the tool to destroy, fragment or fracture a material*.

Thus, parameter H_c can be considered a *general (since it is independent of the tool shape) characteristic of the tool shape.*

In order to investigate the influence of the parameter H_c on the intensity of the material destruction in the general case, a series of *numerical experiments* was carried out. A number of contact stress distributions with different parameters H_c, each corresponding to some indenter shape, was generated. Since the damage growth rate is an increasing function of the damage parameter (Lemaitre, 1992), we used here the initial damage (in this case, surface damage) as a characteristic of the intensity of the destruction of the work material.

The contact stress distribution [i.e. function (11.22)] can be presented as a power function in a rather general case:

$$\sigma_c(x) = q_1 (x/a_c)^{q_2} \tag{11.28}$$

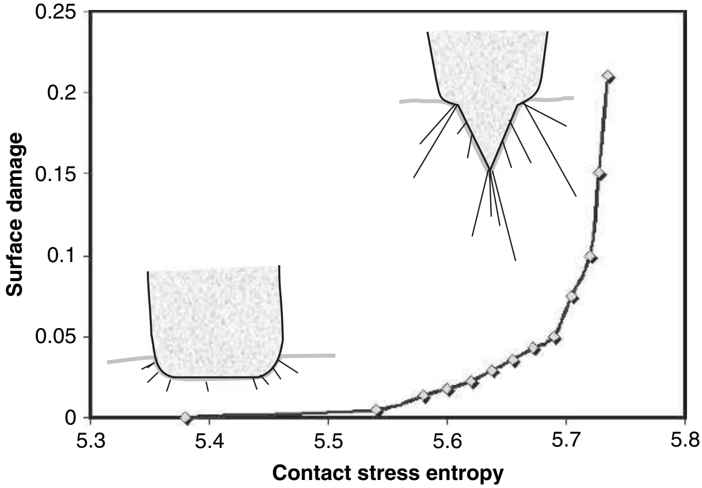

Figure 11.12 *Initial damage plotted versus the contact stress entropy.*

where $2a_c$ is the diameter of the contact area, q_2 is a power coefficient which determines the shape of the contact stress distribution (if $q_2 > 1$, the tool is extremely sharp; the case when $0 < q_2 < 1$ is more realistic: in this case, the tool has a convex surface), q_1 is a coefficient which depends on the applied load and x is a distance between a point and the axis of symmetry of the tool. The applied force is supposed to be constant. The multiplier q_1 is determined by integrating Equation (11.28):

$$q_1 = (q_2 + 1)P/(a_c^{q_2+1}) \tag{11.29}$$

where P is the applied load. In the simulations, the values of initial damage R_o and the contact stress entropy were calculated by Equations (11.26) and (11.24). The coefficient q_2 was varied from 0.25 to 1.8. The following input data were used: $2a_c = 10$, $P = 25$, the number of quantifying levels for stress $N_L = 800$, the step of discretization of contact stress was 0.1, the contact surface was discretized for 1000 elements, the average local strength of the material σ_{cr} was 170. The surface damage R_o plotted versus the contact stress entropy is given in Figure 11.12. From Figure 11.12, one can see that the surface damage increases monotonically with increasing statistical entropy of contact stresses.

Therefore, one can conclude, that the *destruction ability of a tool increases with increasing the statistical entropy of contact stress distribution.*

11.4.2 Effect of the scattering of the tool material properties on the efficiency of the tool

Now let us analyze the wear of the tool and its influence on the tool efficiency. Here we consider a cutting tool, the wear of which is controlled by the mechanical processes (surface fatigue). In Section 11.3, the mathematical model of the tool wear as a transient in a control system with feedbacks was presented. In order to study variations of the contact stress distribution during tool wear, the dynamical system which describes the wearing tool can be transformed in the following manner: the initial contact stress becomes the input signal of the block diagram in Figure 11.7; the output signal is current local contact stress; all elements of the system become feedback elements. Taking the initial contact stress as an input and the current contact stress as an output signal of the system, one may derive the following formula:

$$\sigma_c = \sigma_{c0} \ \exp\left(-C_w \ \sigma_{c0}\right) \tag{11.30}$$

where σ_{c0} is the initial contact stress in a point of the contact surface (before the tool shape begins to change due to wear) and C_w is a coefficient, characterizing the local wear resistance and depending on the local physical properties of the tool working surface, cutting conditions, etc.

As seen from Equation (11.30), the contact stresses decrease due to the wear and approach to some mean level. The rate of the approach is higher, the higher the initial contact stress. It means that the degree of heterogeneity of the stress distribution on the contact surface is reduced, and, after a lapse of time, the contact stresses will be approximately the same over all the contact surface. As shown above, the intensity of the destruction of the work material under mechanical loading depends on the degree of heterogeneity of contact stresses on the contact surface: the efficiency of a tool is higher, the higher the heterogeneity of the contact stress distribution on the surface (i.e. the high stress concentration in some areas, and low stresses in other areas). Therefore, we come to the evident conclusion that the wear of a tool will lead to a reduction in its efficiency.

This conclusion is, however, based on the assumption that the properties of the material are constant over the contact surface: $C_w =$ constant. For instance, if the value C_w and contact stress are related by $C_w \sim 1/\sigma_c$, the degree of the heterogeneity of stress distribution on the contact surface will remain constant.

Let us analyze the redistribution of contact stresses in the case of constant and randomly varied local properties of the material C_w. First, we consider the case of a homogeneous tool material: $C_w =$ constant over all the contact surface. At the initial stage of the loading, the contact stress distribution is supposed to be described by Equation (11.28). The redistribution of contact stresses due to the wear is described with the use of Equation (11.30). The values of initial damage as well as the contact stress entropy are calculated with Equations (11.25) and (11.26). The power coefficient q_2 characterizing the shape of nonworn tool is taken to be 1. The average local strength σ_{cr} of the work material is 15. The number of levels N_L, the width of contact surface and the applied force are the same as above. The coefficient C_w is varied from 2/30 to 7/30. The contact stress entropy plotted versus the value C_w is given in Figure 11.13. One can see that the contact stress entropy (which characterizes the sharpness of the tool, and determines the intensity of the work material fragmentation) decreases with increasing the tool dulling rate.

Now we consider the case, when the tool is made from a heterogeneous material, so that the wear resistances and strengths of different points on the contact surface are randomly distributed. Calculations, similar to those above, but with randomly varied coefficients C_w, have been carried out. It was supposed that the tool material consists of four components, the parameters C_w of which differ and are equal to 0.05, 0.1, 0.15 and 0.2. The volume content of each component was varied from 0.1 to 0.7. In order to characterize the degree of scattering/heterogeneity of the local properties of the tool

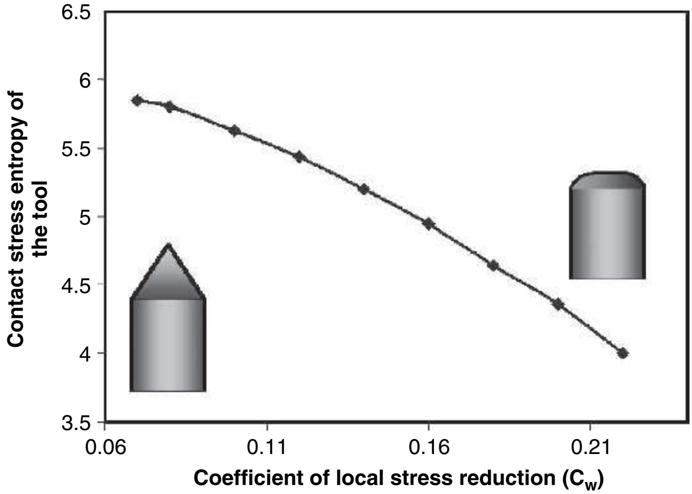

Figure 11.13 *Contact stress entropy plotted versus the coefficient C_w (for the case C_w = constant).*

surface, the statistical entropy of the probability distribution of phase volume contents was used:

$$H_w = \sum_j vc_j \log vc_j \tag{11.31}$$

where $j = 1, 2, 3, 4$ is the number of a constituent in the material and vc_j is the volume content of the jth component.

Figure 11.14 gives the statistical entropy of contact stress distribution (corresponding to the instant of time $t = 1$) plotted versus the entropy of local properties of the tool surface. One can see that the greater the heterogeneity/scattering of local properties on the tool surface, the greater the contact stress entropy (i.e. the sharpness of the tool) even after a lapse of time. One can conclude that the *heterogeneity of local wear resistances over the contact surface leads to the self-sharpening of the tool, and may ensure therefore the long term high ability of the tool to destroy, fragment or fracture a material.*

Practically, the high efficiency and the long term high ability of a tool to destroy, fragment or fracture a material can be ensured, if the working surface of the tool consists of a number of components with different wear resistances. An example of such a tool is the ‘squirrel tooth’ type cutter (Mishnaevsky Jr, 1998a): the cutter consists of regions with different strengths and wear resistances. Components, placed in the areas of expected high stresses, are very strong, while other components are weak and have a low wear resistance. The intensive wear of the weak regions ensures the constant shape and long term sharpness of the teeth.

11.4.3 Principle of the optimal tool design

The conclusion that an increase in the statistical entropy of contact stress distribution leads to the improvement of the destructing ability of tools was obtained in Section 11.4.1

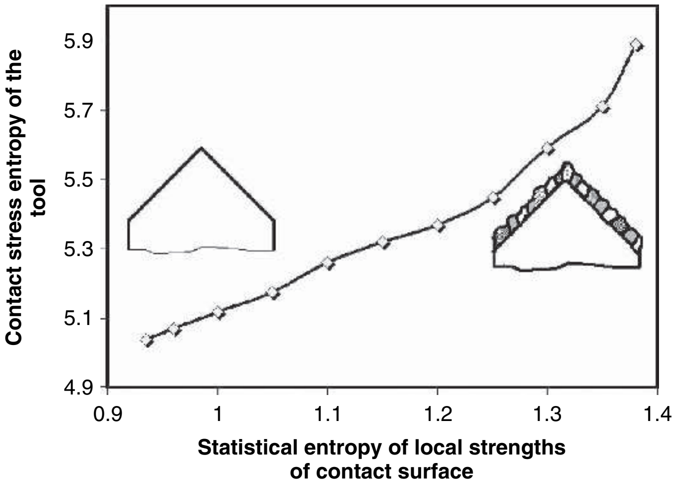

Figure 11.14 *Contact stress entropy plotted versus the entropy of intensities of wear resistances.*

on the basis of the phenomenological analysis of the interrelations between this parameter and the damage growth in indentation, and then verified in numerical experiments. In Section 11.4.2, it was shown that the self-sharpening of a tool can be achieved, if the mechanical properties of different points of the tool working surface are randomly distributed.

Generalizing these results, one may assume that *an improvement of the efficiency of a tool in a general case can be achieved by introducing some heterogeneity into the construction of the tool* (for instance, uneven tool work surface, heterogeneous arrangements of destructing elements on a tool, heterogeneity of local wear resistances or distances between teeth).

In order to verify this assumption, we carried out an analysis of about 250 patents in the area of drilling tool improvement, searching for common approaches and ideas in different patents. As a result of the analysis, the patents were divided into seven groups, corresponding to the main ideas used in the technical solutions. The results of the analysis and some examples are given in Table 11.2. Correlating the ideas from all of the groups, one can see that all the considered methods of the tool improvement consist of introducing some heterogeneity (in other words, information) in the tool constructions. In all the cases, a tool is improved by increasing the unevenness of distributions of different local parameters (teeth orientations, distances between teeth, mechanisms of loading, wear resistances, etc).

Generalizing the results of the patent analysis and the conclusions made in Sections 11.4.1–11.4.3, one can formulate the following general principle of the optimal design of destructing (e.g. drilling) tools: *the efficiency of destructing tools can be increased by increasing the heterogeneity (degree of scattering) of distributions of different local parameters of the tool.* In terms of the theory of information (Stratonovich, 1975), it can be formulated as follows: the efficiency of a complex tool can be improved if the statistical entropies of distributions of local parameters of the tool are increased.

Table 11.2 *Technical solutions in the area of drilling tool design.*

Main ideas	Some examples
1. Unevenness of the tool work surfaces: convex or concave cutting faces or prismatic or cylindrical lugs on cutting face; stepped working surface; cavities, bevels, slopes on the tool work surface	No. 1044765A, 1023062A, 1323706A1, 623958 (Russia/USSR) No.1284539 (UK) No. 57–35357 (Japan)
2. Asymmetry of the tool working surface about the direction of tool movement: a cutting face or its parts are inclined to the cutting vector	No. 723123 and 1046465A (Russia/USSR)
3. Dissimilar shapes or orientations of different teeth on the same bit: combination of radial and tangential cutters; different cutting and wedge angles on different teeth on the same tool; different materials of inserts; the strength of inserts varies from the axis of the auger to periphery	No. 395559, 153680A1, 1366627 Al (Russia/USSR)
4. Irregular arrangement of teeth on a bit: clustered arrangements of teeth or cutters, varied distances between teeth	No. 3726350, 3158216 (USA) No. 1472623A1 (Russia/USSR)
5. Elements with different mechanisms of loading on the same bit are combined: combination of mobile and fixed elements, or rotating and progressively moving elements, or cutting and impact elements	No. 52–48082 (Japan) No. 697711 (USSR)
6. Different wear resistances or different points or tool working surface: layers with different strengths in a cutter; cavities specially introduced in the tool surface	No. 714003, 281349, 145496, 693000, 609884 (USSR)
7. Self-sharpening and self-organization of a tool	No. 4230193 (USA) No. 717327, 719192 (USSR)

Among the parameters are the contact stresses (for increasing the sharpness of the tool), wear resistances local of tool work surface (durability of the tool, self-sharpening of the tool and high efficiency of the drilling tool even after a lapse of time of drilling), orientations of destructing elements (teeth) and distances between them, rates, directions and mechanisms of loadings by each element of a multitoothed tool.

References

Archard, J. F. (1953). Contact and rubbing of flat surfaces, *Journal of Applied Physics*, **24** (1), 18–28.

Axen, N. and Jacobson, S. (1994a). Transitions in the abrasive wear resistance of fibre/and particle/reinforced aluminium, *Wear*, **178**, 1–7.

Axen, N. and Jacobson, S., (1994b). A model for the abrasive wear resistance of multiphase materials, *Wear*, **174**, 187–199.

Bauccio, M. (1994) *ASM Engineered Materials Reference Book*, 2nd Edn, ASM International, Materials Park, OH.

Chen, X. and Rowe, W. B. (1996). Analysis and simulation of the grinding process. Part 1. generation of the grinding wheel surface, *International Journal of Machine Tools and Manufacture*, **36** (8), 871–882.

Chen, X. and Rowe, W. B. (1998) Analysis and simulation of the grinding process. Part 1. Generation of the grinding wheel surface, Part 2. *Mechanics of Grinding*, **36** (8), 883–896; Part 4, Effects of wheel wear process, *International Journal of Machine Tools and Manufacture*, **38** (1–2), 41–49.

Cho, S-J., Hockey, B. J., Lawn, B. R. and Bennison, S. J. (1989). Grain-size and R-curve effects in the abrasive wear of alumina, *Journal of American Ceramics Society*, **72**, 1249–1252.

Friedrich, K., Varadi, K., Goda, T. and Giertzsch, H. (2002). Finite element analysis of a polymer composite subjected to a sliding steel asperity, Part II. Parallel and anti-parallel fibre orientations, *Journal of Materials Science*, **37** (16), 3497–3507.

Galin, L. A. (1961). *Contact Problems in the Theory of Elasticity*, Translated/Eds H. Moss and I. N. Sneddon, North Carolina State College.

Garkunov, D. N., Kragelski, I. V. and Polyakov, A. A. (1969). *Partial Transfer in Friction Units*, Transport, Moscow.

Hegadekatte, V., Huber, N. and Kraft, O. (2005). Finite element based simulation of dry sliding wear, *Modelling Simulations in Materials Science and Engineering*, **13**, 57–75.

Khrushchov, M. M. and Babichev, M. A. (1970). *Abrasive Wear*, Nauka, Moscow.

Kwok, J. and Lim, S. C. (1999). High speed tribological properties of some Al/SiCp composites: Wear mechanisms, *Composites Science and Technology*, **59**, 63–75.

Lancaster, J. (1963). The formation of surface films at the transition between mild and severe metallic wear, *Proceedings of the Royal Society of London, Series A*, **273**, 466–483.

Lawn, B. R. (1975b). A model for the wear of brittle solids under fixed abrasive conditions, *Wear*, **33**, 369–372.

Lee, G. Y., Dharan, C. K. H. and Ritchie, R. O. (2002). A physically-based abrasive wear model for composite materials, *Wear*, **252**, 322–331.

Lemaitre, J. (1992). *A Course on Damage Mechanics*, Springer, Berlin.

Lhymn, C. (1987). Effect of normal load on the specific wear rate of fibrous composites, *Wear*, **120** (1), 1–27.

Lhymn, C., Tempelmeyer, K. E. and Davis, P. K. (1985). The abrasive wear of short fibre composites, *Composites*, **16**, 127–136.

Malkin, S. (1989). *Grinding Technology: Theory and Applications of Machining with Abrasives*, Ellis Horwood Limited, Chicester.

Mishnaevsky L. (1982). *Wear of Grinding Wheels*, Naukova Dumka, Kiev.

Mishnaevsky, L. (1985). Optimization of parameters of superhard drilling tools in grinding metals, *Journal of Superhard Materials*, **7** (3), 45–49.

Mishnaevsky Jr, L. (1994). Investigation of cutting of brittle materials, *International Journal of Machine and Manufacture*, **34** (4), 499–505.

Mishnaevsky Jr, L. (1995b). Mathematical modelling of wear of cemented carbide tools in cutting brittle materials, *International Journal of Machine Tools and Manufacture*, **35** (5), 717–724.

Mishnaevsky Jr, L. (1995c). Physical mechanisms of hard rock fragmentation under mechanical loading: a review, *International Journal of Rock Mechanics and Mining Sciences*, **32** (8), 763–766.

Mishnaevsky Jr, L. (1996a). A new approach to design of drilling tools, *International Journal of Rock Mechanics and Mining Sciences*, **33** (1), 97–102.

Mishnaevsky Jr, L. (1998a). *Damage and Fracture in Heterogeneous Materials*, Balkema, Rotterdam.

Mishnaevsky Jr, L. (1998b). Rock fragmentation and optimisation of drilling tools, in: *Fracture of Rock*, Ed. M. H. Aliabadi, Computational Mechanics Publications, Ashurst, 167–203.

Molinari, J. F., Ortiz, M., Radovitzky, R. and Repetto, E. A. (2001). Finite-element modeling of dry sliding wear in metals, *Engineering Computations*, **18** (3/4), 592–609.

Shaw, M. C. (1984). *Metal Cutting Principles*, Oxford University Press, Oxford.

Stratonovich, R. L. (1975). *Theory of Information*, Sovetskoye Radio, Moscow.

Tjong, S. C., Wu, S. Q. and Liao, H. C. (1997). Wear behaviour of an Al-12% Si alloy reinforced with a low volume fraction of SiC particles, *Composite Science and Technology*, **57**, 1551–1558.

Tsukizoe, T. and Ohmae, N. (1983) Friction and wear of advanced composite materials, *Fibre Science and Technology*, **18**, 265–286.

Usui, E., Shirakashi, T. and Kitagawa, T. (1978). Analytical prediction of three dimensional cutting process, part 3: cutting temperature and crater wear of carbide tool, *Journal of Engineering for Industry*, **100** (5), 236–243.

Van der Bosch, P. P. J. and Van den Klauw, A. C. (1994). *Modeling, Identification and Simulation of Dynamical Systems*, CRC Press, London.

Vulf, A. M. (1973). *Cutting of Metals*, Mashinostroyeniye, Leningrad.

Wilson, A. G. (1970). *Entropy in Urban and Regional Modelling*, Pion Ltd, London.

Xie, L. I. (2004). Estimation of two-dimension tool wear based on finite element method, PhD Thesis, University of Karlsruhe.

Yan W., Busso E. P. and O'Dowd N P. (2000). A micromechanics investigation of sliding wear in coated components, *Proceedings of the Royal Society of London, Series A*, **456**, 2387–2407.

Zhlobinsky, B. A. (1970). *Dynamic Fracture of Rocks Under Indentation*, Nedra, Moscow.

Zum Gahr, K. -H. (1987). *Microstructure and Wear of Materials*, Tribology Series 10, Elsevier, Amsterdam.

12

Future fields: computational mesomechanics and nanomaterials

Nanostructured materials demonstrate many unusual properties, which may be very important for applications in different areas of industry. Among the peculiar properties of the materials, one can mention the increased hardness and strength of nanocrystalline metals, improved ductility and toughness, and low temperature superplasticity in nanocrystalline ceramics, and the combination of the increased toughness and strength in multiphase nanomaterials. According to Gleiter (Gleiter, 2000), the differences between the properties of nanostructured and coarse-structured materials are determined by both the low dimensions of grains and the high volume content of the boundary surface phase in nanomaterials. Some nanostructured materials demonstrate the inverse Hall–Petch effect: their strength increases with increasing grain size. Generally, the discovery and utilization of nanostructured components and phases opens many new opportunities in the optimization of the material properties.

The theory of properties and strength of nanostructured materials is still in development. However, it is remarkable that the methods of continuum mechanics, micromechanics and mesomechanics of materials find their application in the analysis of nanostructured materials.

In the case of pure metallic nanomaterials, the application of micromechanics in the analysis of nanomaterials is based often on the *two-phase model* of a nanocrystalline material, with grains and boundaries, as phases. Suryanarayana (Suryanarayana, 1995) noted in his review that 'nanocrystalline metals can be considered to consist of two structural components – the numerous small crystallites . . . and a network of intercrystalline region.'.

The deformation and the inverse Hall–Petch effect have been studied using the 'rule of mixture' in several works. Carsley *et al.* (Carsley *et al.*, 1995) suggested a model of the strength of nanomaterials which is based on the 'rule of mixture'. A material is considered as consisting of two phases: grains with bulk props and the boundary phase, which represent an amorphous glass material. With this model, Carsley and colleagues studied the grain size softening in nanomaterials.

Kim (Kim, 1998), Kim *et al.* (Kim *et al.*, 1998, 2000), Hong *et al.* (Hong *et al.*, 2000) and Kim and Bush (Kim and Bush, 1999) suggested a composite material model for the analysis of the mechanical behavior of nanomaterials. The micromechanical (unit cell) model of a nanostructured material developed by Kim (Kim, 1998), and consisting of a crystallite, boundary phase and triple line junctions, is shown in Figure 12.1. Using this model and the concept of a critical grain size, Kim and colleagues investigated the plastic behavior of nanomaterials and explained the inverse Hall–Petch relation of nanostructured materials. Further, they used the 'rule of mixture' to study the hardness of nanocrystalline copper. Analyzing the effect of porosity on the elastic behavior and stiffness of nanomaterials, Kim and colleagues concluded that the porosity effect is even more strongly pronounced than the effect of the grain size.

Another interesting work is the area of the application of continuum/structural mechanics for the analysis of nanomaterials was presented by Li and Chou (Li and Chou, 2002). They suggested to model the covalent nanostructures of materials as frame structures from atoms, while the atomic bonds are considered as load carrying elements and the atoms as nodal points of this structure. The model was verified for the case of graphite and carbon nanotubes. Li and Chou demonstrated that the mechanical properties of nanomaterials can be modeled with the use of continuum and structural mechanics methods, although the physical nature of the bonds can be different from that of macroscale materials.

While the general framework of the micro- and mesomechanics of materials is applicable to the analysis of nanostructured materials, the *micromechanisms of the deformation and strength of nanomaterials* are different from those of bulk materials. In nanostructured

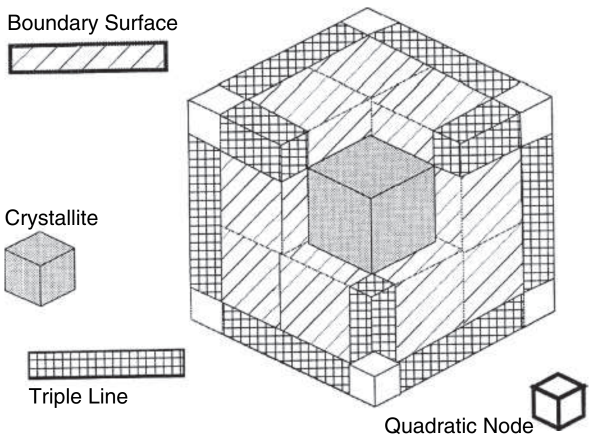

Figure 12.1 *3D micromechanical (unit cell) model of a nanomaterial, consisting of a crystallite, boundary phase, triple line junctions and quadratic nodes, developed by Kim (Kim, 1998). Reprinted from* Scripta Mater., **39***(8), Kim, 'A composite model . . . ', pp. 1057–1061, Copyright (1998), with permission from Elsevier.*

materials, plastic deformation is controlled not (only) by the lattice dislocation motion, as in bulk materials, but rather by the grain boundary sliding and diffusional mass transfer (occurring mostly via the grain boundary diffusion). These effects are associated with the role of the grain boundary phase in nanocrystalline materials (Gutkin *et al.*, 2001; Gutkin and Ovid' ko, 2001; Morris, 2001). To simulate the deformation of nanomaterials, different models of plastic deformation are required.

Pozdnyakov and Glezer (Pozdnyakov and Glezer, 2002) developed an analytical model of the initial stages of the deformation of nanomaterials, based on the analysis of the grain boundary microsliding (GBM) in nanomaterials. This model made it possible to study the effect of the grain size and temperature on the flow stress in the materials. Another model of the deformation behavior of nanomaterials was suggested by Hahn and Padmanabhan (Hahn and Padmanabhan, 1997). Assuming that the plastic flow of nanomaterials is controlled by the mesoscopic grain boundary sliding, they derived an equation for the shear strain rate, and studied the inverse Hall–Petch effect in nanomaterials.

Hasnaoui *et al.* (Hasnaoui *et al.*, 2002) studied the plastic flow of nanomaterials (nano nickel) using molecular dynamics simulations. In their numerical experiments, they observed the formation of shear bands and the motion of grains, and identified the main micromechanisms of deformation: grain–boundary migration, continuity of shear plane via intragranular slip, and rotation and coalescence of grains.

Summarizing, one may state that the continuum mechanics, micromechanics (e.g. 'rule of mixture') and computational micromechanics methods (e.g. micromechanical unit cells) can be successfully employed in the analysis of the strength and mechanical behavior of nanomaterials. One may expect therefore that the analysis of nanostructured materials can become one of the very promising areas of further application of methods, concepts and tools of the computational mesomechanics of composites.

References

Carsley, J. E., Ning, J., Milligan, W. W., Hackney, S. A. and Aifantis, E. C. (1995). A simple, mixtures-based model for the grain size dependence of strength in nanophase metals, *Nanostructured Materials*, **5** (4), 441–8.

Gleiter, H. (2000). Nanostructured materials: basic concepts and microstructures, *Acta Materialia*, **48**, 1–29.

Gutkin, M. Yu. and Ovid'ko, I. A. (2001). *Defects and Plasticity Mechanisms in Nanostructured and Non-crystalline Materials*, Yanus, St Petersburg.

Gutkin, M. Yu., Ovid'ko, I. A. and Pande, C. S. (2001). Theoretical models of plastic deformation processes in nanocrystalline materials, *Reviews on Advanced Materials Science*, **2** (1), 80–102.

Hasnaoui, A., Van Swygenhoven, H. and Derlet, P. M. (2002). Cooperative processes during plastic deformation in nanocrystalline fcc metals: a molecular dynamics simulation, *Physical Review B*, **66**, 184112.

Hong, S. I., Chung, J. H. and Kim, H. S. (2000). Strength and fracture of Cu-based filamentary nanocomposites, *Key Engineering Materials*, **183–187**, 1207–1212.

Kim, H. S. (1998). A composite model for mechanical properties of nanocrystalline materials, *Scripta Materiala* **39** (8), 1057–1061.

Kim, H. S. and Bush, M. B. (1999). The effects of grain size and porosity on the elastic modulus of nanocrystalline materials, *Nanostructured Materials*, **11** (3), 361–367.

Kim, H. S., Suryanarayana C., Kim S. -J. and Chun B. S. (1998). A finite element analysis of mechanical behavior of nanocrystalline copper, *Powder Metallurgy*, **41** (3), 217–220.

Kim, H. S., Sohn, M. -S. and Hong, S. I. (2000). A model on the strengthening and embrittlement of devitrified nanocomposite, *Key Engineering Materials*, **183–187**, 1255–1260.

Li, C. and Chou, T. -W. (2002) A computational structural mechanics appropach to modeling of nanostructures, in: *Proceedings of the 5th World Congress on Compuational Mechanics*, Eds, H. A. Mang, F. G. Rammerstorfer and J. Eberhardsteiner, Vienna, University of Technology, Austria, http://wccm.tuwien.ac.at

Morris, D. G. (2001). Strength and ductility of nanocrystalline materials: what do we really understand?, in: *Proceedings of the 22nd Risϕ International Symposium on Materials Science*, Eds A. R. Dinesen *et al*., Risϕ National Laboratory, Roskilde, pp. 89–104.

Pozdnyakov, V. A. and Glezer, A. M. (2002). Structural mechanisms of plastic deformation in nanocrystalline materials, *Physics of the Solid State*, **44**, 732–737.

Suryanarayana, C. (1995). Nanocrystalline materials, *International Materials Reviews*, **40** (2), 41–63.

13

Conclusions

Performances of composite materials, their strength, toughness and damage resistance can be improved by changing their microstructures. The improvement of microstructures can be realized not only by varying averaged parameters and properties of phases, but also using synergistic effects of the interaction between many microstructural elements and by introducing some heterogeneities into the material microstructures, e.g. localized or graded distributions of phases.

Some promising directions of the optimization of the material properties have been demonstrated in earlier experimental and theoretical investigations. The advantages of gradient microstructures, for instance, have been known for many centuries. Further, the strength and fracture resistance of composite materials can be improved in some cases by reducing sizes of microstructural elements, replacing large inclusions by clusters of small inclusions (so-called 'double dispersion' microstructure), applying coatings, introducing inclusion free layers, arranging the inclusions in networks or in clusters, introducing nanoreinforcements and aligning elongated grains, etc.

Many ideas and hints on the improvement of the composite microstructures can be obtained from the analysis of biomaterials, their structures and mechanical behavior under loading. The review in Chapter 2 leads to some ideas in this direction: staggered arrangement of reinforcing inclusions, reinforcement in the form of bundles of thin fibers, or reinforcement distribution, which follows the expected loading distribution, are some of the bio-inspired ideas on the material improvement.

Computational experiments represent an efficient way to determine optimal microstructures of composites. By systematic numerical testing of different artificial microstructures of composites, one can determine the optimal microstructure which will ensure the required material properties.

The concepts and techniques of the computational analysis of property–microstructure relationships of composites, methods of the incorporation of complex real microstructures of materials into numerical models, and different approaches to modeling damage and

Computational Mesomechanics of Composites L. Mishnaevsky Jr

fracture are reviewed in Chapters 3 and 4. In Chapters 6–11, numerical investigations of the effects of microstructures of different groups of composites on their strength, stiffness and damage resistance are presented. In particular, the computational models of particle reinforced composites with graded and clustered microstructures, interpenetrating phase composites, unidirectional long fiber reinforced composites and machining tools materials have been developed, and tested in numerical experiments. Various potential sources of the improvement of the composite properties have been identified and analyzed: clustered and gradient distribution of microstructural elements (in particular, in view of the increased fracture toughness and damage resistance, respectively), smoothness of the transitional layer in the gradient composites, dimensions of continuous phases in the interpenetrating phase composites, homogeneity of reinforcing elements, etc. The methods and techniques, presented in this book, can be used further in the computational design of optimal composites.

However, some challenges have still to be met on the way to practical applications of the computational mesomechanics in the optimal design of composites. The correct *incorporation of complex 3D heterogeneous microstructures* of materials into numerical models is still one of the main challenges of numerical testing of material microstructures. The resolution of difficult compromises between the limited computational resources and the required fineness of the microstructure representation, as well as between the complex, multilevel, fractal geometries of phases and their discretized continuum models will require further scientific efforts. The development of methods and subroutines for the realistic modeling of *different damage mechanisms* in materials, including void growth, cleavage of brittle inclusions and interface debonding, is still not a fully solved problem, although some new and very efficient methods have been developed recently. Further, the multiscale nature of the deformation and damage in composites, and the interaction between many different physical mechanisms, require the application of multiscale and multiphysical approaches in the modeling.

Index

Note: page numbers in **bold** refer to tables and those in *italic* to figures.

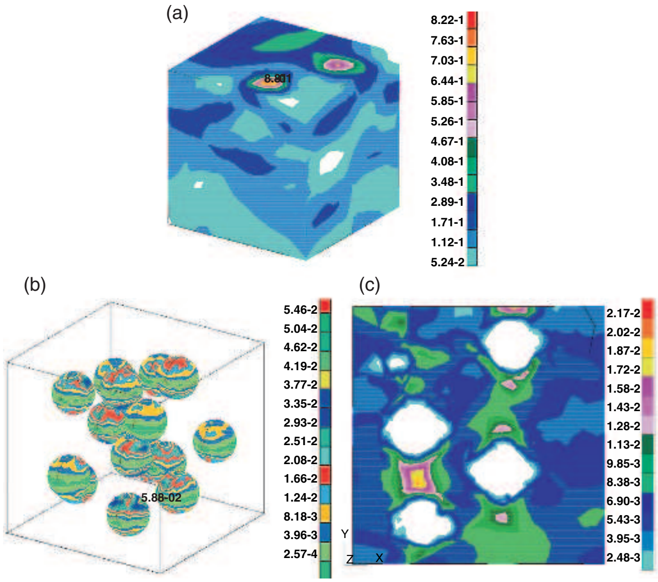

Plate 1 *Distribution of equivalent plastic strains (a) on the box boundary, (b) on the matrix – particle interface and (c) in a vertical section in a microstructure with random particle arrangements (15 particles,* VC = 10 %*). Total strain* = 0.25*. Reprinted from* Acta Mater., **52** *(14), Mishnaevsky Jr, 'Three-dimensional. . . ', pp.4177–4188, Copyright (2004), with permission from Elsevier. (See Figure 6.3)*

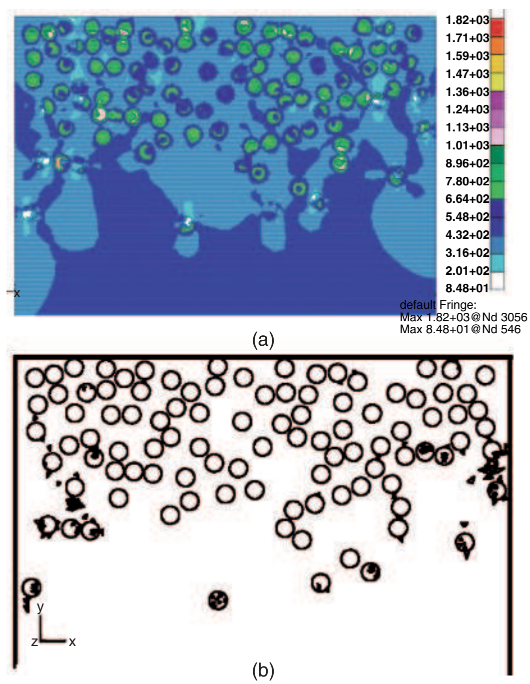

Plate 2 *(a) Von Mises stress distribution in a highly gradient (Grad3) microstructure and (b) damage distribution in the particles and in the matrix (Grad3 microstructure, far field strain 0.29). Reprinted from* Compos. Sci. Technol., **66** *(11–12), Mishnaevsky Jr, 'Functionally . . . ', pp. 1873–1887, Copyright (2006), with permission from Elsevier. (See Figure 7.5)*

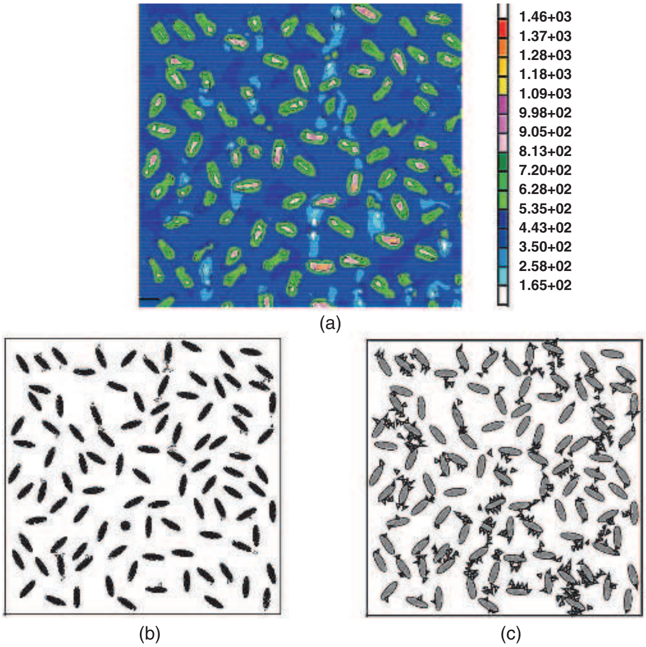

Plate 3 *(a) Von Mises stress* ($u = 0.18\,\text{mm}$) *and (b, c) damage distributions in a composite with randomly oriented elongated particles* ($rr = 0.3$, $u = 0.18\,\text{mm}$ *and* $u = 0.29\,\text{mm}$). *Repriented from* Compos. Sci. Technol., ***66*** *(11–12), Mishnaevsky Jr, 'Functionally . . . ', pp. 1873–1887, Copyright (2006), with permission from Elsevier. (See Figure 7.11)*

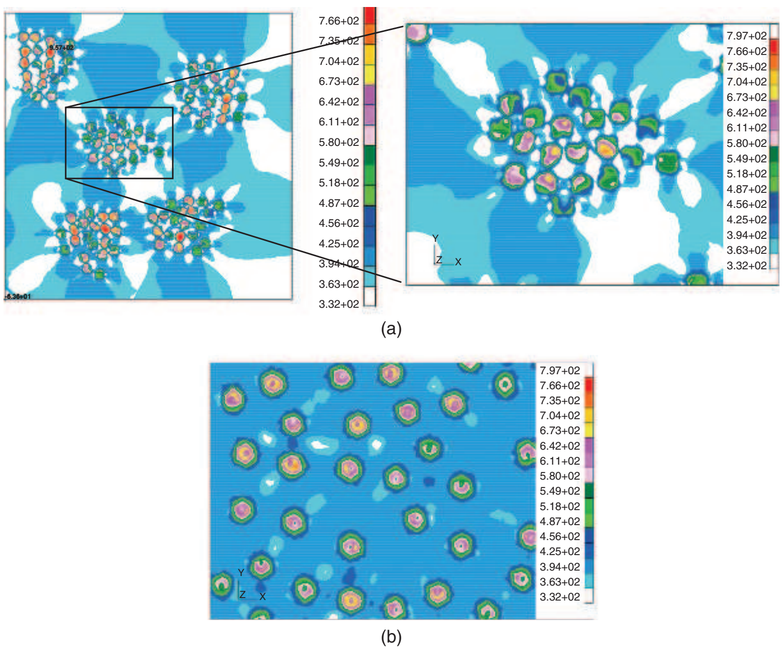

Plate 4 *Von Mises stress distributions for composites with (a) clustered and (b) uniform particle arrangements. Reprinted from* Compos. Sci. Technol., ***64***, *Mishnaevsky Jr* et al., *'Effect of microstructures . . . ', pp. 1805–1818, Copyright (2004), with permission from Elsevier. (See Figure 8.3)*

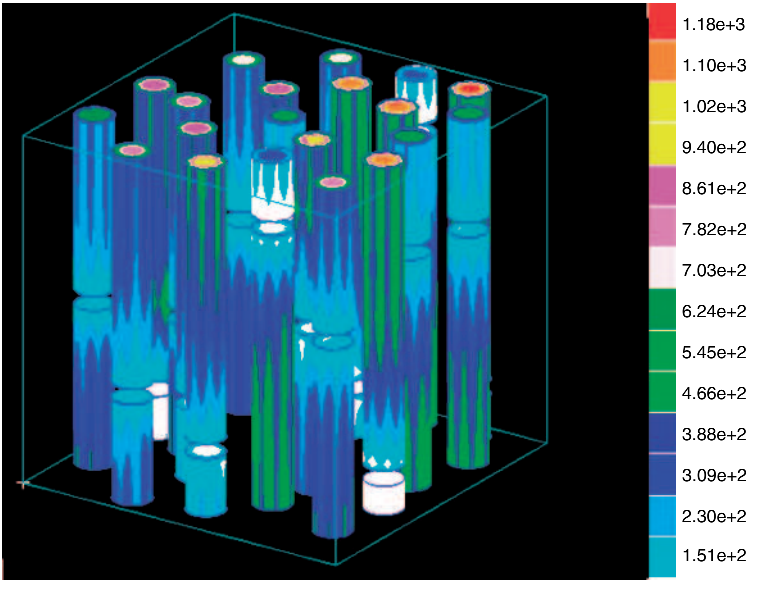

Plate 5 *Von Mises stress distribution in the fibers after the fiber cracking. (See Figure 10.9)*

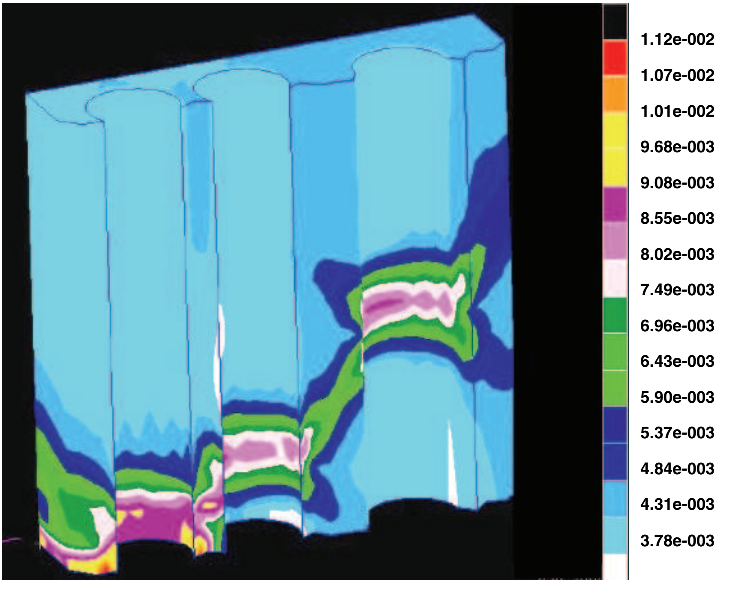

Plate 6 *Von Mises strain distribution in the matrix after the fiber failure. (See Figure 10.10)*

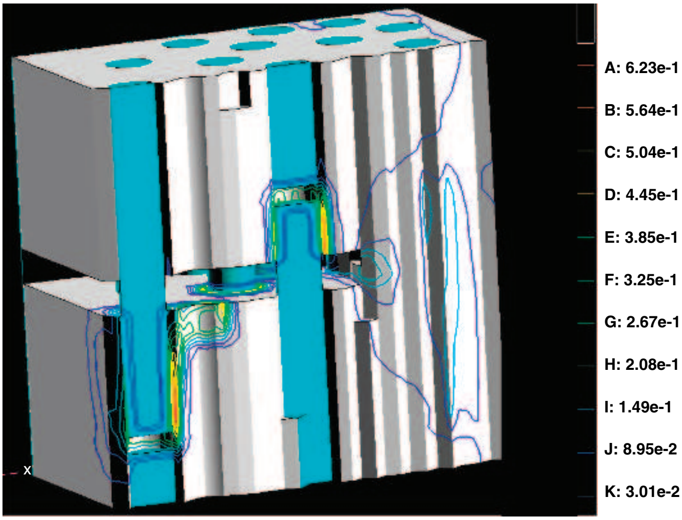

Plate 7 *Von Mises strain distribution in the matrix of a unit cell with a matrix crack after fiber failure. (See Figure 10.13)*

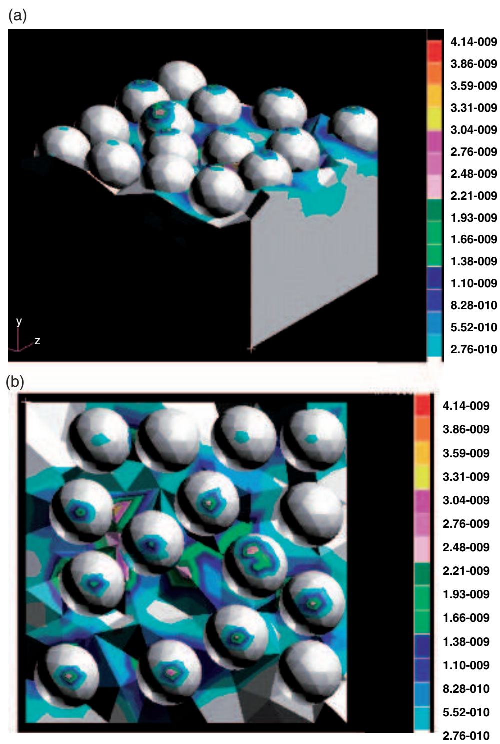

Plate 8 *Von Mises strain distribution in the diamond grains and in the metal bond in grinding: (a) isometric; (b) top view. (See Figure 11.4)*